BIO-INSPIRED ROUTE OF METAL NANOPARTICLES SYNTHESIS AND PHOTOCATALYSTS DOPING

Thesis
Submitted in Partial
Fulfillment of the Requirements for the Degree of

DOCTOR OF PHILOSOPHY

by

Venkatanarasimha Rao Chelli

Department of Chemical Engineering
Indian Institute of Technology Guwahati
June 2018

ABSTRACT

The conventional methods of nanoparticles (NPs) synthesis are sonochemistry, laser ablation, co-precipitation, sol-gel procedures, solvothermal, chemical reduction, and photo-reduction. All these methods are chemical and energy intensive, hence, costly. Thus, a greener route of environmentally benign NPs synthesis has gained tremendous success in recent times. The bio-mediated methods are straightforward and eco-friendly and, the whole process can be carried out at room temperature and pressure. The intercellular synthesis of NPs using microbes often shows a lower synthesis rate as well as difficulty in size and shape control. Such problems can be overcome in many extents by extracting the bio-analytes in a suitable media from the living cells. After that, the particles are synthesized in this media. Faster kinetics and minimization of aggregation of particles are the main challenges of the bio- and bio-mediated processes.

Sechium edule, fruits of a perennial climber, is rich in ascorbic acid (AA 294 mg/kg dry fruit). In the first part of this work, the bio-analytes were extracted in an aqueous media for the synthesis of AgNPs. The study emphasizes on the mechanism of formation of mono-crystalline AgNPs at different pH which in turn controls the kinetics and size of AgNPs. Thermodynamically facile Ag_2O reduction at a higher pH (≥ 9) resulted in spherical particles of smaller sizes; however, the particles were laden with a trace of Ag_2O at pH 12.5. A broad and bimodal distribution of AgNPs of different shapes and sizes were originated at a lower pH ($3 \leq pH \leq 5$) from Ag^+ and Ag_2O reductions where AA mostly exists as dehydro-AA. A single surface plasmon resonance peak at 425 nm exhibited a blue shift with the decrease in AgNPs size and increase in sphericity in the abundance of OH^- ions. The hydrodynamic diameter of AgNPs was around 1.6 times greater than the dry particles from TEM micrograph at the natural pH (5.8) of the bio-extract. AgNPs were tested for the inactivation of *Bacillus subtilis* and *Escherichia coli* bacteria. AgNPs were also found to be highly effective against pathogenic fungi *Aspergillus thermomutans*. The silver-ascorbate layer induced particles destabilization along with the formation of ascorbate free radical (g-factor: 2.0052 to 2.0056) which caused the synergistic affects for the microbial inhibition.

Further, this work could successfully synthesize tailor-made Co and Pt NPs. The prismoidal, spherical, and core-shell structures of Co, Pt, and PtCo NPs were formed and, the mean particle diameter was found as of 47.3, 25.4, and 28.6 nm, respectively. A dense core of Pt or PtCo alloy was formed followed by a shell consisting of mostly Co with an average core-shell diameter of 13.2 nm–26.4 nm. The synergistic effects such as the ligand interaction

between the core and shell, and the geometric effect improved the antimicrobial activity against *Bacillus subtilis* and *Escherichia coli* in comparison to Co nanoprisms and Pt nanospheres and, the results were comparable with ciprofloxacin and cefprozil as the antibiotic controls.

One of the main problems associated with semiconductor photocatalysts is that the photogenerated electron (e^-) and hole (h^+) can recombine very quickly (~20 ns), and the quantum efficiency of the overall reaction reduces. The metal-doped semiconductor photocatalysts have a high Schottky barrier, which acts as e^- traps at a metal-semiconductor junction, facilitating e^- and h^+ separation and promote the interfacial e^- transfer process. In the second part of the work, a facile bio-inspired method is developed for noble metal (Ag) and transition metals (Cu and Zn) doping onto semiconductor supports, namely, TiO_2 and ZnO to harvest the visible light. This technique also uses the bio-analytes present in the *Sechium edule* extract.

Firstly, Ag^+ was immobilized on the catalyst supports and, the immobilization efficiency at the neutral pH was around 70 to 84 % with the initial amount of Ag varying from 0.25 to 2 % (w/w w.r.t. TiO_2 / ZnO). The immobilized Ag^+ was completely doped onto TiO_2 (Ag/TiO_2) and ZnO (Ag/ZnO) in the presence of the bio-analytes. The proposed technique had dramatically shifted the optical absorption (~500 nm) to the visible domain and, the band gap of TiO_2 and ZnO were reduced to 2.5 and 2.8 eV. The crystallite size of TiO_2 and ZnO with the increase in Ag-loading was increased significantly because of Ag^+ induction into the Ti^{4+} and Zn^{2+} lattice. Ag/TiO_2 exhibited 98 % degradation of Congo red dye under the visible light illumination.

The saturation photo-electrochemical current density (46.68 mA/cm^2) at $E_{anode} \geq 0.31$ V vs. Ag/AgCl was almost double with Ag/ZnO than pristine ZnO under visible light illumination (λ_{mean}=525 nm, 18 K lux) and, the current density was insignificant in the dark. Ag/ZnO catalyst exhibited maximum 79.5 % degradation (71 % COD removal) of an anti-analgesic drug, dipyrone (100 µg L^{-1} dipyrone, catalyst 100 mg L^{-1}) resulted from the formation of $O_2^{\bullet-}$ radical (g-factor of 2.002 to 2.008), $^{\bullet}OH$ radical and paramagnetic oxygen vacancies (g-factor of 2.020) and, no effect of dye-sensitization was noted. The highest quantum yield was found to be 34.7%. The catalyst loss was 6% after the fourth cycle, and the dipyrone degradation was reduced to 70.8%.

The photocatalytic activities of bimetal doped TiO_2 ($Zn/Cu/TiO_2$) and its comparison to the bare and mono-metal doped systems (Cu/TiO_2 and Zn/TiO_2) was also performed at the

later part of this work. The proposed method was successful to bring down the band gap of TiO_2 to 2.3 eV for Zn/Cu/TiO_2 at 1:1:98 (w:w:w). The crystallite size of TiO_2 at higher dopants loading was increased significantly (16.3 to 38.4 nm) because of Cu^{2+} and Zn^{2+} induction into the Ti^{4+} lattice and, there was as high as 12% transformation of the anatase phase to the rutile phase of TiO_2. The increase in the absolute value of zeta-potentials of Cu/Zn/TiO_2 was notably faster (5 mV per unit pH increase) at $pH>pH_{zpc}$ which was resulted from the rise in oxygen vacancies and, Cu/Zn/TiO_2 were mostly present as a separated non-aggregated unit in water with a polydispersity index of 0.201. Zn/Cu/TiO_2 exhibited 98% congo red dye decolourization compared to 59.3 and 68.7% with Zn/TiO_2 and Cu/TiO_2 under the visible light illumination (17.7 K lux). COD reduction was 80.6, 71.2, and 75.9% with Zn/Cu/TiO_2, Zn/TiO_2, and Cu/TiO_2 with the quantum efficiency of 41.5%, 23.4, and 30.8, respectively. It was found that reactive oxygen species ($O_2^{\bullet-}$ and $^{\bullet}OH$ radicals) were mostly caused the dye decomposition as evidenced from the electron spin resonance spectroscopy. The pseudo-first order model well fitted with the experimental results for photocatalytic dye degradation. There was about the sixteen-fold increase in the rate constant with Cu/Zn/TiO_2 compared to bare TiO_2.

Keywords: Ag nanoparticles; Cu nanoparticles; Zn nanoparticles; Tailor-made nanoparticles; Green synthesis method; *Sechium edule* extract; Ascorbic acid; Synthesis mechanism; Particles stability; Self-stabilization; Particle sphericity; Ascorbate free radical; Surface plamson resonance; Antibacterial activity; Antifungal activity; Photocatalysis; TiO_2 support; ZnO support; Bio-mediated doping; Noble metal dopant, Transition metal dopant; Phase transformation; Visible light harvesting; Band gap reduction; Photo-current; Dye decomposition; Drug decomposition; Dye sensitization; $O_2^{\bullet-}$ radical; Chemical oxygen demand; Quantum yield; Catalyst loss; Catalyst regeneration

TABLE OF CONTENTS

CERTIFICATE

*This is to certify that the thesis entitled "**Bio-inspired Route of Metal Nanoparticles Synthesis and Photocatalysts Doping**", being submitted by **Mr. Venkatanarasimha Rao Chelli,** to the Indian Institute of Technology Guwahati, India, for the award of Doctor of Philosophy, is a record of bonafide research work carried out by him under my guidance and supervision. The work embodied in this thesis has not been submitted for any other degree or diploma. In my opinion, the thesis is up to the standard of fulfilling the requirements of the doctoral degree as prescribed by the regulations of this Institute.*

Date:

Dr. Animes K Golder
[Thesis Supervisor]
Associate Professor
Department of Chemical Engineering
Indian Institute of Technology Guwahati

Dedicated

To

My Guide and My Family Members for

their Supports and Encouragement

Throughout My Research Work

ACKNOWLEDGEMENT

It is my great pleasure to thank each and everyone who helped directly or indirectly to complete my research work and made this thesis possible. I owe my deepest gratitude to all of them.

The first and foremost gratitude goes to my supervisor **Dr. Animes K. Golder** for his valuable guidance throughout the research work. I thank him for his encouragement, patience towards research and support, which enabled me to develop a better understanding of the subject leading to the present this thesis. I would like to thank him for spending his precious time to discuss thoroughly on the topic and make me what I am today. I would also like to acknowledge my sincere gratitude to my doctoral committee members, **Prof. K. Mohanty, Dr. V.V. Goud** and **Prof. S. Chakraborty,** for their advice and suggestions throughout my research work.

My sincere thanks go to the faculty members of Department of Chemical Engineering, I.I.T. Guwahati, for their continuous suggestions and inspirations. I also like to express my thanks to the staff members for making a homely atmosphere. The analytical facilities from Central Instruments Facilities (CIF) of Indian Institute of Technology Guwahati are also acknowledged.

I am grateful to my senior members from our group, *Dr. M. Gagrai*, and *Dr. A.S. Giri*, for their co-operative assistance and suggestions in performing experiments. I also thank my present lab members *Mr. Raj Kumar Das, Mr. Vinay Kulkarni, Mr. Y. Santosh Kumar, Mr. Smruti Ranjan Dash, Ms. Paulomi Bose, Ms. Devi P, Mr. Anirban, Mr P. Joy* and *Mr. Sagar*.

I cannot forget to thank my friends *Mr. M.M. Reddy, Mr. G. Bharath, Mr. T. Ramesh, Mr. Prudhviraj, Mr. Rahul Saha, Mr. Suman Saha, Mr. Rambabu, Mr. Anudeep, Mr. Pankaj* and *Mr. N. Patro*, for the lovely support in making my stay at IIT Guwahati memorable.

After all, I would like to thank all departmental and office staff for helping me in many ways for my research work.

Deep heartedly, I thank my parents and my family members for their encouragement, blessings and motivation at each and every step.

Last, but not least, I thank the Almighty God for giving me strength to overcome difficulty, which crossed my way to be a pole star.

VENKATANARASIMHA RAO CHELLI

LIST OF FIGURE CAPTIONS

LIST OF TABLE CAPTIONS

Mr. VENKATANARASIMHA RAO CHELLI

Date of Birth: **04th May 1990**
Email: **venkata.rao@iitg.ac..in ; venkat843@gmail.com**

Educations:

Ph.D. in Chemical Engineering
Department of Chemical Engineering
Indian Institute of Technology, Guwahati
Guwahati, Assam, India
2013- 2018

M. Tech in Chemical Engineering
Department of Chemical Engineering
Indian Institute of Technology, Guwahati
Guwahati, Assam, India
2011- 2013
Marks obtained: 7.79/10.00

B. Tech in Chemical Engineering
Department of Chemical Engineering
Jawaharlal Nehru Technological University Anantapur
Anantapur, Andhra Pradesh, India
2007-2011
Marks obtained: 61.12%, 1st Class

Higher Secondary in MPC
Sri Chaitanya Jr. College
Kukatpally, Hyderabad, Telangana, India
2005-2007
Marks obtained: 80.2%, 1st Class

Secondary Education
Z.P.H.S, Chowdawaram,
Khammam, Telangana, India
2005
Marks obtained: 86.16%, 1st Class

Publications

Journal papers

Ch. V. Rao and A.K. Golder, Ag-doping on ZnO support mediated by bio-analytes rich in ascorbic acid for photocatalytic degradation of dipyrone drug, *Chemosphere*, vol 208, pp. 149-158, May 2018.

C.V. Rao, and A.K. Golder, "Development of a bio-mediated technique of silver-doping on titania," *Colloids and Surfaces A: Physicochem. Eng. Aspects*, vol. 506, pp. 557–565, Jul 2016.

C.V. Rao and A.K. Golder, "pH dependent size control, formation mechanism and antimicrobial functionality of bio-inspired AgNPs," *RSC Adv.*, vol. 6, no. 98, pp. 95483–95493, Sep 2016.

C.V. Rao, S.S. Bag, and A.K. Golder, "A biosynthesis route to nearly spherical AgNPs using chayote fruit extract," *Environ. Prog. Sustain. Energy*, vol. 36, no. 1, pp. 192–199, Jan 2017.

C.V. Rao, K. Bakal, and A.K. Golder, "Biomediated synthesis of ZnO nanoparticles (ZnONPs) for photocatalytic application," *Internat. J. Cur. Eng. Sci. Res.*, vol. 1, no. 4, pp. 26–30, Dec 2014.

C.V. Rao, and A.K. Golder, "Bimetal doping on TiO_2 for photocatalytic water treatment: A green route," *European Water*, May 2017. (Accepted)

C.V. Rao, and A.K. Golder, "One Pot green synthesis of Pt–Co bimetallic core-shell nanoparticles using plant extract," *Canadian J. Chem. Eng.*, (Revised manuscript submitted)

C.V. Rao, S. Chakraborty, and A.K. Golder, "Ag-doing on TiO_2 using plant-based glycosidic compounds for high photonic efficiency degradative oxidation under visible light," (Communicated)

Conference Publications

Ch.V. Rao, and A.K. Golder, "Bimetal doping on TiO_2 for photocatalytic water treatment: A green route," European Water Resources Association, National Technical University of Athens, Athens, Greece, Jul 2017.

Ch.V. Rao, and A.K. Golder, "Visible light activation of ZnO photocatalysts for wastewater treatment," Reflux 2017, Indian Institute of Technology Guwahati, Assam, India, Mar 2017.

Ch.V. Rao, A.K. Singh, and A.K. Golder, "Studies on bio-mediated fabrication of AgNPs," Reflux 2017, Indian Institute of Technology Guwahati, Assam, India, Mar 2017.

Ch.V. Rao, R.K. Das, S.R. Dash, P. Ghosh, S. Saha, and A.K. Golder, "A bio-mediated route of AgNPs synthesis and photocatalyst activation," IITG-KIT Joint

Symposium on Soft and Biobased Materials, Kyoto Institute of Technology, Kyoto, Japan, Aug 2016.

Ch.V. Rao, R.K. Das, S.R. Dash, P. Ghosh, S. Saha, and A.K. Golder, "A biological route of AgNPs synthesis: Size control and functionality," Biotechnology, Biomaterials and Renewable Energy, GIFU University, GIFU, Japan, Aug 2016.

Ch.V. Rao, and A.K. Golder, "Nerium Oleander leaf extract mediated synthesis of nickel nanoparticles and its potential application," International Conference on Bioscience and Biotechnology, University of Sri Jayawardenepura, Colombo, Srilanka, Jan 2016.

Ch.V. Rao, A.K. Singh, and A.K. Golder, "One pot green synthesis of Pt-Co bimetallic nanoprisms using plant extract," CHEMCON 2016, A.C.Tech, Anna University, Chennai, India, Dec 2016.

Ch.V. Rao, S. Chakraborty, and A.K. Golder, "Biomediated synthesis of spherical silver nanoparticles using *S. edule* extract and its activity," CHEMCON 2015, Indian Institute of Technology Guwahati, Guwahati, Assam, India, Dec 2015.

Ch.V. Rao, and A.K. Golder, "Synthesis, characterization and photocatalytic behavior of silver-doped ZnO using chayote extract," International Conference on Water, UCentre for Environment Education and Technology, Kottayam, India, Jan 2015.

Ch.V. Rao, K. Bakal, and A.K. Golder, "Biomediated synthesis of ZnO nanoparticles (ZnONPs) for photocatalytic application," International Conference on Civil and Chemical Engineering, Warangal, India, Nov 2014.

Ch.V. Rao, S.S. Bag, and A.K. Golder, "Photolytic degradation of Brilliant Green dye: Process performance and kinetic studies," CHEMCON 2013, Institute of Chemical Technology, Matunga, Mumbai, India, Dec 2013.

Ch.V. Rao, Shivraj, and A.K. Golder, "Spectral sensitization of TiO_2 by copper doping: A biological approach," National Conference on Challenges in Environmental Research, Indian Institute of Technology Guwahati, Assam, India, Jun 2015.

Exhibition

- Ch. V. Rao, S. Chakraborty and A. K. Golder, Bio-mediated synthesis of nanophotocatalyst: A greener initiative, REFLUX-2015, March 28-29, Indian Institute of Technology Guwahati, India.

Workshop

- National workshop on technical writing conducted under the technical education quality improvement programme sponsored by the Ministry of Human Resource Development, Government of India, held on December 6-7, 2014.

Awards

1. Best presentation award for the paper entitled "One pot green synthesis of Pt-Co bimetallic nanoprisms using plant extract", in CHEMCON 2016, 27-30 December

2013, A.C.Tech, Anna University, Chennai, India.

2. Best presentation award for the paper entitled "Visible light activation of ZnO photocatalysts for wastewater treatment", in Reflux-2017-Annual Chemical Engineering Symposium, Department of Chemical Engineering, 24-26 March, 2017, IIT Guwahati, Assam, India.

Other Publications

1. **C.V. Rao**, A.S. Giri, V.V. Goud, and A.K. Golder, Studies on pH-dependent color variation and decomposition mechanism of Brilliant Green dye in Fenton reaction, *Internat. J. Ind. Chem.*, 2016, 7(1), 71–80.
2. A.K. Behera, **C.V. Rao**, R.K. Bag, A.S. Giri, and A.K. Golder, Fabrication and characterization of Ag-doped titania: impact of dye-sensitization, phenol decomposition kinetics and biodegradability index, *Desalin. Water Treat.*, 2016, 57(20), 9488–9497.
3. M. Malika, **C.V. Rao**, R.K. Das, A.S. Giri, and A.K. Golder, Evaluation of bimetal doped TiO_2 in dye fragmentation and its comparison to mono-metal doped and bare catalysts, *App. Surf. Sci.*, 2016, 368, 316–324.
4. S. Chakraborty, **C.V. Rao**, R.K. Bag, A.S. Giri, and A.K. Golder, Bio-mediated silver nanoparticle synthesis: mechanism and microbial inactivation, *Toxicol. Environ. Chem*., 2017, 99(3) 434–447.
5. R.K. Das, S. Saha, **C.V. Rao**, and A.K. Golder, Bio-inspired AgNPs, multilayers reduced graphene oxide and graphite nanocomposite for electrochemical H_2O_2 sensing, *Bull. Mater. Sci*. 2018, 41(3), 86.
6. P. Ghosh, **C.V. Rao**, A.S. Giri, and A.K. Golder, Steroid glycosides as potential analytes for Cu-doping on TiO_2 for photocatalytic water treatment, *Environ. Prog. Sustain. Energy*, 2018. DOI 10.1002/ep.12879.

Chapter 1

Introduction and Literature Review

1.1 Nanotechnology and Nanoparticles: Historical Origin

‘‘Nano’’ was derived from the Greek word, so, ‘‘dwarf’’ was introduced as a new concept in 1960s. The fabrication of nanomaterials through either top-down or bottom-up methods has been the established of decades of scientific investigations (You et al., 2013). Particles of nanometer range generally from 1 to 100 nm are considered as nanoparticles (NPs). It has been seen that if the size of the metal particles is reduced to nanometer range, the electrical, chemical, and physical properties are drastically modified. Since the ancient time, various noble metals have been in use, for example, silver has been used for treating chronic wounds, burns, infections, etc. In fact, silver was used even before the Neothilic

revolution (Ravindran et al., 2013). Though NPs are said to be the discovery of modern science and technology, it is believed that even before the 9th century, artisans used various noble metal (silver/gold) NPs for glittering the surface of the pots. Recently, the potential applications of metal and semiconductor NPs in the field of environment, biotechnology, medicine, material science, etc. have attracted significant research attention towards the fabrication of NPs because of their uncommon physicochemical attributes at nanoscale.

The electromagnetic field of metal NPs are improved a lot upon contact with an electromagnetic field because of the size controlled surface plasmon resonance (SPR) and the quantized oscillation of collectively stimulated conduction band electrons (Bhattacharya and Mukherjee, 2008; Chhatre et al., 2012). The SPR is intensely dependent on the size, shape, dielectric properties of the NPs and its surroundings. By changing the reaction parameters, size, shape, and morphology may vary.

Noble metal NPs possess unique properties, including optical, catalytic, chemical, magnetic, electronic, and mechanical which importantly vary from those of their bulk materials. These exceptional properties of NPs can be assigned to their large specific surface area and small size (Veerasamy et al., 2011).

1.2 Types of Nanoparticles (NPs)

1.2.1 Non-metal nanostructures

Non-metals like graphite, carbon nanotubes are used for fuel cell application (Paredes et al., 2009). Graphene is a new 2-dimensional carbon material that has intriguing properties, such as a high surface area, high electrical conductivity, thermal stability, great electron mobility and a unique graphitic basal plane that guarantees durability (**Figure 1.1**). Another important property of graphene is adsorption; the planar structure of graphene makes it a suitable substance for metal nanoparticle deposition and demonstrates its potential as a supporting material for catalyst particles (Liu et al., 2011). However, metal NPs synthesis or application is more favourable than the non-metal nanostructures (Yoon et al., 2015).

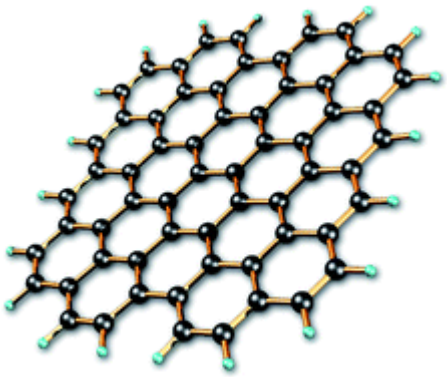

Figure 1.1. Schematic illustration of graphene (Brownson and Banks, 2010).

1.2.2 Metal NPs

In developing modern society, one of the most significant materials is metal NPs. They are all essential constituents for electronic technology, technology to biomedical applications, equipment transportation, architecture, and information science (Duan and Wang, 2013; Singhal et al., 2011). Metal NPs possess special physicochemical properties in surface/support, size/shape and composite engineering, when compared with their counterparts owing electromagnetic, excellent malleability, and high mechanical strength properties (**Figure 1.2**). These special characteristics of metal NPs exhibit due to their significant implications in the fields of sensing, magnetic recording, medical diagnosis, catalysis, and electrocatalysis (Li et al., 2015; Sun et al., 2012; Yang et al., 2015). For instances, NPs like Ag, Au, and Cu exhibit SPR in the visible range which can be utilized as opto-electronic devices, imaging/ bio-sensors (Chairam et al., 2015; Simakin et al., 2002; Yang et al., 2006). NPs such as Pd, Pt as well as Au and Ag, have excellent catalytic applications. Transition metals, such as Ni, Co, and Fe, are ferromagnetic components which have been extensively applied in various spintronic and magnetic devices (Vichery et al., 2013).

Prathna et al., (2011) synthesized silver NPs with size lower than 50 nm using citrus limon aqueous extract. Wu et al. (2010) synthesized spherical nickel NPs by the chemical reduction of nickel chloride using hydrazine at room temperature.

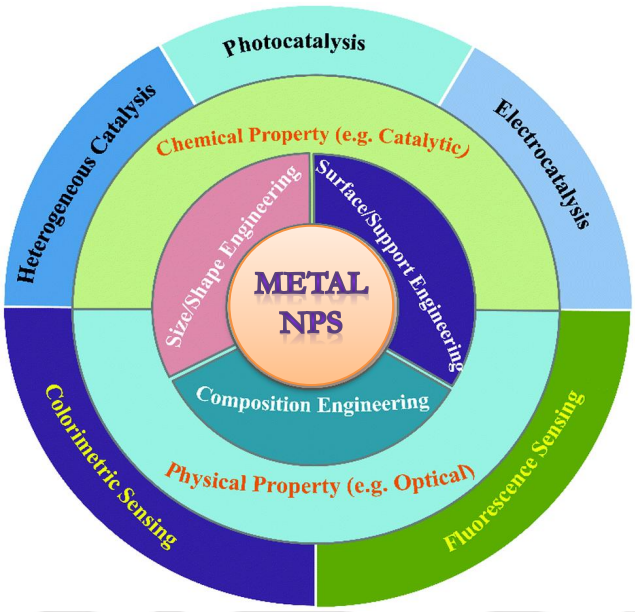

Figure 1.2. Three strategies that can be used to tailor the physicochemical properties of metal NPs, and the use of these physicochemical properties for several emerging applications from the environmental fields (Li et al., 2015).

1.2.3 Metal oxide NPs

Metal oxide NPs play a crucial role in different areas including materials science, physics, and chemistry (Ramachandran et al., 2015; Sangpour et al., 2010). The metal elements are capable to produce a wide variation of oxide combines. These metal oxides can implement a large number of morphological geometries with an electronic complex that can show metallic, insulator or semiconductor character. These are utilized in technological applications as in the manufacture of coatings, circuits of microelectronics, piezoelectric devices, for the passivation of surfaces against corrosion, fuel cells, sensors, and as catalysts. Metal oxide NPs can pose unique physicochemical attributes due to their large edge density or corner surface sites or narrow size distribution.

Various reproducible methodologies have been developed for the preparation of NPs with preferred features like size, monodispersity, shape, defects in the crystal structure, and morphology giving a rich motivation for research related to antibacterial implications. Such NPs can be useful in tuning and modifying their cytotoxic and microbial effects. For example, it has been found that the microbial inhibition enhances with decreasing the NPs size (Ajitha et al., 2015). Metal oxide NPs such as TiO_2, ZnO, CuO, and Fe_3O_4 are being carefully examined in the view of the potential novel antibacterial agents (Niemirowicz et al., 2015). Low cost (Paulino et al., 2016) and toxicity against human cells (Larese et al., 2009),

size-controlled effective inhibition against a wide range of microorganism, capacity to avoid biofilm formation, and even remove spores (Rajakumar et al., 2012) make them desirable for application as antimicrobial agents in the biomedical, food-additive, fabric, and skincare products industries (Gunalan et al., 2012; Paulino et al., 2016). However, for safe applications of wide verity of nanomartials, research to understand cytotoxic effects and the respective mechanism is needed.

Rajakumar et al. (2012) synthesized bio-mediated TiO_2 NPs using *Aspergillus flavus.* NPs are of spherical shape having the dimensions of 200-2000 nm (Rajakumar et al., 2012). Dhandapani et al. (2012) fabricated TiO_2 NPs using a biomediated method employing *Bacillus subtillis* microorganism. *B. subtilis* easily can adapt with heavy metals, and they can produce various sizes and shapes of inorganic NPs through intra or extracellular mechanism. It is found that the fungus secrete extracellular proteins (21-24 kDa size) which can convert hexaflurotitanate complexes into spherical shaped TiO_2 photocatalyst (Dhandapani et al., 2012). ZnO NPs are synthesized using *Poncirus trifoliate* fruit extract (Nagajyothi et al., 2013). The TEM image shows the formation of the ZnO NPs particle in the size range of 8.5-32.5 nm. ZnO NPs are used for the condensation of 3, 4-dimethyl benzaldehyde and acetophenone.

1.2.4 Multi metal NPs

Multi metals in particular bimetallic NPs, compiled of two distinct metal elements, have a definite geometry architecture and chemistry sequence (or mixing pattern), and perform particular operations (Duan and Wang, 2013). They execute not only an improvement of the attributes or simple combination related to their single counterparts, but also many surprising and interesting new attributes with a mixture of various roles and widened application areas, which is described by synergistic effects of NPs (Fakhri et al., 2017). By changing their morphologies and constituents (like dumbbell or core–shell structures), their applicable physical or chemical operations can be effectively altered (Fakhri et al., 2017; Vigneshwaran et al., 2007). The increase of controllable parameters leads to understand the fate complexity of bimetallic NPs fundamental interaction mechanism. *Azadirachta indica*, a plant, is used for the extracellular synthesis of gold, silver, and Au/Ag bimetallic NPs with a particle size range of 50-100 nm (Shankar et al., 2004). Zhang et al. (2017) synthesized Pt-Co core-shell bimetallic NPs by controlled thermal treatment.

Various types of bimetallic NPs includes the core-shell, random alloy, and cluster in cluster NPs. In the case of random alloy NPs, two metals are placed entirely at random. The

formation of the morphology of the random alloy is manipulated by synthesis parameters which play crucial roles such as reagent doses, solution pH, and external ligands. In the case of the core-shell morphology, one metal forms the core and another metal forms on the surface of core to form a skin or shell (**Figure 1.3**). Usually the metal having lower electrode potential forms a core first and, later other metal forms as the shell. Successive reduction and co-reduction methods are common for core-shell structure formation. Core-shell bimetallic structure is one of the significant system as they have been employed to reduce the quantity of precious metals as well as applied to study catalysts electronic properties (Ferrando et al., 2008).

Kasthuri et al. (2009) synthesized anisotropic Au and spherical–quasi-spherical AgNPs using phyllanthin extract. Kovács et al. (2015) fabricated the core–shell structure of Pt–Co bimetallic NPs where Co acts as the core and Pt as rich surfaces or shell. Shankar et al. (2004) synthesized Au/Ag bimetal NPs with a size range of 5-35 nm, where the AgNPs are adsorbed onto the AuNPs, forming a core–shell structure.

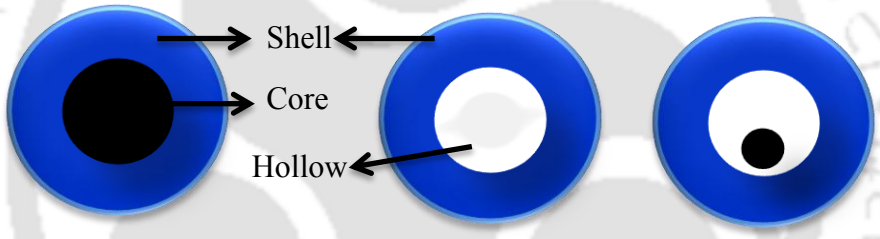

Figure 1.3. Core-shell metal NPs with different shapes (Chaudhuri and Paria, 2012).

1.3 Silver Nanoparticles (AgNPs)

Silver is a transition metal having atomic number 47 and atomic mass 107.87 g/mol. The medicinal uses of silver have been documented since 1000 B.C. The functionality of AgNPs as an antibiotic comes from the fact that it is a nonselective toxic biocide. Ag based antimicrobial biocides are used as wood preservatives. In water usage, Ag and Cu based disinfectants are used in hospital and hotel distribution systems to control infectious agents. Metal particles in the nanometer size range exhibit physical properties that are different from both the ion and the bulk material. This makes them exhibit remarkable properties such as an increased catalytic activity due to morphologies with highly active facets (Dauthal and Mukhopadhyay, 2012).

Silver even has shown to prevent HIV binding to host cells (Elechiguerra et al., 2005). It is also reported that the AgNPs' nontoxic nature to human as well as efficient antibacterial, fungal, viruses, and other micro-organisms at very small doses and without any

side effects (Nymark et al., 2013). AgNPs can play a significant role in bacterial growth inhibition in aqueous and solid media because of their large active specific surface area.

AgNPs are useful substrates for surface enhanced Raman spectroscopy because of a high local field enrichment factor since it partly requires an electrically conducting surface. As a result, AgNPs can be dispersed in colloidal solution or constituted on the substrates. AgNPs can also be utilized for polymer based diffraction patterns modification (Sutradhar and Saha, 2016) which can be latter employed for sensing in grating light reflection spectroscopy. AgNPs formed by chemical reduction in ethylene glycol (reductant) solution, and then polyvinylpyrrolidone (PVP) adsorbed at the surfaces of the AgNPs to induce the formation of chain like structures. PVP plays a role as an adsorbent to protect the NPs in solution and keep the chain-like growth, respectively. When the concentration of Ag^{+} ions and the reducer greatly decrease in the latter period, the growth is driven by the decrease of surface energy. The morphology of the Ag nanostructures changed with prolonging reaction duration (Nymark et al., 2013).

Metallic Ag in finely dispersed form displays unique properties normally associated with noble metals, such as chemical stability, excellent electrical conductivity, catalytic activity along with other more specific ones like anti-bacteriostatic effects and non-linear optical behaviour etc. (Devi and Mandal, 2013) (**Figure 1.4**).

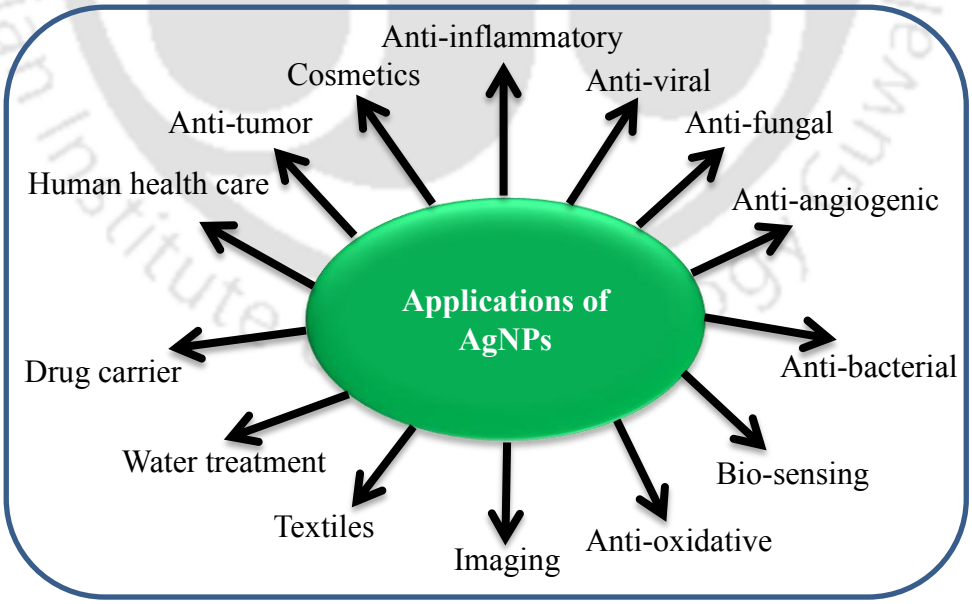

Figure 1.4. Various applications of AgNPs.

1.4 Factors Affecting Formation of AgNPs

The sizes and shapes of the NPs can be manipulated consistently by regulating the synthesis parameters such as the dose of reagents and stabilizing agent, reaction time, temperature, and solution pH (Adegboyega et al., 2013; Khalil et al., 2014). The following sub-sections documents their effects on the formation and physiochemical attributes of NPs.

1.4.1 Amount of reducing agent

The existence of a higher quantity of reductant causes deep interaction between surfaces of NPs and protective molecules as capping agents. The decrease in particle size with the increase in the concentration of reducing agents is a well-known phenomenon. It is normally attributed to increased reaction rates. As the reaction rate increases, Ag^+ ions are consumed faster and smaller and narrower sized particles are formed at a higher reducing agent concentration (Chhatre et al., 2012; Philip, 2010). The reaction mixture stability can be subjective by the amount of reductant and absorbing species present in a solution. The competition between electrostatic repulsion and weak van der Waals forces of attraction decides the stability results from a potential barrier that develops (Prathna et al., 2011).

Dubey et al. (2010) reported the bathochromic shift in the SPR band of AgNPs and AuNPs with a increasing dose of *Sorbus aucuparia* leaf extract from 0.5 to 3.0 mL with 54 mL solutions of $AgNO_3$ and $HAuCl_4$. The subsequent changes in reaction mixture color with time are also reported from reddish yellow to deep red and pink to reddish pink, respectively. With the increase in extract dose, there was a decrease in particle size as well as more particles are formed for both AgNPs and AuNPs (Dubey et al., 2010).

Upon an increase in *Acacia nilotica* pod extract concentration from 0.25 to 2.5 mL to a total volume of 25 mL of 0.01 M $AgNO_3$, the SPR peak (~425 nm) undergoes a red shift indicating an increase in particle size (Edison and Sethuraman, 2013).

1.4.2 Concentration of metal ion

With the increase in the dose of the metal ion from 0.1 to 5 mM, the increase in NPs size as well as no strong absorption band in the visible region can be observed especially in the case of AuNPs or AgNPs. A higher size of NPs is observed at larger concentration of Au^+ than Ag^+. The absorbance band intensity increases at higher Ag^+ ion dose expressing a

modest increase in NPs size, but no significant absorption band is found at optimum or higher concentrations. The formation rate of AgNPs and AuNPs is slower at the lowest concentration of metal ions and, hence, a weaker absorbance peak is found (Dubey et al., 2010). Balakumaran et al. (2015) studied the variation of $AgNO_3$ dose from 2 to 10 mM for the synthesis of AgNPs using *Guignardia mangiferae* fungus. Among them 1 mM concentration possesses good monodispersity NPs (Balakumaran et al., 2015).

Verma and Mehata (2016) synthesized AgNPs at various concentrations of Neem leaf broth and silver salt (1:02, 1:04, 1:08, 1:12, 1:16 v/v). With the increase in concentration of reaction mixture (1:02), the SPR peak intensity increases abruptly, indicating an enhancement in the production of AgNPs with an increase in AgNPs size (Verma and Mehata, 2016).

1.4.3 Reaction time

The contact time of metal NPs synthesis is a significant parameter and, the formation of NPs with time can be monitored by UV– Vis spectra. Generally, with the increase in reaction time, the absorption peak becomes sharper and, the number of NPs formation is also more up to optimum reaction time to avoid the instability and agglomeration of the NPs (Dubey et al., 2010).

Sathishkumar et al. (2009) observed the changes in reaction mixture colour with reaction time, initially light brown, becomes darker look after 2 h. The increase in SPR absorption peak intensity of AgNPs at 435 nm with respect to time, is monitored in UV–vis spectra as well as observed to be very stable in the solution, even 3 months after their synthesis (Sathishkumar et al., 2009).

Verma and Mehata (2016) reported the change in solution colour of Ag^+ from pale yellow to yellowish brown, and finally to dark brown colour in 3 h with subsequent increment in absorbance peak intensity and, after 3 h no change is observed (Verma and Mehata, 2016).

1.4.4 Reaction temperature

In general, The SPR absorption band of NPs becomes sharp with the elevation of the reaction temperature. The NPs with larger size are yielded at a lower temperature and the NPs are usually smaller in size with the increase in temperature, which results in the sharpness of the SPR band of AgNPs and AuNPs (Dubey et al., 2010).

Dauthal and Mukhopadhyay (2012) reported a slight blue shift in the SPR band along with a size reduction with a higher reaction temperature which is due to the increase in the

reaction rate for the conversion of Au^{+} to AuNPs at a higher temperature. The temperature varied from 15 to 55 °C (Dauthal and Mukhopadhyay, 2012).

Verma and Mehata (2016) also reported that the SPR absorption peak of AgNPs shifted toward blue from 433 to 397 nm for the formation smaller AgNPs particles, as the temperature varies from 10 to 50 ºC. It is identified that smaller size NPs were obtained with the blue shift. With the increase in temperature, the reduction of Ag^{+} is enhanced, as indicated by a rapid change in the colour of the reaction mixture.

1.4.5 Reaction pH

As pH increases, the net charge varies from positive to negative and results in an intense repulsion between negatively charged ions and molecules of the reducing agent (Shankar et al., 2004). Lower pH (acidic) nature inhibits the formation of AgNPs but alkaline pH nature increases the NPs formation. In the case of lower pH, large-sized NPs are formed, whereas, at alkaline pH, smaller sized NPs are formed. In acidic pH, the agglomeration of NPs to form bigger NPs is supposed to be favoured over the nucleation to form new NPs (Ajitha et al., 2015; Sivera et al., 2014). At higher pH, however, more functional groups existing for silver bonding facilitate a larger number of Ag^{+} to bind and consequently more NPs is formed with smaller sizes. In addition at alkaline pH, mostly spherical and decahedral shaped NPs are formed rather than ellipsoidal (Sathishkumar et al., 2009).

Ajitha et al. (2015) synthesized AgNPs at different pH from 6 to 12 using poly-vinyl alcohol (PVA) capped chemical reduction method and observed the blue shift in the absorption peak from 429 to 414 nm as well as the decrease in crystallite size from 31 to 14 nm with the increase in solution pH (Ajitha et al., 2015). Edison and Sethuraman (2010) also reported the decrease in particle size from 45 to 20 nm and the SPR peak shift from 430 to 409 nm with the increase in pH from 5 to 9 (Edison and Sethuraman, 2013).

1.5 Role of Metal Nanostructures for Microbial Inhibition

The development of antibacterial agents is believed to be one of the ten significant public health accomplishments of the twentieth century. They made a significant role in the decrease in infectious diseases. At the beginning, antimicrobials are understood as truly amazing drugs and believed the ‘‘panacea’’ of medicine, but nowadays the development of drug-resistant organisms has seriously afflicted their therapeutic efficiency (Khalil et al., 2014; Zuas et al., 2014). The unique properties of metal NPs have made them useful in many such applications as antimicrobial agents

(Sathishkumar et al., 2009), as photocatalysts (Subash et al., 2012), as anti-cancer drugs (Bhat et al., 2013), and for the fabrication of sensing devices (Thiwawong et al., 2013).

Bacteria have typical membrane assemblies on which they are generally classified as Gram-positive and Gram-negative bacteria. The structural variation exists in the association of the key constituents of the cell wall and peptidoglycan, which is placed just outside the cytoplasmic membrane. The Gram-positive bacteria cell wall consists of up to 30 nm thick peptidoglycan layer, whereas the cell wall of Gram-negative contains only 2 - 3 nm thin peptidoglycan layer with an extra outer membrane composed by lipopolysaccharides and phospholipids (Sunada et al., 2003)

NPs enhance chemical activity due to surface crystallographic structure with their large surface to volume ratio. Antibactericidal nanomaterials in particular are significant because for the development of new resistant strains of the microorganism even against the strongest antibiotics. This has gained research interest in the exploration of antibacterial activity of Ag^+ and silver-based compounds, including AgNPs. This antibacterial effect is size and concentration dependent and more effective against Gram-negative bacteria than Gram-positive bacteria (Valli and Vaseeharan, 2012).

The microbial activity is likely due to the release of Ag^+ ions from AgNPs which act as reservoirs for the Ag^+ antimicrobial agent. Bacterial proteins in the cell wall and cytoplasm play a vital role in the proper functioning of the cell. The AgNPs may attach to the cell wall of bacteria and disturb permeability and respiratory functions of the cell which leads to rupturing of cell wall, and finally cell lysis, DNA and mitochondrial damage (Ajitha et al., 2015) (**Figure 1.5**).

As the concentration of NPs increases, the growth of the bacterial colonies on agar plates decreases. NPs may bind to the surface of the cell membrane and disturb its respiration and permeability functions, results in the cell death. The attachment of NPs to the bacteria depends on the surface area available for contact. A high surface area of smaller NPs exhibit greater bacterial inhibition than the bigger NPs (Ajitha et al., 2015).

Ajitha et al. (2015) reported that the bacterial inhibition using AgNPs increases from 3.4 to 10.2 cm zone diameter with increasing pH from 6 to 12 against *Pseudomonas sp.* (Ajitha et al., 2015). Boomi et al. (2014) reported the maximum inhibition zone for polyaniline/Pt-Pd nanocomposite against *Staphylococcus sp*. (28±0.70 mm dia) followed by *Klebsiella sp.* (25 ±0.85 mm dia), *E. coli* (22± 0.36 mm dia), and *Streptococcus sp.* (21± 0.30 mm dia) (Boomi et al., 2014). Singhal et al. (2011) reported the minimum inhibitory

concentration of bio-mediated synthesized AgNPs (14.5 nm average diameter) is 0.314 and 1.25 µg/mL against *E. coli* and *S. aureus* (Singhal et al., 2011).

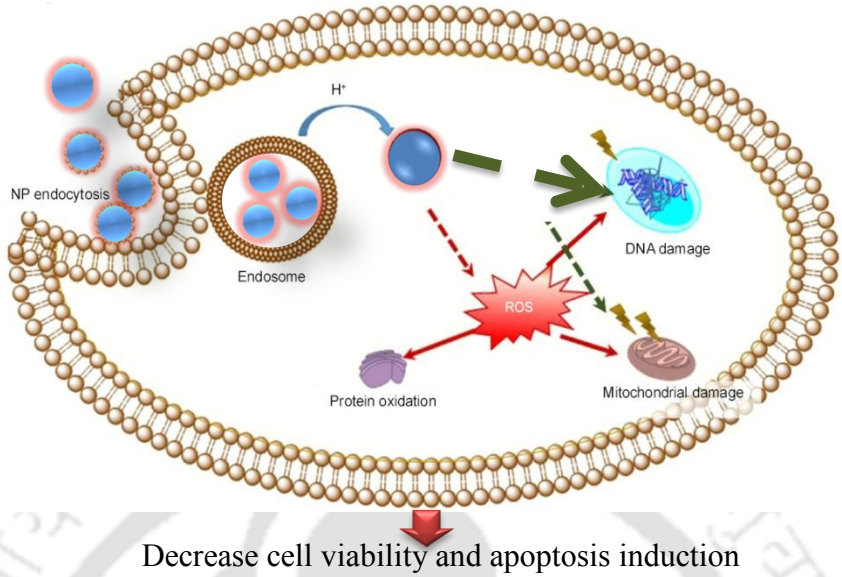

Figure 1.5. Hypothetical mechanism of antimicrobial activity of metal NPs (Niemirowicz et al., 2015).

1.6 Metal Doped Semiconductor Supports for Water Treatment

Water is the most precious natural resource in the world embracing over 70 % of the earth surface. In spite of this, the accessibility of safe drinking water is a high priority issue for the survival of mankind as well as animals. This is because of the fact that water resources such as rivers, lakes, and oceans are being contaminated by human beings through over-use and wastage. This affects the natural environment as well as human health. The major sources of water pollution are manufacturing processes, particularly from chemical and textile industries. The World Health Organization (WHO) reported that in 2008 some 884 million people still relied upon unimproved water sources – 84 % of whom are living in rural areas. Many more are surviving by drinking microbiologically unsafe water and experiencing the agony of waterborne diseases, including cholera, hepatitis, and typhoid (Byrne et al., 2011). The removal of harmful matters from wastewater and detoxification of pollutants in surface-water and groundwater is a key issue in the world. Secondary treatment helps in organic matter decomposition to some extent, but the major oxidation occurs in tertiary treatment where wastewater is disinfected by Cl_2, O_3 or UV light.

Conventional treatment methods are not always adequate and/or appropriate to remove organic contaminants from wastewater streams in a large scale. Conventional methods have their own merits or demerits in real application. Adsorption is a non-destructive method,

which simply transfers pollutants from one medium to another (Ebrahimi and Modrek, 2013). Biological techniques require large reactor volume and less flexibility in design and operation. Moreover, microorganisms are susceptible to toxic chemicals (Majone et al., 2015). Chemical treatments require a huge amount of chemicals and generate hazardous sludge needing further processing/stabilization (Abdel-raouf et al., 2012). The coagulation process also generates a large quantity of sludge and is associated with the problem of sludge disposal (Irfan et al., 2013). Membrane separations are not effective for removal of contaminants present at low concentration (Barakat, 2011). A large degree of aromatics present in organic contaminants increases its stability and conventional biological treatment methods are most often ineffective for mineralization and degradation (Konstantinou and Albanis, 2004).

To overcome these limitations, advanced oxidation processes (AOPs) have been introduced to eliminate different potentially harmful compounds that could not be effectively removed by conventional treatment processes. The typical AOPs include O_3/UV, O_3/H_2O_2/UV, H_2O_2/UV, Fe^{2+}/H_2O_2, Fe^{2+}/H_2O_2/UV, and TiO_2/UV (Andreozzi et al., 1999; Giri and Golder, 2014; Malato et al., 2009). Among these, TiO_2/UV based photocatalytic oxidation processes have received great attention in recent years as an alternative for water detoxification. To make the TiO_2 based photooxidation process economical, solar light can be used as a potential replacement for commercial UV lamps. This again requires modification of TiO_2 and TiO_2 -based photocatalysts for utilization of solar visible spectra (Chowdhury et al., 2012).

In recent years, researchers are interested in applying the 'photocatalytic decomposition process' to degrade hard-to-biodegrade organic pollutants (Curri et al., 2003). Nanostructured semiconductors are a potential candidate for the mineralization of toxic organic and inorganic compounds. It includes the metal oxides such as titanium dioxide (TiO_2), zinc oxide (ZnO), strontium titanate ($SrTiO_3$), tungsten oxide (WO_3), and hematite (α-Fe_2O_3) (Bansal and Kumar, 2013).

The precise definition of the term 'heterogeneous photocatalysis' is a tricky one; particularly as in many cases, the detailed mechanism of the ongoing reactions is uncertain. In the case of photocatalytic reactions, there is a light absorbing solid photocatalyst (semiconductor) which comes in contact with liquid or gas phase reactants and/or products (Chowdhury et al., 2012). All advanced oxidation processes operate through the formation of hydroxyl radical ($^{\bullet}OH$), which has very low selectivity. $^{\bullet}OH$ radical can drive the oxidation process through complete mineralization of even less reactive pollutants. These radicals can

even destroy biologically refractory pollutants that are characterized by high chemical stability (Andreozzi et al., 1999).

The heterogeneous photocatalysis utilizing different semiconductor photocatalysts such as

TiO_2, ZnO, ZnS, CdS, and GaP have established their effectiveness in pollutant degradation and eventually complete mineralization. Among them, TiO_2 and ZnO is the most active photocatalyst under the photon energy of 300 nm< λ< 390 nm and also shows the highest stability compared to other photocatalysts of similar class (Malato et al., 2009). Moreover, TiO_2 has acquired extensive applications in photocatalytic water treatment as well as air purification and self-cleaning surfaces due to its thermal and chemical stability, strong mechanical properties and low cost (Herrmann, 1999).

Heterogeneous photocatalytic oxidation process is primarily because of the following reasons:

(i) The oxidation reaction is usually carried out at ambient temperature and pressure. The use of solar light further reduces the energy footprint of the process,

(ii) The oxidant is strong and causes non-selective oxidation. It leads to complete mineralization in a shorter reaction time,

(iii) The oxidation process doesn't consume any expensive oxidizing chemical and,

(iv) The photocatalysts are less expensive, non-hazardous, stable, and reusable (Patil et al., 2016).

1.6.1 Types of semiconductor supports

The electrical conductivity value of a semiconductor material lies between that of an insulator such as glass, and a conductor, such as copper. Their temperature rises as their resistance reduces, which is the exact reverse activity to that of a metal. Their conducting attributes may be varied in needful modes by the careful, controlled induction of impurities (doping) into the crystal lattice (Linsebigler et al., 1995; Sangpour et al., 2010). A metal–semiconductor junction is created with two various doped regions present in the same crystal. The phenomenon of charge carriers contains ions, electrons, and electron holes at the metal–semiconductor junction are the source of all modern electronics, transistors and diodes. Doping a semiconductor material with a small amount of impurity atoms significantly enhances the number of free electrons (e^-) or holes (h^+) within the semiconductor (Xin et al.,

2005). The *p*-type semiconductor comprises excess h^+, whereas n-type contains excess free e^-. Here, *n* tends for negative e^- and *p* for positive h^+ are the expressions of charge of the bulk mobile charge carriers.

For intrinsic or pure semiconductors, the number of photogenerated e^- and of h^+ are equal ($n = p$). If it is doped with the equal acceptors and donors ($n = p$), then it remains as the intrinsic semiconductor, though doped (Neamen, 2003). Pure semiconductors electrical conductivity can be due to e^- excitation or crystallographic defects. In an intrinsic semiconductor, the numbers of e^- in the conduction band is equal to the number of h^+ in the valence band (Neamen, 2003).

An indirect band gap (E_g) of pure semiconductor is one in which the minimum energy of the conduction band (CB) and the maximum energy of the valence band (VB) occurs at different k-space wave vector. A direct E_g pure semiconductor is one where the minimum energy of the CB occurs at the same k as the maximum energy of the VB. TiO_2 and ZnO semiconductor supports are commonly used for photocatalytic oxidation (Neamen, 2003). **Table 1.1** Summarizes various parameters of different semiconductor supports.

Table 1.1. Semiconductor parameters (Neamen, 2003).

Material	**E_g (eV)**	**Lattice parameter (a, A°)**	**Dielectric constant (ϵ_r)**	**Electron affinity (χ, eV)**	**Index of refraction (η)**
TiO_2	3.2	3.78	10	4.2	2.45
Zinc oxide, ZnO	3.37	3.35	8.5	4.3	1.94
Aluminum arsenide, AlAs	2.16	5.66	12.0	3.5	2.97
Gallium phosphide, GaP	2.26	5.45	10	4.3	3.37
Aluminum phosphide, AlP	2.43	5.46	9.8	-	3.0
Indium phosphide, InP	1.35	5.87	12.1	4.35	3.37
Copper(I) oxide, CuO	2.17	4.27	18.1	4.07	2.63
Zinc sulphide, ZnS	3.54	5.41	8.9	4.43	2.35

1.6.2 TiO_2 as an universally accepted photocatalyst

Titanium (Ti), is known as the world's fourth most abundant metal and the ninth most abundant element discovered in 1791 by Reverend William Gregor in England. Pure TiO_2 does not available in nature, it is primarily found in several minerals like anatase, rutile, perovskite, brookite, ilmenite, leucoxene, and many iron ores (Reyes-Coronado et al., 2008).

Titanium dioxide or titania (TiO_2) is characterized by the presentation of an amazing photoinduced phenomenon, and it has attracted more and more research work in this field. With a wide band gap (3.2 eV), TiO_2 is able to be excited using UV illumination with a wavelength up to 387.5 nm which have higher photon energy than the band gap. An electron (e^-) is promoted to the CB leaving a hole (h^+) in the VB (Malato et al., 2009). The excited e^- can either be used directly to create electricity as in photovoltaic solar cells or used to drive a chemical reaction, which is called photocatalysis. Excited e^-/h^+ pairs can be applied in water photo-splitting for the hydrogen generation or in the chemical process to decompose or create particular organic, inorganic, and biological compounds. The strong oxidative potential of the positive h^+ oxidize water to create $^{\bullet}OH$ radicals. This oxidative potential can also directly oxidize the organic materials (Ola and Maroto-Valer, 2015).

The anatase phase exhibits a slightly higher Fermi level than rutile and, lower capacity to absorb oxygen and higher degree of –OH groups on the surface. So, it exhibits an enhanced photocatalytic activity. Furthermore, there are also reports which proves that a combination of anatase (70-75 %) and rutile (30-25 %) is more active than pure anatase (Bacsa and Kiwi, 1998). The mixture is considered as a kind of composite semiconductor where the photoexcited e^- transfer from anatase CB to rutile CB thus achieving a wide charge separation that prevents early recombination. The current commercialized photocatalyst, *Degussa* P25, is a mixture of anatase and rutile phases (anatase/rutile ratio≈80/20) with a nominal particle size of 50 nm and a surface area of 50±15 $m^2 g^{-1}$.

Recently, the photo-induced super-hydrophilic property of the TiO_2 film surface has been exploited for antifogging coatings and self-cleaning windows (Nakata and Fujishima, 2012). The types of photochemistry responsible for photocatalysis and super-hydrophilicity are totally different, even though both can occur simultaneously on the same surface. TiO_2 integrated into outdoor building materials can considerably decrease concentrations of airborne contaminants such as volatile organic components. **Figure 1.6** shows the main photoinduced processes on TiO_2 material based on different of aspects and applications (Fujishima et al., 1999; Nakata and Fujishima, 2012).

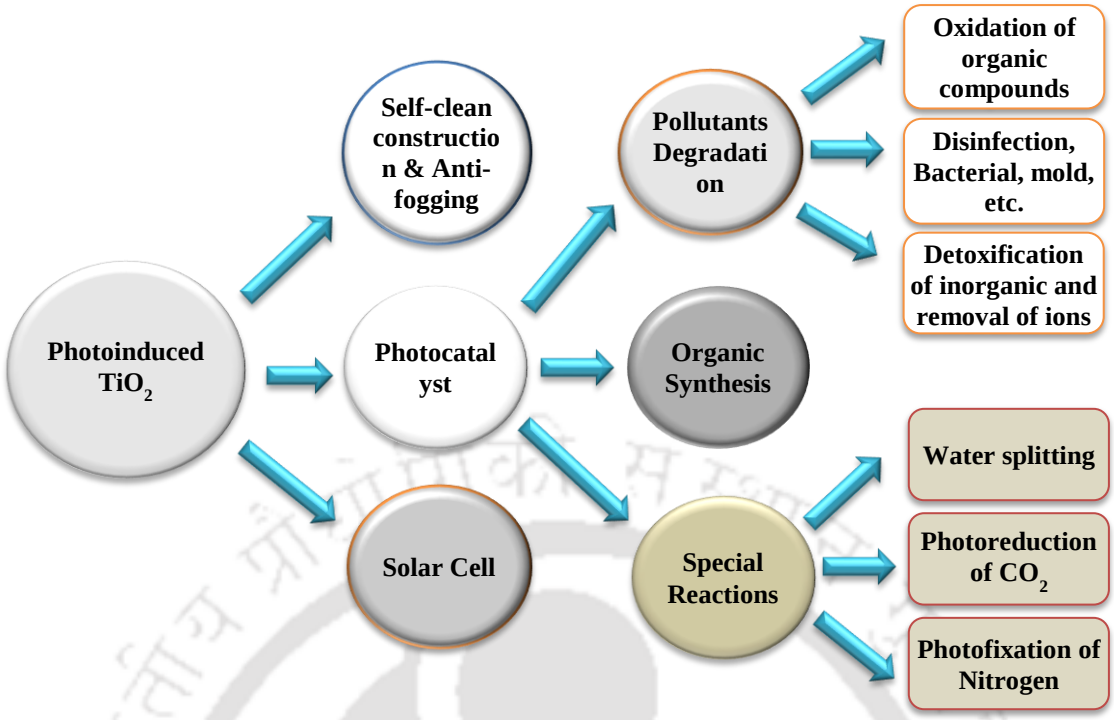

Figure 1.6. Photoinduced processes on TiO_2.

1.6.3 Improving photocatalytic activity of TiO_2

Although, the pure TiO_2 extends unique properties especially at the nanosize, but it suffers from the effective separation of e^-/h^+ charge, usage under visible light (band gap energy of pure TiO_2 is 3.2 eV), fast backward reactions (water to $H_2 + O_2$ to water). Hence, require extended research for superior photocatalysts (Fujishima et al., 1999; Nakata and Fujishima, 2012). Improving the photocatalytic reactions involve more defined crystalline structure and size, increased sorption capacity, larger specific surface area, variable nanoporosity, and induction of several dopants to change the surface activity. In this section, the performance modifications based on different doping methods is primarily discussed.

TiO_2 photocatalysis is governed by the free radical mechanism, and it causes non-selective oxidations (Fujishima et al., 1999; Nakata and Fujishima, 2012). In other words, target reactant/pollutant and intermediate molecules may experience the same decomposition rate during photocatalysis. However, some intermediate compounds show even higher toxicity than the parent compound. Hence, it is essential to improve a TiO_2 based photocatalytic system that can utilize UV and visible light irradiation to increase photonic efficiency (Serpone and Salinaro, 1999).

Shah et al. (2015) fabricated the CuO/Ag/AgCl/TiO_2 catalyst via a reverse microemulsion synthesis. The photocatalytic degradation of methyl orange and phenol with 92 and 85 % removal is achieved under visible light (Shah et al., 2015).

Simamora et al. (2012) synthesized CuO/TiO_2 photocatalyst for splitting of seawater for solar fuel - H_2 and degradation of seawater organic pollutants such as dyes. By irradiating UV light for 5 h, about 99 % of methylene blue dye degradation with simultaneous 3.1 mmol H_2 production per h per g catalyst is obtained (Simamora et al., 2012).

1.6.3.1 *Recombination of photogenerated electron/hole pairs*

The photocatalytic activities of titania photocatalysts are generally limited by the fast recombination of the photogenerated e^-/h^+ pairs. The charge carriers recombination can cause upon heat evolution via accompanied by light emission irradiative routes or nonirradiative pathways (Etacheri et al., 2015). TiO_2 is an indirect bandgap semiconductor, shows only very weak bandgap emission upon the recombination of CB e^- with VB h^+, while the irradiative recombination involving trap states is optically allowed (Emeline et al., 2005).

Knorr et al. (2008) observed a broad visible photoluminescence (PL) band for anatase, which they interpreted as a recombination of trapped e^- with h^+ in the VB. The surface trapped h^+ in anatase is reported to be placed about 1.8−2.5 eV below the CB edge, while the e^- located about 0.7−1.6 eV below the CB edge relating to oxygen vacancies (Knorr et al., 2008).

Yamada and Kanemitsu (2012) studied the recombination dynamics of charge carriers in anatase and rutile TiO_2 single crystals employing a combination of time-resolved PL, transient absorption and photoconductivity measurements, and resulted a longer lifetime for e^- in anatase (>few ms) in comparison to rutile (24 ns), while the decay of the h^+ in both crystal phases occurs on the nanosecond time scale (Yamada and Kanemitsu, 2012).

1.6.3.2 *Inability to utilize visible light*

Since the UV light only accounts for about 4 % of the solar radiation energy while the visible light contributes about 55 %. The inability to utilize visible light limits the efficiency of solar photocatalytic reactions (Schneider et al., 2014).

Various research initiatives have been carried out into the development of visible light responsive photocatalysts by incorporating small amounts of dopants such as cations and metal oxides. However, these initial tests were detected to have limitations (Herrmann et al., 1984; Hoffmann et al., 1995). As an alternative synthesis approach for doped TiO_2, an

advanced metal ion-implantation method has been employed by bombarding them with high energy metal ions to change the electronic attributes of TiO_2 photocatalysts. In particular, the research group of Anpo exposed that the implantation of TiO_2 with several transition metal ions such as Fe, V, Co, Ni, and Cr by high voltage acceleration in the range of 50−200 keV could enable a wide shift in the absorption band of these photocatalysts toward visible domain with different levels of effectiveness (Anpo et al., 2001, 1998).

1.6.3.3 *Fast backward reaction for water splitting*

Decomposition of water into hydrogen and oxygen is an energy intensive process, thus the thermodynamics preferred a backward reaction (recombination of hydrogen and oxygen into water) proceeds easily (Chen and Mao, 2007). Pollutants adsorbed by the photocatalysts are degraded primarily by the VB h^+ and radicals caused by h^+. Therefore, the mechanism regarded in moving this photogenerated h^+ to the interface is of predominant significance. On the other hand, for photocatalytic water splitting, the transfer of CB e^- to the interface and their energy levels are the most effective elements that involve in the H_2 generation rate (Chen and Mao, 2007). Hence, the results based on environmental remediation implications cannot be directly useful to water splitting.

Induction of e^- donors, noble or transition metal ions, dye sensitization, composite semiconductors, carbonate salts, and anions or cations, are all probable pathways to modify bandgap (Chowdhury et al., 2012). However, none of above pathways, in and of themselves, is capable of solving all existing issues.

Adding e^- donors (h^+ scavenger or sacrificial reagents) to react with VB h^+ can improve the photocatalytic e^-/h^+ separation. Organic compounds (hydrocarbons, such as EDTA, methanol, ethanol, lactic acid) are widely used as e^- donors which can be oxidized by VB h^+, meanwhile, the remaining strongly reducing CB e^- can reduce H^+ to H_2 (Schneider et al., 2014). Other inorganic ions S^{2-}/SO_3^{2-}, Ce^{4+}/Ce^{3+}, Fe^{3+}/Fe^{2+}, and IO^{3-}/I^- can also be used as sacrificial reagents. The addition of e^- donors to react irreversibly with the photogenerated VB h^+ can enhance the photocatalytic e^-/h^+ separation. Since, e^- donors are consumed in photocatalytic reaction, continual addition of e^- donors is needed (Chen and Mao, 2007).

1.6.3.4 *Noble metal and group VIII metal loading (metal coating)*

If the Fermi level of TiO_2 is more than that of the metal, e^- are migrated from the TiO_2 particles to near metal particles. This ensues the origin of a Schottky barrier (Pt or Ag gives the maximum) at each semiconductor-metal junction, which extends to an increase in charge

carriers separation and a reduction in e^-/h^+ recombine rate. As a result of the decreased e^-/h^+ recombination rate, metal loading on the surface of TiO_2, improves photocatalytic activity by inducing the transfer of e^- to dissolved-oxygen molecules (Schneider et al., 2014).

Metals such as Ag, Pt, Au, Cu, Pd, Rh, Ir, Os, and Ni (Bu and Zhuang, 2012; Kuo et al., 2007; Noberi et al., 2012; Yu et al., 2013) or combined mixed metals work as e^- scavengers or e^- sinks to trap electrons, while photogenerated VB h^+ remain on TiO_2. These activities greatly enhance the possibility of separation of e^-/h^+ charge carriers, resulting in improved photocatalytic activity.

The cost of noble metal loading is one of obvious disadvantages. Also, there is an optimum loading value of metal particles, if metal loading is above optimum values, several harmful effects could happen. First, a reduction in e^- density happens, due to e^- attraction by metal particles, which has a negative effect on the separation of charge carriers, falling photocatalytic activity (Schneider et al., 2014). Second, extreme metal loading on TiO_2 restricts the quantity of light contacting the surface and, decreases the number of photogenerated e^-/h^+ pairs. Consequently, the photodecomposition rate is dropped (Konstantinou and Albanis, 2004). Third, once negatively charged metal particles, particularly for highly loaded samples (>5 %), attract h^+ and consequently recombine them with e^-. In this case, the metal loadings become recombination centers (Chowdhury et al., 2012; Schneider et al., 2014).

1.6.4 Mechanism of photocatalysis

Similar to complicated thermal catalytic reactions, photocatalysis can vary with respect to the mechanism of a given reaction. Salomon (1982) proposed that photocatalysis could be further classified into two main types including photo-induced and photo-initiated catalytic reactions (Salomon, 1982).

1.6.4.1 *Photogenerated catalysis*

Ground state catalyst interacts with ground state substrate to carry out a chemical reaction in a thermodynamically spontaneous catalytic step, such as photo-induced catalytic reaction, photo-initiated catalytic reaction (Dadashi-Silab et al., 2016).

Typically, the absorption of UV light of a mole of photons gives as 130 times higher energy, as compared to ambient conditions (Dadashi-Silab et al., 2016). This large amount of light energy input would overcome energy barriers for lots of chemical reactions to take

place. Irradiation can be applied using photoinitiators to start chain actions such as cationic or radical polymerization reactions.

Dye/co-initiator molecules have been utilized as visible light photosensitizer components in photo-initiated polymerizations (**Figure 1.7(a).** The co-initiator is used as e^- donor in the reductive quenching, which transfers an e^- to the dye molecule to form reduced dye molecules and e^- donor radical cation species. On the other hand, an e^- transfer takes place from the dye to an e^- acceptor, in the oxidation quenching, which could oxidize dye to radical cation while reducing the co-initiator compound (Dadashi-Silab et al., 2016). **Figure 1.7(b)** shows the mechanism of the semiconducting ZnO NPs formation by free radicals initiation in the presence of several co-initiators. Of great importance, their heterogeneity makes semiconductor NPs effective reusable photoinitiators as after the reaction they are easily recycled, refined, and employed in further reactions while maintaining their reactivity after multiple usages (Dadashi-Silab et al., 2016; Strandwitz et al., 2008).

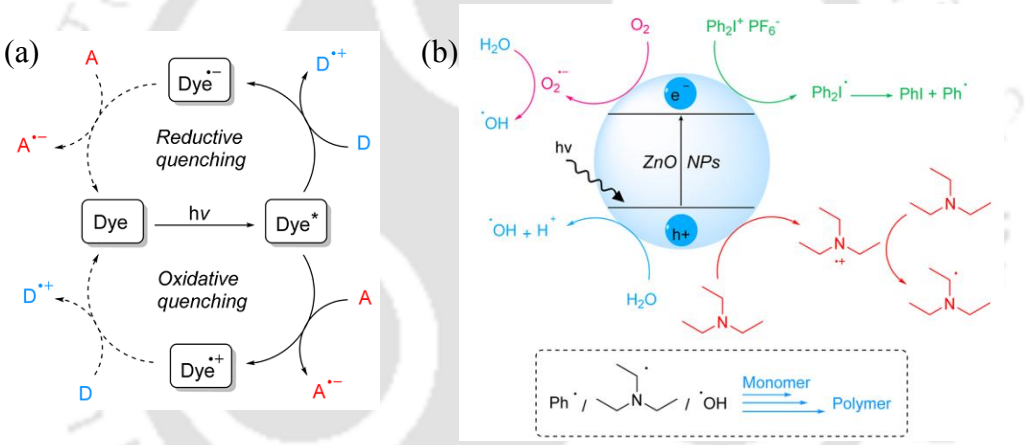

Figure 1.7. (a) Photoinduced e^- transfer reactions of dyes, (b) Photoinitiated free radical polymerization using semiconductor nanoparticles: interaction of the photoinduced e^- and h^+ species with different co-initiators (Dadashi-Silab et al., 2016).

1.6.4.2 *Catalyzed photolysis*

During the catalytic reaction either the substrate or the catalyst or both are in an excited state. Thus, light is used to raise the efficiency of a reaction, such as catalyzed photochemistry, catalyzed photoreaction, photosensitization, photo-assisted catalysis. Photocatalytic reactions are initiated by the absorption of light and use energy from electromagnetic radiation in the form of a photon to provide the activation energy for the reaction (Dadashi-Silab et al., 2016).

Planck's equation (Eq. 1.1 or 1.2) shows the relation between the light frequency, *v*, and wavelength, λ, and the energy associated with the incident photon, *E* (Ramakrishnan et al., 2012).

$$E=hv \quad (1.1)$$

$$E=hc/\lambda \quad (1.2)$$

where, *h* is Planck's constant and *c* is the speed of light.

For semiconductor TiO_2, whose band gap energy is 3.2 eV for the anatase phase with an indirect band gap, the corresponding absorbed light wavelength is 387.5 nm, which is within the UV light range. To be able to generate an e^-/h^+ pair, the semiconductor must be irradiated with light of this frequency or higher. The reaction is simply expressed as in Eq. 1.3 (Hoffmann et al., 1995).

$$TiO_2 \rightarrow TiO_2 + e^-_{CB} + h^+_{VB} \rightarrow \text{Recombination} \quad (1.3)$$

After the pairs of e^-/h^+ are created in the semiconductor, the charge will transfer between e^-/h^+ pairs and adsorbed species (reactants) on the semiconductor surface to create different radicals with different reduction or oxidation power. The photo-excited e^- and h^+ can also recombine in bulk or on the surface of the semiconductor in a few nanoseconds, thus releasing energy in the form of heat or photons. The efficiency of a photocatalyst depends on the competition of e^- and h^+ transfer to absorbed species at different interfaces and their deactivation by recombination.

1.6.4.3 *Photooxidation*

The highly oxidizing characteristics of the VB holes and the generated hydroxyl radicals, $^{\bullet}OH$, are responsible for the decomposition of organic reactants when water is available (Eqs. 1.4 and 1.5) (Konstantinou and Albanis, 2004).

$$h^+_{VB} + H_2O \rightarrow OH^{\bullet} + H^+ \quad (1.4)$$

$$h^+_{VB} + OH^- \rightarrow OH^{\bullet} \quad (1.5)$$

The adsorbed reactant/pollutant can be oxidized directly with the photogenerated h^+ when the concentration of reactant/pollutant is high enough or reactant/pollutant molecules are strongly adsorbed to the surface of photocatalyst. The hydroxyl groups on the photocatalyst surface and water itself also can react with h^+ to generate $^{\bullet}OH$ which have sufficiently high oxidation power to oxidize the reactant/pollutant and intermediates. The oxidative pathway leads, in many cases, to complete oxidation of an organic substrate to CO_2

and H_2O. Depending on the individual organic substance, generated intermediate products may initiate other redox reactions at the same time.

1.6.4.4 *Photoreduction*

When O_2 is present in the reacting system, dissolved O_2 can be is transformed to the superoxide radical anion ($O_2^{-\bullet}$) which can lead to the additional formation of $^{\bullet}OH$, and hydroperoxide radicals $HO_2^{\bullet}$. (Eqs. 1.6-1.9) (Hoffmann et al., 1995; Konstantinou and Albanis, 2004).

$$e_{CB}^{-} + O_2 \rightarrow O_2^{-\bullet} \quad (1.6)$$

$$e_{CB}^{-} + O_2 + H^{+} \rightarrow HO_2^{\bullet} \quad (1.7)$$

$$2HO_2^{\bullet} \rightarrow H_2O_2 + O_2 \quad (1.8)$$

$$H_2O_2^{\bullet} + e_{CB}^{\bullet-} \rightarrow OH^{-} + OH^{\bullet} \quad (1.9)$$

1.6.5 Factors affecting photocatalytic performance

There are several factors that can influence the photocatalysis process. From a chemistry point of view, photocatalysis is a series of chemical reactions, which occur under exposure to light, among reactant, media, and a photocatalyst. The inherent properties of photocatalyst and the experimental conditions can both affect the final photocatalytic activity. Factors related to the properties of the photocatalyst and the experimental conditions can be categorized as intrinsic and extrinsic variables that are affecting photocatalytic reactions in different ways.

1.6.5.1 *Particle size*

The particle size of a photocatalyst is a very important parameter for photocatalytic efficiency. After many years research efforts in nano science, it is well-known that in the nanometer-size range, the physicochemical attributes of semiconductors can be modified (compared with bulk) by simply manipulating the particle size. Quantum size effects (QSE) occur for semiconductor particles (Q particles) whose size is on the order of 1-10 nm. The e^{-} and h^{+} produced in Q-particles are confined in a potential well of small geometrical dimensions (Linsebigler et al., 1995). Due to this confinement, the CB e^{-} and the VB h^{+} do not experience the electronic migrations that present in a bulk semiconductor. Instead, the confinement produces a quantization of discrete electronic states and increases the effective band gap of the semiconductor, which can be observed experimentally as a blue shift in the

absorption and emission spectra. On the other hand, the most important electronic property influenced by particle size is the space charge layer. The driving force to separate the charge carriers is proportional to the magnitude of the potential drop within the space charge layer. The potential difference is higher for large particle size (>100 nm) thus allowing for effective charge separation. However, the transmission time of charge carriers from the particle interior to the surface can be significantly increased as the particle diameter increases.

The light scattering ability of particles depends on their size relative to the wavelength of the light. Light absorption coefficient is much higher and scattering coefficient is much lower when nano-particles are used, and maximum scattering is observed when the sizes of particles are close to half of the wavelength of the incident light. Moreover, for large particles, radiation is primarily absorbed in the outer layer of the particle and the interior bulk is not fully utilized.

However, over-reducing the size of photocatalyst particles (<10 nm) may result in negative consequences to the photocatalysis process, such as band gap increase and faster surface recombination of charge carriers. Larger particle size (>100nm) may result in longer transmit time of charge carriers to the surface, increase recombination of e^-/h^+ pairs before reaching the surface, as well as larger light scattering coefficients. Optimized particle size is desirable for improving photocatalytic activity.

Hoffman et al. (1995) reported the band gap increases and the band edges shift to yield larger redox potentials (Hoffmann et al., 1995). Barajas-Ledesma et al. 2010 reported the adsorption edge for Al_2O_3 doped TiO_2 with fewer amounts of alumina shifting a little toward a lower energy region, leading to a band gap reduction of TiO_2 from 3.2 to 2.8 eV (Barajas-Ledesma et al., 2010).

When TiO_2 is doped with the multielement (C, N, B, F) there is a shift in the absorption edge from 400 nm to 425 nm. The bandgap reduction from 3.14 to 2.92 eV and increment in crystallite size from 18.9 to 81.1 nm are found determined for multielement doped TiO_2 (Ramakrishnan et al., 2012).

1.6.5.2 *Catalyst surface area*

The photocatalytic activity of TiO_2 catalysts majorly depends on absorbability and the separation efficiency of e^-/h^+ recombination. The reaction takes place in heterogeneous catalysis is at the active solid catalyst's surface. The photocatalytic activity of modified TiO_2 photocatalysts can be further improved if the catalyst absorbs more targeted reactants/ contaminants along with effective charge separation. A high surface area is desirable for the

photocatalytic system where adsorption on the surface is the rate-controlling step (Kominami et al., 2002).

Adsorption of pollutants in the locality of the photocatalytic active sites stimulates the photodecomposition of reactants/pollutants that usually in low concentrations adsorb on the surface of photocatalyst (Xin et al., 2005). The adsorption capacity can be generally improved by increasing the specific surface area (SSA) and pore volume of catalysts. However, when several intermediate products appear and intend to re-adsorb strongly during photocatalysis, surface active site may be blocked for further interfacial charge transfer. Meanwhile, surface hydroxyl concentration and distribution influence the adsorption and selectivity significantly.

NPs and thin film are usually associated with a higher specific surface area. The pore structure of highly porous material also plays a key role in photocatalytic activity. Pores must be fabricated as an open cell that can be accessible during the entire photocatalysis reaction process. Pore size distribution and mesopore volume percentage describe the homogeneity of material and uniformity of porous structure.

He et al. (2013) synthesized hollow TiO_2 photocatalyst using pollen grains and obtained 96.2 m^2 g^{-1} specific surface area with a pore size range between 2 and 40 nm with 95 % Rhodamine B dye removal (He et al., 2013).

1.6.5.3 *Crystal structure and properties of catalyst*

In photocatalysis, an important topic to be discussed is the crystallographic structure of the metal oxide that is associated to its photocatalytic activity. TiO_2 has been known to exist in three main polymorphic phases: rutile (tetragonal), anatase (tetragonal) and brookite (orthorhombic). All of them have the same fundamental octahedral structural units, but their arrangements are different. They differ by the assembly patterns of octahedral chains. The crystal structure of rutile phase is built up from octahedrals that are connected by their edges, in anatase, the vertices are connected, and in brookite, both vertices and edges are connected. The lattice structure for anatase and rutile is demonstrated in terms of distorted TiO_6 octahedra. The differences in crystal structures of each type of titania induce the different thermodynamic properties, i.e. stability, and physical properties, i.e. optical refractivity, density (**Table 1.2**) (Reyes-Coronado et al., 2008).

Table 1.2. Some bulk properties of the three main polymorphs of TiO_2 (Anatase, Rutile, Brookite).

Phase	Refractive index	Density (g cm^{-3})	Band gap (eV)	Light wavelength threshold (nm)	Crystal structure
Anatase	2.49	3.895	3.26	384	Tetragonal
Rutile	2.903	4.2743	3.02	410	Tetragonal
Brookite	2.583	4.123	2.96	401	Orthorhombic

Many researchers claim that rutile is a catalytically inactive or much less active form of TiO_2, while others find that rutile has selective activity toward certain substrates. Highly annealed (≥ 800 ºC) rutile appears to be photoinactive (Hoffmann et al., 1995). Due to surface free energy and surface stress, when particle size reduces to the nanoscale level, the relative stability phase may reverse. Anatase is more stable at ≤10 nm sizes, rutile is thermodynamically most stable at ≥35 nm sizes and, brookite is most stable between 11 and 35 nm.

Due to oxygen vacancies, TiO_2 works as an *n*-type transition metal oxide semiconductor in which the density of e^- in the CB is exceeded by the density of h^+ in the VB. The crystal structure of both anatase and rutile has a tetragonal, where the anatase contains larger unit cell volume compared to the rutile (**Table 1.2**). The variances in lattice parameters of anatase and rutile TiO_2 cause diverse electronic band structures and densities, heading to various band gaps (3.20 and 3.02 eV for anatase and rutile). Hence, the absorption thresholds represent to a wavelength of 384 and 410 nm for two TiO_2 forms, respectively (Fujishima et al., 1999). Higher wavelengths are generally found for weak crystallized nanosized materials or thin films (Halley et al., 1991).

1.7 Conventional Methods of Nanoparticles and Photocatalyst Fabrication

The typical methods of nanoparticles and photocatalyst synthesises such as chemical reduction, co-precipitation, sol-gel, solvothermal, flame spray pyrolysis, and chemical vapour deposition are discussed in this section. The focuses are mostly given on AgNPs and TiO_2 support. The process is commonly modified by various cocatalysts including doping, impregnation and photodeposition (**Figure 1.8**).

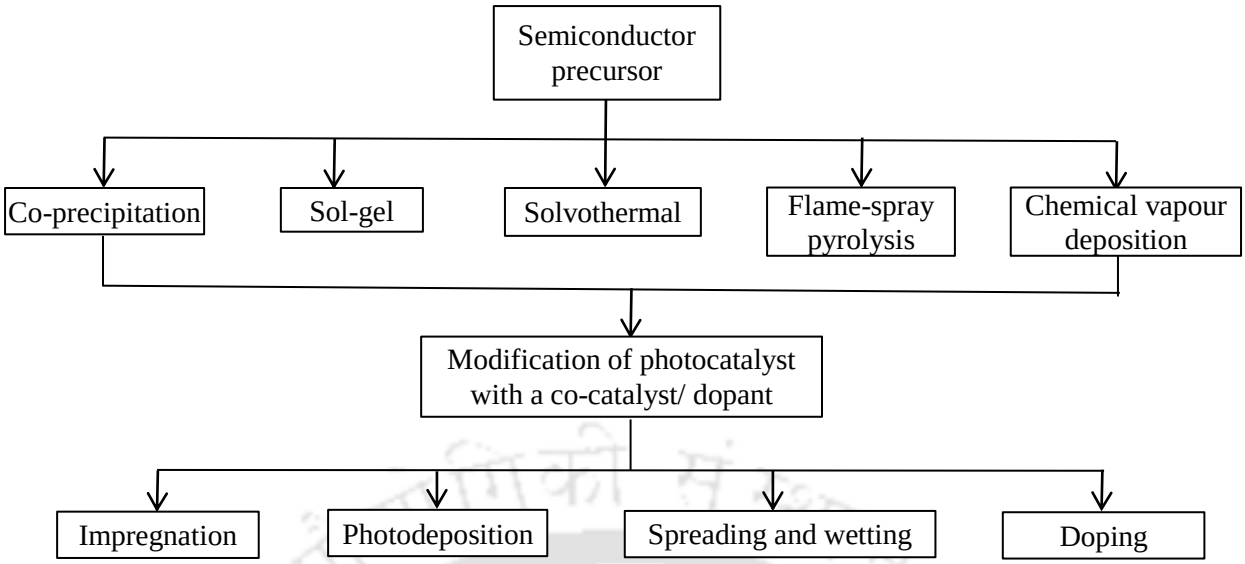

Figure 1.8. Schematic representation of photocatalyst fabrication.

1.7.1 Chemical reduction method

Chemical reduction method is most commonly used for the synthesis of metal NPs, and the particles are formed as stable colloidal dispersions either in organic or water solvents (Khan et al., 2011). Frequently used reducing agents are citrate, ascorbate, hydrazine hydrate, elemental hydrogen, and borohydride (Sondi et al., 2003). The formation of colloidal AgNPs is generally obtained by the reduction of Ag^+ ions in aqueous or organic solutions.

The reduction of different complexes with Ag^+ ions promotes the silver atoms (Ag^o) formation, which is followed by aggregation into clusters of oligomer. These clusters ultimately extend to the formation of colloidal AgNPs (Devi and Mandal, 2013).

Wang et al. (2005) synthesized AgNPs using the chemical reduction method by using polyvinyl pyrrolidone (PVP) and glucose as the reducing and capping agents at a temperature of 60 °C for 10 min of reaction time. The AgNPs are sized between 20 and 80 nm with 5:1 ratio of $AgNO_3$:PVP (Wang et al., 2005).

Guzman et al. (2009) fabricated AgNPs using the chemical reduction method. Here, they used $AgNO_3$ as the precursor of AgNPs which is reduced using hydrazine hydrate and citrate of sodium. Sodium dodecyl sulphate (SDS) and citrate of sodium are used as stabilizing agents. The transparent solution turned pale yellow which indicates the formation of AgNPs. Further, the solution is centrifuged to separate and wash AgNPs. Particle size ranges from 8 to 50 nm (Guzman et al., 2009).

Khan et al. (2011) synthesized AgNPs by the reduction of $AgNO_3$ using aniline in dilute aqueous solutions using cetyltrimethlyammonium bromide (CTAB, 1 mM dm^{-3}) as the

capping agent. AgNPs sizes of 10 to 30 nm are formed in 120 min at pH 10.2 (Khan et al., 2011).

Xia et al. (2011) used hyaluronan as a reducing agent and soft template by varying the temperature from 50 to 70 ^{o}C at pH 1-11 up to the reaction time of 24 h. The maximum Ag^{+} reduction and faster kinetics are observed at 70 ^{o}C at pH 11 for the 60 min reaction time (Xia et al., 2011).

Gudikandula and Maringanti (2016) synthesized AgNPs (10-60 nm) using 1 % trisodium citrate and tested the antimicrobial activity of AgNPs against *B. subtilis, E. coli* and *S. aureus* (Gudikandula and Charya Maringanti, 2016).

1.7.2 Co-precipitation (CP) method

In co-precipitation process, normally soluble compounds are precipitated out in suitable pH range. Kandpal et al. (2014) used this method for preparing iron oxide NPs. In their study, they heated de-ionized water to about 90 ºC and then 3 g of $FeCl_2.4H_2O$ is dissolved with continuous stirring. Then ammonium hydroxide solution is added at a flow rate of 0.007 mol s^{-1}. Precipitant was settled down and collected by separating the supernatant liquid by centrifugation and then by filtration. It was washed with ethanol and then dried (Kandpal et al., 2014).

Petcharoen and Sirivat (2012) synthesized magnetite NPs via CP method using ammonium hydroxide as the precipitating agent. Ferrous and ferric salts at different molar ratio are used under N_2 flow with vigorous stirring at various temperatures (0-90ºC). The structure, morphology and electrical properties are characterized by X-ray diffraction (XRD), field emission scanning electron microscopic (FESEM) micrographs and vibrating sample magnetometer. Particle sizes are in the range of 10-40 nm, and electrical conductivity of the smallest particle size is 1.3×10^{-3} S cm^{-1} (Petcharoen and Sirivat, 2012).

Liu et al. (2012) fabricated TiO_2 and Ag doped TiO_2 by CP method. Urea is first dissolved into DI-water followed by $Ti(SO_4)_2$ and $AgNO_3$ with continuously stirring at 80 °C. Solids are filtered out and dried at 70°C. Ground particles are calcined at 550 °C for 4 h. The average particle size is found to be about 2.5 µm. The antibacterial activities of *E. coli* exhibits about 99 % inactivation within 15 min of reaction (Liu et al., 2012)

Gaikwad et al. (2004) prepared pure ultrafine single phase $SrBi_2Nb_2O_9$ using co-precipitation method. Ammonium hydroxide and ammonium oxalate are used to precipitate Sr^{2+}, Bi^{3+}, and Nb^{5+} simultaneously. Particle size and morphology are determined by

transmission electron microscopy (TEM). The average particle size is 100 nm and the room temperature dielectric constant at 1 kHz is 100 (Gaikwad et al., 2004).

1.7.3 Sono-chemical method for NPs synthesis

Salkar et al. (1999) reported on the sono-chemical method for the formation of AgNPs. In this process they dissolved the silver nitrate solution in 100 mL of de-ionized water and sonicated for 1 h under the atmosphere of argon-hydrogen maintaining the temperature of 10°C. After that the solution was transferred to an inert glove box. The solution is centrifuged and washed with de-ionized water followed by ethanol. Then thus formed solid amorphous AgNPs are sent for subsequent characterization (Salkar et al., 1999).

HgS and PbS nanoparticles of about 15 and 20 nm are prepared by the sonochemical irradiation of an ethylenediamine solution containing elemental S and mercury acetate or lead acetate (Zhu et al., 2000).

Zhanjiang and Jinpei (2012) used silver stearate, hindered phenol, and triphenylphosphine as the silver precursor, reducing agent, and reduction accelerator, respectively, in a sonochemical process. They found an average particle size of 6.8 nm with a narrow distribution from 6.2 to 7.4 nm (Zhanjiang and Jinpei, 2012).

A facile sonochemical method is developed by Darroudi et al. (2012) for preparing colloidal AgNPs in aqueous gelatin solutions. The effects of reducing agent and Ag^+ concentrations, ultrasonic time, and ultrasonic amplitude on the particle size are investigated. The size of the AgNPs decreases with the ultrasonic amplitude, and it increases with the sonication time with a mean particle size of about 3.5 nm (Darroudi et al., 2012).

Nickel and cobalt sulfides with various stoichiometries are synthesized sonochemically from $Ni(CH_3COO)_2{\cdot}4H_2O$, $Co(CH_3COO)_2{\cdot}2H_2O$ and different sulphur precursors using a direct immersion ultrasonic probe. NiS, Ni_3S_4, $CoS_{1.1}$, and Co_9S_8 NPs are originated with average crystallite sizes in the range from 7 to 30 nm (Kristl et al., 2017).

1.7.4 Laser ablation method

This is a very simple technique for synthesizing NPs. Simakin et al. (2004) presented a review on nanoparticle synthesis using laser ablation techniques. In this method, a solid target kept under thin liquid media is exposed to laser radiation. As a result, the solid particles confined in the laser spot come out to the liquid and forms colloidal solution of NPs of that solid. Water and ethanol can be used as liquid media. Different laser sources like Cu vapor

laser, Ti: sapphire laser and Nd: YAG laser are used. Using this method, NPs of silver, gold, silver-gold alloy can be prepared (Simakin et al., 2002).

A stable colloidal solution of free AgNPs (3.8 nm average diameter) are formed in pure acetonitrile and N,N-dimethylformamide solution using laser pulses at 1064 nm (9 ns) focused with a 10 cm focus lens. AgNPs are surrounded by a carbon shell or included in a carbon matrix when AgNPs is synthesized in tetrahydrofuran and dimethyl sulfoxide (Amendola et al., 2007).

Zamiri et al. (2012) synthesized AgNPs by the laser ablation technique using selected natural polymers such as starch, gelatin, and chitosan as stabilizing agents. The size of AgNPs varies between 5 and 35 nm for startch and gelatin, and 10 and 60 nm with chitosan based NPs. The fabrication process is carried out by ablating a pure Ag plate by nanosecond Q-switched Nd–Yg pulsed laser (λ=532 nm, 360 mJ per pulse). The starch based NPs showed the highest formation efficiency and more stability than other polymers during one month storage (Zamiri et al., 2012).

Ag/Ag_2O core shell NPs are prepared by femtosecond laser ablation with the size between 1 and 6 nm using starch, and they find more stable colloids using low energy pulses (100 µJ) than high energy pulses (500 µJ) (Arce et al., 2017).

Li et al. (2016) synthesized reduced TiO_2-graphene oxide heterostructure by the one-step laser ablation method, and the resulting particles achieve drastic increase in the photocatalytic H_2 production rate, up to 23 times with respect to the blank experiment with a maximum H_2 production rate of 16 mmol h^{-1} g^{-1} using Pt as a co-catalyst under the illumination of simulated sunlight (135 mW cm^{-2}). The quantum efficiencies are reported as 5.15 % for λ = 365 nm and 1.84 % for λ = 405 nm. The overall solar energy conversion efficiency is found as 14.3 % (Li et al., 2016).

1.7.5 Electrochemical method (electrolysis)

The metal ion reduction using electrolysis process has long been used. However, there are a few studies in metal NPs synthesis, especially silver using this method. Spherical AgNPs is formed with an average size of 11 nm at room temperature by reducing $AgNO_3$ in polyol solution in the presence of polyvinylpyrrolidone (PVP) and KNO_3 using the electrolysis process. The Ti electrode of about 6 mm diameter, and Pt plate of 2 cm diameter are used as cathode and anode, which resulted in electro-deposited AgNPs formation (Lim et al., 2006).

Guangnian et al. (2013) prepared AgNPs of 1-3 nm size by the electrolysis of deionized water (electrolyte) and PVP (5 % w/w served as stabilizer) solution using highly pure silver flakes as the electrodes (Xu et al., 2013).

Anandgaonker et al. (2014) synthesized TiO_2 nanoparticles (25-30 nm) in an electrochemical route. They used tetra propyl ammonium bromide salt as the stabilizing agent in an organic medium *viz*. tetrahydrofuran and acetonitrile in 4:1 ratio. The nanoparticles are screened for in-vitro antibacterial activity against human pathogens such as *E. coli* and *S. aureus* (Anandgaonker et al., 2014).

Huang et al. (2015) synthesized AgNPs at an applied voltage of 10 V with 5 mg mL^{-1} PVP at 60 ^{o}C using the silver electrodes and obtained the particles sizes between 3 and 18 nm (Huang et al., 2015).

Petica et al. (2017) prepared Ag/TiO_2 nanocomposites with 2 % (w/w) Ag-loading by the electrochemical method. Ag/TiO_2 is tested for the degradation (98.5 %) of orange II dye using UV light (λ = 365 nm) and inhibition of *S. aureus* and *E. coli* with the inhibition zone diameters of 22 and 20 nm, respectively (Petica et al., 2017).

1.7.6 Sol-gel technique

This method is used for the fabrication of metal oxides, especially the oxides of silicon and titanium. It involves physical and chemical processes i.e., hydrolysis, polymerization, gelation, condensation, drying, and densification (Harraz et al., 2013).

The sol-gel process is similar to that of co-precipitation. Instead of fine-grained powders obtained by co-precipitation, the polymeric precipitate formation is observed. Metal-organic compounds, mostly metal alkoxides are the common precursors employed in sol-gel technique. The process commonly begins with the addition of metal salts or alkoxides in water or in a suitable solvent (usually an alcohol) at ambient or slightly elevated temperatures (Ciriminna et al., 2013). Hydrolysis of metal alkoxides at acidic pH develops a gel, whereas hydrolysis at alkaline pH induces the nucleation of oxide or hydroxide directly from solution. By the addition of more amount of water to the nonaqueous solution, gelation takes place at the temperature below 100°C. The gel formation depends on pH, temperature, and water content. The gels are dried and calcined at high temperature to remove chemically bound water and crystallize the amorphous gel. The main disadvantage of sol-gel routes is that the processes are costly with low yields. The general reaction scheme of the sol-gel process is:

TiO_2-silica photocatalyst is prepared by a modified sol-gel technique (Harraz et al., 2013). TiO_2-sol is firstly synthesized by acid hydrolysis of a $TiCl_4$ precursor instead of titanium alkoxides. TiO_2-sol is further modified with SiO_2 to obtain a modified catalyst followed by drying at 70ºC for 24 h and calcination at 400ºC for 3 h. TiO_2-SiO_2 is used for the photocatalytic degradation of cyanide and removal of heavy metals (Cr(III), Co(II) and Pb(II)). The surface area and cyanide removal efficiency have their maximum values at and 286.7 m^2 g^{-1} and 80.3 % after 6 h reaction time (Harraz et al., 2013).

Shaban (2013) studied on visible light active carbon-modified titanium dioxide (CM-n-TiO_2) NPs. Titanium butoxide is dissolved in anhydrous ethanol between pH of 3 and 4. The resulting gel is then aged and dried to form a precursor. CM-n-TiO_2 NPs are obtained by calcination of the precursor. Photocatalytic production of H_2 is found to be 5 to 20 mg L^{-1} at pH 8 and 1.0 g L^{-1} of CM-n-TiO_2 (Shaban, 2013).

1.7.7 Solvo-thermal method

Typically solvothermal methods make use of solvents such as ethanol, toluene and water. The process is widely used for the synthesis of zeolites, inorganic open frame structures and other solid materials. It is operated under moderate to high pressure generally between 1 and 10,000 atm, and temperature between 100 and 1000 °C (Shinji and Masashi, 2008). If water is used as the solvent, the method is called "hydrothermal synthesis." The synthesis under hydrothermal conditions is usually performed below the supercritical temperature of water (374°C). Under solvo (hydro) thermal conditions, certain properties of the solvent, such as density, viscosity, and diffusion coefficient change dramatically and, the solvent behaves much differently from what is expected under ambient conditions. The process can be used to prepare thin films, bulk powders, single crystals, and nanocrystals (Walton, 2002).

Tetrabutyl orthotitanate and ethanol mixture in supercritical CO_2 environment at different reaction temperature and pressure have been developed for the fabrication of nanostructured TiO_2 (S. Wang et al., 2013). Particle sizes are in the range from 1.6 to 10 nm for reaction temperature of 100-140ºC and pressure of 150-450 atm. It exhibits methyl orange degradation of 90 % (500 W Xe visible lamp with a 420 nm cut-off filter, pH 5, reaction time 120 min and catalyst 0.5 g L^{-1}).

In a typical solvothermal method, polyethyleneimine is mixed with absolute ethanol and, tetrabutyl titanate is added drop-wise with a vigorous stirring for 5 h (Zhu et al., 2013). Particle size and BET surface are of 2-50 nm and 118 m^2 g^{-1} are obtained. The activities of synthesized TiO_2 microspheres are evaluated by photodegradation of methyl orange and

phenol from aqueous solutions using simulated sunlight (400 W halogen light). About 86 % methyl orange dye decomposition is reported.

1.7.8 Flame spray pyrolysis (FSP)

FSP is one of the latest repetitions in powder production technology (Bickmore et al., 1996). FSP develops metal oxide powders from extremely volatile gaseous metal chlorides that are oxidized/ decomposed in H_2–O_2 flames to make nano-oxide powders. FSP can be used to generate a broad variety of great purity nanopowders ranging from mono metal oxides such as TiO_2, alumina to other complex catalysts and mixed oxides. This FSP is first established by a research group of Sotiris E. Pratsinis at ETH Zurich, Switzerland (Strobel et al., 2006).

There are two methods of flame pyrolysis practiced in the laboratory scale i.e., flame aerosol synthesis (FAS) and flame spray pyrolysis (FSP). In FAS, metal precursors are dissolved in an appropriate solvent and, the solvent vapour is carried into the flame environment by carrier gas followed by a gas to particle conversion. FSP on the other hand, is more versatile as it uses liquid precursors producing particles of more complex compositions. The controlled synthesis of particles is very important in FSP as a small variation in process conditions change the particle quality.

Chiarello et al. (2008) prepared TiO_2 and Au-TiO_2 by FSP and characterized by Brunauer–Emmett–Teller (BET) surface area, XRD, high resolution transmission electron microscopy (HRTEM) and UV–vis diffuse reflectance Spectrometry (UV-vis DRS) analyses. Simultaneous photocatalytic activity and H_2 production in a closed recirculation photoreactor are studied. The results are compared to those of commercial TiO_2, including Degussa P25, pure rutile, and pure anatase. The highest H_2 production rate of 7180 μmol per h per g catalyst is achieved (Chiarello et al., 2008).

1.7.9 Chemical vapour deposition (CVD)

The majority of CVD applications involve solid thin-film coatings to surfaces. It is also used to produce high-purity bulk materials and powders, as well as composite materials via infiltration techniques. In this process, thermal decomposition of a hydrocarbon vapour is achieved in the presence of a metal catalyst. A precursor gas or gases flow into a chamber containing one or more heated objects to be coated. Chemical reactions occur on and near the hot surfaces resulting deposition of a thin film on the surface (Crutchley, 2013). The temperature typically ranges from 200 to 1600°C.

Iron nanotubes of diameter ranging from 9.5 to 31 nm supported on magnesia is produced by CVD (Bachmatiuk et al., 2008). They examined ethanol and cyclohexane feedstock without additional carrier gas. CVD temperature is used between 650 and 850°C. Sang et al. (2005) prepared TiO_2 photocatalyst by low pressure (1.3×10^{-3} atm) metal organic CVD with varying temperature (150-850°C) and deposition time using titanium tetra-isopropoxide. It gives about 90 % degradation of methylene blue under UV light irradiation. The thickness of TiO_2 film found is 3-5 µm.

TiO_2 films are deposited under 200-500 Pa at 400-580 °C. The photocatalytic decomposition rate of stearic acid (8.8×10^{-3} mol dm^{-3}) on the surface of TiO_2 is investigated under UV light using an optical filter cut-off 410 nm for 24 h of irradiation time (Piszczek et al., 2013).

Gnanasekaran et al. (2015) synthesised TiO_2 quantum dots (QDs) with 0.01 mole of aqueous CTAB solution added drop wise for 24 h. It is then dried and calcined at 350 °C for 30 min. TiO_2 QDs are used as a catalyst for the degradation of methyle orange (MO) and methylene blue (MB) dyes at a concentration of 5×10^{-5} M under UV light irradiation (8 W mercury vapour lamp of 365 nm wavelength) for 80 min. They achieved about 97.1 and 97.9 % removal efficiency for MO and MB, respectively (Gnanasekaran et al., 2015).

1.7.10 Photodeposition method

Tryba et al. (2010) deposited Ag on TiO_2 in the range of 0.11 to 0.98 % (w/w) by the photodeposition method (λ=330 nm). The photocatalytic activity of these particles is studied for the decomposition of phenol using UV light, but the rate of the reaction is slow (14 % degradation after 5 h) (Tryba et al., 2010).

Ismail et al. (2013) synthesized mesoporous TiO_2 nanocrystals using F127 triblock copolymer as a template. Precious metals like Au, Pd, and Pt are photodeposited onto mesoporous TiO_2. The lattice fringes exhibit typical distances, TiO_2 (1 0 1) (3.54˚A) with an average diameter of 10 nm is found. Pd, Pt, and Au NPs are well dispersed and exhibit diameters of 12, 3, and 5 nm, respectively. Photodeposition of Ag on TiO_2 photocatalyst does not enhance phenol decomposition (14 %) (Ismail et al., 2013; Tryba et al., 2010). However, it enhances Reactive Black dye adsorption (95 %) and its decomposition under both UV and artificial solar light irradiation.

Parastar et al. (2013) prepared 1 % (w/w) Ag/TiO_2 by using the photodeposition method under UV light (360 nm and 30 W), and the resulting particles are then calcined at

400 °C. The doped catalyst gives 95.5 % nitrate removal with 0.8 g L^{-1} catalyst dose at pH 5 (Parastar et al., 2013).

Ismail et al. (2013) synthesized 0.5 % (w/w) Au, Pt, Pd, and metal/TiO_2 NPs. The photocatalytic oxidation of methanol (30 mM) to formaldehyde is tested using metal/TiO_2 photocatalysts of 0.5 g L^{-1} under 450 W medium pressure xenon lamp (λ>320 nm). The photonic efficiency increases to 13.9, 15.6 and 17.8 % for Au, Pt, and Pd doped catalysts, respectively (Ismail et al., 2013).

Ag/TiO_2 NPs (1 % w/w) are synthesized using different precursors of silver, namely silver acetylacetonate, silver nitrate, and silver perchlorate under UV light (8 W, λ_{max} = 360 nm). The photocatalytic reduction of Ag species to Ag^0 on TiO_2 is higher with silver nitrate, and they obtained 95 % rhodamine B dye (initial concentration 10 mg L^{-1}) removal at 60 min of reaction under visible light illumination using 150 W Xe lamp (Albiter et al., 2015).

Behera et al. (2015) used the photo-reduction method to dope Ag onto TiO_2. $AgNO_3$ is mixed with TiO_2 and irradiated with 160 W high pressure mercury lamp for 2 h to reduce Ag^+ to form Ag^0. Thus prepared Ag doped TiO_2 is used to degrade phenol (Behera et al., 2016).

1.7.11 Wetness impregnation (WI)

WI or capillary impregnation is commonly used for the synthesis of heterogeneous catalysts. Typically, an active metal precursor is dissolved in an aqueous or organic solution. The metal-containing solution is added to a catalyst support containing the same pore volume as the volume of the solution that is added. Capillary action draws the solution into the pores. Solution in excess of support pore volume causes the solution transport to change from a capillary action process to a diffusion process (Jiang, 2006). The catalyst is then dried and calcined to drive off the volatile components depositing the metal on the catalyst surface. The maximum loading is limited by the solubility of the precursor in the solution (Delannoy et al., 2006).

Riaz et al. (2013) prepared bimetallic-TiO_2 photocatalyst using the WI method by calcining at a different temperature (180-300 °C) for 1 h. Photocatalytic degradation of Orange II dye is found to be more than 98 % at pH 6.8 with an initial concentration of 50 mg L^{-1} under the irradiation of UV light (Riaz et al., 2013a).

Alcala and Real (2006) fabricated iron-silica and iron oxide-silica composites by WI with subsequent heat treatment. The resultant composite is produced with a high content of

iron or iron oxide phase uniformly dispersed in the silica matrix. No pre-treatment before calcinations is necessary to obtain the magnetic phases. The surface area and crystallite size of the composite are obtained as 217 $m^2 g^{-1}$ and 43 nm, respectively (Alcala and Real, 2006).

TiO_2-supported Pd–Au catalysts are fabricated with Pd (0.5 % w/w) by the impregnation technique, and then Au (1.0 % w/w) is doped by the deposition-precipitation technique ($Au/Pd/TiO_2$) and vice versa ($Pd/Au/TiO_2$). The calcined particles (500 °C for 2 h) are applied for the catalytic hydrogenation of 1-heptyne and 1-heptene. The selectivity of 1-heptene decreases to 0 % (which is further hydrogenated to heptane) in 120 min for the $Au/Pd/TiO_2$, but it retains >60 % selectivity for the $Pd/Au/TiO_2$ particles (Kittisakmontree et al., 2013).

Au/TiO_2, $Au/\gamma\text{-}Al_2O_3$, and Au/SiO_2 NPs are made by the wetness impregnation method with gold loadings of 0.7, 1, and 4 % (w/w) at 80 °C for 16 h in a closed reactor in dark condition (Delannoy et al., 2006).

Transition metals (Ag, Co, Cu, Fe, and Ni) doped TiO_2 is fabricated by the WI method followed by calcination (500 °C for 4 h). The photocatalytic activities are tested for the degradation of nitrobenzene (50 mg L^{-1}) at pH 5 using UV light (125 W). The degradation efficiency of 57 % with the bare catalyst increases to 89, 88, 84, 83, and 72 % for Ag-, Co-, Cu-, Fe-, and Ni-impregnated TiO_2 catalysts, respectively (Tayade et al., 2006).

1.8 Bio and Bio-mediated Synthesis of Metal Nanoparticles

1.8.1 Method of metal NPs synthesis: Background

Biosynthesis is the formation of natural products through enzymatic reactions, as in cellular metabolism. Successive enzymatic reactions by a number of enzymes are generally required to achieve a single biologically active compound. It is the production of a chemical compound by a living organism. Biosynthesis can be exploited for chemical synthesis in vitro or in cells like *Escherichia coli* by combining substrates with enzymes using recombinant methods. A bio-mediated synthesis is a process that uses complete living cells or their components (e.g., bacteria, enzymes, chloroplasts) to obtain the desired products.

Various routes have been established for the bio-mediated synthesis of NPs from metal precursors (Balakumaran et al., 2015; Bar et al., 2009; Roopan et al., 2013; Valli and Vaseeharan, 2012; Velusamy et al., 2015). Microorganisms, marine algae, whole plants, plant tissue, fruits, and plant extracts (Philip, 2010; Thakkar et al., 2010) have been employed for AgNPs synthesis. A bio-mediated synthesis process is advantageous not only because of its

decreased environmental effect (Shankar et al., 2004) compared with some of the conventional methods, but also because it can be utilized to yield large amounts of AgNPs consisting of precise size and shape almost without contamination (Mittal et al., 2013). The capability of plant extracts for AgNPs synthesis has been known since the early 1900s, though the availability of reducing agents was not well known. Compared with the utilization of plant tissue and whole plant extracts, the employ of plant extracts for AgNPs synthesis is easier. The method of NPs synthesis using plant extracts are less expensive and readily scalable (Iravani, 2014) compound to the expensive techniques based on microbial routes (Shankar et al., 2003) and whole plants (Mittal et al., 2013). The approaches in the conjugation of NPs to biomolecules usually come under four classifies (Ravindran et al., 2013):

i. The ligand mediated binding of organic molecule to the surface of the inorganic particle core normally by chemisorption such as with thiol groups.
ii. Electrostatic interactions between negatively charged biomolecules and positively charged NPs or vice versa.
iii. Non-covalent, affinity-based organ–ligand systems.
iv. Covalent binding by conjunction, exploiting functional groups on both biomolecules and particles.

NPs need an appropriate surface functional group for conjugation with several organic molecules. A wide variety of biomolecules of different size, complexity, and compositions are existing in nature that gives morphology and function for several bio-mediated processes and organisms. Common biomolecules are alcohol, carboxylic acid, thiol or phosphate group on their surfaces (Ravindran et al., 2013). According to Ravindran et al. (2000), the AgNPs are stabilized using BSA, a bovine serum albumin protein, through chemisorption, and the amended particles could be more responsive toward the implication in bio-sensing (Ravindran et al., 2010).

The extracellular formation of metal NPs by several strains of the fungus *Aspergillus flavus* is reported. Aqueous silver ions when exposed to several *Aspergillus flavus* strains are reduced in solution, thereby leading to the formation of silver hydrosol. The average crystallite sizes of AgNPs are in the range of 20–50 nm. Extracellularly produced NPs are mainly reduced and stabilized by protein and reducing agent secreted by them. The potentialities of this nanotechnological design based on fungal biosynthesis of NPs for several technical applications are important, including their high potential as antibacterial

materials (Vigneshwaran et al., 2007). The extract of unicellular green algae, *Chlorella vulgaris*, is used to synthesize single crystalline metal NPs at room temperature. Proteins in the extract provide a dual function of Ag^{+} reduction and shape-control of AgNPs. Carboxyl groups in aspartic and/or glutamine residues and hydroxyl groups in tyrosine residues of proteins are responsible for the metal ion reduction (Xie et al., 2006).

The intercellular synthesis of NPs using microbes oven shows a lower synthesis rate as well as difficulty in size and shape control (Ahmed et al., 2016). Such problems can be overcome in many extents by extracting the analyte in a suitable media from living cells. After that, the particles are synthesized in this media. For examples, water soluble analytes such as ascorbic acid (AA) (Roopan et al., 2013) and polyphenols (Pandey et al., 2013) including flavonoids (Ahmed et al., 2016) are extracted in water for AgNPs synthesis. It helps to increase the efficiency of synthetic procedures as an alternative to conventional synthesis processes.

These biologically synthesized NPs are found to be highly toxic against different multi-drug resistant human pathogens (Gopinath et al., 2015). A bio-mediated synthesis process is advantageous not only because of its decreased environmental effect (Shankar et al., 2004) compared with some of the conventional methods, but also because it can be utilized to yield large amounts of AgNPs maintaining precise size and shape almost without contamination by utilizing the same biomass species originated from the same geographical location under similar cultivation condition.

1.8.2 Bio-mediated synthesis of AgNPs using reductants of plant origin: Literature survey

This section highlights more on the state-of-the-art literature for the synthesis of metal NPs with a focus on AgNPs using bio-mediated processes.

Shankar et al. (2004) synthesized core-shell Ag/Au bimetallic NPs facilitated by reducing sugars and/or terpenoids present in the *Azadirachta indica* (neem) leaf broth extract with 50–100 nm particle size (Shankar et al., 2004).

Huang et al. (2007) studied that *Cinnamomum camphora* leaf extract can be used to produce silver and gold NPs. It is reported that polyols such as terpinoids, flavones, and polysaccharides present in *C. camphora* are mainly responsible for Ag and Chloroaurate ions (Huang et al., 2007). Vigneshwaran et al. (2007) synthesized silver-protein (core-shell) NPs using spent mushroom substrate with an average size of 30.5 nm and, the antibacterial

activity against two representative bacteria, *Staphylococcus aureus* and *Klebsiella pneumonia* are investigated (Vigneshwaran et al., 2007).

Sathishkumar et al. (2009) used *Cinnamon zeylanicum* bark extract to produce AgNPs reducing Ag precursor. *C. zeylanicum*is is rich in terpinoids including linalool, eugenol and methyl chavical, cinnamaldehyde, ethyl cinnamate, and some proteins. Terpenoids are believed to play an important role in AgNPs biosynthesis. Proteins are also reported to bind to NPs either through free amines groups, or cysteine residues in proteins. Quasi spherical, small, rod shaped AgNPs are produced (Sathishkumar et al., 2009). Kasturi et al. (2009) reported the electron-donating nature of $–OCH_3$ group of *Phyllanthin* extract playing a leading role for the formation and stabilization of AgNPs and AuNPs with an average size of 37.5 and 29 nm, respectively (Kasthuri et al., 2009).

A bioreductive approach of anisotropic gold and silver NPs utilizing the phyllanthin extract provides a simple and efficient way for the synthesis of nanomaterials with tunable optical properties directed by particle shape. The electron donating nature of the methoxy ($-OCH_3$) group of the phyllanthin extract plays a leading role for the formation and stabilization of NPs, respectively. FTIR spectra provide information on the interaction of $-CH_3$ group with the metal ion (Kasthuri et al., 2009).

Dubey et al. (2009) reported the extracellular biosynthesis of AgNPs on the use of the methanolic extract of *Eucalyptus hybrida* leaf. Bioactive AgNPs are prepared by the reaction of the methanolic leaf extract with aqueous $AgNO_3$ solutions at room temperature. The extracts of *E. hybrida* leaf are capable of producing metal NPs extracellularly and, the AgNPs are quite stable in solution. The flavanoid and terpenoid constituents present in *E. hybrida* leaf extract are surface active molecules stabilizing the NPs (Dubey et al., 2009).

Saifuddin et al. (2009) reported that the synthesis of AgNPs by the culture supernatants of *Bacillus subtilis* from aqueous silver nitrate solution (10^{-3} M). The appearance of brown colour clearly indicates the formation of AgNPs in the reaction mixture. The characteristics brown colour of colloidal silver solution is due to the excitation of SPR vibrations in the nanoparticles (Saifuddin et al., 2009).

Jha and Prasad (2010) claimed that plants distributed along the ecological boundaries might be the potential producers of NPs. They produced AgNPs using three types of plants, namely xerophytes, mesophytes, and hydrophytes growing under different ecological conditions (Jha and Prasad, 2010). Dubey et al. (2010) investigated the *Sorbus aucuparia* leaf extract mediated AgNPs and AuNPs formation with spherical, triangular, and hexagonal shapes having an average size of 16 and 18 nm for silver and gold, respectively (Dubey et al.,

2010). Krishnaraj et al. (2010) observed 20-30 nm size AgNPs within 30 min by mediating with *Acalypha indica* leaf extract and, these NPs are equally effective against water borne pathogens viz., *E. coli* and *Vibrio cholera* (Krishnaraj et al., 2010). Philip (2010) investigated the effect of pH on the size, crystallinity, and shape of AgNPs and AuNPs. He observed the carboxylate ion and amine groups in leaf extract of *Hibiscus rosa sinensis* are responsible for the formation of AgNPs and AuNPs (Philip, 2010).

Yilmaz et al. (2011) inquired the existence of aliphatic, alcoholic and olefinic CH_2, and CH_3 groups in the shadow-dried *Stevia rebaudiana* leaf extract, which is resulted in the formation of spherical and polydispersed AgNPs with diameters ranging between 2 and 50 nm (Yilmaz et al., 2011).

Saxena et al. (2012) prepared AgNPs using *Ficus benghalensis* leaf extract. They got size range of diameter around 16 nm (Saxena et al., 2012).

Bhat et al. (2013) prepared gold NPs using edible mushroom, *Pleurotas florida*. It is a photo irradiated biosynthesis process forming AuNPs by reducing gold chloride trihydrate. Mushroom consists of rich proteins like riboflabins played a major role in the synthesis process (Bhat et al., 2013; Saxena et al., 2012). Bharuah et al. (2013) investigated facile one-pot single-phase synthesis of AgNPs stabilized by polyguanidino oxanorbornenes (PG) and polyamino oxanorbornenes (PA), norbornene type cationic polymers. PG stabilizes AgNPs better than PA. AgNP-PG is found to serve as an effective catalyst for the reduction of 4-nitrophenol to 4-aminophenol in the presence of $NaBH_4$. A pseudo-first-order rate constant of 5.50×10^{-3} s^{-1} and an activity parameter of 1375 s^{-1} g^{-1} are found (Baruah et al., 2013). Dauthal and Mukhopadhyay (2013) studied the role of water- soluble polyols present in the *Delonix regia* leaf extract for the synthesis of PdNPs with size range of 2-4 nm (Dauthal and Mukhopadhyay, 2013). Ramteke et al. (2013) tested *Ocimumsanctum* leaf extract mediated AgNPs synthesis with an average size of 18 nm and its antimicrobial activity tested against *Staphylococcus* aureus and *E. coli* (Ramteke et al., 2013).

Sun et al. (2014) synthesized spherical AgNPs using the tea leaf extract with 20 to 90 nm diameter and, evaluated their stability and antibacterial activity against *E. coli* (Sun et al., 2014). Mohamed et al. (2014) investigated serum latex of *Calotropis procera* mediated AgNPs synthesis at 80 °C with an average size of 12.3 nm and, their functionality is tested against bacteria, phytopathogenic fungi, and dermatophytes (Mohamed et al., 2014). Mallikarjuna et al. (2014) used protein present in *Pepper* leaves extract as a reducing and capping agent in the formation of AgNPs (Mallikarjuna et al., 2014). Gaddam and Kotakadi (2014) investigated the role of the carbonyl group on *Cassia alata* leaf extract for spherical

AgNPs synthesis with an average diameter of 41 nm (Gaddam et al., 2014). Zuas et al. (2014) synthesized AgNPs with 10–20 nm size using *Myrmecodia pendan* extract (Zuas et al., 2014).

Balakumaran et al. (2015) synthesized spherical AgNPs with 5-30 nm diameter using endophytic fungi isolated from the leaves of medicinal plants and tested its cytotoxic effects against normal African monkey kidney, HeLa, and breast cells, respectively (Balakumaran et al., 2015). Ahmed et al. (2016) synthesized AgNPs using *Azadirachta indica* aqueous leaf extract with 34 nm size and used for the inhibition of growth of *S. aureus* and *E. coli* (Ahmed et al., 2016). Velusamy et al. (2015) found AgNPs with <30 nm diameter using *Azadirachta indica L.* exract and, tested its antibacterial functionality for the inactivation of *Salmonella enteritidis* and *Bacillus cereus* (Velusamy et al., 2015).

The key results and important literatures along with above are summarized in **Table 1.3.**

Table 1.3. Green synthesis of AgNPs by different researchers using extracts of plant parts.

Plants	**Size (nm)**	**Plant's part**	**Shape**	**References**
Azadirachta indica	5-35	Leaves	Spherical	Shankar et al., 2004
Jatropha curcas	15-50	Seed	Spherical	Bar et al., 2009
Phyllanthin	18-38	Fruit	Different shapes	Kasthuri et al., 2009
mangosteen	6-57	Leaves	Spherical	Veerasamy et al., 2011
Ficus benghalensis	8-32	Leaves	Spherical	Saxena et al., 2012
Acacia nilotica	20-30	Pod	Spherical	Edison and Sethuraman, 2013
Cocos nucifera	5-71	Fruit seed/ mesocarp layer	Spherical	Roopan et al., 2013
Olive	20-25	Leaves	Spherical	Khalil et al., 2014
Myrmecodia pendan	10-20	Route	Spherical	Zuas et al., 2014
Tea extract	20-90	Leaves	Spherical	Sun et al., 2014
Azadirachta indica L	12-30	Gum	Spherical	Velusamy et al., 2015

The advantages and disadvantages of various techniques for preparing metal NPs are summarized in the **Table 1.4.**

Table 1.4. Typical NPs synthesis techniques and their advantages and disadvantages.

Fabrication methods	**Advantages**	**Disadvantages**
Sono-chemical	○ Very simple, efficient and produces NPs of small sizes (20 nm) (Salkar et al., 1999)	○ Sono-chemical reaction occurs within the interfacial region which can result in formation of amorphous NPs and needs calcination at high temperature to make it crystalline.
Laser ablation methods	○ To produce AgNPs without any surface active agents. ○ Laser ablation technique in liquid media is a simple, efficient and can produce a large number of NPs	○ It has limitation of size control of NPs.
Co-precipitation method	○ Low reaction temperature is the major advantage of this technique. ○ Impurity level also remains low.	○ Desired particle size is not obtained so further grinding or milling is required.
Sol-gel method	○ It is also a low temperature technique. ○ Impurity level also remains low.	○ Expensive. ○ Time consuming process.
Solvo-thermal method	○ This method is very helpful for preparing isotropic particles. ○ Particle size is highly controllable.	○ Difficult to recover the product from suspension without agglomeration.
Chemical reduction for NPs fabrication	○ It was producing AgNPs almost instantly. ○ Very small particles are formed.	○ This method is expensive as the process needs a lot of chemicals as reducing and stabilizing agent.
Photo-reduction method	○ Simple technique. ○ Reaction is very fast, within 1-2 h the reaction is expected to complete.	○ Expensive process as UV radiation is employed.
Flame spray pyrolysis	○ Uniform particle distribution ○ High purity products	○ Raw materials are expensive and highly corrosive ○ Controlling size, size distribution, and agglomeration of particles ○ Agglomeration of particles
Chemical vapour deposition	○ Produce highly dense and pure materials ○ High deposition rate ○ Not require high vacuum ○ Low deposition temperature	○ Film deposited at elevated temperature ○ Difficult to deposit multicomponent materials ○ Use of more sophisticated reactor ○ Toxic and corrosive gasses generation

Wetness impregnation	○ Low processing temperature from 100 to 800 °C ○ Easy to produce nano sized particles	○ Some precursor materials are costly ○ Collection without aggregation is difficult ○ Stoichiometric control can be difficult
Bio-mediated synthesis	○ Simple to produce NPs ○ Eco-friendly synthesis ○ Low-cost and no additional chemicals needed other than metal precursors ○ Energy-efficient ○ Usually non-hazard ○ Not require high temperature and pressure ○ Almost free from contamination	○ Prolong reaction time with some bio-extracts

1.9 Metal Doped Semiconductor Photocatalysis

1.9.1 Metal doping in conventional route

UV photo-reduction (Bokare et al., 2013), high thermal energy intensive (Wen et al., 2007), and hazardous chemical intensive (Harraz et al., 2013) processes are conventionally employed for noble and transition metals-doping on semiconductor supports. The desired structural morphology and size of the materials can be achieved by these methods, but they are complex, expensive, and could be harmful.

Trillas et al. (1999) performed heterogeneous photocatalytic oxidation of phenol using TiO_2 using mercury vapour lamp of 125 W. They observed that the efficiency of phenol oxidation depends strongly on the solution pH. Maximum efficiency is reported at pH 8 (Trillas et al., 1992).

Yang and Gao (2004) prepared N-doped TiO_2 by mixing 34 g of tetrabutyl titanate with 30.4 g of thiourea in 300 mL ethanol. The solution is stirred at room temperature for 2 h and then evaporated completely under reduced pressure. The white residue is treated in NH_3 flow at 450° and 500 °C for 6 h, and 450 °C for 3 h. N/TiO_2 shows an enhanced photocatalytic decomposition of methylene blue dye with 90 % degradation efficiency under visible light (300 W mercury lamp) (Yang and Gao, 2004).

Granados et al. (2005) utilized Zn(II) and Co(II) tetracarboxyphthalocyanine (TcPcM) to sensitize TiO_2 and Ag/TiO_2 for the degradation of phenol using visible light. The degradation efficiency is expressed in terms of photonic efficiency (ratio of number of electrons generated by light in the external circuit to the number of incident (monochromatic) photons). The photonic efficiencies of phenol degradation are found as 4.3 and 3.3 % using

immersion lamp (100 W) on TcPcCo/TiO_2 and TcPcZn/TiO_2, respectively. The photo-deposition of silver on TcPcM/TiO_2 enhances the reaction photo-efficiency up to 10 % (Granados et al., 2005).

Park et al. (2006) synthesized bimetal incorporated TiO_2 photocatalysts (Fe/Zn/TiO_2) by a flame method and used for the degradation of 2-propanol dissolved in water. An optimum ratio of Fe and Zn is maintained and, Fe/Zn/TiO_2 shows 75 % decomposition of 2-propanol under the illumination using a high-pressure Hg lamp of 100 W (Park et al., 2006).

Wen et al. (2007) reported a typical experiment to synthesize Zn/SnO_2/TiO_2. An amount of 1.5 mM $SnCl_4.5H_2O$ and 0.5 mM $ZnCl_2$ are added into a solution containing 0.55 g cetyl trimethyl ammonium bromide (CTAB) and 0.08 g (2 mM) NaOH. The mixture is heated at 160 °C for 15 h in a teflon-lined stainless steel autoclave. The photocatalytic activity is tested for rhodamine B dye decomposition under a 200 W Hg mercury discharged lamp (Wen et al., 2007).

Ag doped ZnO (1 % Ag w/w) through the solvothermal method at 160 ºC for 24 h exhibits a better UV-light utilization (4×4 W fluorescent Hg-lamp) and photocatalytic efficiency (Zheng et al., 2008). Four times higher degradation rate of rhodamine 6G dye is found with ZnO/Ag (6.45 % w/w) than that of bare ZnO under the illumination from the solar simulator (0.68 W cm^{-2} at 340 nm wavelength) (Georgekutty et al., 2008).

Sreethawong et al. (2009) investigated on eosin yellow (EY) dye sensitized photocatalytic production of H_2 from water splitting under visible light irradiation over mesoporous-assembled TiO_2 photocatalysts, without and with Pt loading. Pt/TiO_2 is synthesized by the sol–gel process and calcined at 500 ºC. It gives the maximum photocatalytic activity for H_2 generation from 30 % (v/v) diethanolamine aqueous solution with 2 mM dissolved dye at pH 11.5 using 300 W Xe arc lamp (Sreethawong et al., 2009).

Quinones et al. (2010) fabricated Au/Pd/TiO_2 using co-precipitation method. A quantity of 0.6 g TiO_2 is added in Au and Pd precursors' solution followed by the addition of glycerol with stirring. Precipitates are obtained during titration of the mixture with NaOH maintaining the temperature at 8-10 ºC until final pH 14. The synthesized photocatalyst is used for the degradation of methylene blue dye (200 mg L^{-1}) with 2 g L^{-1} of catalyst for 1 h reaction time under a 500 W halogen lamp (Quiñones et al., 2010). Zhang et al. (2010) prepared Cu/Fe/TiO_2 using WI method. The TiO_2 support is added in Cu and Fe precursors' solution and mixed for 1 h. The solvent is evaporated at 80 ºC until a thick paste is obtained. They reported a nearly complete degradation of congo red dye (50 mg L^{-1}) within 1 h under a 500 W Hg lamp (Zhang, 2010).

Ag/ZnO (1.8 % w/w) prepared by the hydrothermal technique in the presence of bovine serum albumin at 100 ºC for 7 h shows the complete degradation of orange G dye (10 mg L^{-1}) under UV light illumination (250 W high pressure fluorescent Hg lamp) (Gao et al., 2011). Zielinska-Jurek et al. (2011) synthesized Ag/Au titania photocatalyst using a water-in-oil micro-emulsion technique. AuNPs of ~90 nm diameter after impregnation on TiO_2 shows the best catalytic activity for hydrogen production, environmental pollution control, low-temperature catalytic combustion, and reduction of nitrogen oxides (Zielińska-Jurek et al., 2011). Cu/Zn/TiO_2 is prepared by using a sol-gel method where titanium (IV) isopropoxide is added to 2-15 % w/w Cu/Zn precursor's solution followed by the glycerol addition. Precipitates are obtained during titration of the mixture with NaOH maintaining the temperature at 20 °C until the final pH of 14. This synthesized photocatalyst is used for the decomposition of methyl orange dye solution of 250 mg L^{-1} using 380 W halogen tungsten lamp (λ : 200–800 nm and average light intensity: 6 mW cm^{-2}). The percentage of degradation is higher with the doped photocatalyst (94 %) compared to bare TiO_2 (10 %) (Zhang and Zeng, 2011). Ag/V_2O_5/TiO_2 photocatalyst is fabricated by using the WI method (Riaz et al., 2013). $AgNO_3$, NH_4VO_3, and oxalic acid are added in TiO_2 (Degussa P25) suspension. It is mixed for 2 h at room temperature, and water is evaporated in a rotary evaporator under reduced pressure at 40 °C. The material is calcined at 400 °C for 20 h. There is an improvement of brilliant blue dye degradation by 73 % compared to bare TiO_2 (98 %) (Delaigle et al., 2011).

Chowdhury et al. (2012) synthesized EY sensitized Pt/TiO_2 catalyst for the degradation of phenol. They achieved 93 % phenol degradation within 90 min at the optimal condition as pH 7.0, catalyst loading 0.8 g L^{-1}, triethnolamine (e^- donor) concentration 0.2 M, and Pt loading 0.5 % using solar light with an intensity of 100 mW cm^{-2}. EY sensitized TiO_2 without Pt doping can degrade only 67 % phenol with the irradiation solar simulator (visible photon flux = 1700 μE/(m^2s) (Chowdhury et al., 2012).

Bokare et al. (2013) studied in Ag-deposition on 1.0 % Neodymium (Nd) doped TiO_2 by the photo-deposition method under 80 W high pressure Hg lamp and, tested for the degradation of methyl orange dye (Bokare et al., 2013). Harraz et al. (2013) prepared SiO_2–TiO_2 photocatalyst using 10 % NH_4OH into $TiCl_4$ (0.18 mol) solution until a white precipitate is obtained at pH 7. Tetraethyl orthosilicate ($Si(OC_2H_5)_4$) solution is added into the above titania sol, and it is calcined at 400 °C for 3 h to obtain SiO_2–TiO_2 catalyst (Harraz et al., 2013). This photocatalyst is used for the degradation of direct blue dye solution of 100 mg L^{-1} with 2 g L^{-1} of catalyst loading for 1 h under100 W high-pressure mercury lamp. An

enhancement of the degradation of 40 % is achieved with the doped catalyst (Mohamed et al., 2013). Cu/Ni-TiO_2 is synthesized by using the co-precipitation method. TiO_2 is added into 10 % w/w of Cu and Ni precursors dissolved in distilled water followed by the addition of glycerol with continuous stirring. Precipitates obtained during titration of the mixture with 0.25 M NaOH (8-10 °C) until the final pH of 14. The dried catalyst (1 g L^{-1}) is used in for orange II dye (50 mg L^{-1}) degradation for the reaction time of 1 h under 500 W halogen lamp (Riaz et al., 2013b).

Malika et al. (2016) synthesized mono- (Cu/TiO_2 and Ni/TiO_2) and bi-metal doped TiO_2 (Cu/Ni/TiO_2) photocatalysts by the co-precipitation method with an equal mass ratio of Cu and Ni. The band gap energy of the bi-metal doped catalyst is reduced to 2.91 eV and, it exhibits an enhanced eriochrome cyanine red (ECR) dye degradation using 200 W visible light (Malika et al., 2016).

The performance of both mono- and bi-metal doped TiO_2 and ZnO for photocatalytic decomposition studies are summarized in **Table 1.5**.

Table 1.5. Different metal-doped TiO_2 for degradation of dye effluents.

Metal doped TiO_2	**Doping method**	**Dopant amount (w/w)**	**Light source**	**Dye/Contaminant**	**Degradation (%)**		**Source**
					Bare catalyst	**Doped catalyst**	
UV/TiO_2	Photoreduction	-	UV, 125 W mercury vapour lamp	Phenol	15	92	Trilas et al., 1999
N/TiO_2	Hydrothermal	-	UV, 300W mercury lamp	Methylene blue	16	90	Yang and Gao 2004
Fe/Zn/TiO_2	Flame aerosol method	Fe: 1 % Zn: 1 %	UV, 100 W high-pressure Hg lamp	2-propanol	35	75	Park et al., 2006
Zn/SnO_2/TiO_2	Hydrothermal	Zn: 1.7 %	Visible, 500 W Xe lamp	Rhodamine B	9	89	Wen et al. 2007
Ag/ZnO	Sol-gel	Ag: 1-10 %	UV, 0.68 W/cm^2 at wavelength 340 nm	Rhodamine 6G	10	99	Georgekutty et al., 2008
Au/Pd/TiO_2	Co-precipitation	Au:0.1- 0.6 % Pd:0.1- 0.6 %	UV lamp, 260 nm, 48W/cm^2	Methylene blue	53	100	Quinones et al., 2010
Cu/Fe/TiO_2	Sol-gel	Cu:0.21% Fe:0.14%	Visible, 500-W	Congo red	35	100	Zhang et al., 2010

			halogen tungsten lamp				
$Cu/Zn/TiO_2$	Sol-gel	Cu/Zn: 2-15 %	Visible, 380 W halogen tungsten lamp	Methyl orange	30	94	Zhang et al., 2011
$Ag/V_2O_5/TiO_2$	Wet impregnation	Ag: 0.02-12.5 %	-	Brilliant blue	25	98	Delaigle et al., 2011
Pt/TiO_2	Photodeposition	Pt: 0.25-1 %	Visible, photon flux of 1700 $\mu E/(m^2\ s)$	Phenol	11	93	Chowdhury et al., 2012
$Cu/SiO_2/TiO_2$	Photo-assisted deposition	Cu: 3 %	Visible, 100 W high-pressure mercury lamp	Direct blue dye	53	92	Mohamed et al., 2013
Nd/TiO_2	Sol-gel	Nd: 0-5 %	Visible, 100 W high-pressure mercury lamp	Methyl orange	9	100	Bokare et al., 2013
SiO_2/TiO_2	Sol-gel	-	300 W UV lamp	Cyanide	-	98.4	Harraz et al., 2013
$Cu/Ni/TiO_2$	Co-precipitation	Cu: 1-10 % Ni: 1-10 %	Visible, 500 W halogen lamp (46.16 $W\ m^{-2}$)	Orange II	21	100	Riaz et al., 2013
$Cu/Ni/TiO_2$	Co-precipitation	Cu: 1 % Ni: 1 %	Visible, 200 W at 525 nm	Eriochrome cyanine red	20.9	99	Malika et al., 2016

1.9.2 Bio-mediated metal doping of semiconductor supports

The reduction of metal ions into zero valence and nucleation onto the surface of semiconductor is a basic step of metal doping for the semiconductor supports. The processes involve the use of harmful chemicals such as ethanediol (Pacholski et al., 2004), hydroquinone (Shan et al., 2007) or energy intensive processes such as thermal or UV photo-reduction (Lu et al., 2008). Therefore, there is an urgent of an environmental-friendly green method that could avoid the usage of high energy inputs and hazard chemicals. Recently, various research work initiatives (**Section 1.8**) have been taken to study the bio-reduction efficiency of metal ions like Pd, Au, Pt, and Ag into metal NPs (Basavegowda et al., 2015; Huang et al., 2007; Mohamed et al., 2014). It primarily involves the exploration of reduction

potentiality of biomolecules in natural and renewable resources such as plant extracts (Tahir et al., 2015; Zuas et al., 2014) and microbes (Sadowski et al., 2008). In addition, the bio-extracts comprise natural capping agents that could hinder agglomeration of particles. So, it help to obtain improved size and shape control of the resultant metal NPs (Sathishkumar et al., 2009).

There are no existing studies on bio-mediated doping for the functionalization of semiconductor photocatalysts using metal dopants. This technique is rather ecofriendly, cost-effective, and energy-saving.

Bu and Zhuang (2012) fabricated Cu/TiO_2 hollow microspheres by the direct coating of shells on the surface of rape pollen using an improved sol-gel process followed by calcination (500 ºC) and pulverization. The average diameter, thickness, and specific surface area are 15-20 μm, 0.6 μm and 227 m^2 g^{-1}, respectively. Cu/TiO_2 exhibits a maximum photocatalytic degradation of 86 % (500 W Xe lamp) within 1 h reaction (Bu and Zhuang, 2012).

Xiao et al. (2013) investigated on Ce-doped TiO_2 mesoporous nanofibers by the one-pot facile synthesis method using collagen fiber (CF) as the biotemplate. Initially, CF is suspended in deionized water at pH 1.8-2.0. $Ti(SO_4)_2$ and $Ce(SO_4)_2$ are mixed and kept under constant stirring. Subsequently, $NaHCO_3$ solution is added drop wise into the reaction system to increase its pH, followed by filtration. Intermediates are calcined at 600 °C. Ce/TiO_2 nanofibers are used for photo-degradation of Rhodamine B dye under visible light illumination (150 W halogen lamp). They achieved up to 99.59 % removal in 80 min with TOC removal efficiency of 77.6 %. The band energy gap of Ce/TiO_2 nanofibers decreases from 2.756 to 1.678 eV. The specific surface area is reported as 81.56 m^2 g^{-1} (Xiao et al., 2013). Bioinspired hierarchical mesoporous TiO_2 photocatalysts are prepared using pollen grains as the biotemplate (He et al., 2013). Pollen grains are rinsed in ethanol and dried naturally. $Ti(OBu)_4$ is mixed with ethanol and stirred until the solution becomes clear. Pollen grains are immersed into the precursor solution with vigorous stirring. It is separated from the solution by filtration, cleaned by ethanol, rinsed in distilled water, dispersed in ethanol, and dried. The as-treated pollen grains are again immersed in the precursor solution. After being separated and cleaned, it is hydrolysed in the ethanol and water solution, further dispersed into ethanol, dried and calcined. BET surface area and pore size are determined as 96.2 m^2/g and 600-800 nm. The synthesised catalyst degrades about 95 % Rhodamine B under UV irradiation (300 W mercury lamp) in 2 h.

He et al. (2014) investigated in situ phosphate transfer to porous TiO_2 nanostructures using *Staphylococcus aureus* as a bio-template. The average size of colloidal titania particles

increases from 18.8 to 92 nm with the elevation of solution pH from 0.7 to 3.0. It shows an excellent photocatalytic activity using UV light (<365 nm) with 87 % methylene blue dye degradation (He et al., 2014).

Vivekanandan et al. (2014) studied on maple leaf extract mediated biological functionalization of ZnO with AgNPs (AgNPs). ZnO is dispersed in $AgNO_3$ solution, sonicated, and then maffle leaf extract is added with continuous stirring. The resultant AgNPs are obtained through centrifugation followed by repeated washing with water and ethanol mixture and dried in a hot-air oven before analysis. The crystallite size of the AgNPs on ZnO surfaces is determined as 9 nm. Ag functionalized ZnO particles reaches about 90 % decomposition of Trypan blue dye within 1 h (Vivekanandhan et al., 2014). This process is more about AgNPs accumulation on ZnO surface rather than doping.

The major outcomes of these studies are summarized in **Table 1.6.**

Table 1.6. Functionalization of semiconductor supports using bio-template and nearly bio-mediated process.

Bio-extract / Catalyst / Contaminant	**Illumination details**	**Experimental conditions**	**Key results**	**Source**
Pollen grains / Cu-TiO_2 / chlortetracycline hydrochloride	Xe lamp of 500 W	pH 3.0-4.0 Mixing for 3 h $CuCl_2$ 2 % w/w (TiO_2) DT: 100 °C CT: 500 °C	▪ Average diameter of 15-20 µm ▪ Thickness 0.6 µm and specific surface area 227 $m^2 g^{-1}$ ▪ Degradation efficiency of 86 %	(Bu and Zhuang, 2012)
Pollen grains/ TiO_2 / Rhodamine B (10 mg L^{-1})	Mercury lamp (300 W)	DT: 60 ºC for 3 h CT: 450 ºC for 1 h CD: 5 g L^{-1} IT: 120 min	▪ BET surface area of 96.2 $m^2 g^{-1}$ ▪ Pore size 600-800 nm	(He et al., 2013)
Yeast cell / Fe_2O_3 / Methyl orange (20 mg L^{-1})	300 W mercury lamp	DT: 80 °C CT: 300 °C CD: 2 g L^{-1} IT: 60 min	▪ Surface area of 116 $m^2 g^{-1}$ ▪ Degradation efficiency of 99 %	(Z. Wang et al., 2013)
Staphylococcus aureus/ P-TiO_2 / Methylene blue (8 mg L^{-1})	LED lamp 0.6 W cm^{-2} WL: 365 nm	CD: 1 g L^{-1} IT: 90 min	▪ Crystallite size of 24.4 nm ▪ Point of zero charge of TiO_2 NPs was 5.5 ▪ Maximum 87 % photocatalytic degradation	(He et al., 2014)
Maple leaf /	UV lamp	CD: 0.001 g L^{-1}	▪ Diameter of ZnO-	(Vivekanandhan

Ag-ZnO / Trypan blue (350 mg L^{-1})		IT: 90 min	coated AgNPs was 5-20 nm ▪ Crystallite size was 9 nm ▪ Degradation efficiency of 90 %	et al., 2014)
IT: Irradiation time WL: Wavelength CD: Catalyst dose DT: Samples drying temperature CT: Calcination temperature		DT: Samples drying temperature CT: Calcination temperature		

1.10 Hypothesis and Objectives of Work

Bio-mediated synthesis of highly intricate metal nanostructures using biological materials as precursors or templates has gained accelerating attention by environmental researchers. Among the various biological methods of AgNPs synthesis, microbe mediated synthesis is not industrial feasibility due to the requirement of maintaining highly aseptic conditions. Therefore, the use of plant extracts for this purpose is potentially advantageous over the microorganism based route.

Plant extract based bio-reduction processes utilize the analytes (reductants) present in plant organs such as leaf, flower, bark, or tuber for the synthesis of AgNPs. The components such as reducing sugars, proteins, terpenoids, and other phenolic compounds in the plant extracts are responsible for the reduction of silver ions into AgNPs. However, the reduction mechanism is extremely complicated, and the reduction potential and availability of reducing agents vary from species to species. Therefore, by changing the plant extract, not only the reduction mechanism but also the size, shape, and reaction kinetics also vary.

The main challenges with the bio-mediated synthesis of metal NPs are the broad distributions of particles (5 – 2000 nm) and slower kinetics of NPs formation (reaction time up to 72 h). Most of the studies are focused to explore the potential capability of various plants and plant parts, algae, and fungi for metal NPs synthesis. A very little is known about the formation mechanism of these particles mediated by the bio-analytes. Moreover, no attention is paid for the synthesis of tailor made metal NPs using a bio-mediated approach.

The main barriers of semiconductor photocatalysts include rapid recombination of photogenerated electron/hole pairs as well as the backward reaction, high band gap, and activity only in the UV region. These barriers make the poor activation of the photocatalysts. In the case of metal-doping on semiconductor supports, so far, the bio-templates are used solely for achieving various morphologies of Cu(II)-TiO_2 and Ag(II)-ZnO particles and, the functionalization/ doping takes place when it is calcined at a higher temperature (600 °C). In

fact, there was no existing study to the best in our knowledge on bio-mediated doping of semiconductor supports at room temperature and pressure without using external chemicals and energy inputs to process except stirring. Development of a simple and effortless environment-friendly technique for metal-doping on semiconductor photocatalyst for solar/ visible light driven wastewater treatment is a prudent area of research.

Sechium edule (Chayote) is an herbaceous perennial climber (Siciliano et al., 2004), and it grows abundantly in the North Eastern part of India. This fruit is commonly known as Squash in Assam, India. The fruits look similar to pears with rough skin and length from 10 to 20 cm. *S. edule* contains a lot of natural antioxidants, amino acids, and ascorbic acids (AA) along with many polyphenolic compounds, like phenylalanine and tyrosine (Ordonez et al., 2003). The organs of *S. edule* are rich in AA and flavonoids with as high as ~3 and 35 mg per 10 g of dried part, respectively (Siciliano et al., 2004). The fruit extracts exhibit strong reducing power as evidenced by the conversion of potassium ferricyanide to potassium ferrocyanide used for the antioxidant activity test. The analytes present in the extract act as strong electron and hydrogen donors. It could break the radical chain reaction and convert the free radicals to stable products (Ordonez et al., 2006). Therefore, *S. edule* was selected based on literature survey along with the supports of initial laboratory trials for the bio-mediated synthesis of Ag, Pt, and Co nanoparticles and bio-mediated doping of TiO_2 and ZnO using metal dopants, namely, Ag, Cu, and Zn.

Likewise, the following objectives are designed to carry out this work.

i. To develop a green route for the synthesis of Ag, Pt, and Co nanoparticles using *S. edule* extract
ii. To investigate the size dependent antimicrobial and antifungal functionalities using mono-metal and tailor made bimetal nanoparticles
iii. To develop a bio-mediated doping technique of Ag, Cu, and Zn doping onto TiO_2 and ZnO supports using *S. edule* extract
iv. To study the photocatalytic activity of doped catalysts for the degradation of organic compounds by harvesting visible light

1.11 Organization of Thesis

This thesis has seven chapters and the synopsis of the chapters is as follows.

Chapter 1

Introduction and Literature Review

This chapter introduces the problem, includes literature survey and outlines the research objectives. A glimpse of this chapter is already outlined at the beginning of this dissertation.

Chapter 2

Materials and Methods

Chapter 2 describes the procedures for the synthesis of metal NPs, metal-doping on semiconductor supports, and photocatalytic treatment along with the analytical procedures for antimicrobial, antifungal, and photoelectrochemical tests by various analytical techniques.

Chapter 3

AgNPs Synthesis: Physiochemical Attributes, Formation Mechanism and Antimicrobial Functionalities

In the first part of this chapter, the synthesis of AgNPs was carried out at natural pH of the bio-extract of *S. edule*. The structural and morphological properties as well as the antibacterial and antifungal activities of AgNPs, were investigated. In the second part of the chapter, the effect of pH on the kinetics, particles purity, particle sizes, and mechanisms of AgNPs formation was studied.

Chapter 4

Pt-Co Core-Shell Prismoidal Nanoparticles Synthesis

This chapter investigates the synthesis of Co, Pt, and CoPt nanoparticles of prismoidal, spherical, and core-shell structures and its physicochemical properties. The comparison of mono and bimetallic Co and Pt core-shell nanoparticles for the inactivation of *B. subtilis* and *E. coli* bacteria were also carried out.

Chapter 5

Development of a Technique of Silver-doping on Semiconductor Supports

The main barriers of semiconductor photocatalysts include rapid recombination of photogenerated electron/hole pairs as well as the backward reaction, high band gap, and activity only in the UV region. These barriers make the poor activation of the photocatalysts. Here, we have developed a bio-inspired doping technique for the functionalization of semiconductor materials to make them active in the visible light without application of external chemical and energy (except stirring).

Chapter 6

Synergistic Effects of Cu/Zn Bimetal Doping on TiO_2 for Photocatalytic Water Treatment

This chapter presents Cu and Zn bimetal-doping onto the TiO_2 support. The photocatalytic activity of Cu/Zn/TiO_2 was investigated for the degradation of Congo red dye and reduction of chemical oxygen demand under the visible light illumination and determination of quantum yield.

Chapter 7

Conclusions, Limitations and Future Work Directions

This chapter summarizes the key conclusions, limitations of the present work, and some directions for future research based on this study.

References

Abdel-raouf, N., Al-Homaidan, A.., Ibraheem, I.B.., 2012. Microalgae and wastewater treatment. Saudi J. Biol. Sci. 19, 257–275.

Adegboyega, N.F., Sharma, V.K., Siskova, K., Zbořil, R., Sohn, M., Schultz, B.J., Banerjee, S., 2013. Interactions of aqueous Ag+ with fulvic acids: Mechanisms of silver nanoparticle formation and investigation of stability. Environ. Sci. Technol. 47, 757–764.

Ahmed, S., Saifullah, Ahmad, M., Swami, B.L., Ikram, S., 2016. Green synthesis of silver nanoparticles using Azadirachta indica aqueous leaf extract. J. Radiat. Res. Appl. Sci. 9, 1–7.

Ajitha, B., Reddy, Y.A.K., Reddy, P.S., 2015. Enhanced antimicrobial activity of silver nanoparticles with controlled particle size by pH variation. Powder Technol. 269, 110–117.

Albiter, E., Valenzuela, M.A., Alfaro, S., Valverde-Aguilar, G., Martínez-Pallares, F.M., 2015. Photocatalytic deposition of Ag nanoparticles on TiO_2: Metal precursor effect on the structural and photoactivity properties. J. Saudi Chem. Soc. 19, 563–573.

Alcala, M.D., Real, C., 2006. Synthesis based on the wet impregnation method and characterization of iron and iron oxide-silica nanocomposites. Solid State Ionics 177, 955–960.

Amendola, V., Polizzi, S., Meneghetti, M., 2007. Free silver nanoparticles synthesized by laser ablation in organic solvents and their easy functionalization. Langmuir 23, 6766–6770.

Anandgaonker, P., Kulkarni, G., Gaikwad, S., Rajbhoj, A., 2014. Synthesis of TiO_2 nanoparticles by electrochemical method and their antibacterial application. Arab. J. Chem. 1–7.

Andreozzi, R., Caprio, V., Insola, A., Marotta, R., 1999. Advanced oxidation processes (AOP) for water purification and recovery. Catal. Today 53, 51–59.

Anpo, M., Ichihashi, Y., Takeuchi, M., Yamashita, H., 1998. Design of unique titanium oxide photocatalysts by an advanced metal ion-implantation method and photocatalytic reactions under visible light irradiation. Res. Chem. Intermed. 24, 143–149.

Anpo, M., Kishiguchi, S., Ichihashi, Y., Takeuchi, M., Yamashita, H., Ikeue, K., Morin, B., Davidson, A., Che, M., 2001. The design and development of second-generation titanium oxide photocatalysts able to operate under visible light irradiation by applying a metal ion-implantation method. Res. Chem. Intermed. 27, 459–467.

Arce, V.B., Santillán, J.M.J., Muñetón Arboleda, D., Muraca, D., Scaffardi, L.B., Schinca, D.C., 2017. Characterization and stability of silver nanoparticles in starch solution obtained by femtosecond laser ablation and salt reduction. J. Phys. Chem. C 121, 10501–10513.

Bachmatiuk, A., Kalenczuk, R., Rummeli, M., Gemming, T., Borowiak-Palen, E., 2008. Preparation of ultra-large-scale catalysts for catalytic vapour deposition of carbon nanotubes. Mater. Sci. 26, 105–111.

Bacsa, R.R., Kiwi, J., 1998. Effect of rutile phase on the photocatalytic properties of nanocrystalline titania during the degradation of p-coumaric acid. Appl. Catal. B Environ. 16, 19–29.

Balakumaran, M.D., Ramachandran, R., Kalaichelvan, P.T., 2015. Exploitation of endophytic fungus, Guignardia mangiferae for extracellular synthesis of silver nanoparticles and their in vitro biological activities. Microbiol. Res. 178, 9–17.

Bansal, A., Kumar, J., 2013. Photocatalysis by nanoparticles of titanium dioxide for drinking water purification: A conceptual and state-of-art review. Mater. Sci. Forum 764, 130–150.

Bar, H., Bhui, D.K., Sahoo, G.P., Sarkar, P., Pyne, S., Misra, A., 2009. Green synthesis of silver nanoparticles using seed extract of Jatropha curcas. Colloids Surfaces A Physicochem. Eng. Asp. 348, 212–216.

Barajas-Ledesma, E., García-Benjume, M.L., Espitia-Cabrera, I., Ortiz-Gutiérrez, M., Espinoza-Beltrán, F.J., Mostaghimi, J., Contreras-García, M.E., 2010. Determination of the band gap of TiO_2–Al_2O_3 films as a function of processing parameters. Mater. Sci. Eng. B 174, 71–73.

Barakat, M.A., 2011. New trends in removing heavy metals from industrial wastewater. Arab. J. Chem. 4, 361–377.

Baruah, B., Gabriel, G.J., Akbashev, M.J., Booher, M.E., 2013. Facile synthesis of silver nanoparticles stabilized by cationic polynorbornenes and their catalytic activity in 4-nitrophenol reduction. Langmuir 29, 4225–4234.

Basavegowda, N., Mishra, K., Lee, Y.R., 2015. Ultrasonic-assisted green synthesis of palladium nanoparticles and their nanocatalytic application in multicomponent reaction. New J. Chem. 39, 972–977.

Behera, A.K., Rao, C.V., Das, R.K., Giri, A.S., Golder, A.K., 2016. Fabrication and characterization of Ag-doped titania: impact of dye-sensitization, phenol decomposition kinetics and biodegradability index. Desalin. Water Treat. 57, 9488–9497.

Bhat, R., Sharanabasava, V.G., Deshpande, R., Shetti, U., Sanjeev, G., Venkataraman, A., 2013. Photo-bio-synthesis of irregular shaped functionalized gold nanoparticles using edible mushroom Pleurotus florida and its anticancer evaluation. J. Photochem. Photobiol. B Biol. 125, 63–69.

Bhattacharya, R., Mukherjee, P., 2008. Biological properties of "naked" metal nanoparticles. Adv. Drug Deliv. Rev. 60, 1289–1306.

Bickmore, C.R., Waldner, K.F., Treadwell, D.R., Laine, R.M., 1996. Ultrafine spinel powders by flame spray pyrolysis of a magnesium aluminum double alkoxide. J. Am. Ceram. Soc. 79, 1419–1423.

Bokare, A., Pai, M., Athawale, A.A., 2013. Surface modified Nd doped TiO_2 nanoparticles as photocatalysts in UV and solar light irradiation. Sol. Energy 91, 111–119.

Boomi, P., Prabu, H.G., Mathiyarasu, J., 2014. Synthesis, characterization and antibacterial activity of polyaniline/Pt-Pd nanocomposite. Eur. J. Med. Chem. 72, 18–25.

Brownson, D.A.C., Banks, C.E., 2010. Graphene electrochemistry: an overview of potential applications. Analyst 135, 2768–2778.

Bu, D., Zhuang, H., 2012. Synthesis, characterization, and photocatalytic studies of copper-doped TiO_2 hollow spheres using rape pollen as a novel biotemplate. Catal. Commun. 29, 24–28.

Byrne, J.A., Fernandez-iba, P.A., Dunlop, P.S.M., Alrousan, D.M.A., Hamilton, J.W.J., 2011. Photocatalytic enhancement for solar disinfection of water : A review. Int. J. Photoenergy 2011, 1–12.

Chairam, S., Sroysee, W., Boonchit, C., Kaewprom, C., 2015. Nonenzymatic Sensor for Hydrogen Peroxide using a Carbon Paste Electrode Modified with a Composite Consisting of Silver Nanoparticles , poly (o -aminobenzoic acid) and Magnetite 10, 4611–4625.

Chaudhuri, R.G., Paria, S., 2012. Core/shell nanoparticles : classes, properties, synthesis mechanisms, characterization, and applications. Chem. Rev. 112, 2373–2433.

Chen, X., Mao, S.S., 2007. Titanium dioxide nanomaterials :Synthesis, properties, modifications, and applications. Chem. Rev. 107, 2891–2959.

Chhatre, A., Solasa, P., Sakle, S., Thaokar, R., Mehra, A., 2012. Color and surface plasmon effects in nanoparticle systems: Case of silver nanoparticles prepared by microemulsion

route. Colloids Surfaces A Physicochem. Eng. Asp. 404, 83–92.

Chiarello, G.L., Selli, E., Forni, L., 2008. Photocatalytic hydrogen production over flame spray pyrolysis-synthesised TiO_2 and Au/TiO_2. Appl. Catal. B Environ. 84, 332–339.

Chowdhury, P., Moreira, J., Gomaa, H., Ray, A.K., 2012. Visible-solar-light-driven photocatalytic degradation of phenol with dye-sensitized TiO_2: Parametric and kinetic study. Ind. Eng. Chem. Res. 51, 4523–4532.

Ciriminna, R., Fidalgo, A., Pandarus, V., Ilharco, L.M., Pagliaro, M., Pais, A.R., 2013. The sol−gel route to advanced silica-based materials and recent applications. Chem. Rev. 113, 6592–6620.

Crutchley, R.J., 2013. CVD and ALD precursor design and application. Coord. Chem. Rev. 257, 3153.

Curri, M.L., Comparelli, R., Cozzoli, P.D., Mascolo, G., Agostiano, A., 2003. Colloidal oxide nanoparticles for the photocatalytic degradation of organic dye. Mater. Sci. Eng. C 23, 285–289.

Dadashi-Silab, S., Doran, S., Yagci, Y., 2016. Photoinduced electron transfer reactions for macromolecular syntheses. Chem. Rev. 116, 10212–10275.

Darroudi, M., Khorsand Zak, A., Muhamad, M.R., Huang, N.M., Hakimi, M., 2012. Green synthesis of colloidal silver nanoparticles by sonochemical method. Mater. Lett. 66, 117–120.

Dauthal, P., Mukhopadhyay, M., 2013. Biosynthesis of palladium nanoparticles using Delonix regia leaf extract and its catalytic activity for nitro-aromatics hydrogenation. Ind. Eng. Chem. Res. 52, 18131–18139.

Dauthal, P., Mukhopadhyay, M., 2012. Prunus domestica fruit extract-mediated synthesis of gold nanoparticles and its catalytic activity for 4-nitrophenol reduction. Ind. Eng. Chem. Res. 51, 13014–13020.

Delaigle, R., Eloy, P., Gaigneaux, E.M., 2011. Necessary conditions for a synergy between Ag and V2O5 in the total oxidation of chlorobenzene. Catal. Today 175, 177–182.

Delannoy, L., Hassan, N. El, Musi, A., To, N. Le, Krafft, J., Louis, C., Nguyen, N., To, L., 2006. Preparation of supported gold nanoparticles by a modified incipient wetness impregnation method. J. Phys. Chem. B 110, 22471–22478.

Devi, L.B., Mandal, A.B., 2013. Self-assembly of Ag nanoparticles using hydroxypropyl cyclodextrin: synthesis, characterisation and application for the catalytic reduction of p-nitrophenol. RSC Adv. 3, 5238–5253.

Dhandapani, P., Maruthamuthu, S., Rajagopal, G., 2012. Bio-mediated synthesis of TiO_2 nanoparticles and its photocatalytic effect on aquatic biofilm. J. Photochem. Photobiol. B Biol. 110, 43–49.

Duan, S., Wang, R., 2013. Bimetallic nanostructures with magnetic and noble metals and their physicochemical applications. Prog. Nat. Sci. Mater. Int. 23, 113–126.

Dubey, M., Bhadauria, S., Kushwah, B.S., 2009. Green synthesis of nanosilver particles from extract of Eucalyptus hybrida (Safeda) leaf. Dig. J. Nanomater. Biostructures 4, 537–543.

Dubey, P.S., Lahtinen, M., Särkkä, H., Sillanpää, M., 2010. Bioprospective of Sorbus aucuparia leaf extract in development of silver and gold nanocolloids. Colloids Surfaces B Biointerfaces 80, 26–33.

Ebrahimi, H.R., Modrek, M., 2013. Photocatalytic decomposition of methyl red dye by using nanosized zinc oxide deposited on glass beads in various pH and various atmosphere. J. Chem. 2013, 1–5.

Edison, J.I.E.T.N., Sethuraman, M.G., 2013. Electrocatalytic reduction of benzyl chloride by green synthesized silver nanoparticles using pod extract of Acacia nilotica. ACS Sustain. Chem. Eng. 1, 1326–1332.

Elechiguerra, J.L., Burt, J.L., Morones, J.R., Camacho-, A., Gao, X., Lara, H.H., Yacaman, M.J., 2005. Interaction of silver nanoparticles with HIV-1. J. Nanobiotechnology 3, 1–10.

Emeline, A. V, Ryabchuk, V.K., Serpone, N., May, R. V, 2005. Dogmas and misconceptions in heterogeneous photocatalysis. Some enlightened reflections. J. Phys. Chem. B 109, 18515–18521.

Etacheri, V., Di Valentin, C., Schneider, J., Bahnemann, D., Pillai, S.C., 2015. Visible-light activation of TiO_2 photocatalysts: Advances in theory and experiments. J. Photochem. Photobiol. C Photochem. Rev. 25, 1–29.

Fakhri, A., Tahami, S., Naji, M., 2017. Synthesis and characterization of core-shell bimetallic nanoparticles for synergistic antimicrobial effect studies in combination with doxycycline on burn specific pathogens. J. Photochem. Photobiol. B Biol. 169, 21–26.

Ferrando, R., Jellinek, J., Johnston, R.L., 2008. Nanoalloys: From theory to applications of alloy clusters and nanoparticles. Chem. Rev. 108, 846–904.

Fujishima, A., Hashimoto, K., Watanabe, T., 1999. TiO_2 photocatalysis: fundamentals and applications, 1st ed. BKC, Tokyo, Japan.

Gaddam, S.A., Kotakadi, V.S., Gopal, D.V.R.S., Rao, Y.S., Reddy, A. V., 2014. Efficient and robust biofabrication of silver nanoparticles by cassia alata leaf extract and their antimicrobial activity. J. Nanostructure Chem. 4, 1–9.

Gaikwad, S.P., Samuel, V., Pasricha, R., Ravi, V., 2004. Preparation of nanocrystalline ferroelectric BaBi2Nb2O9 by citrate gel method. Mater. Lett. 58, 3729–3731.

Gao, S., Jia, X., Yang, S., Li, Z., Jiang, K., 2011. Hierarchical Ag/ZnO micro/nanostructure: Green synthesis and enhanced photocatalytic performance. J. Solid State Chem. 184, 764–769.

Georgekutty, R., Seery, M.K., Pillai, S.C., 2008. A highly efficient Ag-ZnO photocatalyst : Synthesis, properties, and mechanism. J. Phys. Chem. C 112, 13563–13570.

Giri, A.S., Golder, A.K., 2014. Fenton, photo-Fenton, H2O2 photolysis, and TiO2 photocatalysis for dipyrone oxidation: Drug removal, mineralization, biodegradability, and degradation mechanism. Ind. Eng. Chem. Res. 53, 1351–1358.

Gnanasekaran, L., Hemamalini, R., Ravichandran, K., 2015. Synthesis and characterization of TiO_2 quantum dots for photocatalytic application. J. Saudi Chem. Soc. 19, 589–594.

Gopinath, P.M., Narchonai, G., Dhanasekaran, D., Ranjani, A., Thajuddin, N., 2015. Mycosynthesis, characterization and antibacterial properties of AgNPs against multidrug resistant (MDR) bacterial pathogens of female infertility cases. Asian J. Pharm. Sci. 10, 138–145.

Granados, G.O., Páez M., C.A., Martínez O., F., Páez-Mozo, E.A., 2005. Photocatalytic degradation of phenol on TiO_2 and TiO_2/Pt sensitized with metallophthalocyanines. Catal. Today 107–108, 589–594.

Gudikandula, K., Charya Maringanti, S., 2016. Synthesis of silver nanoparticles by chemical and biological methods and their antimicrobial properties. J. Exp. Nanosci. 11, 714–721.

Gunalan, S., Sivaraj, R., Rajendran, V., 2012. Green synthesized ZnO nanoparticles against bacterial and fungal pathogens. Prog. Nat. Sci. Mater. Int. 22, 693–700.

Guzman, M.G., Dille, J., Godet, S., 2009. Synthesis of silver nanoparticles by chemical reduction method and their antibacterial activity. Int. J. Chem. Biomol. Enigineering 2, 104–111.

Halley, J.W., Kozlowski, M., Michalewicz, M., Smyrl, W., Tit, N., 1991. Photoelectrochemical spectroscopy studies of titanium dioxide surfaces: theory and experiment. Surf. Sci. 256, 397–408.

Harraz, F.A., Abdel-Salam, O.E., Mostafa, A.A., Mohamed, R.M., Hanafy, M., 2013. Rapid synthesis of titania-silica nanoparticles photocatalyst by a modified sol-gel method for cyanide degradation and heavy metals removal. J. Alloys Compd. 551, 1–7.

He, T., Weng, Y.G., Yu, P., Liu, C.L., Lu, H.Q., Sun, Y.P., Zhang, S.Z., Yang, X., Liu, G.Q., 2014. Bio-template mediated in situ phosphate transfer to hierarchically porous TiO_2 with localized phosphate distribution and enhanced photoactivities. J. Phys. Chem. C 118, 4607–4617.

He, Z., Que, W., He, Y., 2013. Synthesis and characterization of bioinspired hierarchical mesoporous TiO_2 photocatalysts. Mater. Lett. 94, 136–139.

Herrmann, J., 1999. Heterogeneous photocatalysis: fundamentals and applications to the removal of various types of aqueous pollutants. Catal. Today 53, 115–129.

Herrmann, J.M., Disdier, J., Pichat, P., 1984. Effect of chromium doping on the electrical and catalytic properties of powder titania under UV and visible illumination. Chem. Phys. Lett. 108, 618–622.

Hoffmann, M.R., Martin, S.T., Choi, W., Bahnemann, D.W., 1995. Environmental applications of semiconductor photocatalysis. Chem. Rev. 95, 69–96.

Huang, J., Li, Q., Sun, D., Lu, Y., Su, Y., Yang, X., Wang, H., Wang, Y., Shao, W., He, N., Hong, J., Chen, C., 2007. Biosynthesis of silver and gold nanoparticles by novel sundried Cinnamomum camphora leaf. Nanotechnology 18, 105104.

Huang, Z., Jiang, H., Liu, P., Sun, J., Guo, D., Shan, J., Gu, N., 2015. Continuous synthesis of size-tunable silver nanoparticles by a green electrolysis method and multi-electrode design for high yield. J. Mater. Chem. A 3, 1925–1929.

Iravani, S., 2014. Bacteria in nanoparticle synthesis: Current status and future prospects. Int. Sch. Res. Not. 2014, 1–18.

Irfan, M., Butt, T., Imtiaz, N., Abbas, N., Ahmad, R., Shafique, A., 2013. The removal of COD , TSS and colour of black liquor by coagulation – flocculation process at optimized pH, settling and dosing rate. Arab. J. Chem.

Ismail, A.A., Al-Sayari, S.A., Bahnemann, D.W., 2013. Photodeposition of precious metals onto mesoporous TiO_2 nanocrystals with enhanced their photocatalytic activity for methanol oxidation. Catal. Today 209, 2–7.

Jha, A.K., Prasad, K., 2010. Green synthesis of silver nanoparticles using cycas leaf. Int. J. Green Nanotechnol. Phys. Chem. 1, 110–117.

Jiang, S.P., 2006. A review of wet impregnation - An alternative method for the fabrication of high performance and nano-structured electrodes of solid oxide fuel cells. Mater. Sci. Eng. A 418, 199–210.

Kandpal, N.., Sah, N., Loshali, R., Joshi, R., Prasad, J., 2014. Co-precipitation method of synthesis and characterization of iron oxide nanoparticles. J. Sci. Ind. Res. 73, 87–90.

Kasthuri, J., Kathiravan, K., Rajendiran, N., 2009. Phyllanthin-assisted biosynthesis of silver and gold nanoparticles : a novel biological approach. J. Nanoparticle Res. 11, 1075–1085.

Khalil, M.M.H., Ismail, E.H., El-Baghdady, K.Z., Mohamed, D., 2014. Green synthesis of silver nanoparticles using olive leaf extract and its antibacterial activity. Arab. J. Chem. 7, 1131–1139.

Khan, Z., Al-Thabaiti, S.A., Obaid, A.Y., Al-Youbi, A.O., 2011. Preparation and characterization

of silver nanoparticles by chemical reduction method. Colloids Surfaces B Biointerfaces 82, 513–517.

Kittisakmontree, P., Pongthawornsakun, B., Yoshida, H., Fujita, S.I., Arai, M., Panpranot, J., 2013. The liquid-phase hydrogenation of 1-heptyne over Pd-Au/TiO_2 catalysts prepared by the combination of incipient wetness impregnation and deposition-precipitation. J. Catal. 297, 155–164.

Knorr, F.J., Mercado, C.C., Mchale, J.L., 2008. Trap-state distributions and carrier transport in pure and mixed-phase TiO_2: Influence of contacting solvent and interphasial electron transfer. J. Phys. Chem. C. Chem. C 112, 12786–12794.

Kominami, H., Murakami, S., Kato, J., Kera, Y., Ohtani, B., 2002. Correlation between some physical properties of titanium gioxide particles and their photocatalytic activity for some probe reactions in aqueous systems. J. Phys. Chem. B 106, 10501–10507.

Konstantinou, I.K., Albanis, T.A., 2004. TiO_2-assisted photocatalytic degradation of azo dyes in aqueous solution : kinetic and mechanistic investigations A review. Appl. Catal. B Environ. 49, 1–14.

Kovács, G., Kozlov, S.M., Matolínová, I., Vorokhta, M., Matolín, V., Neyman, K.M., 2015. Revealing chemical ordering in Pt–Co nanoparticles using electronic structure calculations and X-ray photoelectron spectroscopy. Phys. Chem. Chem. Phys. 17, 28298–28310.

Krishnaraj, C., Jagan, E.G., Rajasekar, S., Selvakumar, P., Kalaichelvan, P.T., Mohan, N., 2010. Synthesis of silver nanoparticles using Acalypha indica leaf extracts and its antibacterial activity against water borne pathogens. Colloids Surfaces B Biointerfaces 76, 50–56.

Kristl, M., Dojer, B., Gyergyek, S., Kristl, J., 2017. Synthesis of nickel and cobalt sulfide nanoparticles using a low cost sonochemical method. Heliyon 3, 1–19.

Kuo, Y.L., Chen, H.W., Ku, Y., 2007. Analysis of silver particles incorporated on TiO_2 coatings for the photodecomposition of o-cresol. Thin Solid Films 515, 3461–3468.

Larese, F.F., D'Agostin, F., Crosera, M., Adami, G., Renzi, N., Bovenzi, M., Maina, G., 2009. Human skin penetration of silver nanoparticles through intact and damaged skin. Toxicology 255, 33–37.

Li, J., Zhao, T., Chen, T., Liu, Y., Ong, C.N., Xie, J., 2015. Engineering noble metal nanomaterials for environmental applications. Nanoscale 7, 7502–7519.

Li, L., Yu, L., Lin, Z., Yang, G., 2016. Reduced TiO_2-graphene oxide heterostructure as broad spectrum-driven efficient water-splitting photocatalysts. ACS Appl. Mater. Interfaces 8, 8536–8545.

Lim, P.Y., Liu, R.S., She, P.L., Hung, C.F., Shih, H.C., 2006. Synthesis of Ag nanospheres particles in ethylene glycol by electrochemical-assisted polyol process. Chem. Phys. Lett. 420, 304–308.

Linsebigler, A.L., Lu, G., Yates, J.T., 1995. Photocatalysis on TiO_2 surfaces: Principles, mechanisms, and selected results. Chem. Rev. 95, 735–758.

Liu, R., Wu, H.S., Yeh, R., Lee, C.Y., Hung, Y., 2012. Synthesis and bactericidal ability of TiO_2 and Ag-TiO_2 prepared by coprecipitation method. Int. J. Pho 2012, 1–7.

Liu, S., Tian, J., Wang, L., Sun, X., 2011. Microwave-assisted rapid synthesis of Ag nanoparticles/graphene nanosheet composites and their application for hydrogen peroxide detection. J. Nanoparticle Res. 13, 4539–4548.

Lu, W., Gao, S., Wang, J., 2008. One-Pot Synthesis of Ag/ZnO Self-Assembled 3D Hollow Microspheres with Enhanced Photocatalytic Performance. J. Phys. Chem. C 112, 16792–16800.

Majone, M., Verdini, R., Aulenta, F., Rossetti, S., Tandoi, V., Kalogerakis, N., Agathos, S., Zanaroli, G., Fava, F., 2015. In situ groundwater and sediment bioremediation : barriers and perspectives at European contaminated sites. N. Biotechnol. 32, 133–146.

Malato, S., Fernandez-Ibanez, P., Maldonado, M.I., Blanco, J., Gernjak, W., 2009. Decontamination and disinfection of water by solar photocatalysis: Recent overview and trends. Catal. Today 147, 1–59.

Malika, M., Rao, C.V., Das, R.K., Giri, A.S., Golder, A.K., 2016. Evaluation of bimetal doped TiO_2 in dye fragmentation and its comparison to mono-metal doped and bare catalysts. Appl. Surf. Sci. 368, 316–324.

Mallikarjuna, K., John Sushma, N., Narasimha, G., Manoj, L., Deva Prasad Raju, B., 2014. Phytochemical fabrication and characterization of silver nanoparticles by using Pepper leaf broth. Arab. J. Chem. 7, 1099–1103.

Mittal, A.K., Chisti, Y., Banerjee, U.C., 2013. Synthesis of metallic nanoparticles using plant extracts. Biotechnol. Adv. 31, 346–356.

Mohamed, N.H., Ismail, M.A., Abdel-Mageed, W.M., Mohamed Shoreit, A.A., 2014. Antimicrobial activity of latex silver nanoparticles using Calotropis procera. Asian Pac. J. Trop. Biomed. 4, 876–883.

Mohamed, R.M., Mkhalid, I.A., Al-Thabaiti, S.A., Mokhtar, M., 2013. Nano Cu metal doped on TiO_2-SiO_2 nanoparticle catalysts in photocatalytic degradation of direct blue dye. J. Nanosci. Nanotechnol. 13, 4975–4980.

Nagajyothi, P.C., Minh An, T.N., Sreekanth, T.V.M., Lee, J. Il, Joo, D.L., Lee, K.D., 2013. Green route biosynthesis: Characterization and catalytic activity of ZnO nanoparticles. Mater. Lett. 108, 160–163.

Nakata, K., Fujishima, A., 2012. TiO_2 photocatalysis: Design and applications. J. Photochem. Photobiol. C Photochem. Rev. 13, 169–189.

Neamen, D.A., 2003. Semiconductor physics and devices: Basic prinicples, fourth. ed. McGraw-Hill Higher Education.

Niemirowicz, K., Prokop, I., Wilczewska, A.Z., Wnorowska, U., Piktel, E., Wątek, M., Savage, P.B., Bucki, R., 2015. Magnetic nanoparticles enhance the anticancer activity of cathelicidin LL-37 peptide against colon cancer cells. Int. J. Nanomedicine 10, 3843–3853.

Noberi, C., Zaman, A.C., Üstündağ, C.B., Kaya, F., Kaya, C., 2012. Electrophoretic deposition of hydrothermally synthesised Ag-TiO_2 hybrid nanoparticles onto 3-D Ni filters. Mater. Lett. 67, 113–116.

Nymark, P., Catal??n, J., Suhonen, S., J??rventaus, H., Birkedal, R., Clausen, P.A., Jensen, K.A., Vippola, M., Savolainen, K., Norppa, H., 2013. Genotoxicity of polyvinylpyrrolidone-coated silver nanoparticles in BEAS 2B cells. Toxicology 313, 38–48.

Ola, O., Maroto-Valer, M.M., 2015. Review of material design and reactor engineering on TiO_2 photocatalysis for CO_2 reduction. J. Photochem. Photobiol. C Photochem. Rev. 24, 16–42.

Ordonez, A.A.., Gomez, J.., Vattuone, M.., Isla, M.., 2003. Phospholipid analogue profiles of human Porphyromonas gingivalis isolates from different geographical locations. Microb. Ecol. Health Dis. 15, 33–39.

Ordonez, A.A.L., Gomez, J.D., Vattuone, M.A., Isla, M.I., 2006. Antioxidant activities of Sechium edule (Jacq.) Swartz extracts. Food Chem. 97, 452–458.

Pacholski, C., Kornowski, A., Weller, H., 2004. Site-specific photodeposition of silver on ZnO nanorods. Angew. Chemie - Int. Ed. 43, 4774–4777.

Pandey, S., Mewada, A., Thakur, M., Shinde, S., Shah, R., Oza, G., Sharon, M., 2013. Rapid

Biosynthesis of Silver Nanoparticles by Exploiting the Reducing Potential of Trapa bispinosa Peel Extract. J. Nanosci. 2013, 1–9.

Parastar, S., Nasseri, S., Borji, S.H., Fazlzadeh, M., Mahvi, A.H., Javadi, A.H., Gholami, M., 2013. Application of Ag-doped TiO_2nanoparticle prepared by photodeposition method for nitrate photocatalytic removal from aqueous solutions. Desalin. Water Treat. 51, 7137–7144.

Paredes, J.I., Villar-Rodil, S., Solis-Fernandez, P., Martinez-Alonso, A., Tascon, J.M.D., 2009. Atomic force and scanning tunneling microscopy imaging of graphene nanosheets derived from graphite oxide. Langmuir 25, 5957–5968.

Park, H., Jie, H.S., Neppolian, B., Tsujimaru, K., Ahn, J.P., Lee, D.Y., Park, J.K., Anpo, M., 2006. Preparation of highly active TiO_2 nano-particle photocatalysts by a flame aerosol method for the complete oxidation of 2-propanol. Top. Catal. 47, 166–174.

Patil, S.S., Tamboli, M.S., Patil, D.R., Kulkarni, M. V, Yoon, H., Kim, H., Al-deyab, S.S., Yoon, S.S., Kolekar, S.S., Kale, B.B., 2016. Green approach for hierarchical nanostructured Ag-ZnO and their photocatalytic performance under sunlight. Catal. Today 260, 126–134.

Paulino, P.N., Salim, V.M.M., Resende, N.S., 2016. Zn-Cu promoted TiO_2 photocatalyst for CO_2 reduction with H2O under UV light. Appl. Catal. B Environ. 185, 362–370.

Petcharoen, K., Sirivat, A., 2012. Synthesis and characterization of magnetite nanoparticles via the chemical co-precipitation method. Mater. Sci. Eng. B 177, 421–427.

Petica, A., Florea, A., Gaidau, C., Balan, D., Anicai, L., 2017. Synthesis and characterization of silver-titania nanocomposites prepared by electrochemical method with enhanced photocatalytic characteristics, antifungal and antimicrobial activity. J. Mater. Res. Technol. 1–13.

Philip, D., 2010. Green synthesis of gold and silver nanoparticles using Hibiscus rosa sinensis. Phys. E 42, 1417–1424.

Piszczek, P., Muchewicz, Z., Radtke, A., Gryglas, M., Dahm, H., Rózycki, H., 2013. CVD of TiO_2 and TiO_2/Ag antimicrobial layers: Deposition from the hexanuclear μ-oxo Ti(IV) complex as a precursor, and the characterization. Surf. Coatings Technol. 222, 38–43.

Prathna, T.C., Chandrasekaran, N., Raichur, A.M., Mukherjee, A., 2011. Biomimetic synthesis of silver nanoparticles by Citrus limon (lemon) aqueous extract and theoretical prediction of particle size. Colloids Surfaces B Biointerfaces 82, 152–159.

Quiñones, C., Ayala, J., Vallejo, W., 2010. Methylene blue photoelectrodegradation under UV irradiation on Au/Pd-modified TiO_2 films. Appl. Surf. Sci. 257, 367–371.

Rajakumar, G., Rahuman, A.A., Roopan, S.M., Khanna, V.G., Elango, G., Kamaraj, C., Zahir, A.A., Velayutham, K., 2012. Fungus-mediated biosynthesis and characterization of TiO_2 nanoparticles and their activity against pathogenic bacteria. Spectrochim. Acta - Part A Mol. Biomol. Spectrosc. 91, 23–29.

Ramachandran, R., Chen, S.M., Gnana Kumar, G.P., Gajendran, P., Devi, N.B., 2015. An overview of fabricating nanostructured electrode materials for biosensor applications. Int. J. Electrochem. Sci. 10, 8607–8629.

Ramakrishnan, R., Kalaivani, S., Amala Infant Joice, J., Sivakumar, T., 2012. Photocatalytic activity of multielement doped TiO_2 in the degradation of congo red. Appl. Surf. Sci. 258, 2515–2521.

Ramteke, C., Chakrabarti, T., Sarangi, B.K., Pandey, R., 2013. Synthesis of silver nanoparticles from the aqueous extract of leaves of Ocimum sanctum for enhanced antibacterial activity. J. Chem. 2013, 1–8.

Ravindran, A., Chandran, P., Khan, S.S., 2013. Biofunctionalized silver nanoparticles: Advances and prospects. Colloids Surfaces B Biointerfaces 105, 342–352.

Ravindran, A., Singh, A., Raichur, A.M., Chandrasekaran, N., Mukherjee, A., 2010. Studies on interaction of colloidal Ag nanoparticles with Bovine Serum Albumin (BSA). Colloids Surfaces B Biointerfaces 76, 32–37.

Reyes-Coronado, D., Rodríguez-Gattorno, G., Espinosa-Pesqueira, M.E., Cab, C., de Coss, R., Oskam, G., 2008. Phase-pure TiO_2 nanoparticles: anatase, brookite and rutile. Nanotechnology 19, 145605.

Riaz, N., Chong, F.K., Man, Z.B., Khan, M.S., Dutta, B.K., 2013a. Photodegradation of Orange II under visible light using Cu–Ni/TiO_2 : Effect of calcination temperature. Ind. Eng. Chem. Res. 52, 4491–4503.

Riaz, N., Chong, F.K., Man, Z.B., Khan, M.S., Dutta, B.K., 2013b. Photodegradation of Orange II under visible light using Cu−Ni/TiO_2 : Influence of Cu:Ni mass composition, preparation, and calcination temperature. Ind. Eng. Chem. Res. 52, 4491–4503.

Roopan, S.M., Rohit, Madhumitha, G., Rahuman, A.A., Kamaraj, C., Bharathi, A., Surendra, T. V., 2013. Low-cost and eco-friendly phyto-synthesis of silver nanoparticles using Cocos nucifera coir extract and its larvicidal activity. Ind. Crops Prod. 43, 631–635.

Sadowski, Z., Malliszewska, I., GrochoWalska, B., Polowczyk, I., Kozlexki, T., 2008. Synthesis of silver nanoparticles using microorganisms. Mater. Sci. 26, 419–424.

Saifuddin, N., Wong, C.W., Yasumira, A.A.N.U.R., 2009. Rapid biosynthesis of silver nanoparticles using culture supernatant of bacteria with microwave irradiation. E-Journal Chem. 6, 61–70.

Salkar, R. a., Jeevanandam, P., Aruna, S.T., Koltypin, Y., Gedanken, a., 1999. The sonochemical preparation of amorphous silver nanoparticles. J. Mater. Chem. 9, 1333–1335.

Salomon, G.R., 1982. Homogeneous metal-catalysis in organic photochemistry. Tetrahedron 39, 485–575.

Sangpour, P., Hashemi, F., Moshfegh, A.Z., 2010. Photoenhanced degradation of methylene blue on cosputtered M:TiO_2 (M = Au, Ag, Cu) nanocomposite systems: A comparative study. J. Phys. Chem. C 114, 13955–13961.

Sathishkumar, M., Sneha, K., Won, S.W., Cho, C.-W., Kim, S., Yun, Y.-S., 2009. Cinnamon zeylanicum bark extract and powder mediated green synthesis of nano-crystalline silver particles and its bactericidal activity. Colloids Surfaces B Biointerfaces 73, 332–338.

Saxena, A., Tripathi, R.M., Zafar, F., Singh, P., 2012. Green synthesis of silver nanoparticles using aqueous solution of Ficus benghalensis leaf extract and characterization of their antibacterial activity. Mater. Lett. 67, 91–94.

Schneider, J., Matsuoka, M., Takeuchi, M., Zhang, J., Horiuchi, Y., Anpo, M., Bahnemann, D.W., 2014. Understanding TiO_2 photocatalysis: mechanisms and materials. Chem. Rev. 114, 9919–9986.

Serpone, N., Salinaro, A., 1999. Terminology, relative photonic efficiencies and quantum yields in heterogeneous photocatalysis. Part I: Suggested protocol. Pure Appl. Chem. 71, 303–320.

Shaban, Y.A., 2013. Simultaneous hydrogen production with the degradation of naphthalene in seawater using solar light-responsive. Mod. Res. Catal. 2, 6–12.

Shah, Z.H., Wang, J., Ge, Y., Wang, C., Mao, W., Zhang, S., Lu, R., 2015. Highly enhanced plasmonic photocatalytic activity of Ag/AgCl/TiO_2 by CuO co-catalyst. J. Mater. Chem. A 3, 3568–3575.

Shan, G., Xu, L., Wang, G., Liu, Y., 2007. Enhanced raman scattering of ZnO quantum dots on

silver colloids. J. Phys. Chem. C 111, 3290–3293.

Shankar, S.S., Ahmad, A., Sastry, M., 2003. Geranium leaf assisted biosynthesis of silver nanoparticles. Biotechnol. Prog. 19, 1627–1631.

Shankar, S.S., Rai, A., Ahmad, A., Sastry, M., 2004. Rapid synthesis of Au, Ag, and bimetallic Au core-Ag shell nanoparticles using Neem (*Azadirachta indica*) leaf broth. J. Colloid Interface Sci. 275, 496–502.

Shinji, I., Masashi, I., 2008. Solvothermal synthesis of inorganic materials and their performance as catalysts. J. Japan Pet. Inst. 51, 143–156.

Siciliano, T., Tommasi, D.N., Morelli, I., Braca, A., 2004. Study of flavonoids of *sechium edule* (Jacq) swartz (*Cucurbitaceae*) different edible organs by liquid chromatography photodiode array mass spectrometry. J. Agric. Food Chem. 52, 6510–6515.

Simakin, A. V., Voronov, V. V., Kirichenko, N.A., Shafeev, G.A., Dolgaev, S.I., Simakin, A. V., Voronov, V. V., Shafeev, G.A., Bozon-Verduraz, F., 2002. Nanoparticles produced by laser ablation of solids in liquid environment. Appl. Phys. A Mater. Sci. Process. 79, 546–551.

Simamora, A.J., Hsiung, T.L., Chang, F.C., Yang, T.C., Liao, C.Y., Wang, H.P., 2012. Photocatalytic splitting of seawater and degradation of methylene blue on CuO/nano TiO_2. Int. J. Hydrogen Energy 37, 13855–13858.

Singhal, G., Bhavesh, R., Kasariya, K., Sharma, A.R., Singh, R.P., 2011. Biosynthesis of silver nanoparticles using Ocimum sanctum (Tulsi) leaf extract and screening its antimicrobial activity. J. Nanoparticle Res. 13, 2981–2988.

Sivera, M., Kvitek, L., Soukupova, J., Panacek, A., Prucek, R., Vecerova, R., Zboril, R., 2014. Silver nanoparticles modified by gelatin with extraordinary pH stability and long-term antibacterial activity. PLoS One 9, 103675.

Sondi, I., Goia, D. V., Matijevic, E., 2003. Preparation of highly concentrated stable dispersions of uniform silver nanoparticles. J. Colloid Interface Sci. 260, 75–81.

Sreethawong, T., Junbua, C., Chavadej, S., 2009. Photocatalytic H2 production from water splitting under visible light irradiation using Eosin Y-sensitized mesoporous-assembled Pt/TiO_2 nanocrystal photocatalyst. J. Power Sources 190, 513–524.

Strandwitz, N.C., Khan, A., Boettcher, S.W., Mikhailovsky, A.A., Hawker, C.J., Nguyen, T.Q., Stucky, G.D., 2008. One- and two-photon induced polymerization of methylmethacrylate using colloidal CdS semiconductor quantum dots. J. Am. Chem. Soc. 130, 8280–8288.

Strobel, R., Baiker, A., Pratsinis, S.E., 2006. Aerosol flame synthesis of catalysts. Adv. Powder Technol. 17, 457–480.

Subash, B., Krishnakumar, B., Velmurugan, R., Swaminathan, M., Shanthi, M., 2012. Synthesis of Ce co-doped Ag–ZnO photocatalyst with excellent performance for NBB dye degradation under natural sunlight illumination. Catal. Sci. Technol. 2, 2319.

Sun, Q., Cai, X., Li, J., Zheng, M., Chen, Z., Yu, C.P., 2014. Green synthesis of silver nanoparticles using tea leaf extract and evaluation of their stability and antibacterial activity. Colloids Surfaces A Physicochem. Eng. Asp. 444, 226–231.

Sun, X., Guo, S., Liu, Y., Sun, S., 2012. Dumbbell-like PtPd-Fe_3O_4 nanoparticles for enhanced electrochemical detection of H_2O_2. Nano Lett. 12, 4859–4863.

Sunada, K., Watanabe, T., Hashimoto, K., 2003. Studies on photokilling of bacteria on TiO_2 thin film. J. Photochem. Photobiol. A Chem. 156, 227–233.

Sutradhar, P., Saha, M., 2016. Silver nanoparticles: synthesis and its nanocomposites for heterojunction polymer solar cells. J. Phys. Chem. C 120, 8941–8949.

Tahir, K., Nazir, S., Li, B., Khan, A.U., Khan, Z.U.H., Ahmad, A., Khan, Q.U., Zhao, Y., 2015.

Enhanced visible light photocatalytic inactivation of Escherichia coli using silver nanoparticles as photocatalyst. J. Photochem. Photobiol. B Biol. 153, 261–266.

Tayade, R.J., Kulkarni, R.G., Jasra, R. V, 2006. Transition metal ion impregnated mesoporous TiO_2 for photocatalytic degradation of organic contaminants in water. Ind. Eng. Chem. Res. 45, 5231–5238.

Thakkar, K.N., Mhatre, S.S., Parikh, R.Y., 2010. Biological synthesis of metallic nanoparticles. Nanomedicine Nanotechnology, Biol. Med. 6, 257–262.

Thiwawong, T., Onlaor, K., Tunhoo, B., 2013. A Humidity Sensor Based on Silver Nanoparticles Thin Film Prepared by Electrostatic Spray Deposition Process. Adv. Mater. Sci. Eng. 2013, 1–7.

Trillas, M., Pujol, M., Domenech, X., 1992. Phenol photodegradation over titanium dioxide. J. Chem. Technol. Biotechnol. 55, 85–90.

Tryba, B., Piszcz, M., Morawski, A.W., 2010. Photocatalytic and self-cleaning properties of Ag-doped TiO_2. Open Mater. Sci. J. 4, 5–8.

Valli, J.S., Vaseeharan, B., 2012. Biosynthesis of silver nanoparticles by Cissus quadrangularis extracts. Mater. Lett. 82, 171–173.

Veerasamy, R., Xin, T.Z., Gunasagaran, S., Xiang, T.F.W., Yang, E.F.C., Jeyakumar, N., Dhanaraj, S.A., 2011. Biosynthesis of silver nanoparticles using mangosteen leaf extract and evaluation of their antimicrobial activities. J. Saudi Chem. Soc. 15, 113–120.

Velusamy, P., Das, J., Pachaiappan, R., Vaseeharan, B., Pandian, K., 2015. Greener approach for synthesis of antibacterial silver nanoparticles using aqueous solution of neem gum (Azadirachta indica L.). Ind. Crops Prod. 66, 103–109.

Verma, A., Mehata, M.S., 2016. Controllable synthesis of silver nanoparticles using Neem leaves and their antimicrobial activity. J. Radiat. Res. Appl. Sci. 9, 109–115.

Vichery, C., Maurin, I., Proux, O., Kie, I., Hazemann, J., Corte, R., Boilot, J., Gacoin, T., 2013. Introduction of cobalt ions in γ - Fe_2O_3 nanoparticles by direct coprecipitation or postsynthesis adsorption: Dopant localization and magnetic anisotropy. J. Phys. Chem. C 117, 19672–19683.

Vigneshwaran, N., Arati, K.A., Perianambi, V. V, Rajan, N.P., Rudrapatna, B.H., 2007. Silver − Protein (Core − Shell) Nanoparticle Production Using Spent Mushroom Substrate. Langmuir 23, 7113–7117.

Vivekanandhan, S., Schreiber, M., Mason, C., Kumar, A.M., Misra, M., 2014. Biointerfaces Maple leaf (Acer sp.) extract mediated green process for the functionalization of ZnO powders with silver nanoparticles. Colloids Surfaces B Biointerfaces 113, 169–175.

Walton, R.I., 2002. Subcritical solvothermal synthesis of condensed inorganic materials. Chem. Soc. Rev. 31, 230–238.

Wang, H., Qiao, X., Chen, J., Ding, S., 2005. Preparation of silver nanoparticles by chemical reduction method. Colloids Surfaces A Physicochem. Eng. Asp. 256, 111–115.

Wang, S., Qian, H., Hu, Y., Dai, W., Zhong, Y., Chen, J., Hu, X., 2013. Facile one-pot synthesis of uniform TiO_2-Ag hybrid hollow spheres with enhanced photocatalytic activity. Dalt. Trans. 42, 1122–1128.

Wang, Z., Yang, C., Lin, T., Yin, H., Chen, P., Wan, D., Xu, F., Huang, F., Lin, J., Xie, X., Jiang, M., 2013. Visible-light photocatalytic, solar thermal and photoelectrochemical properties of aluminium-reduced black titania. Energy Environ. Sci. 6, 3007–3014.

Wen, Z., Wang, G., Lu, W., Wang, Q., Zhang, Q., Li, J., 2007. Enhanced photocatalytic properties of mesoporous SnO_2 induced by low concentration ZnO doping. Cryst. Growth

Des. 7, 1722–1725.

Wu, Z.G., Munoz, M., Montero, O., 2010. The synthesis of nickel nanoparticles by hydrazine reduction. Adv. Powder Technol. 21, 165–168.

Xia, N., Cai, Y., Jiang, T., Yao, J., 2011. Green synthesis of silver nanoparticles by chemical reduction with hyaluronan. Carbohydr. Polym. 86, 956–961.

Xiao, G., Huang, X., Liao, X., Shi, B., 2013. One-pot facile synthesis of cerium-doped TiO_2 mesoporous nano fibers using collagen fiber as the biotemplate and its application in visible light photocatalysis. J. Phys. Chem. C, 9739–9746.

Xie, Y., Ye, R., Liu, H., 2006. Synthesis of silver nanoparticles in reverse micelles stabilized by natural biosurfactant. Colloids Surfaces A Physicochem. Eng. Asp. 279, 175–178.

Xin, B., Jing, L., Ren, Z., Wang, B., Fu, H., 2005. Effects of simultaneously doped and deposited Ag on the photocatalytic activity and surface states of TiO_2. J. Phys. Chem. B 109, 2805–2809.

Xu, G., Qiao, X., Qiu, X., Chen, J., 2013. Green synthesis of highly pure nano-silver sols—electrolysis. Rare Met. Mater. Eng. 42, 249–253.

Yamada, Y., Kanemitsu, Y., 2012. Determination of electron and hole lifetimes of rutile and anatase TiO_2 single crystals. Appl. Phys. Lett. 133907.

Yang, S., Gao, L., 2004. New method to prepare nitrogen-doped titanium dioxide and its photocatalytic activities irradiated by visible light. J. Am. Ceram. Soc. 87, 1803–1805.

Yang, W., Li, Y., Bai, Y., Sun, C., 2006. Hydrogen peroxide biosensor based on myoglobin/colloidal gold nanoparticles immobilized on glassy carbon electrode by a Nafion film. Sensors Actuators, B Chem. 115, 42–48.

Yang, X., Wang, L.N., Zhou, G.Z., Sui, N., Gu, Y.X., Wan, J., 2015. Electrochemical detection of H_2O_2 based on Fe_3O_4 nanoparticles with graphene oxide and polyamidoamine dendrimer. J. Clust. Sci. 26, 789–798.

Yilmaz, M., Turkdemir, H., Kilic, M.A., Bayram, E., Cicek, A., Mete, A., Ulug, B., 2011. Biosynthesis of silver nanoparticles using leaves of Stevia rebaudiana. Mater. Chem. Phys. 130, 1195–1202.

Yoon, M., Lee, J.E., Jang, Y.J., Lim, J.W., Rani, A., Kim, D.H., 2015. Comprehensive study on the controlled plasmon-enhanced photocatalytic activity of hybrid Au/ZnO systems mediated by thermoresponsive polymer linkers. ACS Appl. Mater. Interfaces 7, 21073–21081.

You, H., Yang, S., Ding, B., Yang, H., 2013. Synthesis of colloidal metal and metal alloy nanoparticles for electrochemical energy applications. Chem. Soc. Rev. 42, 2880–2904.

Yu, X., Yu, W., Li, H., Tu, S.T., Han, Y.F., 2013. Preparation, characterization and application of K-PtCo/Al_2O_3 catalyst coatings for preferential CO oxidation. Appl. Catal. B Environ. 140–141, 588–597.

Zamiri, R., Azmi, B.Z., Ahangar, H.A., Zamiri, G., Husin, M.S., Wahab, Z.A., 2012. Preparation and characterization of silver nanoparticles in natural polymers using laser ablation. Bull. Mater. Sci. 35, 727–731.

Zhang, B.-W., Sheng, T., Wang, Y.-X., Qu, X.-M., Zhang, J.-M., Zhang, Z.-C., Liao, H., Zhu, F., Dou, S.X., Jiang, Y., Sun, S.-G., 2017. Platinum–Cobalt bimetallic nanoparticles with Pt skin for electro-oxidation of ethanol. ACS Catal. 7, 892–895.

Zhang, D., 2010. Enhanced photocatalytic activity for titanium dioxide by co-modification with copper and iron. Transit. Met. Chem. 35, 933–938.

Zhang, D., Zeng, F., 2011. Photocatalytic oxidation of organic dyes with nanostructured zinc

dioxide modified with silver metals. Russ. J. Phys. Chem. A 85, 1077–1083.

Zhanjiang, Z., Jinpei, L., 2012. Synthesis and characterization of silver nanoparticles by a sonochemical method. Rare Met. Mater. Eng. 41, 1700–1705.

Zheng, Y., Chen, C., Zhan, Y., Lin, X., Zheng, Q., Wei, K., Zhu, J., 2008. Photocatalytic activity of Ag/ZnO heterostructure nanocatalyst: Correlation between structure and property. J. Phys. Chem. C 112, 10773–10777.

Zhu, J., Liu, S., Palchik, O., Koltypin, Y., Gedanken, A., 2000. A novel sonochemical method for the preparation of nanophasic sulfides: Synthesis of HgS and PbS nanoparticles. J. Solid State Chem. 153, 342–348.

Zhu, L., Liu, K., Li, H., Sun, Y., Qiu, M., 2013. Solvothermal synthesis of mesoporous TiO_2 microspheres and their excellent photocatalytic performance under simulated sunlight irradiation. Solid State Sci. 20, 8–14.

Zielińska-Jurek, A., Kowalska, E., Sobczak, J.W., Lisowski, W., Ohtani, B., Zaleska, A., 2011. Preparation and characterization of monometallic (Au) and bimetallic (Ag/Au) modified-titania photocatalysts activated by visible light. Appl. Catal. B Environ. 101, 504–514.

Zuas, O., Hamim, N., Sampora, Y., 2014. Bio-synthesis of silver nanoparticles using water extract of *Myrmecodia pendan* (Sarang Semut plant). Mater. Lett. 123, 156–159.

Chapter 2

Materials and Methodology

This chapter details the experimental investigations, procedures, and the methods of analyses followed throughout the study. It includes the determination of physicochemical attributes of metal NPs and metal doped semiconductor materials such as structural morphology, size, and crystallinity along with antimicrobial, antifungal, photocatalytic, and photoelectrochemical activities. Specifications of all reagents and chemicals are documented in this chapter. Any specific change or deviation from what is stated here is detailed in the respective section(s) / chapter(s).

2.1 Materials and Reagents

Dipyrone drug (purity > 99% w/w) and Congo red (CR) dye purity (purity 90% w/w) were procured from Sigma Aldrich, Bangalore (India) and Merck, Mumbai (India). The chemical structure of CR dye and Dipyrone is illustrated in **Figure 2.1**. Other chemicals and reagents were procured mostly from Merck, Mumbai (India), Loba-Chemie, Mumbai (India), and Himedia (India). The chemical and reagent details are listed in **Table 2.1**.

P25-TiO_2 is consisting of 80% anatase and 20% rutile phases with 99.5% (w/w) purity (Sigma Aldrich, Bangalore, India). ZnO was purchased from Loba-Chemie, Mumbai (India). Bandgap energy, surface area, pore diameter, and pore volume of TiO_2 and ZnO are listed in **Table 2.2**.

Escherichia coli (*E. coli*) XL 10GOLD was collected from the Department of Biotechnology, Indian Institute of Technology Guwahati. Yeast (99% w/w purity) and tryptone (98% w/w purity) were obtained from Himedia (India). Deionized (DI) water (conductivity 0.055 µS cm^{-1}) of Millipore Filtration Unit (Elix-3, USA) was used to prepare all the reagents and solutions. All the plastic wares used were made of polypropylene procured from Tarson Products Pvt. Ltd., Kolkata (India). Glassware with a low coefficient of thermal expansion was mostly obtained from Borosil, Mumbai (India).

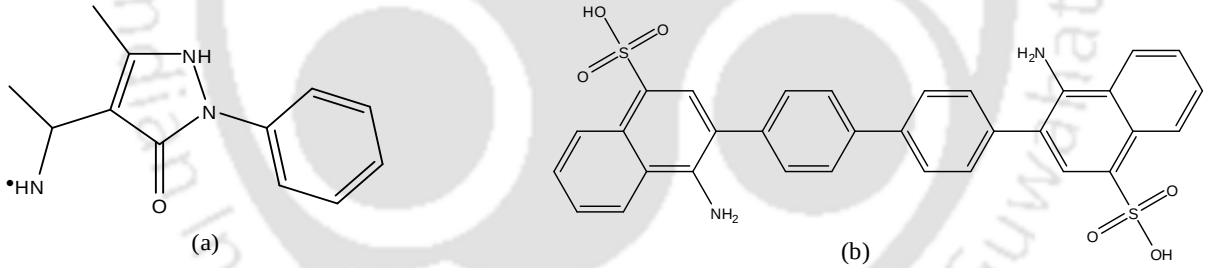

Figure 2.1. Chemical structure of (a) Dipyrone drug [(2,3-dihydro- 1,5-dimethyl- 3-oxo- 2-phenyl-1-pyrazol-4-yl) methyl amino] and (b) Congo red dye (3,3′-([1,1′-biphenyl]-4,4′-diyl)bis(4-aminonaphthalene-1-sulfonic acid).

Table 2.1. List of chemicals/reagents used to prepare model effluent and reagents/ solutions to carry out this work.

Reagents/chemicals	Purity (%)	Grade	CAS/ Catalogue no.	Make
Ethanol (C_2H_5OH)	99.9	AR	GB678-90	Changshu Yangyuan Chemicals (China)
Ampicillin sodium	99	AR	69-52-3	Hi-media (India)
Cefprozil ($C_{18}H_{19}N_3O_5S$)	99	AR	SD 209	

Ciprofloxacin ($C_{17}H_{18}FN_3O_3$)	98	AR	SD 060	
Streptomycin ($C_{21}H_{39}N_7O_{12}$)	99	AR	SD 031	
Tryptone	98	HPLC	ATTCC 25922	
Yeast	98	AR	ATCC 16404	
Acetonitrile (C_2H_3N)	99	AR	75-05-8	Loba-Chemie, Mumbai (India)
Congo red ($C_{32}H_{22}N_6Na_2O_6S_2$)	90	AR	573-58-0	
Isopropyl alcohol(C_3H_8O)	99.5	AR	67-63-0	
Zinc oxide (ZnO)	99	AR	1314-13-2	
Agar solution	99	AR	10-29-2	Merck (India)
Buffer solution pH 4.0 (phthalate)	99	AR	91-05-11	
Buffer solution pH 7.0 (phosphate)	99	AR	99-62-00	
Cobalt nitrate ($Co(NO_3)6H_2O$)	99	AR	10026-22-9	
Copper sulfate ($CuSO_4.5H_2O$)	99	AR	7758-98-7	
Ferroin solution ($C_{36}H_{24}FeN_6^{2+}$)	0.1	AR	14634-91-4	
Ferrous ammonium sulfate (FAS) ($Fe(NH_4)_2(SO_4)_2$)	98.5	AR	7783-85-9	
L(+)-Ascorbic acid ($C_6H_8O_6$)	99	ACS	50-81-7	
Methanol (CH_4OH)	99	AR	67-56-1	
Potassium bromide (KBr)	99.5	GR	03-02-7758	
Potassium dichromate ($K_2Cr_2O_7$)	99	AR	7778-50-9	
Silver sulfate (Ag_2SO_4)	99	AR	10294-26-5	
Sodium chloride (NaCl)	99.5	GR	7647-14-5	
Silver nitrate ($AgNO_3$)	99	AR	7761-88-8	
Sulphuric acid (H_2SO_4)	98	AR	7664-93-9	
Zinc nitrate ($ZnNO_3.6H_2O$)	99	AR	19154-63-3	
Chloroplatinic acid (H_2PtCl_6)	8	AR	16941-12-1	Sigma Aldrich (India)
Dipyrone ($C_{13}H_{17}N_3O_4S$)	98	HPLC	68-89-3	
Titanium dioxide (TiO_2)	99.5	AR	13463-67-7	
Bacillus subtilis (B. subtilis)	98	AR	5433	National Chemical Laboratory, Pune (India)
Escherichia coli (*E. coli*)	98	AR	5346	

Table 2.2. Surface area, pore diameter, and pore volume of TiO_2 and ZnO.

Catalyst type	TiO_2	ZnO
Bandgap	3.2	3.13
Surface area, $m^2 g^{-1}$	66.475	15.42
Pore diameter, nm	17.68	31.82
Pore volume, $cm^3 g^{-1}$	0.293945	0.0587

2.2 Selection of *Sechium Edule* and Fruit-extract Preparation

In this study, NPs were synthesized using the bio-extract prepared from the fruit of *Sechium edule* (or simply *S. edule*) (**Figure 2.2(a)**). It grows abundantly in the North Eastern part of India, and fruits are available in almost all seasons. *S. edule* is fleshy-fibrous and come in different sizes (3-11 cm wide and 4.3-26.5 cm long), colors (from dark or light green

to white to pale yellow), and shapes (elongated pyriform, pyriform, subovoid, ovoid, globose) (Cadena-Iñiguez et al., 2007). The surface of these fruits contains woody ridges and, the pulp is whitish pale or green and tastes sweet or insipid. The seed is ovoid, smooth, compressed, and germinates within the fruit. The composition of the *S. edule* is shown in **Table 2.3**.

This species was originally discovered by Browne (1756) in Jamaica (Browne, 1756) and in 1763 it was classified simultaneously as *Sicyos edulis* by Jacquin (Cadena-Iñiguez et al., 2007) and as *Chocho edulis* by Adanson (Cadena-Iñiguez et al., 2007). Later, Jacquin (1788) changed it to *C. edulis* and placed it in genus Chayota. A few years later, Swartz (1800) became the first to include this species in *Sechium*, when he proposed the combination by which it is still known, *Sechium edule* or *S. edule*.

The major producer countries are Mexico, Costa Rica, Brazil, and the Dominican Republic with 360, 170, 50, and 2.3 thousand tons per year. In Mexico, *S. edule* is in fourth place after avocado, tomato, and coffee as an export product (Cadena-Iñiguez et al., 2007).

In India, Mizoram has the largest production of *S. edule* mainly in Sihphir area being a cooler climate (8-32 ºC) and good annual rainfall (2500-3000 mm) (Singh et al., 2015). In Mizoram, the area of *S. edule* production is increased to 714 hectare (hec) in 2008 from 535 hectare in 2002 and, a typical production is in between 20 and 25 tons hec^{-1} in organic-rich soil. The production of *S. edule* in Assam (India) is about 20-22 tons hec^{-1} with a total production area of 110 hec in Assam, and the average production in India is about 10-15 tons hec^{-1} based on the total area for vegetable cultivation (Morton, 1981).

The fruit extracts exhibit strong reducing power and, it could convert potassium ferricyanide to potassium ferrocyanide of about 2000 ASE/mg which was used for the antioxidant activity test (Ordonez et al., 2006). ASE means that reducing power of 1 mg sample is equivalent (E) to reducing power of 1 nmol ascorbic acid (AS). The analytes present in the extract act as strong electron and hydrogen donors. It could break the radical chain reaction and convert the free radicals to stable products. In fact, this particular study provides the foundation for the selection of *S. edule* for the bio-mediated synthesis of Ag, Pt, and Co nanoparticles and bio-mediated TiO_2 and ZnO doping using metal dopants such as Ag, Cu, and Zn.

Table 2.3. *S. edule* plant details and chemical composition. Data are reported per 100 g of dry matter (Cadena-Iñiguez et al., 2007; Shiga et al., 2015).

Botanical name	*Sechium edule*
Family	Cucurbits

Genus	Sechium
Kingdom	Plant
Tribe	Sicyeae
Order	Cucurbitales
Species	*S. edule*

Composition	**Leaf**	**Fruit**	**Root**
Ascorbic acid, mg	16	29.8	19
Flavonoid content, g	35	19.3	30.5
Energy, cal	60	26-30	79
Protein, g	4	0.9-1.1	2
Carbohydrates, g	4.7	3.5-8.4	17.8
Phosphorus, µg	108	20-27	34
Calcium, mg	21.7-69.5	6.1-19	6.1-17.5
Nitrogen, g	0.49-0.778	0.95- 0.156	0.332
Thiamine, mg	0.043-0.0119	0.03-0.33	0.041-0.08
Roboflavin, mg	0.124-0.208	0.03-0.37	0.05-0.028
Niacin, mg	0.919-1.19	0.35-1.1	0.7-1.04

2.3 Preparation of Bio-extract

S. edule (**Figure 2.2(a)**) was purchased from the market located at Indian Institute of Technology Guwahati, India. The cleaned fruits were cut into small pieces (10 mm x 10 mm x 10 mm) and, the bio-extract was prepared by heating 1 g fruit pieces (**Figure 2.2(b)**) per 8 mL deionized water (DI water) for 12 h at 90±2 °C. The clear bio-extract was collected after the filtration using the nylon mesh followed by the membrane filter (0.45 µm, Pall membrane filter, India). The color of the bio-extract was slightly yellowish (**Figure 2.2(c)**) without a distinct spectral absorption peak, but it exhibited a broad absorption band between 200 and 250 nm (**Figure 2.3**). The fresh bio-extract was employed immediately for the AgNPs synthesis.

AA present in *Sechium edule* was first extracted in water and, after that AA concentration in the bio-extract was determined using high performance liquid chromatography (model: 26462, Shimadzu, Japan).

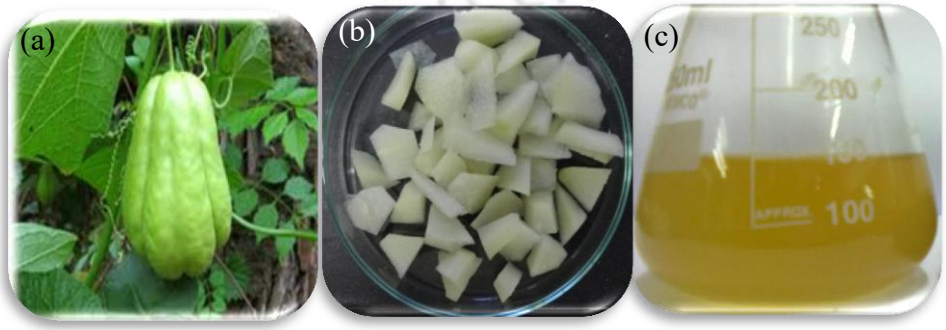

Figure 2.2. Pictorial view of fruits (a), fruit pieces (b) and aqueous bio-extract (c) of *S. edule*.

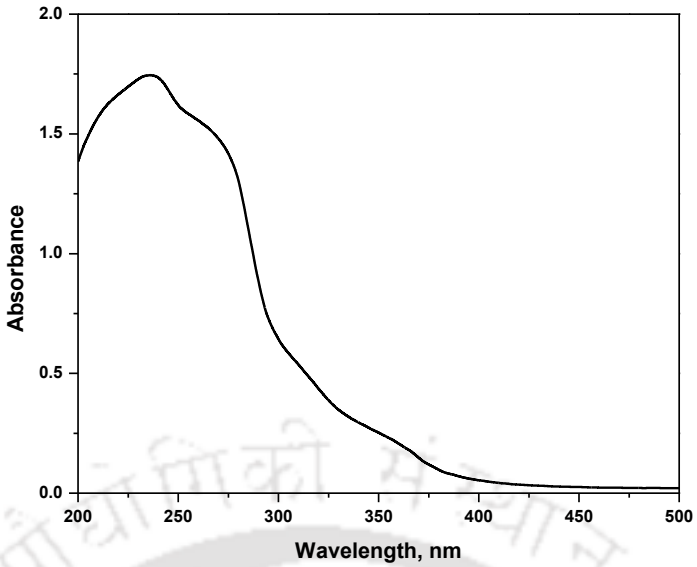

Figure 2.3. Spectral absorbance of *S. edule* fruit aqueous extract at natural pH of 5.8.

2.4 Analytical Techniques

2.4.1 High performance liquid chromatography (HPLC) for ascorbic acid (AA) and drug concentration determination

C18 HPLC column (150 mm length, Ø 3.5 mm) was used for the determination of concentration of drug and AA. The HPLC instrument (model: 26462, Shimadzu, Japan) equipped with a UV-visible detector was employed for the chromatographic measurement. AA concentration in the bio-extract was measured with a mobile phase consisting of acetic acid (0.05 %) and acetonitrile (80:20 v/v) with a flow rate of 1 mL min^{-1} and wavelength of 254 nm. The mobile phase used for dipyrone was methanol and water mixture (80:20 v/v) at the flow rate of 0.5 mL min^{-1} and wavelength of 254 nm (Giri and Golder, 2014). The suspended particle appeared, if any, were removed by filtration using 0.45 µm cellulose acetate filter (make: Pall India Pvt. Ltd., India; serial no. 08091ID0683). The calibration curve was obtained in the range of 17.6 to 176 mg L^{-1} for AA and 5 to 100 mg L^{-1} for dipyrone (**Figure 2.4)**. The fitted equations were found as Peak-area = 389315.2[AA] (R^2 = 0.99) and 67595.2[dipyrone] (R^2 = 0.99). The concentration of AA and dipyrone were determined from its calibration curve corresponding to the retention time of 2.9 and 8.82 min, respectively dipyrone (**Figure 2.5)**. AA was detected for the retention time of 2.82 min in the case *S. edule* extract. The experiments were usually conducted in triplicate, and the corresponding errors in the analytical results are shown in the graphs.

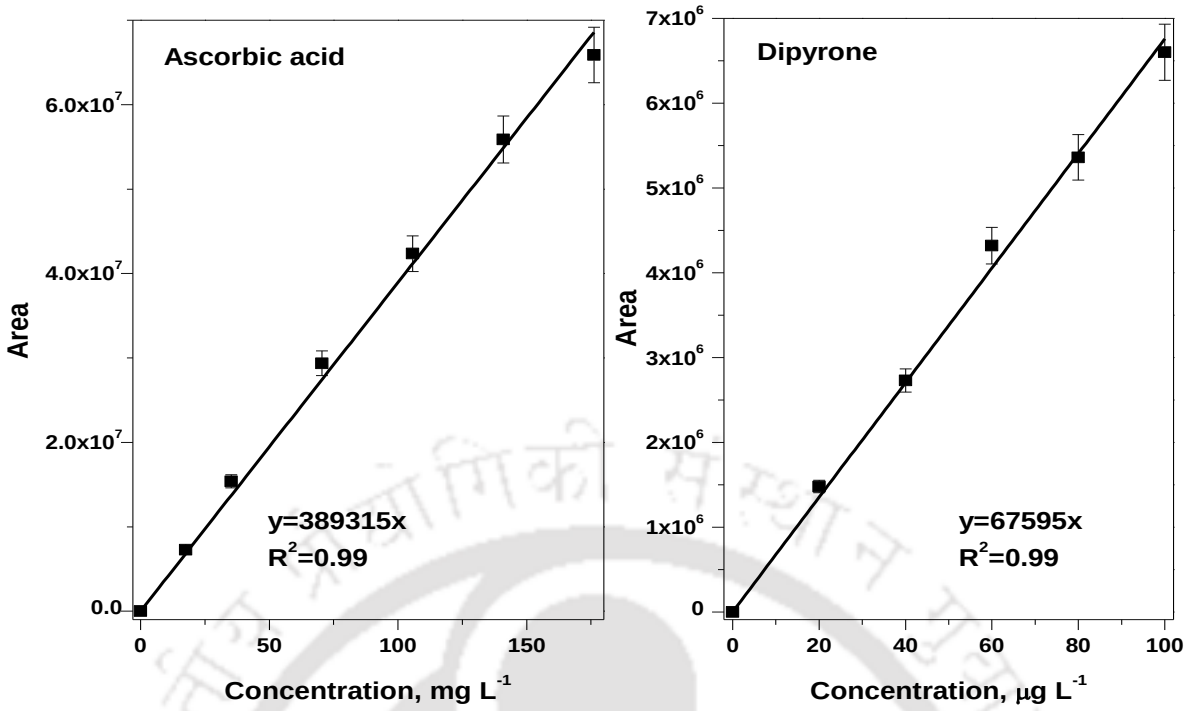

Figure 2.4. Calibration curves of AA and dipyrone drug obtained from HPLC.

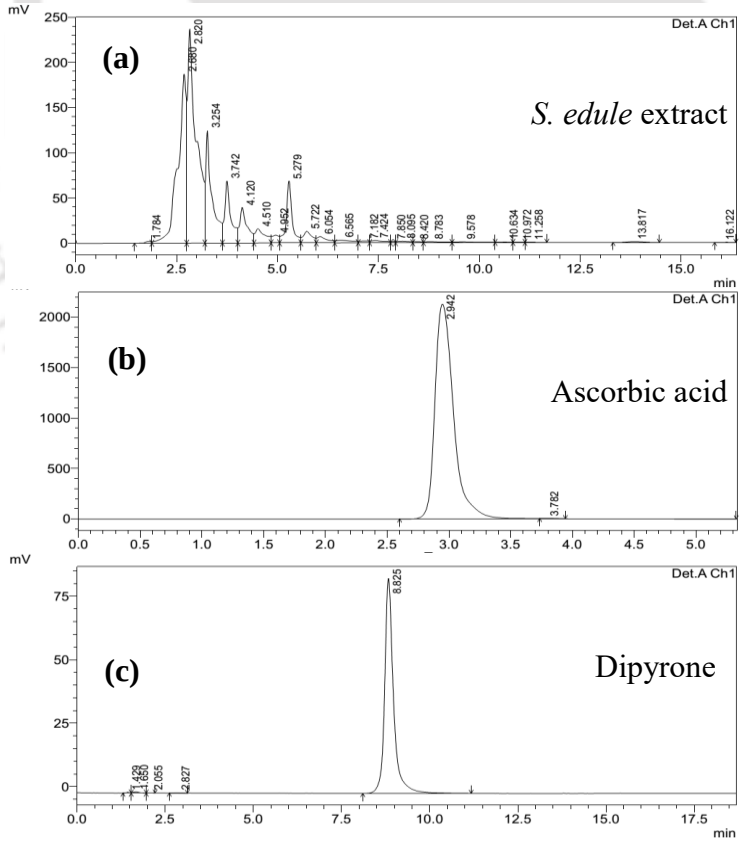

Figure 2.5. Representative HPLC chromatograms of (a) *S. edule* aqueous extract, (b) AA, and (c) dipyrone drug obtained from HPLC.

2.4.2 Determination of chemical oxygen demand (COD)

COD was determined according to the HACH method. A closed reflux digester of HACH (model: DRB 200, Hach, USA) was used for digestion. The digestion solution (0.25 N $K_2Cr_2O_7$) was prepared by dissolving 4.9 g $K_2Cr_2O_7$ in 500 mL DI water followed by the addition of 167 mL concentrated H_2SO_4 and 33.3 g $HgSO_4$. The final volume was adjusted to 1 L. $K_2Cr_2O_7$ was dried at 103 ^oC for 2 h prior to preparation of reagent. The acid reagent solution was made using 5.5 g Ag_2SO_4 per kg of concentrated sulphuric acid. It was kept for two days for the dissolution. Ferrous ammonium sulfate (FAS) of 0.25N was prepared by dissolving 39.2 g in 1 L of DI water with 20 mL of concentrated H_2SO_4 (APHA, 1998). A COD digestion vessel of 10 mL capacity was employed as the reaction chamber. A sample of 2.5 mL was added to 3 mL acid reagent followed by 1.5 mL of digestion solution. A second digestion vessel with the same quantity of these reagents and DI water instead of the sample was used as the blank. All the samples including blank were then kept in the COD digester at 150 ºC for 120 min. The digested samples were then cooled down to room temperature and titrated with standard FAS using Ferroin as an indicator. The end point of titration was identified with the change in color from bluish green to reddish brown. The volume of FAS consumed in titration was used for COD calculation using Eq. 2.1. The COD measurement method adopted was suitable for analysis in the range from 0 to 1500 mg L^{-1} COD.

$$\text{COD} = \frac{(a-b)\times N\times 800}{\text{sample volume}},\ \text{mgL}^{-1} \qquad (2.1)$$

Where,

a = volume of FAS used in blank run, mL

b= volume of FAS used in sample run, mL

N= normality of FAS titrant

Sample volume = actual volume of the sample used before dilution, mL

2.4.3 Liquid chromatography-mass spectrometry (LC-MS)

HPLC method outlined earlier was adopted for the subsequent bio-extract introduction to MS detector before and after NPs synthesis. The chromatographic separation was performed using a YMC Hydrosphere C18 150 mm×4.6 mm (5 µm particle size) reverse phase analytical column (Wilmington, NC, US) following a YMC Hydrosphere 10 mm×4 mm (5 µm particle size) guard column. The mobile phase flow rate was 0.8 mL min^{-1}. H_2O and acetonitrile with 0.1% (v/v) formic acid was employed as the mobile phase for all experiments. A linear gradient from 95 to 50 % water for 15 min was used. A 10 µL of both

sample and calibration solution were injected into the column using an AS 3000 auto injector (Thermo Finnigan, USA). The atmospheric pressure chemical ionization method in positive ion mode over the mass range of 50 to 500 amu was adopted. N_2 at a flow rate of 400 L h^{-1} for drying and 150 L h^{-1} for sheathing were purged. The source temperature at 120 °C and a cone voltage of 25 V were maintained to determine the mass (mass to charge ratio, m/z) of the parent ion and isotope. A cone voltage of 75 V was used for the fragmentation of daughter ions. The electrospray source voltage was held at 3.5 kV and, the temperature was maintained at 200 °C.

2.4.4 FTIR spectroscopic analysis

The presence of different functional groups of various compounds in the bio-extract as well as on the NPs and doped catalysts was confirmed by acquiring the FTIR spectra using KBr pellet method. KBr salt was dried in a hot air oven (model: N-101, Navyug, India) at 105 °C. KBr to the sample in the ratio of 99:1 (w/w) was ground in a clean mortar and pestle for homogenization. It was then transferred to the pellet casting die. The pressure of 5 to 7 tons was imposed to create a thin pellet. The background correction was done with pure KBr pellet by scanning from 450 to 4500 cm^{-1} with a resolution of 4 cm^{-1}. The number of scans was 40 for each specimen for noise reduction. For the liquid sample, a small drop of the bio-extract was added on KBr pellet film. An FTIR spectrophotometer (model: IR affinity 1, Shimadzu, Japan) was employed for this work.

2.4.5 UV-Vis spectroscopy

Congo red dye concentrations were determined by using a UV-Vis spectrophotometer (model: UV-2300, Thermo Scientific, India) with an optical path length of 1 cm. The concentration of Congo red dye was measured at 497 nm. A series of standard solution (0 to 10 mg L^{-1}) of dye was prepared for the calibration of the instrument. A linear relationship was found as Absorbance=0.0544[Congo red] (R^2=0.99) (**Figure 2.6**). The sample solution was appropriately diluted to analyze the dye concentration using this equation. The spectral absorbance of AgNPs solution/suspension owing to the surface plasmon resonance (SPR) effect was recorded using the same instrument. The optical absorption by the pigments present in the bio-extract was also recorded using this spectrophotometer.

Diffuse reflectance solid UV–vis spectrometer of Shimadzu (model: Solid Spec 3700/3700DUV, Shimadzu, Japan) was employed to acquire the spectral absorbance of doped and bare catalysts. The catalysts were scanned in the range from 200 to 800 nm.

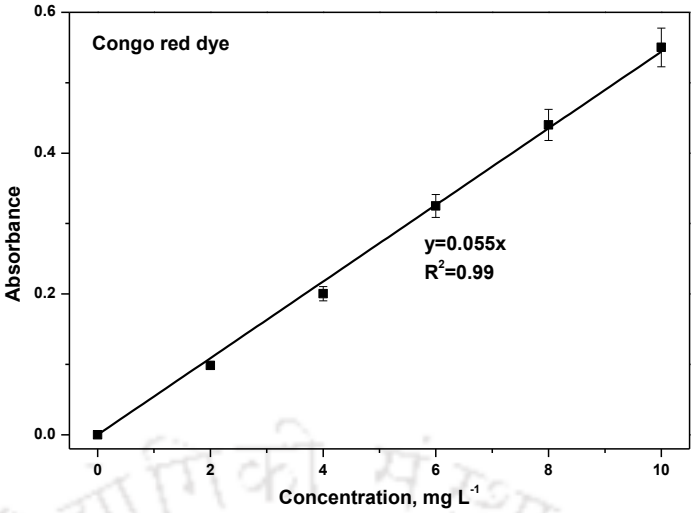

Figure 2.6. Calibration curve of Congo red dye.

2.4.6 Atomic absorption spectroscopy (AAS)

The concentration of metal ions like Ag^{+} Cu^{2+}, Zn^{2+}, Pt^{2+}, and Co^{2+} in solution during NPs synthesis and catalyst-doping were determined using AAS (model: AA240FS, Varian, USA). The calibration curve was obtained in the range of 1 to 10 mg L^{-1} for all metal ions separately, and calibration samples were prepared each time before the analysis. Air-acetylene gas at a flow rate of 400 L h^{-1} for drying and 150 L h^{-1} for sheathing were purged. The specific metal hollow cathode lamps were used during analysis.

2.4.7 BET surface area analyzer

The catalyst surface area was obtained using BET analyzer (model: SA 3100, Beckman Coulter, Switzerland). Before N_2 adsorption, an amount of 50 mg either bare or doped catalyst powders were degassed at 200 °C for 4 h. The parameters like pore size, pore volume, and Barrett, Joyner, Halenda (BJH) surface area, adsorption or desorption curve were obtained from BET analysis.

2.4.8 Electron spin resonance (ESR) spectroscopy

The photogenerated radicals on catalysts were identified using ESR spectrometer (model: JES-FA200, JEOL, USA) with 1 mW microwave power and 9.42 GHz frequency at room temperature. An amount of 20 mg NPs or catalyst powder was added into a Teflon tape and covered/folded it completely before the analysis. The g-values were recorded in the magnetic field range between 100 and 600 mT for all samples which may vary for different radicals.

2.4.9 Electron microscopic analyses

The size and surface morphology of metal NPs and catalyst particles were obtained using transmission electron microscopy (TEM) (model: JEM 2100, JEOL, Japan). A quantity of 50 mg specimen particles were dispersed in 25 mL acetone and, the suspension was then placed in the ultrasonic bath for about 30 min to segregate individual particles. One drop suspension was deposited onto the carbon-coated copper grid, and the film on the TEM grid was left for 2 min. The grid was allowed to dry in the hot air oven for about 1 h at 60 °C. High resolution TEM (HRTEM), and selected area diffraction pattern (SAED) were also measured to find out the interplanor spacing and crystal planes with the same instrument.

The same sample preparation procedure was also adopted for field emission scanning electron microscopy (FESEM) using a glass slide instead of a copper grid (model: Sigma, Zeiss, Germany). Energy-dispersive X-ray (EDX) spectroscopy equipped with FESEM was employed for the surface elemental analyses.

The surface topography of AgNPs and doped catalysts were obtained by atomic force microscope (AFM) (model: 5500 series, Agilent, USA) using 20 nm Si probe cantilever with 209-286 kHz resonance frequency. The sample was prepared following the same procedure as mentioned for TEM analysis. One drop of suspension was added to a glass slide and allowed to dry for 30 min at 60 ˚C. Both 2D and 3D micrographs were recorded in the area of 10 x 10 to 1 x 1 µm range.

2.4.10 Temperature programmed reduction (TPR)

TPR analysis was carried out by the chemisorption technique (model: I2720, Micromeritics, Germany). A sample of 50 mg was placed in a quartz tube, and the temperature was increased to 950 °C starting from 30 °C at 10 °C min^{-1} heating rate with 30 mL min^{-1} of H_2 and He mixture (1.75: 98.25 %). A thermal conductivity detector was used to record the hydrogen consumption. The analyses were carried out in the temperature range of 30 to 950 °C.

2.4.11 Thermal gravimetric analyses (TGA)

The mass losses of metal NPs and metal doped TiO_2 or ZnO particles with the temperature were studied by thermal gravimetric analyses (model: TG 209 F1 Libra, NETZSCH, Germany) under nitrogen gas at a heating rate of 10 °C min^{-1}. An amount of 10 mg sample was used to analyses in the temperature range of 30 to 950 °C.

2.4.12 X-ray diffraction

The crystallinity of the synthesized metal NPs and metal doped semiconductor photocatalysts were studied by employing an X-ray diffractometer (model: D8 Advance, Bruker, Germany) with λ = 0.15406 nm of CuKα radiation at 5° per min scan rate. An amount of 20 mg dried sample was placed into the holder and, the XRD patterns were recorded between 20 and 80° 2θ angle.

2.4.13 Zeta potential and particle size measurements

The hydrodynamic particle diameter and zeta-potential were obtained by the dynamic light scattering (DLS) and electrophoretic light scattering (ELS) methods (model: Delsa Nano-C, Beckman Coulter, Switzerland). An amount of 0.2 g catalyst powder was dispersed in 100 mL DI water and then placed in the ultrasonic bath for 20 min at different pH (3-10). The suspended particles were filtrated using 0.2 µm membrane syringe filter (Part no.: C-129M, Axiva Sichem Biotech, India), and the final sample pH was measured (pH/ion 510, Eutech Instruments, Malaysia) before zeta potential measurement. After that, the particle size distribution with average size, poly dispersity index, and zeta potential values were recorded.

2.4.14 Photoelectrochemical (PEC) measurements

The PEC measurements were carried out with a three-electrode system in a single cell. The ZnO and ZnO/Ag nanoparticles deposited on indium tin oxide (ITO)-coated conductive glass substrate (25 x 25 x 1.1 mm, Sigma-Aldrich, India) was used as the working electrode. The electrocatalyst of 7.5 mg was dispersed in 200 µl of nafion+IPA (1:5) mixture as the binder followed by 30 min sonication. The suspension was coated on the glass slide (~2 mg cm^{-2}) and dried at 80 ºC. The working electrode's total effective area was 5 cm^2. Pt wire and Ag/AgCl were employed as the counter and reference electrodes. Na_2SO_4 solution of 0.5 M was used as the electrolyte and, N_2 gas at 1.2 LPM was purged for 30 min before the electrolysis (Patil et al., 2016). A visible lamp (λ_m (mean)= 525 nm, 18 K lux; Bajaj, India) was used as the light source and, the photocurrent was measured using a potentiostat (AUTOLAB 302N, Metrohm Autolab B.V, Netherlands. λ_m was determined by spectrofluorometry (Fluoromax-4C-L, HORIBA Instruments Inc., New Jersey, USA) as shown in **Figure 2.7**. The same light source was used for photocatalytic studies.

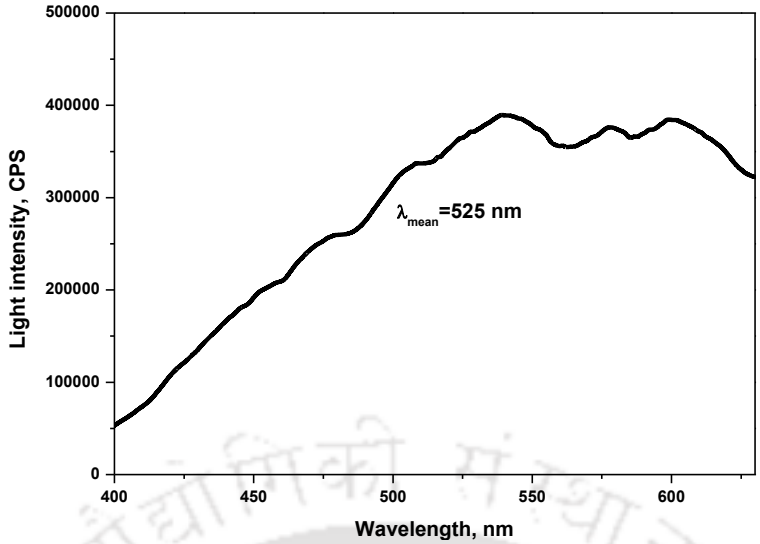

Figure 2.7. Light spectrum recorded by a spectrofluorometer (using a 200 W light with 18000 lux intensity).

2.4.15 Antimicrobial activity test

The biosynthesized AgNPs were tested for antibacterial activity against both Gram-positive and Gram-negative bacteria, i.e., using *B. subtilis* and *E. coli*, respectively, by disc diffusion method and compared with the antibiotic (Streptomycin-S10 and Ampicillin) control media. The antibiotic control media with 30 mg mL^{-1} concentration was prepared by dissolving a suitable amount in 100 mL DI water (Singh et al., 2014). The stock solution of the Luria–Bertani (LB) media was made with the composition of NaCl (10 g L^{-1}), tryptone (10 g L^{-1}) and yeast extract (5 g L^{-1}). A 20 mL LB media in a borosilicate glass tube was sterilized by autoclaving (model: NSW- 229, Narang Scientific Works, India) for 20 min at 120 ^{o}C and 15 kg cm^{-2} pressure. The bacteria culture was transferred into the sterile LB media and incubated in an orbital shaker (model: LSI- 3016R, Labtech, India) with swirling at 160 rpm at 37 ºC for 24 h (Sondi and Salopek-Sondi, 2004). On the other hand, the LB media with agar agar (1.5%, w/v) was spread on the sterilized petri dishes and left it for 15 min for solidifying. After that 4 mL, bacterial culture was soaked into the solidified media surface. The sterile discs (10 mm, Himedia, India) were soaked in S 10 and Amp control media, bio-extract and AgNPs suspension (20 mg mL^{-1}) and, placed over the bacteria infused media surface. Finally, the petri dishes were incubated at 37 ºC for 24 h. The same procedure was applied in the antimicrobial activity test of mono and bimetallic core-shell Co and Pt NPs using cefprozil and ciprofloxacin as the antibiotic control media.

The growth kinetics of *B. subtilis* and, *E. coli*, were also studied at various concentrations of AgNPs (2-50 μg mL^{-1}) using an optical density technique (Sathishkumar et

al., 2009). The test included a control consisting of a 20 mL nutrient LB media and bacterial strains without AgNPs and with AgNPs. The test samples were incubated at 37 ºC with an agitation speed of 160 rpm. All the tests were conducted in triplicate. The growth kinetics were evaluated by recording the change in the optical absorbance at 600 nm (Agnihotri et al., 2014).

2.4.16 Antifungal assay

The antifungal activity of synthesized AgNPs was also carried out by the disc diffusion method (Liu et al., 2002). Potato dextrose broth (2.4 g) and agar (2 g) are dissolved in 100 mL DI water and autoclaved at 120 ºC and 15 kg cm^{-2} pressure for 20 min. It was solidified in 15 min under UV light illumination (30 W, Philips, India) in a biosafety laminar hood. A 100 mL of microbial suspension of *A. thermomutans* was spread and the sterile discs (6 mm) soaked in control media (DI water), and AgNPs (20 mg mL^{-1}) suspension were placed in the middle of it. It was point inoculated in the above medium and incubated at 37 ºC for 72 h. Afterward, the images were captured to determine the area of the inhibition zone.

The details of various instruments used in different parts of this work are summarized in **Table 2.4**.

Table 2.4. Instrumental details for analysis of water quality parameters, NPs and catalyst characterizations and experimental work.

Instrument	Model and make	Purpose	Detection/ working/performance range
Atomic absorption spectrometer	Model: AA240FS Make: Varian, USA	Metal ion concentration determination	Concentration: 1- 100 mg L^{-1}
Atomic force microscopy	Model: 5500 series Make: Agilent, USA	Surface topography	Scanning area: 70 – 100 µm
Analytical balance	Model: BSA 224S-W Make: Sartorius, India	Weight measurement	0 to 220 g Resolution: 0.1 mg
BET surface area analyzer	Model: SA 3100 Make: Beckman Coulter, Switzerland	Surface area determination	Surface area: 0 to 5000 m^2 g^{-1}
Centrifuge	Model: PR23 Make: Remi, India	Sludge separation	Maximum speed: 8000 rpm
COD digester	Model: DRB 200 Make: HACH, USA	Chemically oxygen demand determination	0-1500 mg L^{-1}
DRS UV–vis Spectrometer	Model: Solid Spec 3700/3700DUV Make: Shimadzu, Japan	Absorbance measurement	Wavelength: 190-1100 nm Resolution: 0.05 nm

ESR spectrometer	Model: JES-FA200 Make: JEOL, USA	Free radical analysis	100 to 600 mT
Field emission scanning electron microscopy	Model: Sigma Make: Zeiss, Germany	size and surface morphology	
FTIR spectrometer	Model: IR affinity 1 Make: Shimadzu, Japan	Functional group characterization	Frequency: 350 to 7500 cm^{-1}
Hot air oven	Model: ISO 9001-2008 Make: Navyug, India	Moisture removal	Temperature: 30 to 250 °C
HPLC instrument	Model: LC-20AD Make: Shimadzu, Japan	Concentration determination	0.01 to 1 µg mL^{-1}
Liquid chromatography mass spectrometer	Model: YMC Make: Wilmington, USA	Mass analysis	50-1000, m/z
Magnetic stirrer	Model: Spinot 6020 Make: Tarson, India	Mixing/agitation	Stirrer speed: 100 to 1000 rpm
Micropipette	Model: T100 & T1000 Make: Tarsons products Pvt Ltd., India	µL range liquid dispensing for analytical work	Capacity T100:10 to 100 µL T1000:100 to 1000 µL
Microwave oven	Model: MH-2046HB Make: LG Electronics, India	Microwave assisted drying of glasswere	Frequency: 2450 MHz (fixed) Microwave: 800 W (fixed)
Millipore water purification unit	Model: Elix 3 Make: Millipore, USA	Preparation of all reagent and test solutions	TOC: <30 µg L^{-1} Pyrogens (endotoxins):<0.001 EU mL^{-1} Water resistivity (@ 25 °C): >5 MΩ cm
Orbital shaker	Model: LSI-3016R Make: Lab Tech, Korea	Agitation	Maximum speed: 350 rpm Temperature: ± 0.5 °C
Particle size analyzer	Model: Delsa Nano-C, Make:BeckmanCoulter, Switzerland	Particle size and zeta potential determination	Zeta potential: –100 to + 100 mV Size: 0.6 nm to 30 µm
pH meter	Model: pH 510 Make: Eutech Instruments, Singapore	pH measurement	pH: 0 to 14 Resolution: 0.01 pH
Temperature program reduction	Model: I2720 Make: Micrometrics, Germany	Reducibility of catalyst	Temperature: 0 to 1500 °C
Thermal gravimetric analyses	Model: TG 209 F1 Libra Make: NETZSCH, Germany	Mass loss determination	Temperature: 30 to 1100 °C
Transmission electron microscopy	Model: JEM 2100 Make: JEOL, Japan	Size and surface morphology	Size: 0.6 nm to 250 µm
Ultrasonic bath	Model: Lab Companion UC-02 Make: Jeiotech, Korea	Mixing	Frequency (sound wave): 40 kHz (fixed) Ultrasonic power: 70 W
UV-vis spectrophotometer	Model: UV-2300 Make: Thermofisher Scientific, India	Absorbance measurement	Wavelength: 190-1100 nm Resolution: 0.05 nm

X-ray diffraction	Model: D8 Advance Make: Bruker, Germany	Crystal structure determination	$2\theta = 2$ to 100 °

2.5 Experimental Procedure

2.5.1 Metal NPs synthesis procedure

AgNPs biosynthesis experiment was first carried out at room temperature. The equal volume (30 mL each) of both bio-extract (pH 5.8) and 1 mM $AgNO_3$ solution were mixed under constant stirring (model: Spinot, Tarsons, India) at 320 rpm. The mixture reached an initial pH of 5.8. The proportionate of $AgNO_3$ and bio-extract was selected to achieve almost complete Ag^+ conversion to AgNPs. The reaction was continued for 72 h in the dark. The intermediate sample volume of 5 mL was collected to monitor the progress of the reaction by recording the absorbance using UV-vis spectrophotometer (model: UV2300, Fisher Scientific Pvt. Ltd., India). It was then centrifuged at 4000 rpm for 20 min (model: PR23, Remi instruments Ltd., India). The supernatant was analyzed for residual Ag^+ ions concentration and pH. The precipitate was washed with DI water followed by ethanol for the removal of bio-residuals and, dried at 90±5 ºC in a hot-air oven for 12 h (model: N-101, Navyug, India). The dry powder was ground in a mortar and pestle for the subsequent analyses. Dried particles, termed as AgNPs, were kept in an air tight container and used for subsequent analyses and tests.

The particles after the ethanol wash were also re-dispersed by sonication for 20 min (model: UC-02, Jeio Tech, Korea) in DI water for the determination of hydrodynamic diameter using the dynamic light scattering (DLS) technique.

The suitable concentration of $AgNO_3$ and water to bio-extract ratio for the synthesis of AgNPs were selected by varying these parameters from 0.1 to 2 mM and 1: 50 to 1:5 (v/v), respectively. In the case of AgNPs synthesis at different pH, the mixture pH (bio-extract + 1 mM $AgNO_3$ as in the above paragraph) was brought between pH 1 and 12.5 using 0.1 M H_2SO_4 or NaOH at the beginning of the reaction and, the reaction time was reduced to 24 h.

A similar procedure was adopted for the synthesis of Pt and Co mono and bimetal NPs synthesis with 1 mM of each Co^{2+} and Pt^{2+} concentration at pH 9 for 24 h (**Figure 2.8**). In the case of bimetal core-shell NPs (PtCoNPs), the molar concentration of precursors (Pt^{2+}:Co^{2+}) was varied as 1:3, 1:1, and 3:1 with a total metal concentration (Pt^{2+}+ Co^{2+}) of 1 mM. The ratio of bio-extract and metal concentration optimized for AgNPs was also adopted for the Pt^{2+} and Co^{2+} system.

The control experiment using commercial AA was carried out for the synthesis of AgNPs with 0.6 mM AA concentration (Ag^+:AA:: 1:0.6 w/w) and 3 mM sodium citrate as a capping agent at room temperature and 300 rpm with a reaction volume of 200 mL, and the reaction was conducted for 10 min. The resulting particles were collected by centrifugation at 4000 rpm for 20 min.

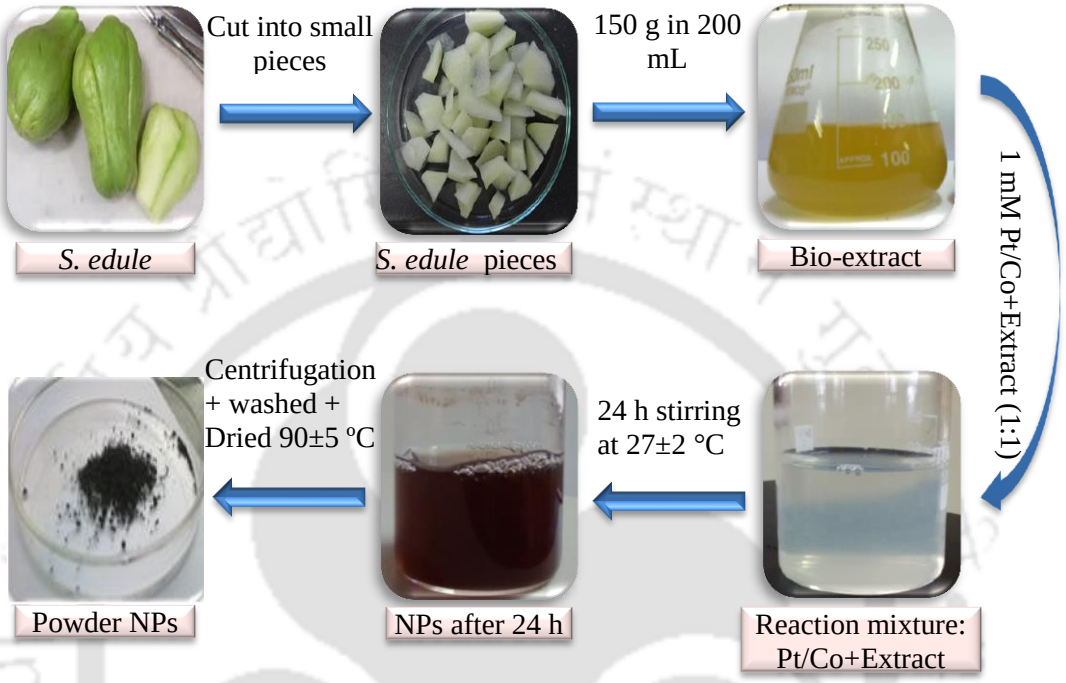

Figure 2.8. Schematically experimental steps of NPs synthesis.

2.5.2 Bio-mediated doping method

An amount of 2 g of semiconductor supports, i.e., TiO_2 or ZnO powder was dispersed in 200 mL of $AgNO_3$ solution (ethanol: water = 1: 99 v/v) corresponding to Ag-concentration from 0.25 to 2 g per 100 g catalyst, and adjusted the solution pH (3 to 11) using 0.1 N H_2SO_4 or NaOH. Ethanol acts as e^- donor to react irreversibly with h^+ leading to the suppression of e^- and h^+ recombination (Chowdhury et al., 2012). The obtained dispersion was stirred for 60 min to equilibrate Ag^+ adsorption onto TiO_2 or ZnO. It was then centrifuged at 4500 rpm for 20 min, and the clear solution obtained was separated for the residual Ag^+ concentration determination. Ag^+/TiO_2 or Ag^+/ZnO residue was collected and rinsed with DI water to remove loosely or un-adsorbed Ag^+ ions. The true Ag-loading onto the surface of TiO_2 or ZnO was determined from the concentration of un-adsorbed Ag^+ in the discards. Thus formed residue was again dispersed in 180 mL DI water, and a 20 mL *Sechium edule* extract was added under a continuous stirring at 320 rpm on a magnetic stirrer (stirring bar: ϕ 0.8 mm and length 40 mm) of Tarsons (Spinnot, India). The stirring was continued for 24 h to achieve the

complete reduction of Ag^+. The reaction time was determined by the highest concentration of Ag^+ used in bio-mediated doping, however, without TiO_2 or ZnO. It was found that the conversion of Ag^+ to AgNPs was complete in 24 h **(Section 2.5.1)**. In fact, the color of the reaction mixture was turned from milky white to light brown even within 3 h of reaction, which was indicative to the conversion of Ag^+ ions to AgNPs on the semiconductor surface. The resulting brown colored Ag-doped semiconductor was collected by filtration using 0.45-micron filter paper (Pall membrane filter, India) and rinsed 4 times with ethanol followed by DI water to eliminate the bio-residuals. Ag/TiO_2 or Ag/ZnO were then dried at 100 ºC in a hot-air oven (N-101, Navyug, India) for 12 h and ground in a mortar and pestle. The functionalization of metal doped titania photocatalyst at different stages showed in **Figure 2.9.** The synthesized particles were stored in an airtight container in the dark before the characterizations and catalyst activity test.

A similar procedure was employed for Cu/TiO_2 (2:98 % w/w), Zn/TiO_2 (2:98 % w/w) as well as bimetal doped $Cu/Zn/TiO_2$ (1:1:98 % w/w) systems.

The reduction potential and abundance of both reducing and capping agents present in the same biological entity is significantly affected by the geographical location, and cultivation and conditions. So, the quality assurance (QA) and quality control (QC) studies were performed using the *S. edule* of similar maturity from the same geographical location through the calculation of error bars. The triplicated experimental results are provided in the corresponding chapters. The triplicated analytical results for the experiment are also included.

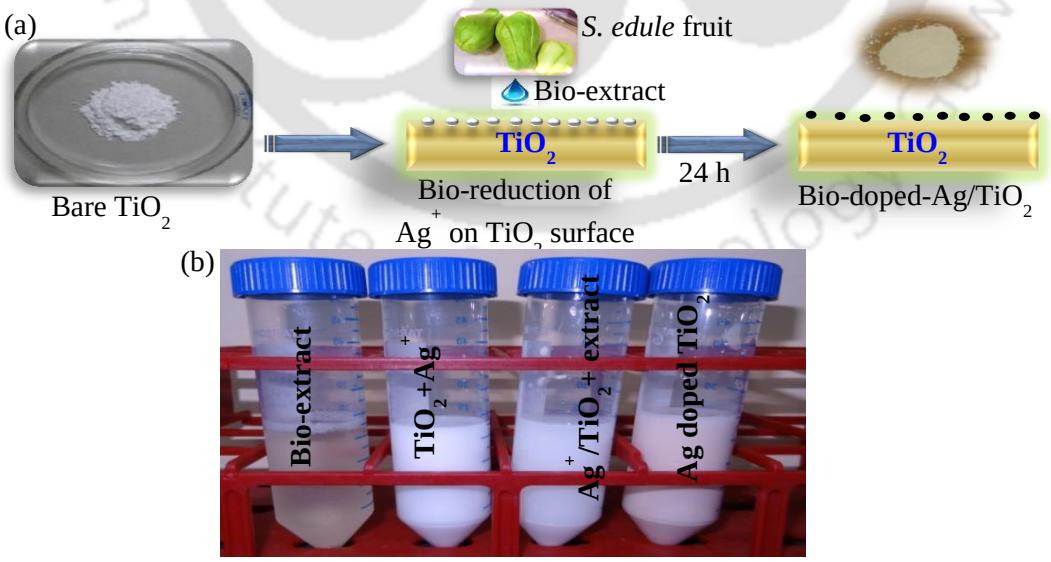

Figure 2.9. (a) Schematic steps showing functionalization of metal doped TiO_2 photocatalyst using Ag-dopant. (b) The pictorial view of bio-extract and reaction mixture.

2.5.3 Photocatalytic activity test using bio-mediated doped catalysts

The photocatalytic activity of Ag/TiO_2 was tested for the Congo red dye degradation in a 200 mL cylindrical borosilicate glass vessel at room temperature (25±2ºC) and normal pH of 5.8 using a 200 W (Bajaj, India) visible lamp which was equipped 20 cm above the reactor (Riaz et al., 2013). An amount of 0.1 g L^{-1} Ag/TiO_2 or bare TiO_2 catalyst was dispersed in 100 mg L^{-1} CR dye solution in the ultrasonic bath (UC-02, Jeiotech Instruments, Korea) for 15 min, and then the stirring (320 rpm) was continued for another 45 min in the dark without sonication to equilibrate dye adsorption. The dye concentration determined (8 % maximum adsorption) just before the initiation of photocatalytic reaction was used to calculate the dye degradation efficiency. After that, the initial concentration of dye just before the photoreaction was determined. 5 mL sample was taken out to find out the initial concentration of dye before the illumination of the light. At every 15 min for a total reaction time of 120 min, 5 mL sample was collected and filtered (0.45 µm syringe filter, Axiva, India) to eliminate the catalyst particles before the record of the absorbance.

Cu and Zn (Cu/TiO_2, Zn/TiO_2) mono, and bimetal doped TiO_2 ($Cu/Zn/TiO_2$) also followed the similar procedure and experimental conditions including Congo red dye and catalyst concentrations of 0.1 g L^{-1} at pH 7.

In the case of Ag/ZnO, the degradation of dipyrone drug was carried out with 100 µg L^{-1} and 0.1 g L^{-1} drug and Ag/ZnO concentrations at pH 6.8. Ag/ZnO catalyst was separated out after the experiment by centrifugation at 4000 rpm for 3 min. It was then washed with 3×15 mL DI water followed by ethanol. There was about dye 8 % adsorption in dark before the initiation of photocatalytic reaction. The catalyst was reused till the fourth cycle following the same procedure using Ag/ZnO with 1.18% (w/w) dopant.

2.5.4 Experimental data plotting and representation

All the graphs of the experimental results are plotted by the squared distance minimization (SDM) method which is commonly known as the *B-spline* curves readily comes with Origin Lab software. SDM is assigned to the skeleton with the minimal distance if a data point is visited by multiple skeletons (Bo et al., 2016).

References

Agnihotri, S., Mukherji, S., Mukherji, S., 2014. Size-controlled silver nanoparticles synthesized over the range 5–100 nm using the same protocol and their antibacterial efficacy. RSC Adv. 4, 3974–3983.

Bo, P., Luo, G., Wang, K., 2016. A graph-based method for fitting planar B-spline curves with intersections. J. Comput. Des. Eng. 3, 14–23.

Browne, P., 1756. Civil and natural history of Jamaica. London, England.

Cadena-Iñiguez, J., Arévalo-Galarza, L., Avendaño-Arrazate, C.H., Soto-Hernández, M., Ruiz-Posadas, L. del M., Santiago-Osorio, E., Acosta-Ramos, M., Cisneros-Solano, V.M., Aguirre-Medina, J.F., Ochoa-Martínez, D., 2007. Production, genetics, postharvest management and pharmacological characteristics of *Sechium edule* (Jacq.) Sw. Fresh Prod. 1, 41–53.

Chowdhury, P., Moreira, J., Gomaa, H., Ray, A.K., 2012. Visible-solar-light-driven photocatalytic degradation of phenol with dye-sensitized TiO_2: Parametric and kinetic study. Ind. Eng. Chem. Res. 51, 4523–4532.

Giri, A.S., Golder, A.K., 2014. Fenton, photo-Fenton, H_2O_2 photolysis, and TiO_2 photocatalysis for dipyrone oxidation: Drug removal, mineralization, biodegradability, and degradation mechanism. Ind. Eng. Chem. Res. 53, 1351–1358.

Liu, Y., Tortora, G., Ryan, M.E., Lee, H.M., Golub, L.M., 2002. Potato dextrose agar antifungal susceptibility testing for yeasts and molds: Evaluation of phosphate effect on antifungal activity of CMT-3. Antimicrob. Agents Chemother. 46, 1455–1461.

Morton, J.F., 1981. The chayote, A perennial, climbing, subtropical vegetable. Proc. Florida State Hortic. Soc. 94, 240–245.

Ordonez, A.A.L., Gomez, J.D., Vattuone, M.A., Isla, M.I., 2006. Antioxidant activities of *Sechium edule* (Jacq.) Swartz extracts. Food Chem. 97, 452–458.

Patil, S.S., Tamboli, M.S., Patil, D.R., Kulkarni, M. V, Yoon, H., Kim, H., Al-deyab, S.S., Yoon, S.S., Kolekar, S.S., Kale, B.B., 2016. Green approach for hierarchical nanostructured Ag-ZnO and their photocatalytic performance under sunlight. Catal. Today 260, 126–134.

Riaz, N., Chong, F.K., Man, Z.B., Khan, M.S., Dutta, B.K., 2013. Photodegradation of Orange II under visible light using Cu−Ni/TiO_2 : Influence of Cu:Ni mass composition, preparation, and calcination temperature. Ind. Eng. Chem. Res. 52, 4491–4503.

Sathishkumar, M., Sneha, K., Won, S.W., Cho, C.-W., Kim, S., Yun, Y.-S., 2009. Cinnamon zeylanicum bark extract and powder mediated green synthesis of nano-crystalline silver particles and its bactericidal activity. Colloids Surfaces B Biointerfaces 73, 332–338.

Shiga, T.M., Peroni-Okita, F.H.G., Carpita, N.C., Lajolo, F.M., Cordenunsi, B.R., 2015. Polysaccharide composition of raw and cooked chayote (Sechium edule Sw.) fruits and tuberous roots. Carbohydr. Polym. 130, 155–165.

Singh, B.K., Ramakrishna, Y., Verma, V.K., 2015. Chow-chow (*Sechium edule*): Best alternative to shifting cultivation in Mizoram. Indian J. Hill Farming 28, 158–161.

Singh, K., Panghal, M., Kadyan, S., Chaudhary, U., Yadav, J.P., 2014. Antibacterial activity of synthesized silver nanoparticles from Tinospora cordifolia against multi drug resistant strains of Pseudomonas aeruginosa isolated from burn patients. J. Nanomed. Nanotechnol. 05, 1–6.

Sondi, I., Salopek-Sondi, B., 2004. Silver nanoparticles as antimicrobial agent: a case study on *E. coli* as a model for Gram-negative bacteria. J. Colloid Interface Sci. 275, 177–182.

Chapter 3

Bio-Mediated AgNPs Synthesis: Physiochemical Attributes, Formation Mechanism and Antimicrobial Functionalities

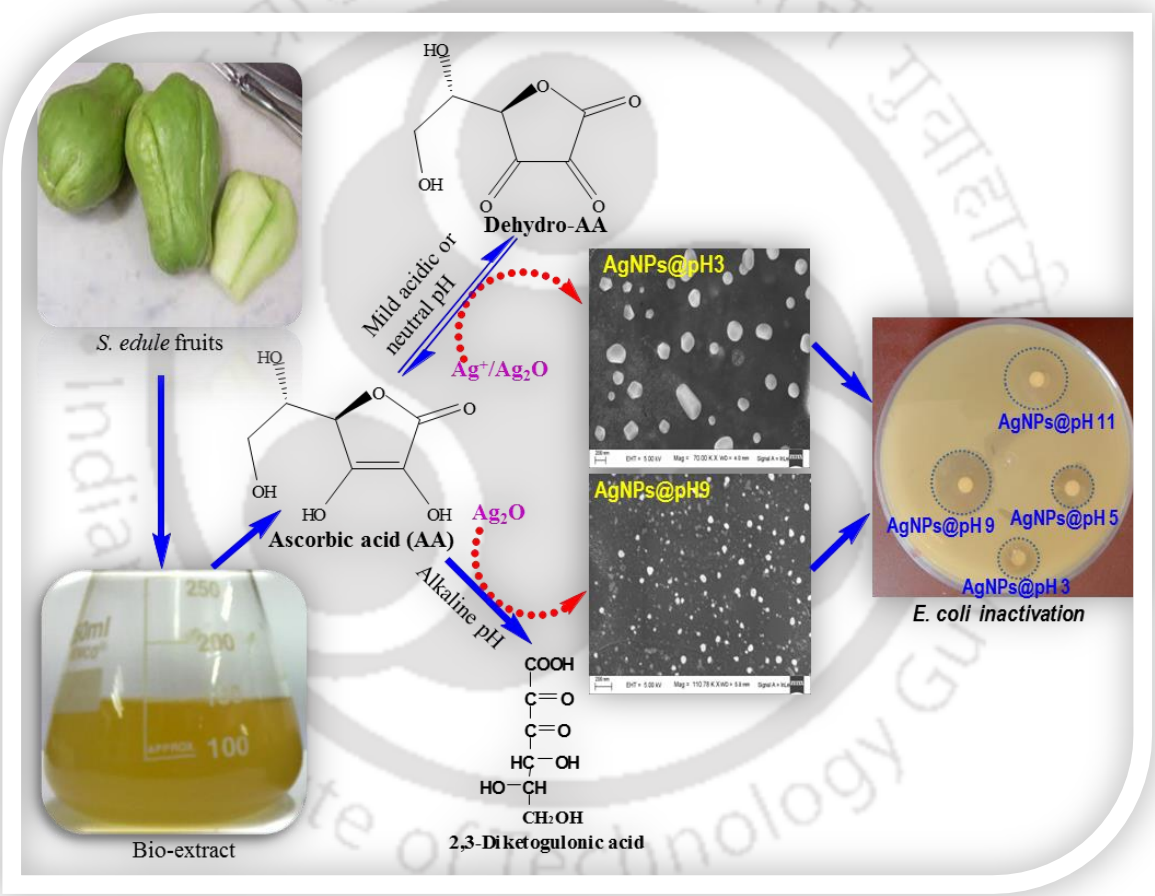

This chapter comprises of two parts. In the first part, the potential of AgNPs synthesis at the natural (pH 5.8) of aqueous bio-extract of S. edule was studied. In the second part, AgNPs was synthesized with the variation of pH of the bio-extract. It primarily covers the effect of pH on size control, particles purity, and mechanism of AgNPs formation. The antibacterial and antifungal activities of AgNPs were also tested following a typical protocol.

3.1 Specific Background

Recently, various research initiatives have been taken up to investigate on bioreduction of noble metal ions like Ag, Au, Pd, and Pt into metal nanoparticles. It primarily involves exploration of reduction efficiency of bioactive compounds present in renewable and natural materials like microbes (Sadowski et al., 2008), algae (Castro et al., 2013), fungi (Gajbhiye et al., 2009), and plant and plant-based extracts (Ahmed et al., 2016). The reducing agents believed to be mostly are water soluble metabolites such as phenolic compounds, terpenoids, reducing sugars, enzymes, flavonoids, and proteins (Sun et al., 2014). Moreover, the bio-mediated processes could produce nanoparticles (NPs) of precise size and shape almost without contamination (Mittal et al., 2013). The natural capping agents hinder the aggregation of particles leading to size improvement and morphological control (Agnihotri et al., 2014). Very recently, it is reported that carboxylate ions and quinone compounds present in *Prunus domestica* (Dauthal and Mukhopadhyay, 2012) and *Delonix regia* (Dauthal and Mukhopadhyay, 2013) extracts stabilize PdNPs and AuNPs during its formation. However, the nature of reducing agents as well as the mechanism of reduction is not well studied (Mittal et al., 2013) and also the availability of reducing agents differs from species to species. In fact, most of the studies have focused on the biosynthesis of AgNPs because of its potential application in biomedicine, cosmetics, water purification, agriculture, and semiconductor photocatalysis.

As discussed in Chapter 1, Section 1.10, *S. edule* fruit extracts exhibit strong reducing power and act as strong electron and hydrogen donors. The existing studies of *S. edule* plant extract for certainly open up the potential of *S. edule* extract for biosynthesis of metal nanoparticles which is not yet explored. Moreover, the mechanism of AgNPs formation In this work, an aqueous fruit extract was employed for a single stage synthesis of spherical AgNPs at room temperature. The reduction process was easy to handle and monitored by UV-vis spectroscopy and Atomic absorption spectroscopy (AAS). AgNPs were characterized by Dynamic light scattering (DLS), Fourier transform infrared (FTIR) spectroscopy, X-ray diffraction (XRD), Zeta-potential, Field emission scanning electron microscopy (FESEM), Transmission electron microscopy (TEM), Atomic force microscopy (AFM), and Thermogravimetric analysis (TGA).

Moreover, polyphenolic compounds present in plant extracts viz., caffeic, chlorogenic, and gallic acids are decomposed irreversibly when they are exposed to a high pH (> 9) (Friedman and Jurgens, 2000). Ascorbic acid (AA) is converted to dehydro-AA at

pH≤4.2 (Chebrolu et al., 2012). The organs of the plants such as *Ocimum sanctum* leaf (Singhal et al., 2011), *Citrus limon* (Prathna et al., 2011), *Citrus sinensis* peel (Konwarh et al., 2011), tea leaf (Sun et al., 2014), and *Manilkara zapota* fruit (Sutradhar and Saha, 2016) laden with AA are used for AgNPs synthesis. However, the fate of AA with the change in pH and its effect on the quality and purity of particles synthesized using a bio-mediated process is still not known. On the other hand, higher pH increases the stability of colloid formation and cluster distribution due to repulsive electrosteric interactions (Badawy et al., 2010). It also enhances the nucleation and growth rates with the subsequent crystallization leading to the formation of smaller particles (Ajitha et al., 2015; Sathishkumar et al., 2009).

Therefore, the second part of this work (**Chapter 3**) investigates the effect of pH on the formation kinetics of AgNPs, particles purity, and particle sizes along with the fates of analytes and influences of Ag_2O which is readily formed at a higher pH. Also, the role of AgNPs for the inactivation of *E. coli* and *B. subtilis* bacteria and, fungus *A. thermomutans* were studied.

3.2 Results and Discussion

3.2.1 AgNPs formation at natural bio-extract pH

3.2.1.1 AgNPs formation with progress of reaction time

The reaction mixture consisting of $AgNO_3$ and bio-extract showed the variation in color as the reaction proceeds. The solution color changes from light yellow to orange within 1 h and, then it shifted from light brown to deep brown and finally appeared to be dark brown after 24 h (**Figure 3.1**). The color of AgNPs changes with the size of NPs due to variation in surface plasmon resonance effect (Dauthal and Mukhopadhyay, 2012). **Figure 3.2** shows the particle size distribution of AgNPs formed at different reaction time. The particle diameter was between 1 and 3 nm within the first 3 h of reaction which was increased up to 30 nm after 9 h reaction. It was further increased with the progress of reaction, and AgNPs was found to be between 26 and 246 nm in 24 h (**Figure 3.2**). It was found that almost 86 % Ag^+ was converted to Ag^0 in 15 h reaction time and remained almost invariant even after 18 h with 97 % conversion (**Figure 3.3**). The diameter of the largest particle was found to be less than 100 nm in 15 h. However, around 43 % AgNPs had a diameter of above 100 nm by 24 h of contact. The formation of Ag^0 nuclei became insignificant with the exhaustion of residual Ag^+ ions and, AgNPs were formed by the coalescence of the nascent nuclei. There was negligible change in particle size even after 72 h of contact. It implies that the growth of

AgNPs was mostly continued long with the nucleation of Ag^0. The repulsive behavior of natural capping agents prevented from the long-time aggregation of fabricated AgNPs (Devi and Joshi, 2015).

Figure 3.4 shows UV-vis spectra of bio-synthesized AgNPs at different time intervals. The characteristic band was found at 450 nm which was due to the vibration of longitudinal plasmon resonance (Dauthal and Mukhopadhyay, 2012). A transverse plasmon vibration was also evident at 388 nm for AgNPs formed between 3 and 12 h of reaction time. A similar peak for the bio-synthesized AgNPs using *Pelargonium graveolens* leaf extract is observed by (Shankar et al., 2003). The broad band at λ_{max} (**Figure 3.4**) is indicative of wider size distribution (**Figure 3.2**) of AgNPs. **Figure 3.5** shows the optical absorption intensity at λ_{max} with the reaction time up to 72 h. After 15 h, the reduction was 90.7 % complete, and, it was 99 % for 18 h, and the change afterward was insignificant. It also implies in the same line of DLS that the rate of AgNPs formation was varied linearly as long as residual Ag^+ present in the solution (>1 %) and the particle size didn't change after that. The reduction time required for the fabrication of AgNPs was comparable with the previous reports. Huang et al. (2011) synthesized AgNPs using *Cacumen Platycladi* extract and reported 94.1% conversion of Ag^+ within 24 h of reaction (Huang et al., 2011). AgNPs synthesis using *S. edule* fruit extract was even faster than some of the chemicals such as N,N-Dimethylformamide, Poly(N-vinylpyrrolidone) (Pastoriza-Santos et al., 2000) and photochemical (Huang et al., 1996) techniques. The results provided in the subsequent sections are for AgNPs formed after 24 h of reaction unless and otherwise stated.

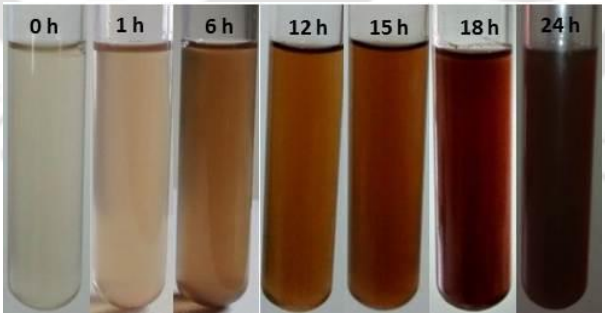

Figure 3.1. Pictorial view of progressive change in color of $AgNO_3$/bio-extract mixture. Experimental conditions: $AgNO_3$ concentration 1 mM, pH 5.8, reaction temperature 28±2 °C, and volume 200 mL.

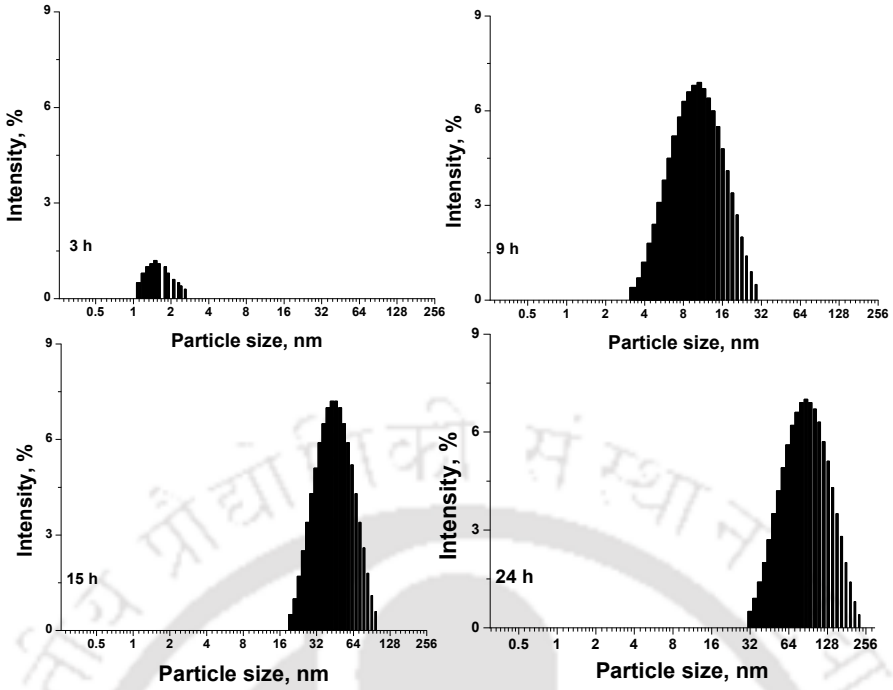

Figure 3.2. Variation of size of AgNPs formed at different reaction time. Experimental conditions: $AgNO_3$ concentration 1 mM, pH 5.8, reaction temperature 28±2 °C, and volume 200 mL.

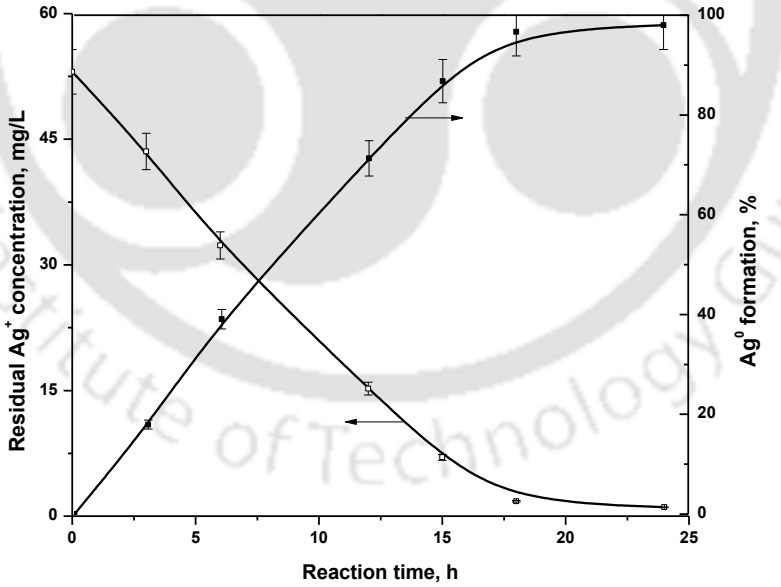

Figure 3.3. Kinetics of Ag^+ forming AgNPs. Experimental conditions: $AgNO_3$ concentration 1 mM, pH 5.8, reaction temperature 28±2 °C, and volume 200 mL.

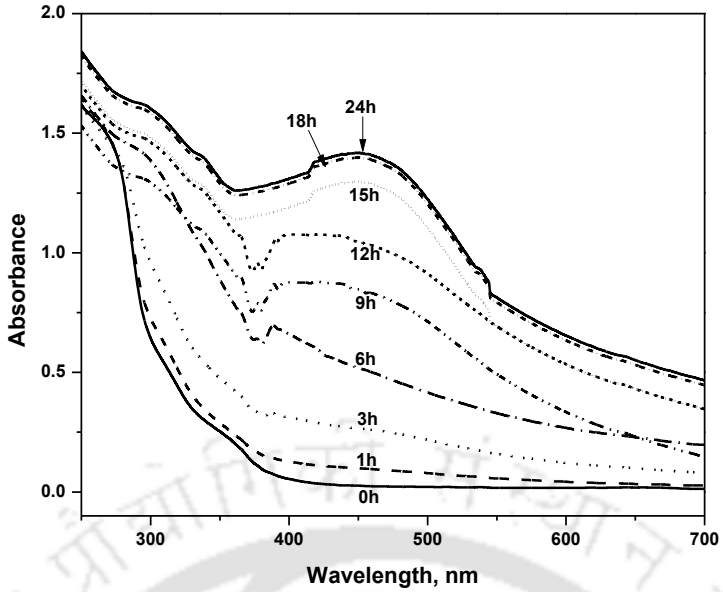

Figure 3.4. UV–vis spectra of bio-extract/$AgNO_3$ mixture recorded at different reaction time. Experimental conditions: $AgNO_3$ concentration 1 mM, pH 5.8, reaction temperature 28±2 °C, volume 200 mL.

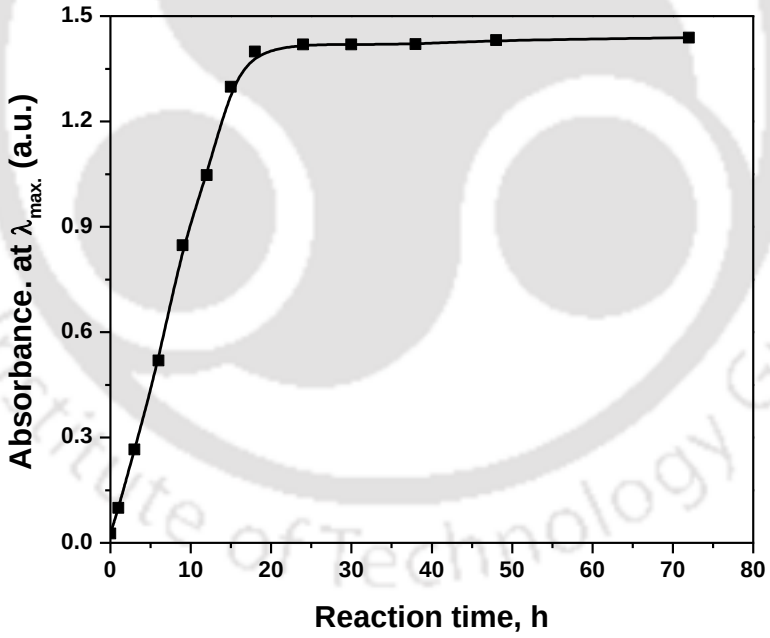

Figure 3.5. Absorbance at λ_{max} with reaction time from Figure 3.4. Experimental conditions: $AgNO_3$ concentration 1 mM, pH 5.8, reaction temperature 28±2 °C, and volume 200 mL.

3.2.1.2 Optimization of precursor and bio-extract concentrations

The concentration of $AgNO_3$ was varied between 0.1 and 2 mM, to find out the maximum yield of AgNPs (**Figure 3.6**) for a fixed concentration of bio-extract (water to bio-extract of 8:1 v/v). The color of the reaction mixture was observed as yellowish brown and light reddish brown for the lower $AgNO_3$ concentrations (0.1 to 0.5 mM) at after 24 h of reaction time and, it turned the dark reddish brown color at >1.0 to 2.0 mM. The SPR peak was intense with the increase in precursor concentration and, the maximum absorption was observed at 1.0 mM. **Figure 3.7** shows the residual Ag^+ ions in the reaction mixture after 24 h of reaction and, the residual of Ag^+ was also increased at higher Ag^+/ precursor concentration. There was about 7 % Ag^+ in solution up to 1 mM $AgNO_3$ and, it increased to 13.3 and 18.7 % with 1.5 and 2.0 mM, respectively. This was due to the presence of excess Ag^+ ions in comparison to available active analytes in the bio-extract. Hence, the precursor concentration of 1.0 mM was selected as an optimum dose.

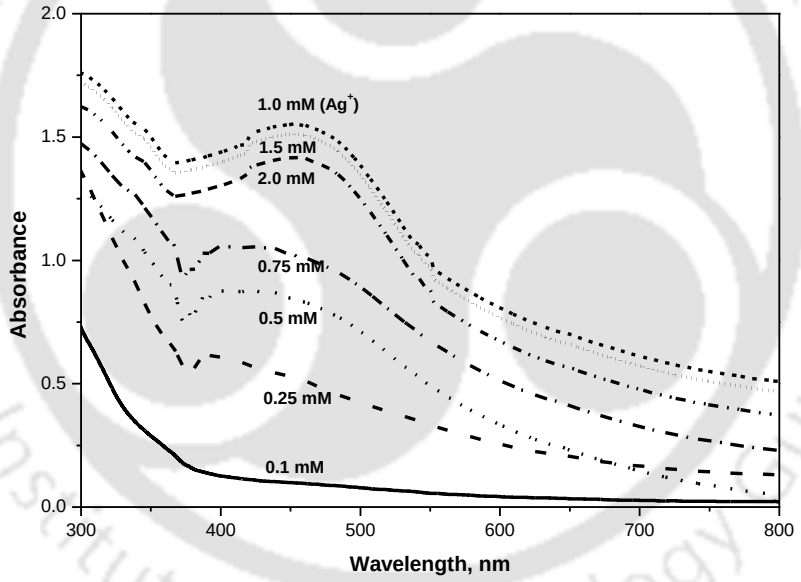

Figure 3.6. Effect of Ag^+ ions/ precursor concentration ($AgNO_3$) on the formation of AgNPs with water to bio-extract ratio of 8:1 (v/v) at pH 5.8 after 24 h. Experimental conditions: pH 5.8, reaction temperature 28±2 °C, and volume 200 mL.

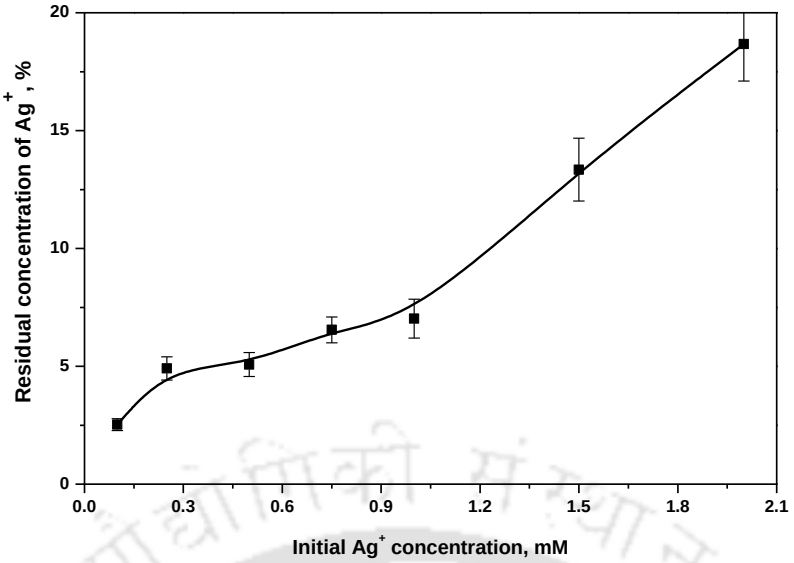

Figure 3.7. Residual Ag^+ ion in solution at different initial Ag^+/ precursor concentration ($AgNO_3$) with water to bio-extract ratio of 8:1 (v/v) at pH 5.8 after 24 h.

S. edule plant fruits were cut into small pieces as mentioned earlier (**Chapter 2, Section 2.3**) and mixed with water at a different ratio as 1: 50, 1:25, 1:10, 1:8 and 1:5 with a $AgNO_3$ concentration of 1.0 mM. The residual Ag^+ concentration vs. water to bio-extract ratio is plotted in **Figure. 3.8(a)** and, from the graph, it can be seen that as the water to bio-extract ratio decreases, the concentration of residual Ag^+ fell down. At water to bio-extract ratio of 25:1 and 50:1, the conversion of Ag^+ to Ag was about 76.6 and 78.9 %, whereas, at 5:1 and 8:1 ratios, it was around 92.6 and 94.2 %. With the increase in the concentration of active analytes in the bio-extract, Ag^+ reduction increases (Sathishkumar et al., 2009)**.**

In addition, the water to bio-extract ratio variation was also compared with the zeta-potential variation (**Figure 3.8(b)**). In general, a colloidal solution that shows an absolute zeta-potential (ζ) more than 20 mV is considered stable (Sun et al., 2014). The absolute ζ lower than 20 mV is unstable and could result in potential agglomeration of particles in a suspension (Badawy et al., 2010). In the present study, ζ of AgNPs suspension/solution was found as -27.1 and -26.9 mV with water to bio-extract ratios of 5:1 and 8:1, respectively. ζ increased to -12.4 and -11.5 mV with 25:1 and 50:1 which indicates that AgNPs were less stable at higher water to bio-extract ratios. Hence, the water to bio-extract ratio of 8:1 was selected in the subsequent studies.

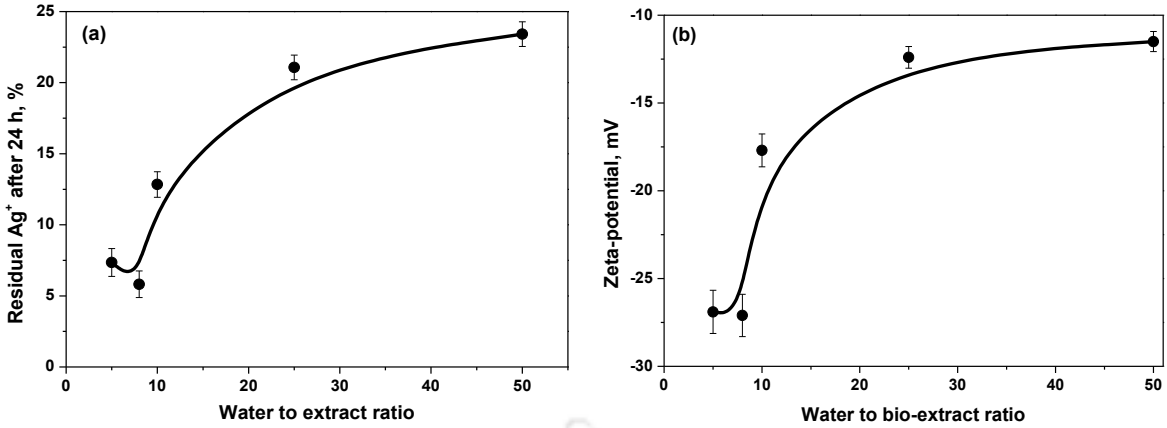

Figure 3.8. Effects of water to bio-extract ratio on (a) residual Ag^+ (mg L^{-1}) and (b) zeta-potential variation after 12 h of reaction time. Experimental conditions: Initial $AgNO_3$ concentration 1 mM, pH 5.8, reaction temperature 28±2 °C, and volume 200 mL.

3.2.2 Characteristics of bio-mediated synthesized AgNPs

3.2.2.1 FTIR spectra and formation of AgNPs

The Fourier transform IR spectra were recorded to identify the biomolecules that bound on the surface of AgNPs through the identification of the characteristic functional groups. The FTIR spectra of bio-extract and bio-synthesized AgNPs are represented in **Figure 3.9**. A band at 3604 cm^{-1}, the characteristic stretching vibration of H–O–H, of bio-extract, was found to be shifted to 3471 cm^{-1} in AgNPs with higher bandwidth. The shift is large. But, it came within the characteristic IR bands in the region of 3600-3100 cm^{-1} corresponding to -OH valence vibrations .The bands appeared at 2100, 1681, 1595, 1446, 1350, 1240, 968, and 854 cm^{-1} could be attributed to –C≡C– stretch of alkynes, N–C=O amide I bond, C–O stretch of carboxylic acid group, aromatic C–C stretch, CH_2 of alkanes, C-O bending of esters/ or ethers, =C–H bending of alkenes and N–H of amines, respectively (Ibrahim, 2015). A band at 3100 cm^{-1} assigned to C–H stretch, was disappeared in AgNPs, while a new peak formed at 2972 and 736 cm^{-1} was assigned to C–H stretch of alkane group and C–H "oop" of aromatics.

Various functional groups appeared upon formation of AgNPs and their shift in wavelength in comparison to the bio-extract is summarized in Table 3.1. The peaks shifted from 2100 to 2106, 1681 to 1633, 1595 to 1546, 1446 to 1425, 1350 to 1305, 1240 to 1265 and 968 to 964 cm^{-1}, respectively, might be of hydroxyl, carboxyl and amine groups. Phenolic hydroxyl groups are responsible for the reduction of Ag^+ into Ag^0 which after the reduction could form quinones. The amine and acid functional groups are mostly responsible for the stability of AgNPs (Bar et al., 2009). The absorption peak appeared at 513 cm^{-1} could

be assigned to the Ag-O stretching vibration (Nemade and Waghuley, 2015). AgNPs formed by the bio-inspired method and also using the commercial AA and sodium citrate exhibited the similar characteristics peaks of AgNPs.

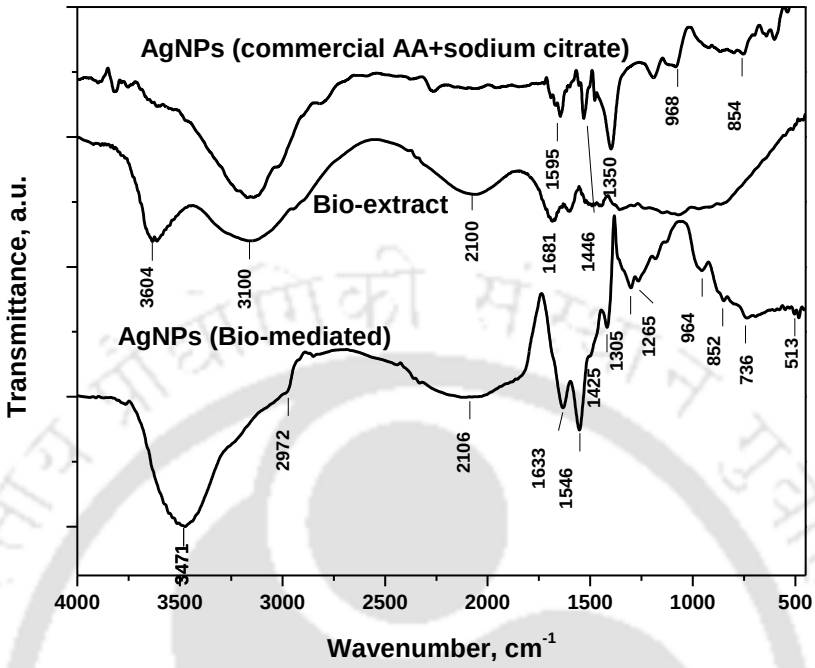

Figure 3.9. FTIR spectra of bio-extract and synthesized AgNPs (KBr to sample ratio:: 95:5 w/w).

Table 3.1. Functional groups appeared in FTIR spectra.

Peak position (bio-extract), cm^{-1}	**Peak position (AgNPs), cm^{-1}**	**Bond**	**Source of bond**	**Results owing to Ag^{+} reduction**
3604	3471	O–H stretch	Alcohols, Phenols	Shifted and band width increased
3100	--	O–H stretch	Carboxylic acids	Disappeared
--	2972	C–H stretch	Alkanes	New peak appeared
2100	2106	–C≡C– stretch	Alkynes	Shifted and band width increased
1681	1633	N–C–O bend	1° amines	Shifted and small sharp band formed
1595	1546	C–O stretch	Aromatic	Shifted and sharp band formed
1446	1425	C–C stretch (in–ring)	Aromatics	Shifted and small sharp band formed
1350	1305	CH_2	Alkanes	Shifted and band width decreased
1240	1265	C–O stretch	Esters/ Ethers	Shifted and no change in band width

968	964	=C–H bend	Alkenes	Shifted and band width increased
854	852	N–H	Amines	-
--	736	C–H "oop"	Aromatics	New peak appeared

3.2.2.2 XRD diffractogram of AgNPs

Figure 3.10 shows the XRD diffractogram of biosynthesized AgNPs. The XRD pattern confirmed the crystalline phases of AgNPs. The major 2θ peaks were observed at 38, 46, 65, and 78° that were due to reflections from (1 1 1), (2 0 0), (2 2 0) and (3 1 1) planes, respectively. The crystal planes indicated a face-centered cubic (FCC) crystal of AgNPs. 2θ values (JCPDS no. 04-0783) are in good agreement with the previous report for AgNPs synthesized using an aqueous extract of *Myrmecodia pendan* (Zuas et al., 2014). The lattice parameter of AgNPs was found to be 4.02 Å which is comparable to the earlier reported values for AgNPs (Vivekanandhan et al., 2014). The crystallite size calculated by Scherrer's formula at the major peak (2θ value 38°) was found to be 22 nm which is closer to the previous report for AgNPs synthesized using *Boerhaavia diffusa* plant (Vijay Kumar et al., 2014). The XRD pattern of AgNPs formed using commercial AA is illustrated in **Figure 3.10**. The intense diffraction peaks were detected with a crystallite size of 18 nm at 2θ= 38° for the diffraction from the (1 1 1) plane. However, AgNPs didn't form without the use of the capping agent (Inset of **Figure 3.10)**.

Moreover, the appearance of a minor peak at 2θ=32.2° (**Figure 3.10**) indicates the presence of Ag_2O. Thus, our synthesized AgNPs appears to be bi-crystalline in nature at natural pH of 5.8. Similar results are also reported for the fabrication of AgNPs using tea leaf extract (Sun et al., 2014). The colloidal Ag_2O was likely to be formed by the reaction between Ag^+ and OH^- ions. This result is also supported by the FTIR spectra of AgNPs (**Figure 3.9**). The organic compounds of free radical character also could be involved in the formation of Ag_2O (Adegboyega et al., 2013).

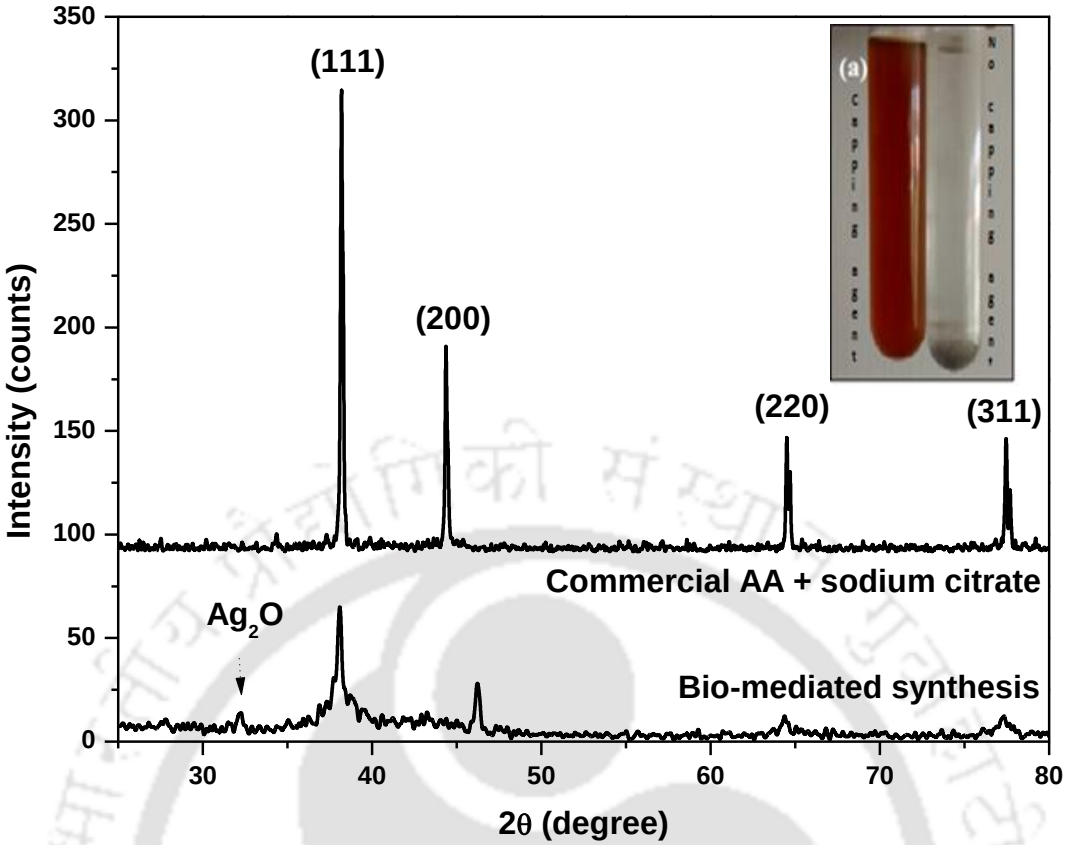

Figure 3.10. XRD patterns of synthesized AgNPs. Inset: Pictorial view of AgNPs formed using commercial with and without capping agent, sodium citrate.

3.2.2.3 Variation of zeta-potential of AgNPs in aqueous media

The effect of pH on the variation of zeta-potential of AgNPs is shown in **Figure 3.11**. The surface charge of AgNPs was negative in the dispersing medium of pH ranging from 3 to 9. The negative surface potential is believed to be imparted by the natural capping agents. Zeta-potential was found to decrease from -2.8 at pH 3 to -28.7 at pH 9 (**Figure 3.11**). The variation of zeta-potential with pH implies that AgNPs were likely to destabilize at lower pH and the stability was more at high pH because of electrostatic repulsion. Hence, the lower pH favored aggregation of AgNPs while the sizes are smaller at higher pH. From the above results, it is clear that the point of zero charge may exist at pH <<3. At pH>5, zeta-potential was decraesed almost linearly with the pH variation up to 9.

FTIR spectra (**Figure 3.9**) and TGA (**Figure 3.12**) also confirm that the bio-molecules (also referred as natural capping agents) coordinated and/or adhered onto AgNPs. TGA showed two steps down peaks (**Figure 3.12**). The first mass loss occurred at 110 °C due to evaporation of water molecule adsorbed onto AgNPs surface. The second steady weight loss of 28 % at about 205-792 °C corresponds to the removal of bioorganic compounds.

Thus, the presently synthesized AgNPs showed more stability in terms of mass loss in comparison to the earlier study (Khalil et al., 2014).

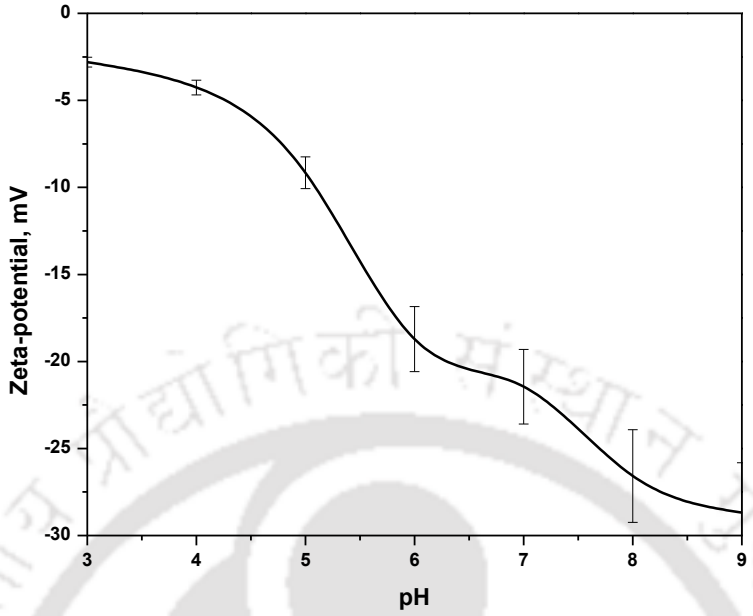

Figure 3.11. Variation of zeta-potential of AgNPs dispersed in aqueous media at different pH after 24 h. Experimental conditions: Initial $AgNO_3$ concentration 1 mM, temperature 28±2 °C, and volume 10 mL.

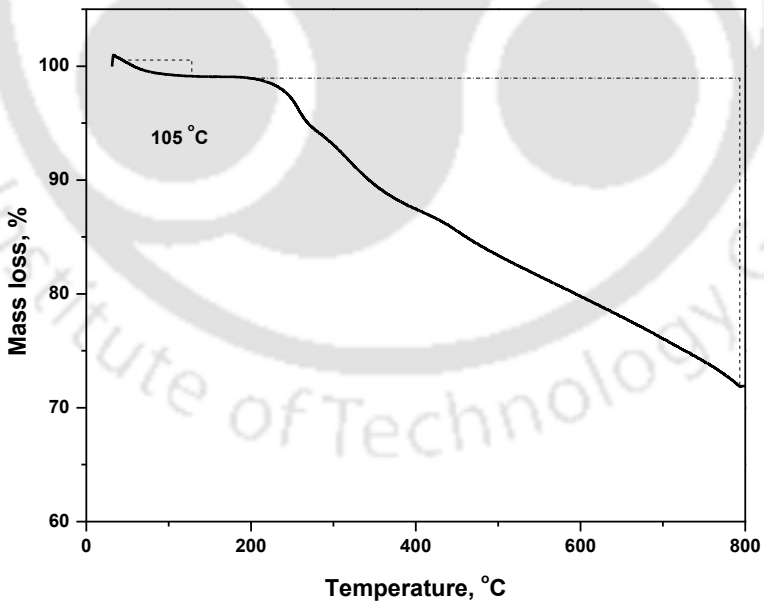

Figure 3.12. Variation of mass loss from TGA of synthesized AgNPs after 24 h. Experimental conditions: Initial $AgNO_3$ concentration 1 mM, temperature 28±2 °C, pH 5.8, and volume 10 mL.

3.2.2.4 TEM and AFM images

TEM micrographs give important insights into the structural morphology, shape, and size of our synthesized AgNPs. Thus, the bio-synthesized AgNPs is found to be nearly spherical in shape (**Figure 3.13(a)**). The individual AgNPs and a number of aggregates of various sizes are also observed in the TEM image. The size of AgNPs ranges from 20 to 70 nm with an average diameter of 46 nm. The corresponding particle size histogram of AgNPs determined using ImageJ software is shown in **Figure 3.14(a)**. TEM images of the dried particles were acquired and whereas a layer of water molecule is associated with the hydrodynamic diameter (Gajbhiye et al., 2014). For this reason, the particles appeared in TEM images were smaller in size than that was observed in DLS measurement. The crystalline nature of AgNPs can be seen from the selected area electron diffraction (SAED) pattern indexed to (1 1 1), (2 0 0) and (3 1 1) (**Figure 3.13(b)**). The Bragg reflection planes are consistent with XRD patterns (**Figure 3.10**).

Figure 3.13 (c and d) illustrate the 2D and 3D tapping mode AFM topographical images of AgNPs. The 3D topography and morphology of AgNPs were obtained by analyzing the AFM images using WSxM image browser software through image scanning in a 1 μm×1 μm area. The direct topographical image showed that AgNPs were spherical with little aggregation which is in agreement with TEM micrograph. The single particle line profile analysis gave the size of AgNPs to be 35 nm **(Figure 3.14(b)**). The surface of the AgNPs was moderately smooth with a root mean square (RMS) roughness of 3.44 nm. The height of AgNPs (**Figure 3.14(c)**) was found to be between 20 and 70 nm which is comparable to the size distribution determined from TEM micrograph (**Figure 3.14(a**)) signifying the formation of nearly spherical AgNPs (Velusamy et al., 2015).

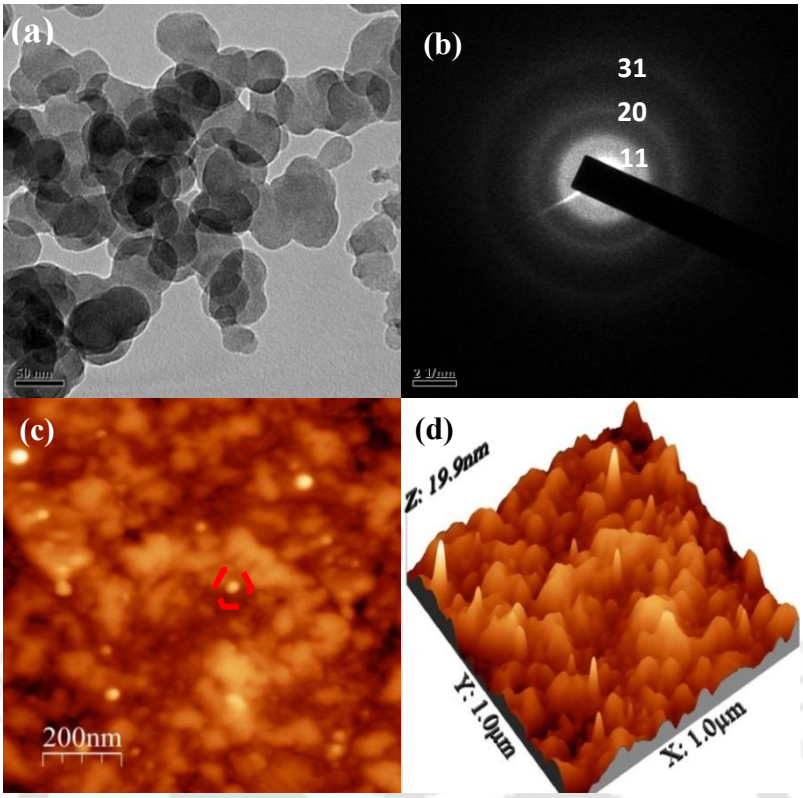

Figure 3.13. TEM and AFM images of synthesized AgNPs. (a) TEM micrograph, (b) SAED pattern, (c) AFM 2D view (top view) and, (d) AFM 3D view (cross sectional view).

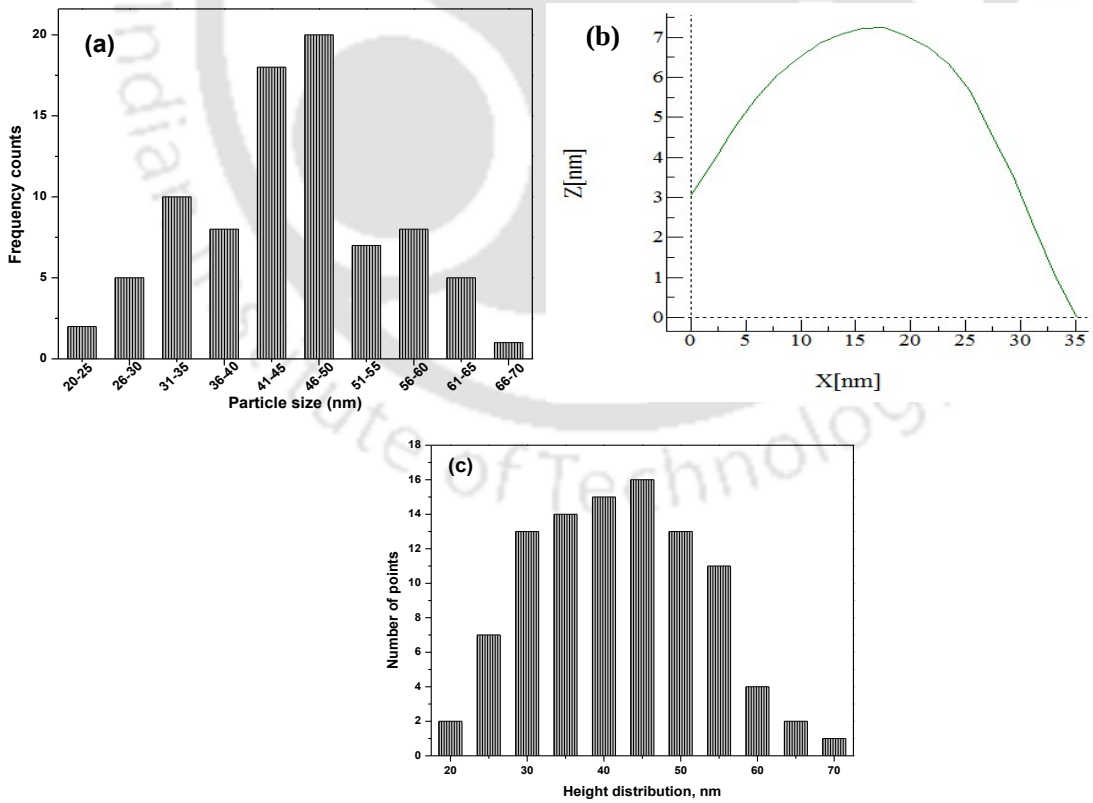

Figure 3.14. (a) Size distribution of synthesized AgNPs determined from TEM micrographs, (b) Line profile analysis of single particle for size determination using 200 nm scale and (c) Height distribution of AgNPs determined from AFM micrographs.

3.2.3 Antibacterial and antifungal functionalities of AgNPs

Chemically synthesized NPs could adversely affect the antibacterial activity assay due to the presence of some toxic chemicals on its surface (Gunalan et al., 2012). On the other hand, the bio and bio-mediated synthesized NPs are expected to be more biocompatible for the microbial activity test (Jha and Prasad, 2010). Therefore, the antimicrobial activity of both aqueous bio-extract and AgNPs were evaluated and, the results were compared with the control media. For this purpose, we had chosen Streptomycin (S 10) and Ampicillin (Amp) as controls for inactivation study of *B. subtilis* and *E. coli* bacteria, respectively (**Figures 3.15(a) – 3.15(d)**). It was found from the disc diffusion study that the bio-extract alone inhibited the growth of both *B. subtilis* and *E. coli* with 20 and 26 mm zone diameter. The control media S 10 showed the highest inhibition of *B. subtilis.* However, both the strains were resistant to control Amp, and the growth was not inhibited. The control media S 10 exhibited maximum *B. subtilis* inactivation with 40 mm zone formation followed by AgNPs (22 mm diameter zone). AgNPs were the most effective for suppression of growth of *E. coli* with 36 mm zone of inhibition compared to the inhibition of *B. subtilis* (zone diameter 22 mm). The difference in growth inhibition of Gram-negative and Gram-positive bacteria by AgNPs may be attributed to the extent of variation of permeability to the bacterial cell wall. While the Gram-negative bacteria possess an outer protective membrane of the peptidoglycan layer, Gram-positive organisms do not have (Li et al., 2010). AgNPs possessing free radical (Adegboyega et al., 2013) might cross the barrier of permeability of the outer membrane resulting in the leakage of cellular materials. This event would lead to the turbulence of membranes permeability which we think as an important factor to inhibit the bacterial growth by AgNPs. Moreover, crossing the first outer membrane, AgNPs might enter into the inner membrane and inhibit the respiration and cell growth. **Figure 3.16** shows a typical ESR spectrum for AgNPs recorded at 3 and 24 h of reaction time. The resonance lines are quite narrow and exhibit a slight asymmetry and, the central peak (336.337 mT) indicates the existence of free radical character. Thus, the generation of free-radical may be responsible for strong antimicrobial effects (Kim et al., 2007).

Figure 3.15(e) portrays the antifungal activity of AgNPs against *Aspergillus thermomutans*. It can be seen that the bio-synthesized AgNPs effectively reduced the growth of *A. thermomutans* with an inhibition zone diameter of 78 mm. There was no fungal growth and the clear area in comparison to the control media signifies the death of *A. thermomutans*. These results are in agreement with the earlier studies related to inactivation of ambrosia

fungus *Raffaelea sp*. by AgNPs (Kim et al., 2009). AgNPs destroy the membrane of the fungal hyphae and impede the conidial germination (Ajitha et al., 2015; Kim et al., 2009).

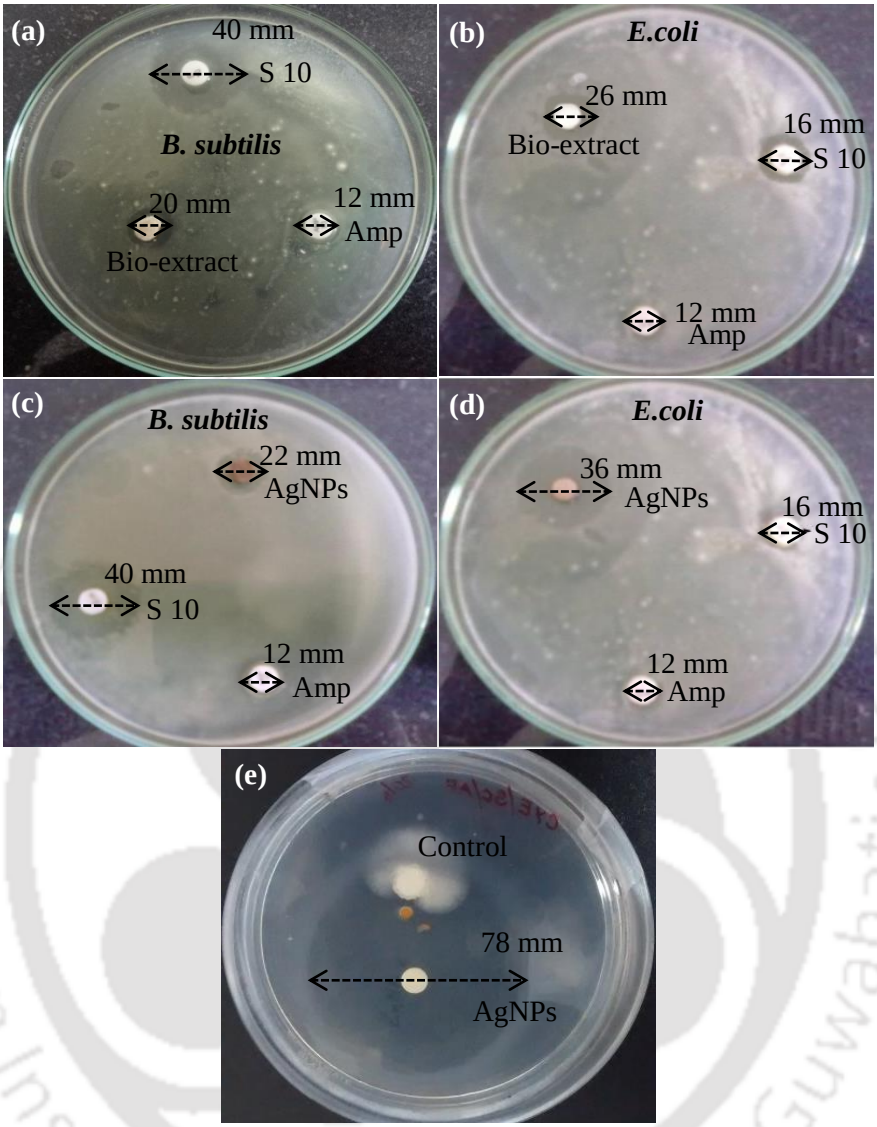

Figure 3.15. Antibacterial activity assay: *S. edule* extract against (a) *B. subtilis* and (b) *E. coli* and, AgNPs against (c) *B. subtilis* and (d) *E. coli* in comparison with control media. (e) Antifungal activity of bio-extract and AgNPs against *Aspergillus thermomutans.* Experimental conditions: Concentration of S10, Amp 30 mg mL^{-1}, AgNPs concentration 20 µg mL^{-1}, pH 5.8, incubation temperature 37 ºC, and reaction time 24 h.

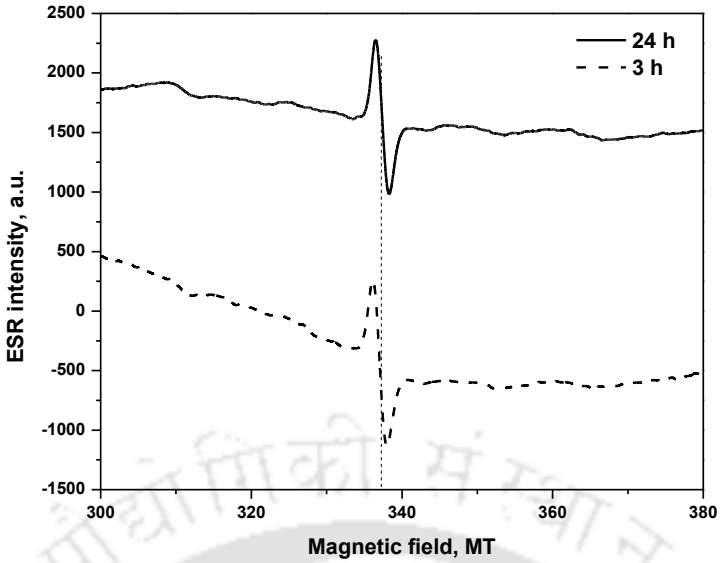

Figure 3.16. ESR spectra of AgNPs formed at 3 and 24 h of reaction time at room temperature (28±2 °C).

3.3 pH dependent size control, formation mechanism and antibacterial functionality of AgNPs

3.3.1 pH dependent AgNPs formation and effect of reaction time

AgNPs was synthesized by varying the pH from 3 to 12.5 and, the particles formed at pH 3 are designated as 'AgNPs-pH3'. Similar notation is used for AgNPs formed at different pH. The color of the reaction mixture and the variations in the optical absorbance at different pH are shown in **Figures 3.17 and 3.18**. There was no AgNPs formation at pH 1. So, no absorbance peak was identified. However, the absorption peak was found to appear with the further increase in pH. There was a minor peak at 428 nm at pH 3. The peak intensity was gradually enhanced and, shifted to a lower wavelength, i.e., to 427, 424, 417, 416, and 414 nm at pH 5, 7, 9, 11, and 12.5, respectively. These are the characteristic peaks of AgNPs in the suspension form resulted from the SPR effect (Chhatre et al., 2012; Smitha et al., 2008) which is mostly size and shape dependent. This hypsochromic shift is indicative of the reduction in the size and degree of anisotropy of the particles (Edison and Sethuraman, 2013; Yilmaz et al., 2011). The full width at half maximum decreased from 168.7 to 108.9 nm for AgNPs-pH3 to AgNPs-pH12.5 (Table 3.2). It indicates the reduction in the polydispersity of the particles (Agnihotri et al., 2014) at a higher pH due to smaller particles size.

Table 3.2. SPR peak position, full width at half maxima, and crystallite size of AgNPs formed at different pH.

Sample	UV-vis absorption		XRD	
	SPR peak (nm)	FWHM	d-spacing (nm)	Crystallite size (nm)
AgNPs-pH3	428±0.9	168.7±0.1	0.23591±0.002	54.069±0.7
AgNPs-pH5	427±0.7	146.9±0.98	0.2354±0.01	35.159±0.8
AgNPs-pH7	424±0.5	136.6±0.21	0.2354±0.009	34.479±0.1
AgNPs-pH9	417±0.4	116.9±0.55	0.2354±0.02	22.247±0.5
AgNPs-pH11	416±0.79	113.7±0.65	0.23543±0.007	22.344±0.9
AgNPs-pH12.5	414±0.57	108.9±0.42	0.23537±0.01	20.716±0.8

The above results are also in line with the variation in solution color during synthesis (**Figure 3.17**). There was little change in the solution color even after 24 h of reaction with AgNPs-pH3. The color was light red-brown in the case of AgNPs-pH5 and, a dark red-brown color appeared with the particles formed at an elevated pH. The rate of Ag^{+} conversion to AgNPs was faster at the initial period with a higher rate at an elevated pH (**Figure 3.19**). There was about 11.5 % residual Ag^{+}, i.e., 88.5 % AgNPs-pH12.5 was formed by 12 h and, it increased to 96 % in 24 h. The yield of AgNPs in 24 h of the reaction was found to be 62.3, 77.4, 86.4, 93.4, and 94.7 % at pH 3, 5, 7, 9, and 11, respectively.

The particles size distribution is shown in **Figure 3.20**. The distribution width was reduced with the increase in pH. It was also shifted towards the lower particles size. So, the average particles size was reduced at a higher pH. The lowest and highest particles in differential number distribution varied from 51 to 193.9, 46.7 to 188.9, 34.4 to 130.9, 14.1 to 57.6, 11.8 to 44.4, and 7.1 to 10.9 nm for AgNPs-pH3 to AgNPs-pH12.5, respectively. The average hydrodynamic diameter followed the decreasing trends as 68.2, 60.1, 44.9, 31.2, 14.5, and 8.9 nm where 90 % AgNPs came under 87.6, 76.8, 57.6, 44.6, 17.8, and 9.2 nm, respectively.

The size, shape, and morphology of AgNPs-pH3 and AgNPs-pH9 were also examined using TEM (**Figure 3.21**) and FESEM (**Figure 3.22**). AgNPs-pH3 size was higher with a significant agglomeration (**Figure 3.21(a)**). However, the small particles were mostly separate and, the agglomeration was also reduced notably for AgNPs-pH9 (**Figure 3.21(b)**). The bright concentric circles (SAED patterns) depict the (111), (200), and (311) planes of the face-centred cubic (fcc) AgNPs crystals **(Section 3.2.2.4)**. The high-resolution TEM micrograph of a single AgNP showed the clear lattice fringes with an interplanar d-spacing of 0.2354 and 0.236 nm for AgNPs-pH3 (**Figure 3.21(a)**) and AgNPs-pH9 (**Figure 3.21(b)**),

respectively. The mean, lowest, and highest particle size both in TEM and FESEM analyses were very close (Table 3.2). However, the dry particles sizes of AgNPs-pH3, AgNPs-pH5.8, and AgNPs-pH9 were about 80 % lower than the particles size measurements in the aqueous media using DLS (Table 3.3) due to the aggregation of particles as well as a few layers of water molecules are included in the size measurement.

Table 3.3. AgNPs particles determined using DLS, TEM, and FESEM techniques.

Sample	**Particle size from DLS**		**Particle size from TEM**		**Particle size from FESEM**	
	Mean	**Size range**	**Mean**	**Size range**	**Mean**	**Size range**
AgNPs-pH3	68.2±0.7	51-194	57.31±0.9	20-110	58.56±0.5	20-110
AgNPs-pH5	60.1±0.9	47-189				
AgNPs-pH7	44.9±0.2	34-131				
AgNPs-pH9	31.2±0.6	14-58	25.94±0.81	5-50	25.37±0.7	5-50
AgNPs-pH11	14.5±0.3	12-44				
AgNPs-pH12.5	8.9±0.9	7-11				

OH^- ions preferably react with Ag^+ yielding Ag_2O particles (Eq. 3.1) (**Figure 3.23**). Ag^0 clusters would form on the surface of Ag_2O. Eventually, it would grow to tiny AgNPs (Adegboyega et al., 2013; Cai et al., 2016). However, Ag^+ and Ag_2O reduction takes place at a slower rate under base-free condition. In fact, Ag_2O particles are more easily reduced than Ag^+ due to a lower electrode potential (Cai et al., 2016) (Eqs. 3.2 and 3.3). AgNPs also are formed through the formation of ascorbate radicals (Eqs. 3.4 and 3.5). It is in agreement with a minor reduction in solution pH after the synthesis (**Figure 3.24**). The free radical character of organic compounds also eases Ag_2O formation at a lower pH (Adegboyega et al., 2013). Therefore, a bimodal distribution of AgNPs-pH3 and AgNPs-pH5 was observed (**Figure 3.20**). The detail discussion is also provided in the later part of this section.

$$2Ag^+ + 2OH^- \leftrightarrow 2AgOH \leftrightarrow Ag_2O + H_2O \quad (3.1)$$

$$Ag^+ + e^- \rightarrow Ag^0 \qquad (E^0 = 0.7996\ V) \quad (3.2)$$

$$Ag_2O + H_2O \rightarrow 2Ag^0 + 2OH^- \qquad (E^0 = 0.342V) \quad (3.3)$$

$$C_6H_8O_6 + Ag_2O \xrightarrow{OH^-} 2Ag^0 + C_6H_7O_6^{\bullet -} + H_2O_2 \quad (3.4)$$

$$2C_6H_7O_6^{\bullet -} + Ag_2O + H^+ \rightarrow \text{Ascorbate anion} + \text{dehydro - AA} + 2Ag^0 + H_2O \quad (3.5)$$

The variation of the zeta-potential (ζ) of AgNPs was determined to study its destabilization tendency in the aqueous media. ζ was negative for all the particles irrespective to the pH of synthesis (**Figure 3.25**). The negative surface charge mostly resulted from the adsorption of biomolecules (**Section 3.2.2.3**) such as the formation of AgNPs-ascorbate layer (Zhang et al., 2009). ζ gradually decreased with the increase in pH from 3 to 12.5. In the case of AgNPs-pH3, ζ was found to decrease from -3.8 to -25.8 mV between pH 3 and 11 and, it varied from -22.1 to -86.2 mV for AgNPs-pH12.5. It implies that AgNPs-pH12.5 promoted destabilization compared to the particles formed at a lower pH. Moreover, the concentration of silver-ascorbate layer increases with the increase in pH. Hence, there may be better passivation of the nanocrystals surface (Oluwafemi et al., 2010).

The presence of biomolecules on the surface of AgNPs was also confirmed by TGA (**Figure 3.26**). The mass losses took place in three distinct temperature regions (**Figure 3.27**). A similar explanation as in **Section 3.2.2.3** is also applicable here. There was about 20 % mass loss at 200-390ºC resulted from the degradation of organic constituents, like AA, ferulic acid, carbohydrates, quercetins, and lignin molecules (Sun et al., 2014). The third steady mass loss was about 15 % at 370-950ºC. It may be for the removal of bio-organic salt like carbonates and decomposition of resistive aromatic complexes (Carballo et al., 2008). An average overall mass loss of 32.6±4 % was found within the whole temperature range. Shahzad et al. (2015) observed 16 % mass loss up to 410 °C for AgNPs synthesized using branched polyethyleneimine (Shahzad et al., 2015). Sun et al. (2014) reported 19 % mass loss at 380 ºC and, it increased to 39 % at 1000 ºC for AgNPs synthesized using the tea extract (Sun et al., 2014).

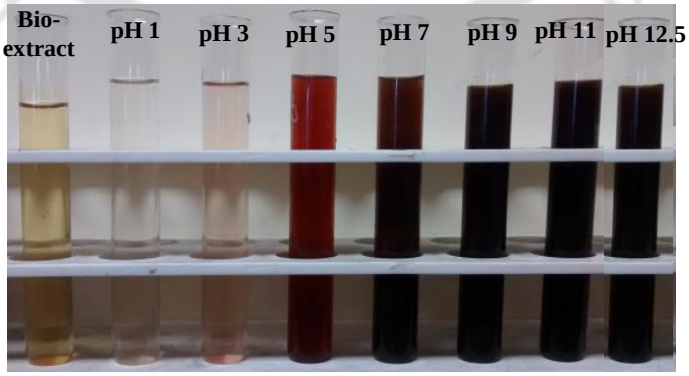

Figure 3.17. Color variation at the end of 24 h reaction as from Figure 3.18. Experimental conditions: $AgNO_3$ concentration 1 mM, reaction temperature 28±2 °C, and volume 200 mL.

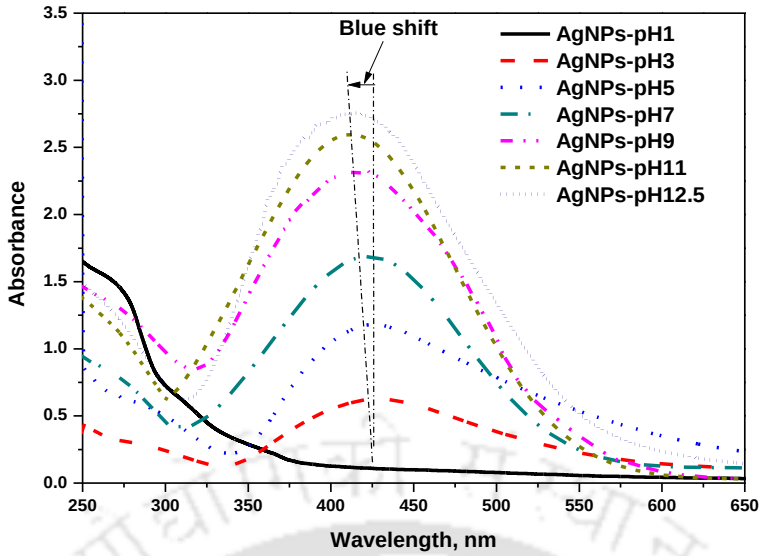

Figure 3.18. Spectral absorbance of bio-extract and $AgNO_3$ mixture at different pH. Reaction time 24 h and room temperature (25±2ºC).

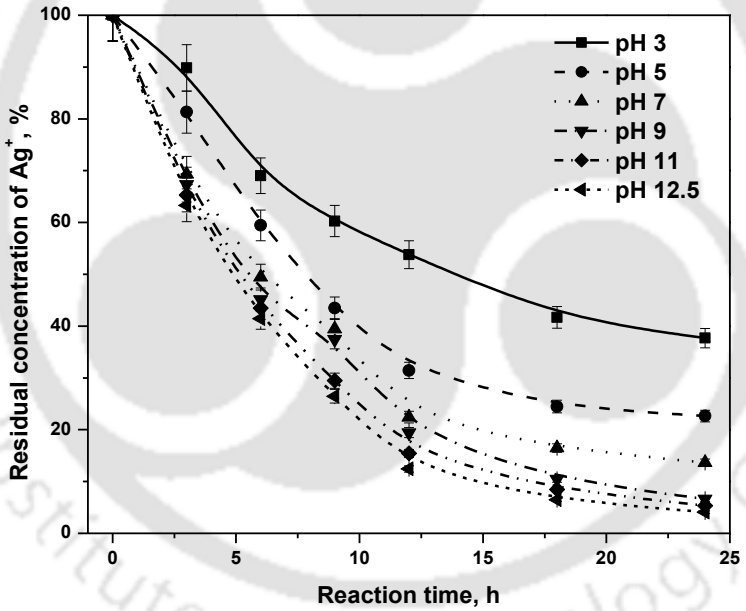

Figure 3.19. Residual concentration of Ag^+ with reaction pH at room temperature (25±2ºC). Experimental conditions: $AgNO_3$ concentration 1 mM, reaction temperature 28±2 °C, and volume 200 mL.

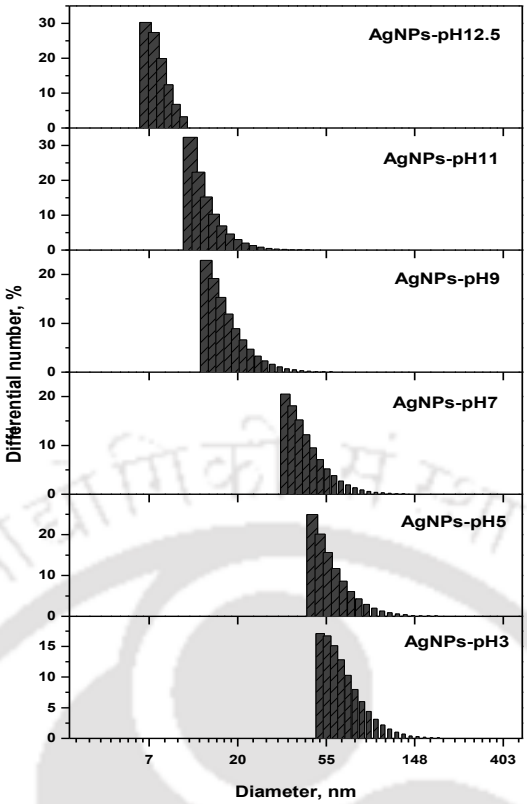

Figure 3.20. Particle size variation with change in pH during AgNPs synthesis.

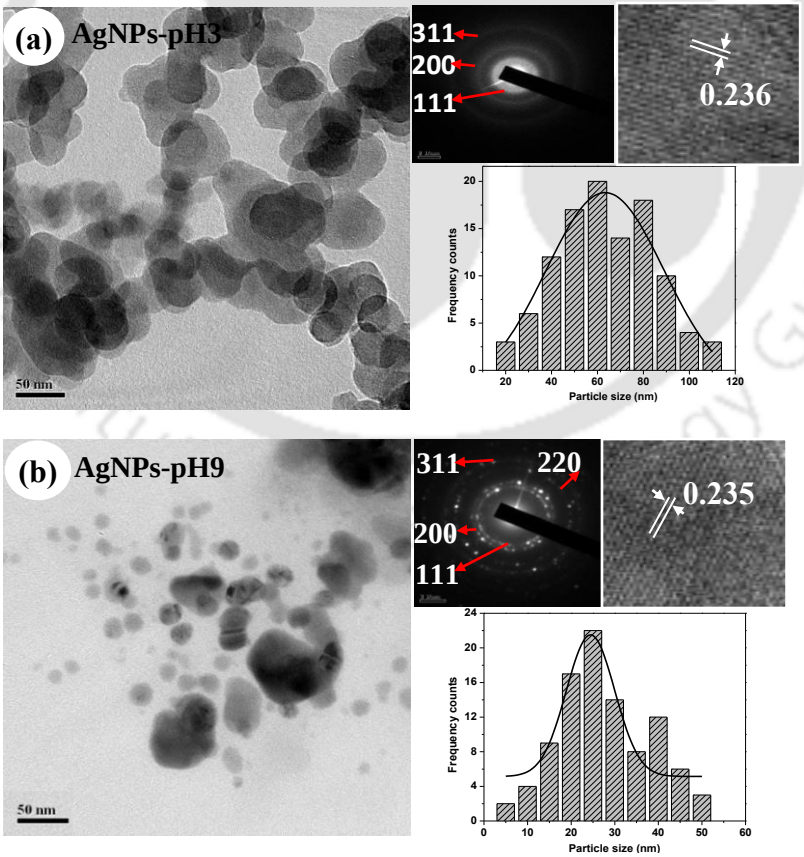

Figure 3.21. TEM micrographs, SAED, HRTEM and size distribution of (a) AgNPs-pH 3 and (b) AgNPs-pH 9.

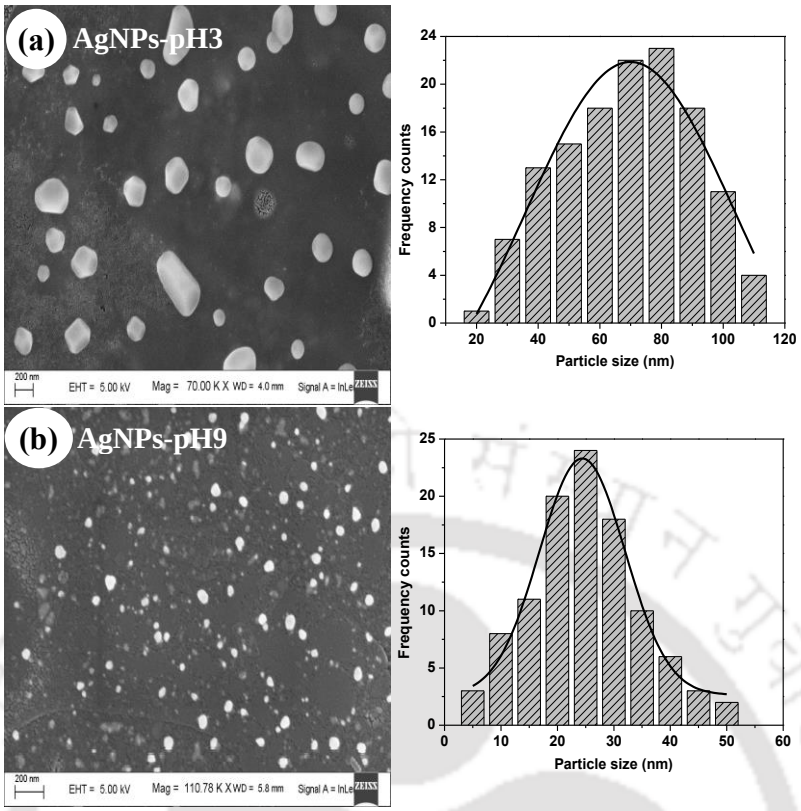

Figure 3.22. FESEM micrographs of (a) AgNPs-pH3 and (b) AgNPs-pH9.

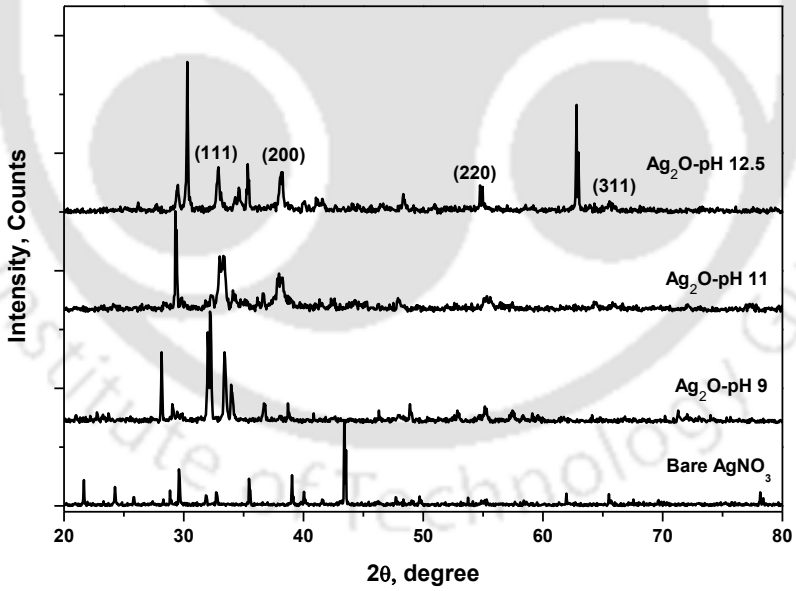

Figure 3.23. XRD patterns of Ag_2O formed only with pH variation (without bio-extract).

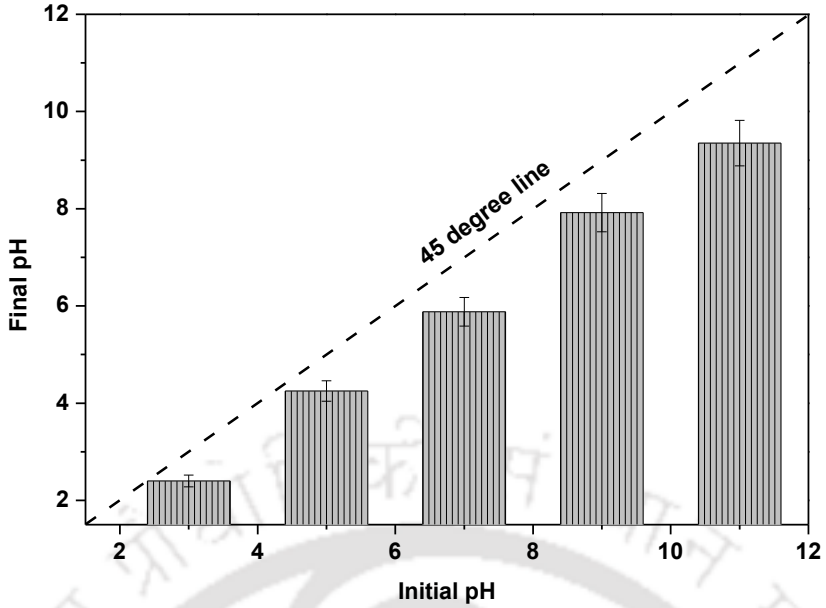

Figure 3.24. Variation of final pH with initial pH during synthesis of AgNPs. Experimental conditions: $AgNO_3$ concentration 1 mM, reaction temperature 28±2 °C, and volume 200 mL.

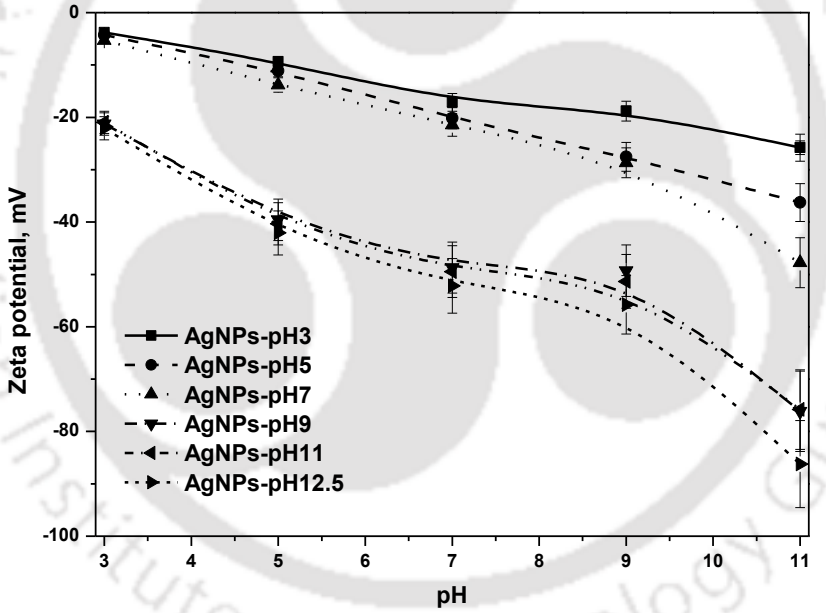

Figure 3.25. Zeta-potential of synthesized AgNPs with pH variation. Experimental conditions: $AgNO_3$ concentration 1 mM, reaction temperature 28±2 °C, and volume 200 mL.

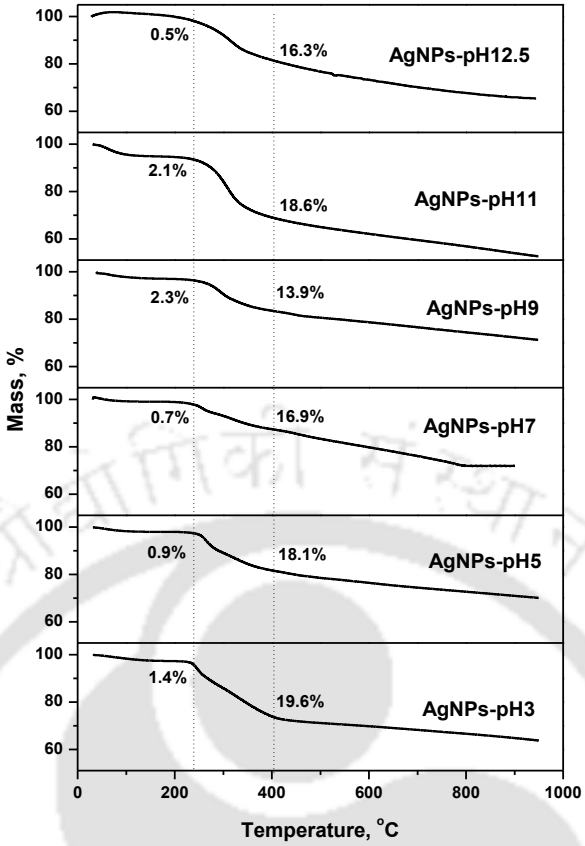

Figure 3.26. TGA profile of AgNPs formed at different pH.

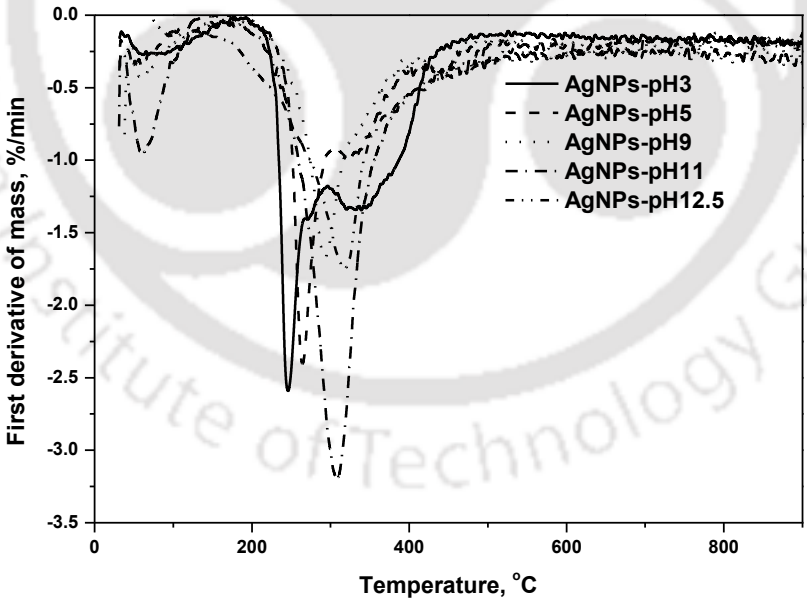

Figure 3.27. First derivative function of TGA plots of AgNPs.

FTIR spectra supported the variation of the functional groups of the biomolecules involved in AgNPs formation and, the effect of pH variation in the absence of metal precursor is shown in **Figure 3.28(a)**. The bio-extract at different pH showed important peaks

at 3312-3337, 2885-2889, 2285-2293, 1668-1683, 1444-1446, 1361-1373, 1090-1130, and 780-870 cm^{-1} wavenumber. The distinct broad peaks at around 3300 and 1675 cm^{-1} correspond to the phenolic-OH groups (Sadeghi et al., 2015). The peak at around 3313 cm^{-1} at pH 3 was shifted to 3157 and 3298 cm^{-1} at pH 9 and 12.5, respectively. The positioning of this band relies upon the degree of the intensity of hydrogen bonding and, it moves to the lower wavenumbers when H–O–H bond is dominant (Thanganathan, 2013). The bands at around 1614, 1365, and 1130 cm^{-1} attributed to the stretching vibration of C=O, C–O, and O–C–C bonds of AA (Oluwafemi et al., 2010) and, the band intensity was more at a higher pH.

AgNPs displayed a gradual shift of the peak position to a lower wavenumber with the rise in the intensities with pH elevation (**Figure 3.28(b)**). It implies to hydrogen-AA bond breaking and formation of ascorbate ions (Oluwafemi et al., 2010). The peaks at 1722, 1602, and 1614 cm^{-1} at pH 3, 11, and 12.5 (**Figure 3.28(a)**), respectively, correspond to the C=O bond of the five-membered lactone ring of AA. It shifted to 1641, 1600, and 1643 cm^{-1} in the case of AgNPs-pH3, AgNPs-pH11, and AgNPs-pH12.5 (**Figure 3.28(b)**) as the -C=O group of the lactone ring primarily bound on AgNPs (Sreeja et al., 2015). The bands appeared at around 1377, 1400, and 1406 cm^{-1} for AgNPs-pH3, AgNPs-pH-9, and AgNPs-pH12.5, respectively, with the dominance for AgNPs-pH12.5 owing to the C=O bond of ascorbate ion (Oluwafemi et al., 2010). So, the formation of silver-ascorbate layer (capping layer) was significant at a higher pH.

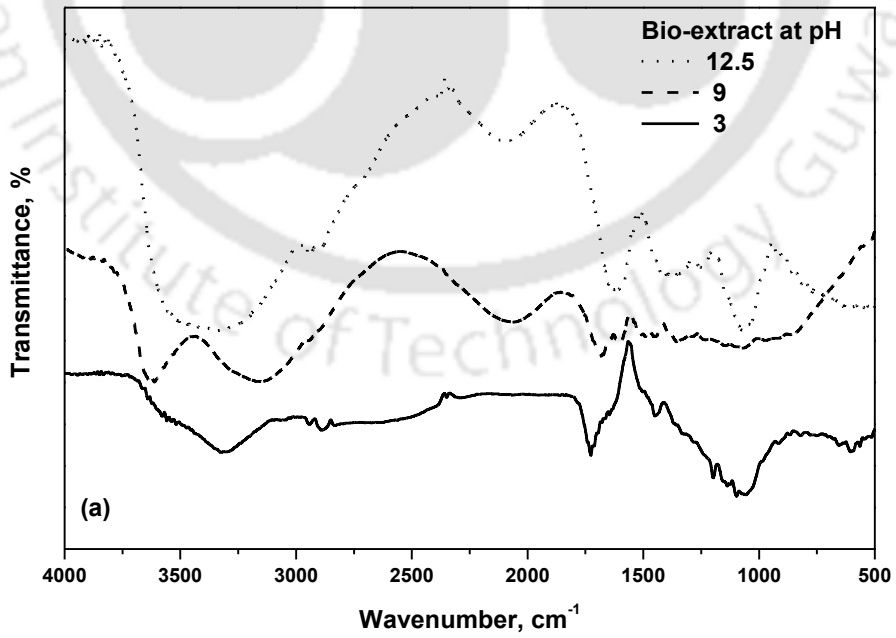

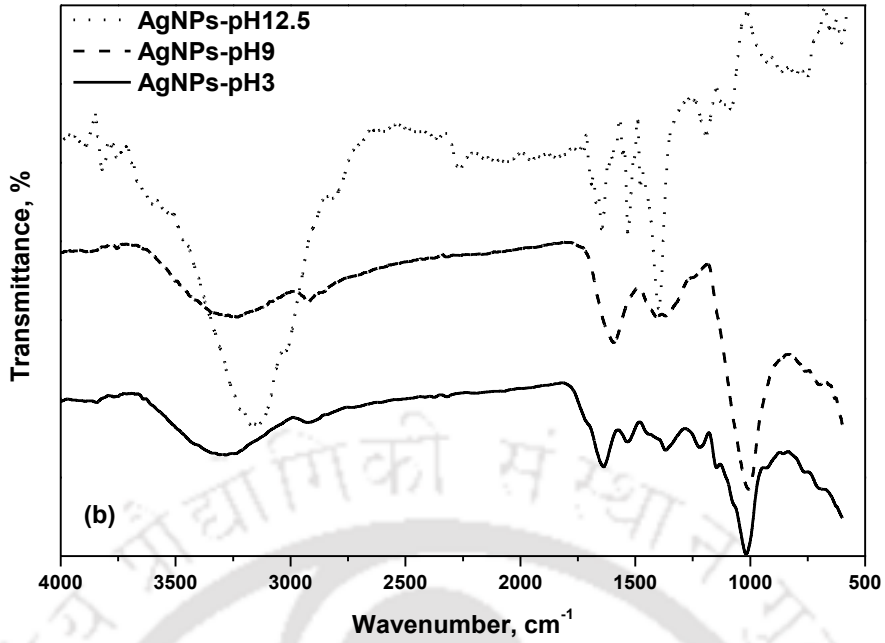

Figure 3.28. FTIR spectra of (a) *S. edule* extract and (b) AgNPs with different pH (KBr to sample ratio:: 95:5 w/w).

The XRD patterns of the particles formed at various pH are shown in **Figure 3.29**. It corresponds to the fcc AgNPs crystal. List as in **Section 3.2.2.2**, the major peaks at 38, 46, 65, and 78° attribute to (1 1 1), (2 0 0), (2 2 0), and (3 1 1) planes, respectively (Zuas et al., 2014). The crystallite size was calculated by the Scherrer's formula at $2\theta = 38°$ and, the reduction in crystallite size was more till pH 7 and, the raise was minor even at a higher pH (Table 3.2). The crystallite size of 54.1 nm for AgNPs-pH3 decreased to 21.7 nm for AgNPs-pH12.5 due to peak broadening. However, the d-spacing between the adjacent lattice planes didn't change with the pH variation (Table 3.2). A minor peak at 2θ=32.2° (**Figure 3.29**) for AgNPs-pH3 and AgNPs-pH12.5 corroborates the existence of Ag_2O. Thus, AgNPs were bi-crystalline both at a very low and high pH. Similar results are also found for AgNPs synthesized with the tea leaf extract (Sun et al., 2014).

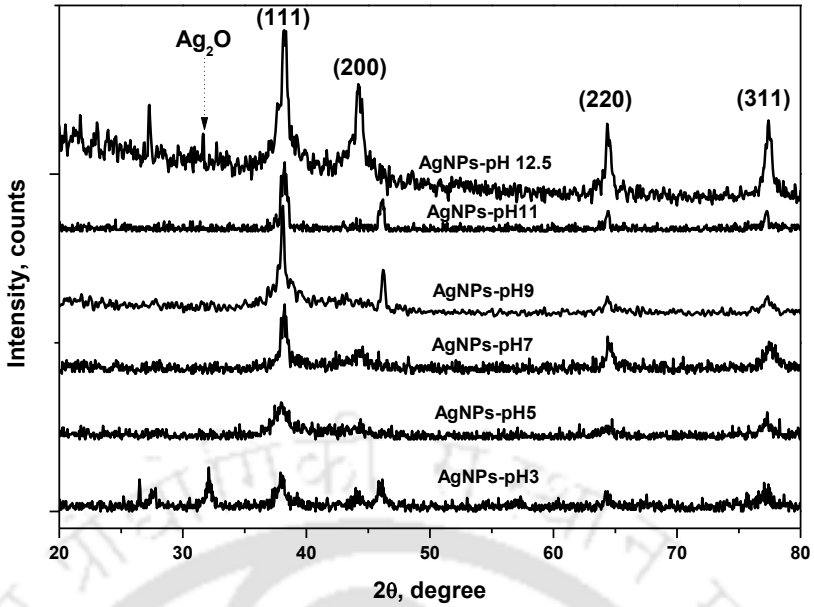

Figure 3.29. XRD patterns of synthesized AgNPs.

3.3.2 Size and stability monitoring of AgNPs-pH9 over thirty days

The retention of the size of AgNPs-pH9 and zeta-potential with the post-synthesis aging time was tested for 30 days. Particles were separated after 24 h of synthesis time, washed and redispersed with the same amount of water. A gradual increment in particle size was observed with the aging time (**Figure 3.30**). The initial size of 43 nm increased to 46, 53, and 65 nm after 7, 20, and 30 days, respectively. Initially, zeta-potential was -40.5 mV and, thereafter, it increased slowly to -38.5 mV after 30 days (**Figure 3.30**). A clear co-relation between zeta-potential variation and particle size with the aging time could be observed. The increase in particle size was relatively slower for first 15 days and, a similar trend was also noted for the zeta-potential increase. The negative-negative repulsive force assisted the colloidal stability and dispersity of AgNPs.

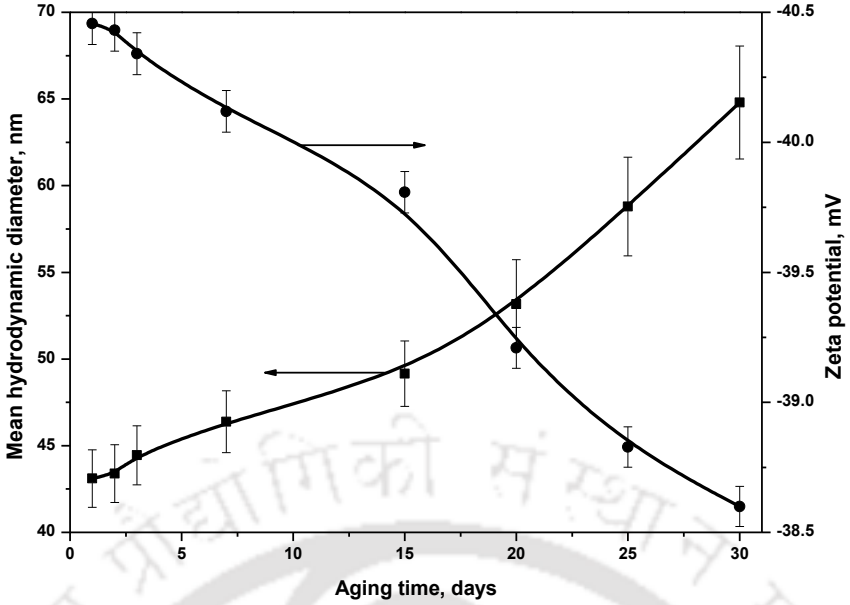

Figure 3.30. Effect of ageing time on particle size and zeta potential of AgNPs-pH9. Experimental conditions: $AgNO_3$ concentration 1 mM, reaction temperature 28±2 °C, and volume 10 mL.

3.3.3 Size dependent antimicrobial activity of AgNPs

The bacterial growth kinetics was studied using the spectrophotometric technique at different doses of AgNPs-pH9. Two bacterial strains, i.e., *B. subtilis* and *E. coli* were tested. **Figures 3.31(a) and 3.31(b)** show the bacterial growth inhibition in the presence of AgNPs-pH9 and its comparison with the control media. The rate of inhibition increased gradually with the increase in particles concentration. Both *B. subtilis* and *E. coli* with AgNPs-pH9 ≥25 μg mL^{-1} exhibited the complete growth inhibition. The growth didn't propagate with *E. coli*, so, the lag phase appeared early. In the case of *B. subtilis*, the stationary phase could not be visualized distinctly. However, the stationary phase was clearly distinguishable with *E. coli* due to a higher growth inhibition (Agnihotri et al., 2014). 2, 5, and 10 μg mL^{-1} AgNPs-pH9 caused 6, 34, and 45 % decrease in *B. subtilis* growth compared to the control media. *E. coli* at the same concentration of AgNPs-pH9 showed 12, 45, and 68 % reduction in the cell density. A Gram-negative bacterium has a protective peptidoglycan membrane whereas a Gram-positive bacterium doesn't have it (**Section 3.2.3**). AgNPs owning to free radical character can break the membrane lipids (Adegboyega et al., 2013) resulting in the damage of cellular materials (**Figure 3.32**). The g-factor varied from 2.0052 to 2.0058 which is close to ascorbate free radical (Eq. 3.4) (Buettner and Jurkiewicz, 1993).

It was also noticed that the illumination of visible light (60 W, Bajaj, India) improved the antimicrobial activity of AgNPs (**Figure 3.31**). The growth inhibition was even faster in the presence of light. Tahir et al. (2015) found the complete growth inhibition of *E. coli* within 4 h using AgNPs (15-40 nm) under the visible light illumination, but it took 24 h in the absence of light (Tahir et al., 2015).

The kinetic studies for the inactivation of *B. subtilis* and *E. coli* were performed at first using AgNPs-pH9 to determine the time required to reach the steady growth phase which is in particular useful to visualize the effects of size-dependent antimicrobial activity of AgNPs. Usually, the smaller particles give better penetrability into the bacterial cell membrane, and the NPs with higher surface area interacts more with the bacteria leading to a higher antimicrobial activity (Ajitha et al., 2015; Balakumaran et al., 2015). Similar results were also obtained in this work for AgNPs with different particles sizes (**Figure 3.33**) (Agnihotri et al., 2014; Ruparelia et al., 2008).

Small and symmetrical NPs with a narrow FWHM exhibits a better inhibitory action against the bacterial growth compared to the asymmetric or skewed SPR with a wider FWHM (Mlalila et al., 2017). They have a low NPs dispersity due to their larger size distribution compared to NPs with a narrow size distribution (mostly monodispersed and skewed at the center. The symmetric NPs exhibit a better contact with microbial cells owing to large area to volume ratio. So, the polydispersed NPs exhibit a lower contact with microbial cells, and thus it shows a lower inhibitory effect on both *E. coli* and *B. subtilis* growth.

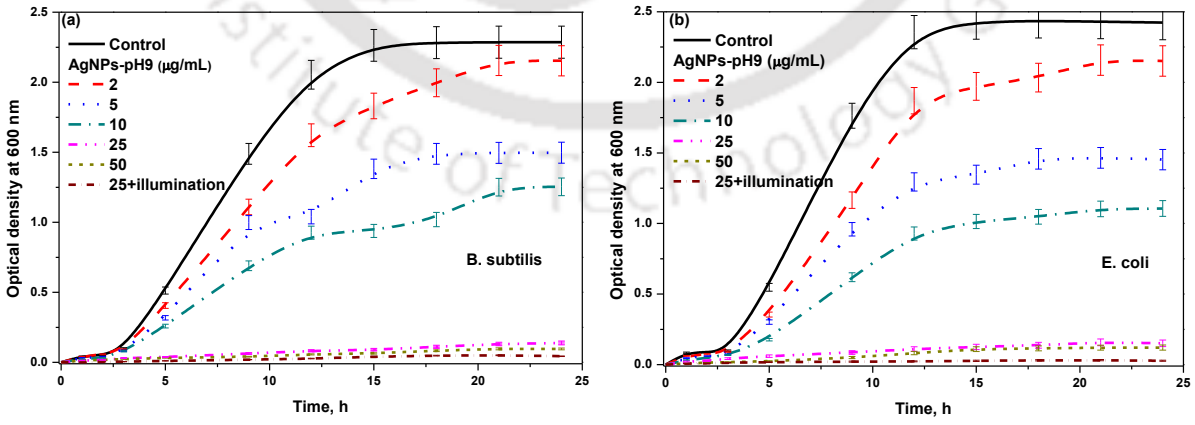

Figure 3.31. Bacterial growth in terms of optical density measurements against doses of AgNPs-pH9 at a wavelength of 600 nm for (a) *B. subtilis* and (b) *E. coli*.

The antibacterial activity of AgNPs was also examined by the disk diffusion method at 25 mg L^{-1} AgNPs (**Figure 3.32**) as in **Section 3.2.3**. The results were compared with Streptomycin (S 10) and Ampicillin (Amp) controls at 30 mg L^{-1} concentration for the inactivation study. It was found that bio-extract alone inhibited the growth of both *B. subtilis* and *E. coli* with 18 and 17 mm zone diameter. S 10 control media exhibited the maximum inhibition zone of 36 mm against *E. coli*. However, both the bacterial strains were resistant to Amp control, and the growth was quite less (15 mm inhibition zone). AgNPs synthesized at different pH also showed notable variation in the inhibition behavior. The inhibition efficiency was increased with the increase in synthesis pH. The antimicrobial activity of AgNPs-pH3 was the lowest and, after that, it increased up to AgNPs-pH9 with both the strains.

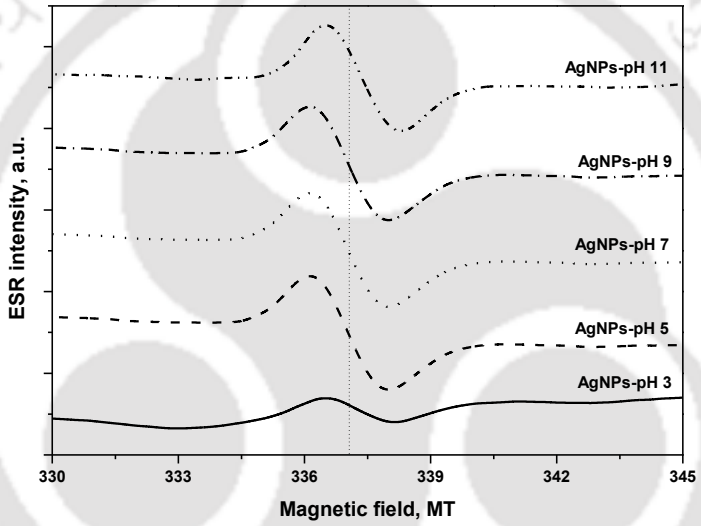

Figure 3.32. ESR spectra of AgNPs.

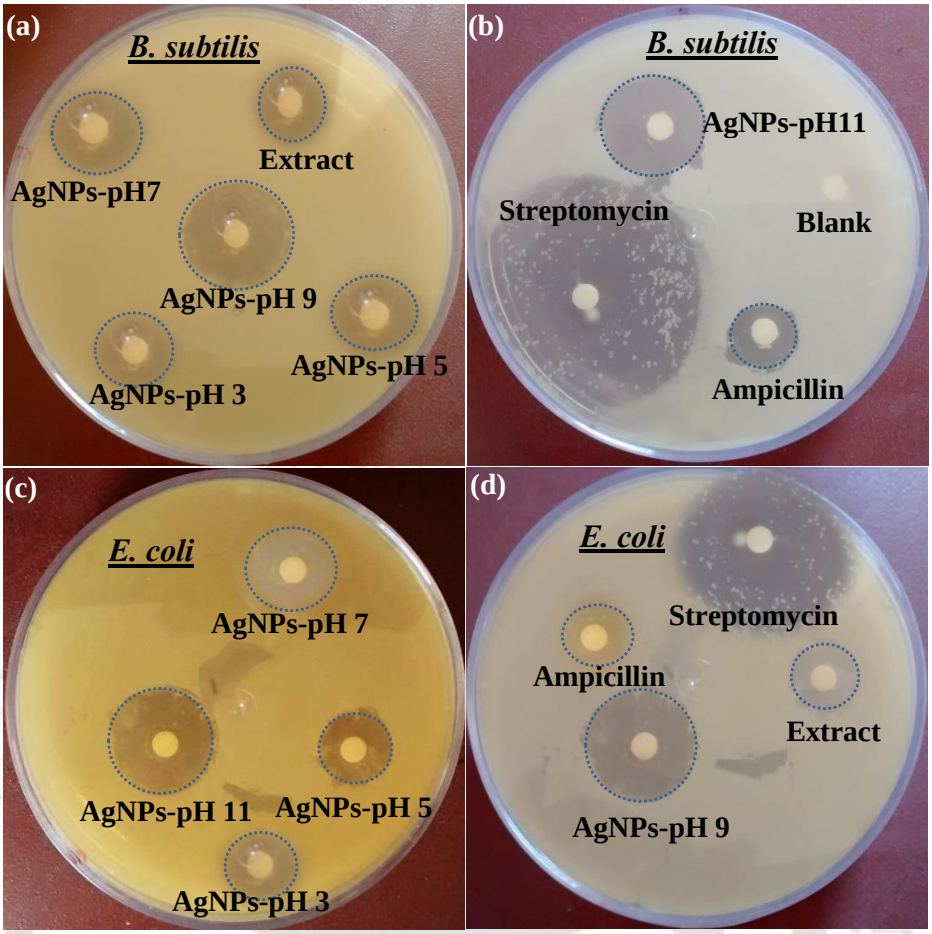

Figure 3.33. *B. subtilis* and *E. coli* inhibition by AgNPs and antibiotic control media. Experimental conditions: Concentration of S10, Amp: 30 mg mL^{-1}, AgNPs concentration 20 mg mL^{-1}, incubation temperature 37ºC and reaction time 24 h.

3.3.4 AA stability and mechanism of AgNPs formation

The effect of pH on the stability of AA is shown in **Figure 3.34**. AA concentration was found to be 170 mg L^{-1} at pH 5.8 (natural extract pH). There was a gradual decay in AA concentration in the bio-extract with the decrease in pH, but, it increased at a higher pH (5.8<pH<9). AA is converted to dehydro-AA through a free radical intermediate in a reversible process at mild acidic and neutral pH (Bachmann et al., 2014; Fenoll et al., 2011). However, the inter-conversion is irreversible at a higher pH (Wechtersbach and Cigic, 2007). These results are in line with a slightly higher concentration of residual AA in the extract after AgNPs synthesis at a higher pH (**Figure 3.34**). AA (m/z 175) didn't appear in the mass spectra of the bio-extract after AgNPs formation at pH 3 but dehydro-AA (m/z 174.1) was identified (**Figures 3.35** and **3.36**). The mass spectrum of commercial AA is shown in **Figure 3.37**. AA, as a sacrificial electron donor, reduces Ag_2O (or Ag^+) and, dehydro-AA or 2,3-

diketogulonic acid (2,3-DKG, m/z 192) is formed (Eq. 3.6) (Smuda and Glomb, 2013). 2,3-DKG appeared in the spectra at pH 9 and 12.5. The fragments with m/z of 127, 147.9, and 165.9 may be of oxalic acid, xylosone, and xylonic acid, respectively (Smuda and Glomb, 2013; Zhang et al., 2014). Dehydro-AA, 2,3-DKG, oxalic, pyruvic, glyceric, and threonic acids were detected in the mass spectra which are usually the degradation products of AA (Smuda and Glomb, 2013) (**Figures 3.35** and **3.36**). Zhang et al. (2014) found that the oxidation of AA to 2,3-DKG can yield the fragments like pyruvic acid (m/z 87.01), glyceric acid (m/z 104.1), and threonic acid (m/z 134) from the degradation of 2,3-DKG during synthesis of palladium nanoparticles (Zhang et al., 2014). Flavonoids are also could be responsible for the formation of AgNPs (Sahu et al., 2016) but, protein molecules usually provide the stability of the particles as it acts as the capping agents (Mandal et al., 2005).

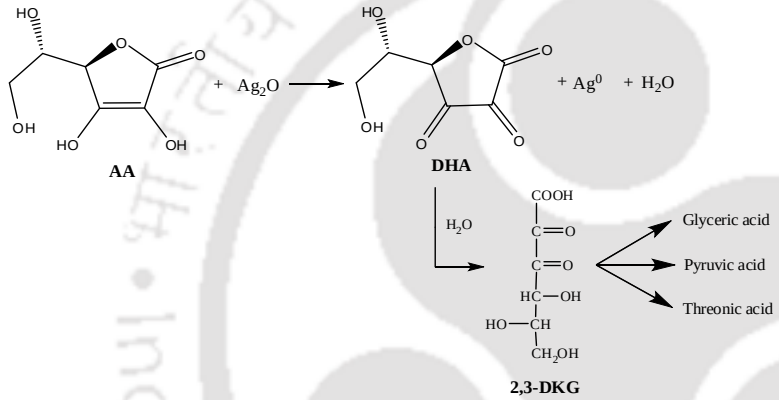

(3.6)

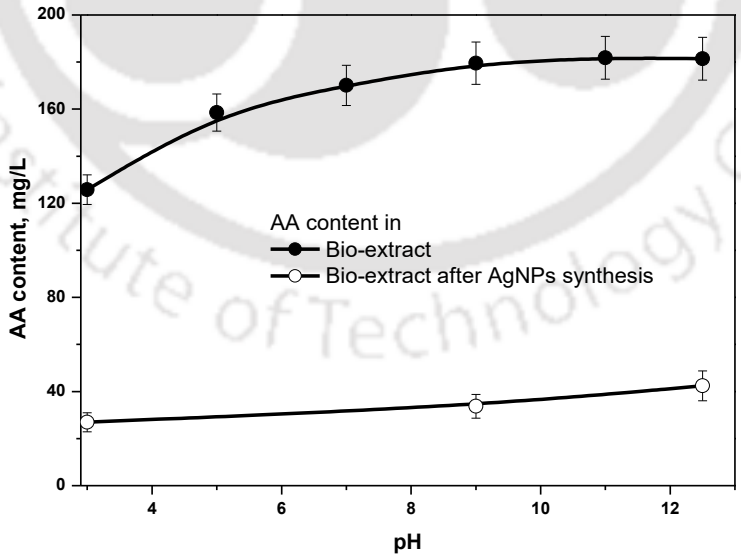

Figure 3.34. AA in bio-extract at different pH. Mobile phase of acetic acid (0.05 %) and acetonitrile (80:20 v/v), flow rate of 1 mL min^{-1} and wavelength of 254 nm.

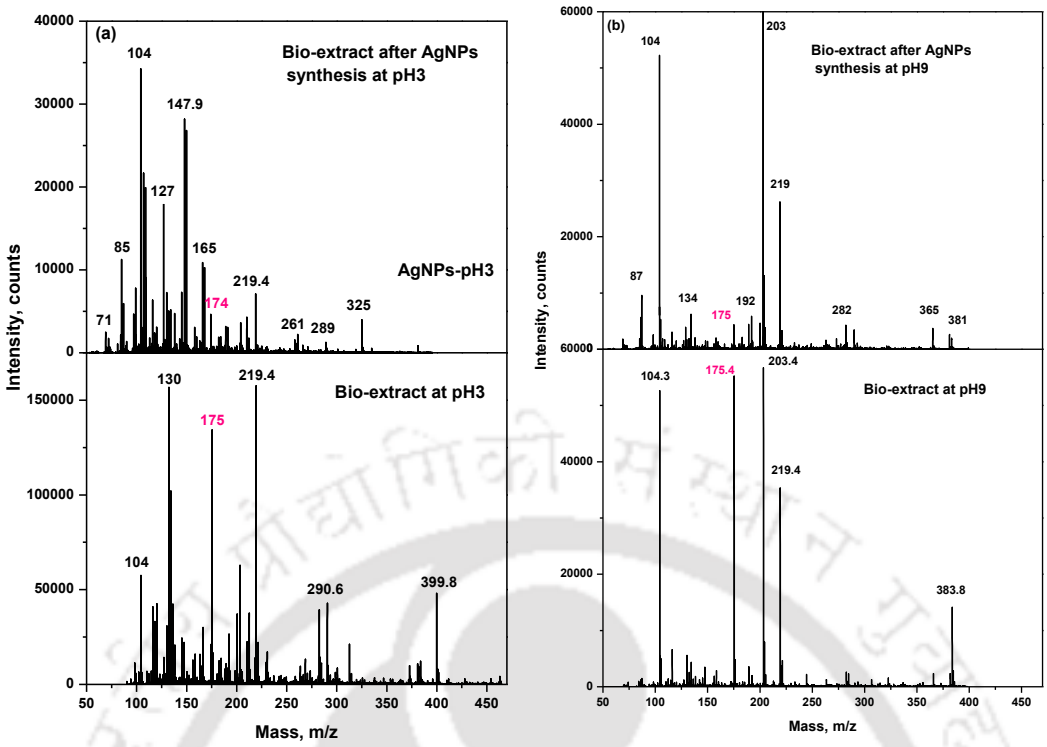

Figure 3.35. Mass spectra of *S. edule* fruit fresh bio-extract and bio-extract after AgNPs formation at (a) pH 3, (b) pH 9.

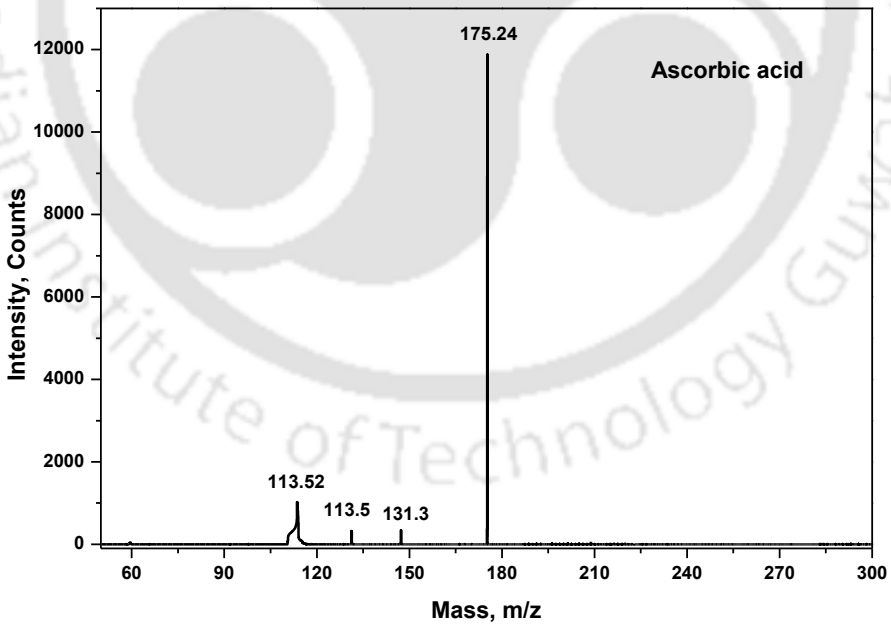

Figure 3.36. Mass spectra of commercial AA.

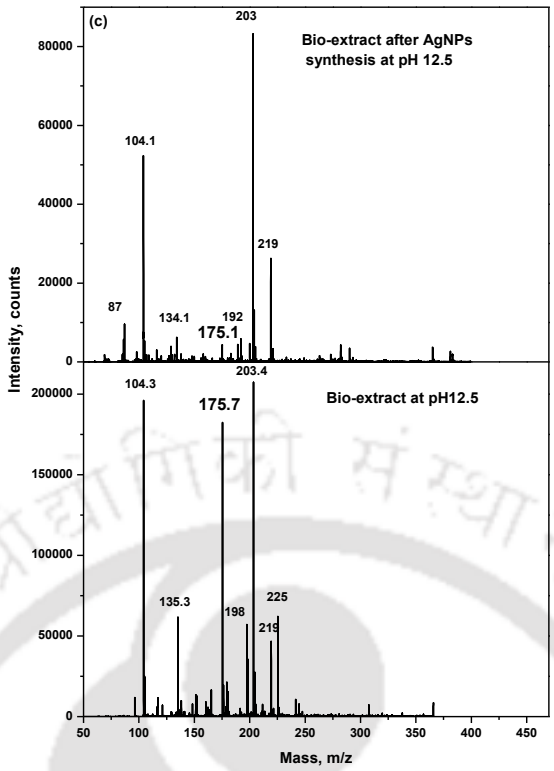

Figure 3.37. Mass spectra of *S. edule* fruit fresh bio-extract and bio-extract after AgNPs formation at pH 12.5.

3.4 Major Findings

Nearly spherical AgNPs was successfully synthesized at room temperature using the aqueous *S. edule* fruit extract. The linear yield of AgNPs with the reaction time was even faster than many chemical and UV-photo reduction processes. The natural capping agents protected particle aggregation with 98% AgNPs formation within 24 h. The characteristic optical absorption band of AgNPs appeared at around 450 nm owing to longitudinal plasmon resonance vibration. The biosynthesized AgNPs possessed good crystallinity with FCC crystals, and the selected area electron diffraction planes were consistent with the XRD patterns. The mean hydrodynamic diameter of AgNPs was found to be dependent on the size of (dry) particles yielded with the reaction time. AFM images confirmed that AgNPs were around 35 nm. The sharp rise in negative zeta potential from a highly acidic medium with the increase in pH was indicative of its affinity for destabilization over a wide range of pH.

Bio-inspired synthesis of AgNPs using the *S. edule* extract is strongly pH dependent which in turn determines the size, shape, self-stabilization, and purity of particles and, its mechanism of formation. pH also controls the concentration of AA in the bio-extract. However, the residual AA concentration didn't vary significantly after the formation of

AgNPs at different pH. AgNPs were formed through the reduction of both Ag^+ and Ag_2O; but, the smaller particles of nearly spherical shape were found at a higher pH with a faster kinetics where Ag_2O is abundant. A gradual blue shift in the SPR peak at around 425 nm was noticed with the decrease in particle sizes with the increase in synthesis pH. The intense negative zeta-potential and formation silver-ascorbate layer on AgNPs at a higher pH facilitated the prevention of particles aggregation. The average hydrodynamic diameters were 68, 60, 45, 31, 15, and 9 nm at pH 3, 5, 7, 9, 11, and 12.5, respectively. AgNPs exhibited the character of ascorbate free radicals which might cause the synergistic effects for the antimicrobial activities. AgNPs outperformed Streptomycin and, Ampicillin control media for the inactivation of Gram negative bacterium, *E. coli* and the order of inhibition was AgNPs>> Streptomycin> Ampicillin. AgNPs also was effective for the inhibition of growth of pathogenic fungus, *A. thermomutans.* This bio-mediated synthesis is rather simple, eco-friendly and cost effective as compared to conventional techniques which uses harmful chemicals and energy intensive processes. This study has opened up that metal nanoparticles synthesized using a biological route would be further applied for wound healing, and electrocatalytic CO_2 reduction to value added chemical and electrochemical sensing of H_2O_2, PhACs, pesticides, etc.

References

Adegboyega, N.F., Sharma, V.K., Siskova, K., Zbořil, R., Sohn, M., Schultz, B.J., Banerjee, S., 2013. Interactions of aqueous Ag+ with fulvic acids: Mechanisms of silver nanoparticle formation and investigation of stability. Environ. Sci. Technol. 47, 757–764.

Agnihotri, S., Mukherji, S., Mukherji, S., 2014. Size-controlled silver nanoparticles synthesized over the range 5–100 nm using the same protocol and their antibacterial efficacy. RSC Adv. 4, 3974–3983.

Ahmed, S., Ahmad, M., Swami, B.L., Ikram, S., 2016. A review on plants extract mediated synthesis of silver nanoparticles for antimicrobial applications: A green expertise. J. Adv. Res. 7, 17–28.

Ajitha, B., Reddy, Y.A.K., Reddy, P.S., 2015. Enhanced antimicrobial activity of silver nanoparticles with controlled particle size by pH variation. Powder Technol. 269, 110–117.

Bachmann, C., Probst, B., Guttentag, M., Alberto, R., 2014. Ascorbate as an electron relay between an irreversible electron donor and Ru(ii) or Re(i) photosensitizers. Chem. Commun. 50, 6737–6739.

Badawy, A.M.E., Luxton, T.P., Silva, R.G., Scheckel, K.G., Suidan, M.T., Tolaymat, T.M., 2010. Impact of environmental conditions (pH, ionic strength,and electrolyte type) on the surface charge and aggregation of silver nanoparticle suspensions. Environ. Sci. Technol. 44, 1260–1266.

Balakumaran, M.D., Ramachandran, R., Kalaichelvan, P.T., 2015. Exploitation of endophytic fungus, Guignardia mangiferae for extracellular synthesis of silver nanoparticles and their in vitro biological activities. Microbiol. Res. 178, 9–17.

Bar, H., Bhui, D.K., Sahoo, G.P., Sarkar, P., Pyne, S., Misra, A., 2009. Green synthesis of silver nanoparticles using seed extract of Jatropha curcas. Colloids Surfaces A Physicochem. Eng. Asp. 348, 212–216.

Buettner, R.G., Jurkiewicz, B.A., 1993. Ascorbate free radical as a marker of oxidative stress: An EPR study. Free Radic. Biol. Med. 14, 49–55.

Cai, Y., Tan, F., Qiao, X., Wang, W., Chen, J., Qiu, X., 2016. Room-temperature Synthesis of Silica Supported Silver Nanoparticles in Basic Ethanol Solution and Their Antibacterial Activity. RSC Adv. 6, 18407–18412.

Carballo, T., Gil, M.V., Gomez, X., Gonzalez-Andres, F., Moran, A., 2008. Characterization of different compost extracts using Fourier-transform infrared spectroscopy (FTIR) and thermal analysis. Biodegradation 19, 815–830.

Castro, L., Blazquez, M.L., Munoz, J.A., Gonzalez, F., Ballester, A., 2013. Biological synthesis of metallic nanoparticles using algae. IET Nanobiotechnology 7, 1–8.

Chebrolu, K.K., Jayaprakasha, G.K., Yoo, K.S., Jifon, J.L., Patil, B.S., 2012. An improved sample preparation method for quantification of ascorbic acid and dehydroascorbic acid by HPLC. LWT - Food Sci. Technol. 47, 443–449.

Chhatre, A., Solasa, P., Sakle, S., Thaokar, R., Mehra, A., 2012. Color and surface plasmon effects in nanoparticle systems: Case of silver nanoparticles prepared by microemulsion route. Colloids Surfaces A Physicochem. Eng. Asp. 404, 83–92.

Dauthal, P., Mukhopadhyay, M., 2013. Biosynthesis of palladium nanoparticles using Delonix regia leaf extract and its catalytic activity for nitro-aromatics hydrogenation. Ind. Eng. Chem. Res. 52, 18131–18139.

Dauthal, P., Mukhopadhyay, M., 2012. Prunus domestica fruit extract-mediated synthesis of gold nanoparticles and its catalytic activity for 4-nitrophenol reduction. Ind. Eng. Chem. Res. 51, 13014–13020.

Edison, J.I.E.T.N., Sethuraman, M.G., 2013. Electrocatalytic reduction of benzyl chloride by green synthesized silver nanoparticles using pod extract of Acacia nilotica. ACS Sustain. Chem. Eng. 1, 1326–1332.

Fenoll, J., Martínez, A., Hellín, P., Flores, P., 2011. Simultaneous determination of ascorbic and dehydroascorbic acids in vegetables and fruits by liquid chromatography with tandem-mass spectrometry. Food Chem. 127, 340–344.

Friedman, M., Jurgens, H.S., 2000. Effect of pH on stability of plant phenolic compounds. J. Agric. Food Chem. 48, 2101–2110.

Gajbhiye, M., Kesharwani, J., Ingle, A., Gade, A., Rai, M., 2009. Fungus-mediated synthesis of silver nanoparticles and their activity against pathogenic fungi in combination with fluconazole. Nanomedicine Nanotechnology, Biol. Med. 5, 382–386.

Gajbhiye, V., Leah, E., Chen, G., Alex, L., Zheng, Q., Steyer, B., Gong, S., Saha, K., 2014. Drug-loaded nanoparticles induce gene expression in human pluripotent stem cell derivatives. Nanoscale 6, 521–531.

Gunalan, S., Sivaraj, R., Rajendran, V., 2012. Green synthesized ZnO nanoparticles against bacterial and fungal pathogens. Prog. Nat. Sci. Mater. Int. 22, 693–700.

Huang, H.H., Ni, X.P., Loy, G.L., Chew, C.H., Tan, K.L., Loh, F.C., Deng, J.F., Xu, G.Q., 1996. Photochemical formation of silver nanoparticles in poly(N -vinylpyrrolidone). Langmuir 12, 909–912.

Huang, J., Zhan, G., Zheng, B., Sun, D., Lu, F., Lin, Y., Chen, H., Zheng, Z., Zheng, Y., Li, Q., 2011. Biogenic silver nanoparticles by Cacumen Platycladi extract: Synthesis, formation mechanism, and antibacterial activity. Ind. Eng. Chem. Res. 50, 9095–9106.

Ibrahim, H.M.M., 2015. Green synthesis and characterization of silver nanoparticles using banana

peel extract and their antimicrobial activity against representative microorganisms. J. Radiat. Res. Appl. Sci. 8, 265–275.

Jha, A.K., Prasad, K., 2010. Green synthesis of silver nanoparticles using cycas leaf. Int. J. Green Nanotechnol. Phys. Chem. 1, 110–117.

Khalil, M.M.H., Ismail, E.H., El-Baghdady, K.Z., Mohamed, D., 2014. Green synthesis of silver nanoparticles using olive leaf extract and its antibacterial activity. Arab. J. Chem. 7, 1131–1139.

Kim, J.S., Kuk, E., Yu, K.N., Kim, J.-H., Park, S.J., Lee, H.J., Kim, S.H., Park, Y.K., Park, Y.H., Hwang, C.-Y., Kim, Y.-K., Lee, Y.-S., Jeong, D.H., Cho, M.-H., 2007. Antimicrobial effects of silver nanoparticles. Nanomedicine Nanotechnology, Biol. Med. 3, 95–101.

Kim, S.W., Kim, K.S., Lamsal, K., Kim, Y.J., Kim, S. Bin, Jung, M., Sim, S.J., Kim, H.S., Chang, S.J., Kim, J.K., Lee, Y.S., 2009. An in vitro study of the antifungal effect of silver nanoparticles on oak wilt pathogen Raffaelea sp. J. Microbiol. Biotechnol. 19, 760–764.

Konwarh, R., Gogoi, B., Philip, R., Laskar, M.A., Karak, N., 2011. Biomimetic preparation of polymer-supported free radical scavenging, cytocompatible and antimicrobial "green" silver nanoparticles using aqueous extract of Citrus sinensis peel. Colloids Surfaces B Biointerfaces 84, 338–345.

Li, W.R., Xie, X.B., Shi, Q.S., Zeng, H.Y., Ou-Yang, Y.S., Chen, Y. Ben, 2010. Antibacterial activity and mechanism of silver nanoparticles on Escherichia coli. Appl. Microbiol. Biotechnol. 85, 1115–1122.

Mandal, S., Phadtare, S., Sastry, M., 2005. Interfacing biology with nanoparticles. Curr. Appl. Phys. 5, 118–127.

Mittal, A.K., Chisti, Y., Banerjee, U.C., 2013. Synthesis of metallic nanoparticles using plant extracts. Biotechnol. Adv. 31, 346–356.

Mlalila, N.G., Swai, H.S., Hilonga, A., Kadam, D.M., 2017. Antimicrobial dependence of silver nanoparticles on surface plasmon resonance bands against Escherichia coli. Nanotechnol. Sci. Appl. 10, 1–9.

Nemade, K.R., Waghuley, S.A., 2015. LPG sensing performance of CuO–Ag2O bimetallic oxide nanoparticles. St. Petersbg. Polytech. Univ. J. Phys. Math. 1, 249–255.

Oluwafemi, O.S., Revaprasadu, N., Adeyemi, O.O., 2010. A facile "green" synthesis of ascorbic acid-capped ZnSe nanoparticles. Colloids Surfaces B Biointerfaces 79, 126–130.

Pastoriza-Santos, I., Koktysh, D.S., Mamedov, A.A., Giersig, M., Kotov, N.A., Liz-Marzán, L.M., 2000. One-pot synthesis of Ag@TiO_2 core-shell nanoparticles and their layer-by-layer assembly. Langmuir 16, 2731–2735.

Prathna, T.C., Chandrasekaran, N., Raichur, A.M., Mukherjee, A., 2011. Biomimetic synthesis of silver nanoparticles by Citrus limon (lemon) aqueous extract and theoretical prediction of particle size. Colloids Surfaces B Biointerfaces 82, 152–159.

Ruparelia, J.P., Chatterjee, A.K., Duttagupta, S.P., Mukherji, S., 2008. Strain specificity in antimicrobial activity of silver and copper nanoparticles. Acta Biomater. 4, 707–716.

Sadeghi, B., Mohammadzadeh, M., Babakhani, B., 2015. Green synthesis of gold nanoparticles using *Stevia rebaudiana* leaf extracts: Characterization and their stability. J. Photochem. Photobiol. B Biol. 148, 101–106.

Sadowski, Z., Malliszewska, I.., GrochoWalska, B., Polowczyk, I., Kozlexki, T., 2008. Synthesis of silver nanoparticles using microorganisms. Mater. Sci. 26, 419–424.

Sahu, N., Soni, D., Chandrashekhar, B., Satpute, D.B., Saravanadevi, S., Sarangi, B.K., Pandey, R.A., 2016. Synthesis of silver nanoparticles using flavonoids: hesperidin, naringin and diosmin, and their antibacterial effects and cytotoxicity. Int. Nano Lett. 6, 173–181.

Sathishkumar, M., Sneha, K., Won, S.W., Cho, C.-W., Kim, S., Yun, Y.-S., 2009. Cinnamon zeylanicum bark extract and powder mediated green synthesis of nano-crystalline silver particles

and its bactericidal activity. Colloids Surfaces B Biointerfaces 73, 332–338.

Shahzad, A., Kim, W.-S., Yu, T., 2015. Synthesis, stabilization, growth behavior, and catalytic activity of highly concentrated silver nanoparticles using a multifunctional polymer in an aqueous-phase. RSC Adv. 5, 28652–28661.

Shankar, S.S., Ahmad, A., Sastry, M., 2003. Geranium leaf assisted biosynthesis of silver nanoparticles. Biotechnol. Prog. 19, 1627–1631.

Singhal, G., Bhavesh, R., Kasariya, K., Sharma, A.R., Singh, R.P., 2011. Biosynthesis of silver nanoparticles using *Ocimum sanctum* (Tulsi) leaf extract and screening its antimicrobial activity. J. Nanoparticle Res. 13, 2981–2988.

Smitha, S.L., Nissamudeen, K.M., Philip, D., Gopchandran, K.G., 2008. Studies on surface plasmon resonance and photoluminescence of silver nanoparticles. Spectrochim. Acta Part A Mol. Biomol. Spectrosc. 71, 186–190.

Smuda, M., Glomb, M.A., 2013. Maillard degradation pathways of Vitamin C. Angew. Chemie - Int. Ed. 52, 4887–4891.

Sun, Q., Cai, X., Li, J., Zheng, M., Chen, Z., Yu, C.P., 2014. Green synthesis of silver nanoparticles using tea leaf extract and evaluation of their stability and antibacterial activity. Colloids Surfaces A Physicochem. Eng. Asp. 444, 226–231.

Sutradhar, P., Saha, M., 2016. Silver nanoparticles: synthesis and its nanocomposites for heterojunction polymer solar cells. J. Phys. Chem. C 120, 8941–8949.

Tahir, K., Nazir, S., Li, B., Khan, A.U., Khan, Z.U.H., Ahmad, A., Khan, Q.U., Zhao, Y., 2015. Enhanced visible light photocatalytic inactivation of Escherichia coli using silver nanoparticles as photocatalyst. J. Photochem. Photobiol. B Biol. 153, 261–266.

Thanganathan, U., 2013. Investigation on Ammonium Phosphate Mixed SiO_2/Pilymer Hybrid composite Membranes, in: Materials Challenges in Alternative and Renewable Energy II: Ceramic Transactions. John Wiley & Sons, Inc., pp. 215–221.

Velusamy, P., Das, J., Pachaiappan, R., Vaseeharan, B., Pandian, K., 2015. Greener approach for synthesis of antibacterial silver nanoparticles using aqueous solution of neem gum (*Azadirachta indica L.*). Ind. Crops Prod. 66, 103–109.

Vijay Kumar, P.P.N., Pammi, S.V.N., Kollu, P., Satyanarayana, K.V. V, Shameem, U., 2014. Green synthesis and characterization of silver nanoparticles using *Boerhaavia diffusa* plant extract and their anti bacterial activity. Ind. Crops Prod. 52, 562–566.

Vivekanandhan, S., Schreiber, M., Mason, C., Kumar, A.M., Misra, M., 2014. Biointerfaces Maple leaf (*Acer sp.*) extract mediated green process for the functionalization of ZnO powders with silver nanoparticles. Colloids Surfaces B Biointerfaces 113, 169–175.

Wechtersbach, L., Cigic, B., 2007. Reduction of dehydroascorbic acid at low pH. J. Biochem. Biophys. Methods 70, 767–772.

Yilmaz, M., Turkdemir, H., Kilic, M.A., Bayram, E., Cicek, A., Mete, A., Ulug, B., 2011. Biosynthesis of silver nanoparticles using leaves of Stevia rebaudiana. Mater. Chem. Phys. 130, 1195–1202.

Zhang, A., Liu, M., Liu, M., Xiao, Y., Li, Z., Chen, J., Sun, Y., Zhao, J., Fang, S., Jia, D., Li, F., 2014. Homogeneous Pd nanoparticles produced in direct reactions: green synthesis, formation mechanism and catalysis properties. J. Mater. Chem. A 2, 1369–1374.

Zhang, Y., Chen, Y., Westerhoff, P., Crittenden, J., 2009. Impact of natural organic matter and divalent cations on the stability of aqueous nanoparticles. Water Res. 43, 4249–4257.

Zuas, O., Hamim, N., Sampora, Y., 2014. Bio-synthesis of silver nanoparticles using water extract of *Myrmecodia pendan* (Sarang Semut plant). Mater. Lett. 123, 156–159.

Chapter 4

Pt-Co Core-Shell Prismoidal Nanoparticles Synthesis

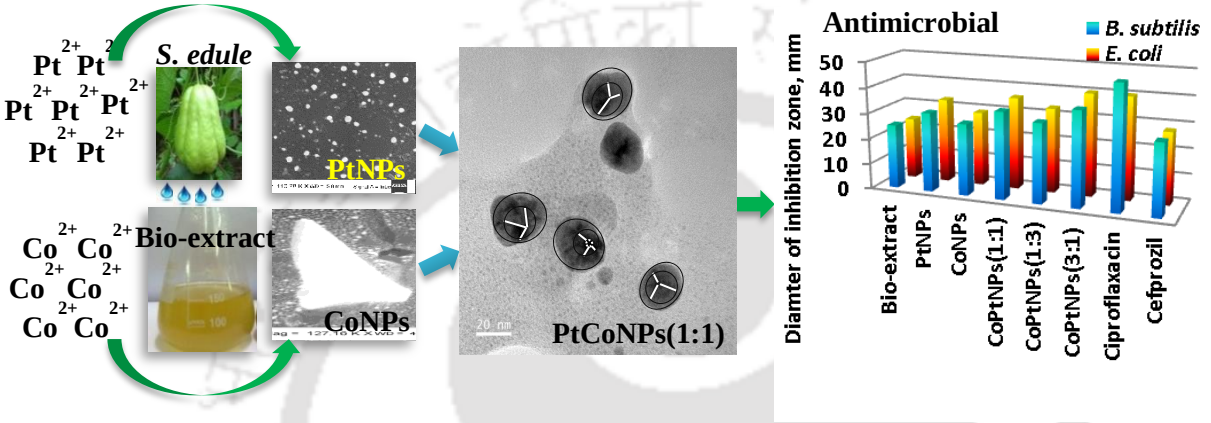

In this work, the aqueous fruit extract of S. edule was employed for a one pot synthesis of Co, Pt, and PtCo nanoparticles of prismoidal, spherical, and core-shell structures. The synthesis route is rather eco-friendly, cost-effective and energy-saving, and it doesn't need any additional chemicals apart from the metal precursor.

4.1 Specific Background

The bimetallic NPs usually exhibit activities better than mono metal NPs because they build a synergistic effect when two metals are joined together (Yu et al., 2013; Zhang et al., 2017). The bimetallic NPs synthesis is a quite interesting which involves a successive or simultaneous reduction of two metals resulting into either alloy form or core–shell structures. The sequential reduction refers to the reduction of shell metal over the pre-formed seed of core metal. The bimetallic NPs formation depends on purity, non-reactivity, and reducibility of metal ions. Core–shell NPs are a class of nanostructured materials that have recently gained attraction owing to their exciting properties and broad range of applications in biology, materials chemistry, sensors, and catalysis (Fakhri et al., 2017; Vigneshwaran et al., 2007). Platinum (Pt) and cobalt (Co) in nanostructures could possess enhanced antimicrobial

activities when they are mixed to form bimetallic NPs. Pt-based nanoalloys can be remarkably active catalysts regardless of the lower Pt-content and accordingly, the cost is reduced (Kovács et al., 2015).

In this work (**Chapter 4**), the aqueous fruit extract of *S. edule*, fruits of a perennial climber rich in AA (**Chapter 1 and Chapter 3**) was employed for a single stage synthesis of Pt and Co bimetallic core-shell nanostructures. The reduction process was simple, easy to handle, and monitored by AAS. The mono and bimetal Co and Pt NPs were characterized by DLS, FTIR spectroscopy, XRD, zeta-potential, FESEM, Field emission- TEM (FETEM) and TGA. The role of bimetallic Pt and Co core-shell NPs was also compared with mono metal NPs for the inactivation of *B. subtilis* and *E. coli* bacteria.

4.2 Results and Discussion

4.2.1 Physicochemical characteristics of PtCo NPs

To examine the formation mechanism of PtCo bimetallic core-shell particles, the investigations were performed using FESEM, FETEM, and powder XRD to understand the morphological evolution and crystal structure (**Figures 4.1 and 4.2**). It can be seen from **Figures 4.1(a), 4.1(b), 4.2(a) and 4.2(b)** that the Co nanostructures were composed of uniform solid prisms whereas PtNPs were obtained mostly in spherical shape. In the case of PtCoNPs after complete reaction at 90 ºC for 24 h, the colour of the reaction mixture turns to black from an initial orange colour which is indicative of the formation of metal NPs. It exhibited a well-defined shell and a solid core at the center forming a unique core–shell nanostructure (**Figures 4.1(c)** and **4.2(c)**). Such a core–shell nanostructure possesses a shell consisting of Co while it retains a dense core of Pt or PtCo alloy. The high-resolution TEM micrograph of a single particle indicated the clear lattice fringes with an interplanar d-spacing of edge/shell of 0.222 nm and the d-spacing of the centre/core of 0.227 nm which could attribute to Pt and Co nanostructures (**Figure 4.1(d)**), respectively (Zhang et al., 2017). Zhang et al. reported similar results with Pt and PtCo nano alloy using the controlled thermal treatment method (Zhang et al., 2017). The bright concentric circles (SAED patterns) depict the (111), (200), and (311) planes of face-centered cubic (FCC) PtCo crystals (**Figure 4.1(d-inset)**). The mean, lowest, and highest particle size, both in FESEM and FETEM analyses were very close (**Table 4.1**) and, the size distribution is shown in **Figure 4.2(d).** However, the dry particles sizes of PtNPs, CoNPs, and PtCoNPs(1:1) were about 60 % lower than the particles size measurements in the aqueous media using DLS (**Table 4.1**) as a few layers of

water molecules are counted with dynamic light scattering measurement (Kuehner et al., 1997). The polydispersity index of PtNPs and CoNPs were 0.18 and 0.38, and, it lied in between for the bimetallic core-shell particles (**Table 4.1**).

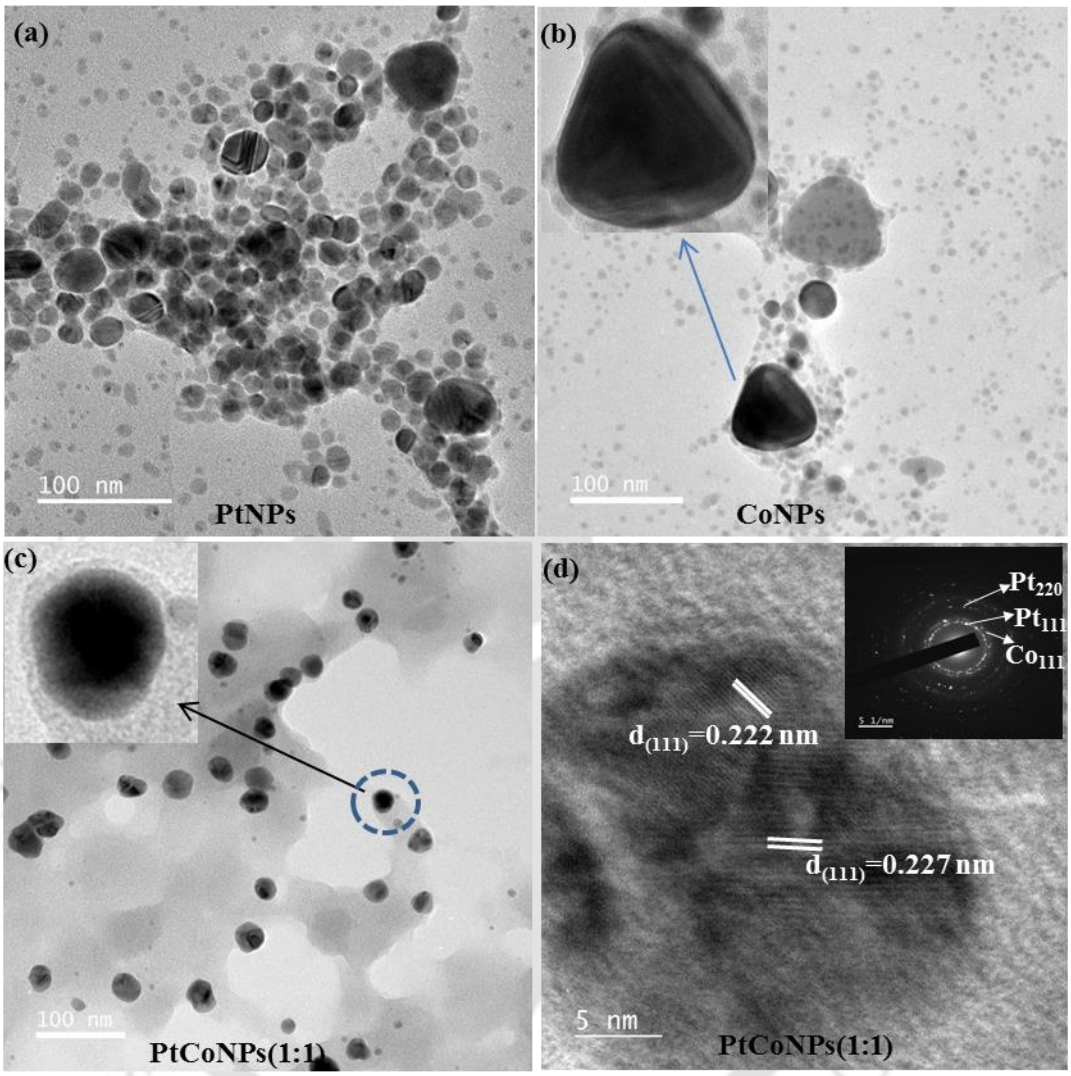

Figure 4.1. FETEM micrographs of (a) PtNPs, (b) CoNPs, (c) PtCoNPs and (d) High resolution TEM, and SAED patterns (inset) of PtCoNPs (d).

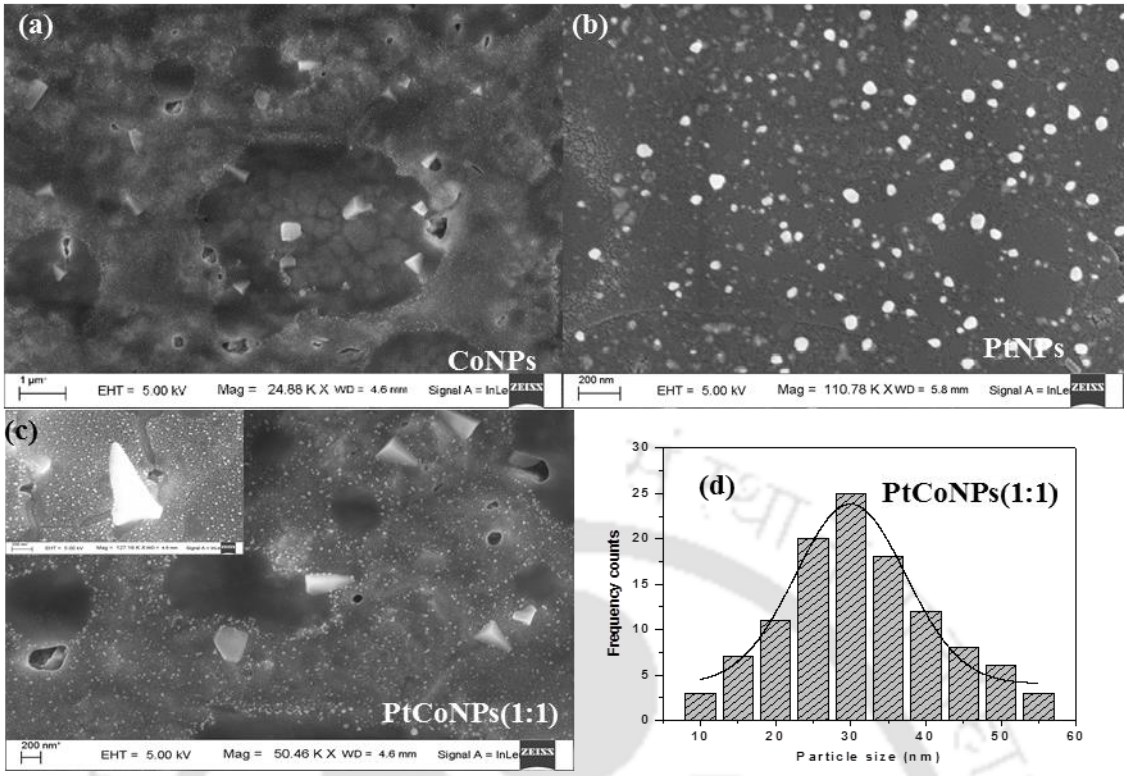

Figure 4.2. FESEM images of (a) CoNPs, (b) PtNPs, (c) PtCoNPs, and (d) particle size distribution of bimetallic PtCoNPs.

The XRD patterns of PtCoNPs are shown in **Figure 4.3**. The diffraction peaks at 40.3, 45.45, 53.42, 67.8 and 75.23° 2θ angle attributes to the FCC of Pt and Co NPs with the characteristic peaks from diffraction from Pt/Co(1 1 1), Pt(2 0 0), Co(2 0 0), Pt/Co(2 2 0), and Pt/Co(3 1 1) planes, respectively (Zhang and Chan, 2002). The peak positions of PtCoNPs were shifted to higher 2θ values in comparison to the characteristic peaks of pure PtNPs. The shift in 2θ angles indicates to a reduced lattice constant for Pt owing to the induction of a Co atom. The peak intensities of the PtCo and Co phases were weaker than that of the Pt phase. Zhang and Chan also observed similar results of lower peak intensity of the Co or PtCo alloy phases than the Pt phase which was for the lower crystallinity of Co phases (Zhang and Chan, 2002). The Scherrer's formula was used to determine the crystallite size at the major diffraction plane (1 1 1) (Rao and Golder, 2016). The crystallite sizes of PtNPs and CoNPs were 22.24 and 35.16 nm, whereas PtCo bimetallic NPs crystallite size lied in between the Pt and Co NPs (Table 1). The d-spacing of bimetal NPs was comparable with the interplanar spacing obtained from TEM micrograph. A weak peak at 2θ~33.5º corresponded to the presence of CoO. CoNPs in the ambient air could easily transform into CoO at the surface of NPs. So, a new CoO peak was observed.

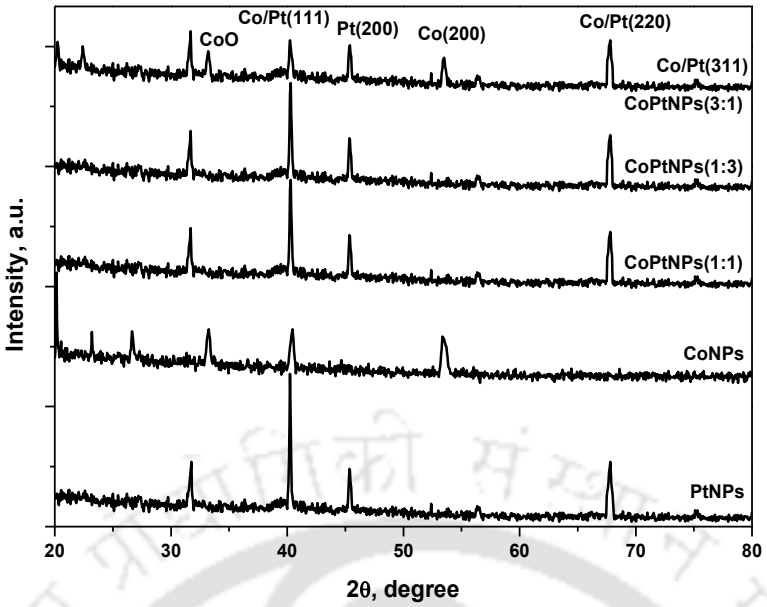

Figure 4.3. XRD patterns of Pt and Co mono and bimetallic nanostructures.

Table 4.1. Characteristic parameters of synthesized Co and Pt mono and bimetallic NPs.

Sample	Particle size from FESEM		Particle size from FETEM		Particle size from DLS		Poly dispersity index	XRD	
	Mean (nm)	Size range	Mean (nm)	Size range	Mean (nm)	Size range		d-spacing (nm)	Crystallite size (nm)
PtNPs	25.37	10-70	-	-	43.5	9-124	0.183	0.2293	22.247
CoNPs	47.31	30-110	-	-	68.8	21-146	0.387	0.2125	35.159
PtCo(1:1)	28.56	10-80	27.6	10-80	59.4	14-173	0.253	0.2185	31.344
PtCo(3:1)	-	-	-	-	55.1	12-147	0.281	0.2213	29.479
PtCo(1:3)	-	-	-	-	61.7	14-204	0.307	0.2245	33.425

Energy-dispersive X-ray (EDX) spectroscopic micrograph of PtCoNPs is shown in **Figure 4.4(a)**. The average composition of PtCo(1:1) gave an atom ratio of Co:Pt of 1:1.25 **(Figure 4.4(b))**. Pt and Co elemental distributions are shown in **Figures 4.4(c)** and **4.4(d)**. The composite image of Pt versus Co (**Figure 4.4(a)**) suggested that the surface of this nanoparticles contained more amount of Pt than Co.

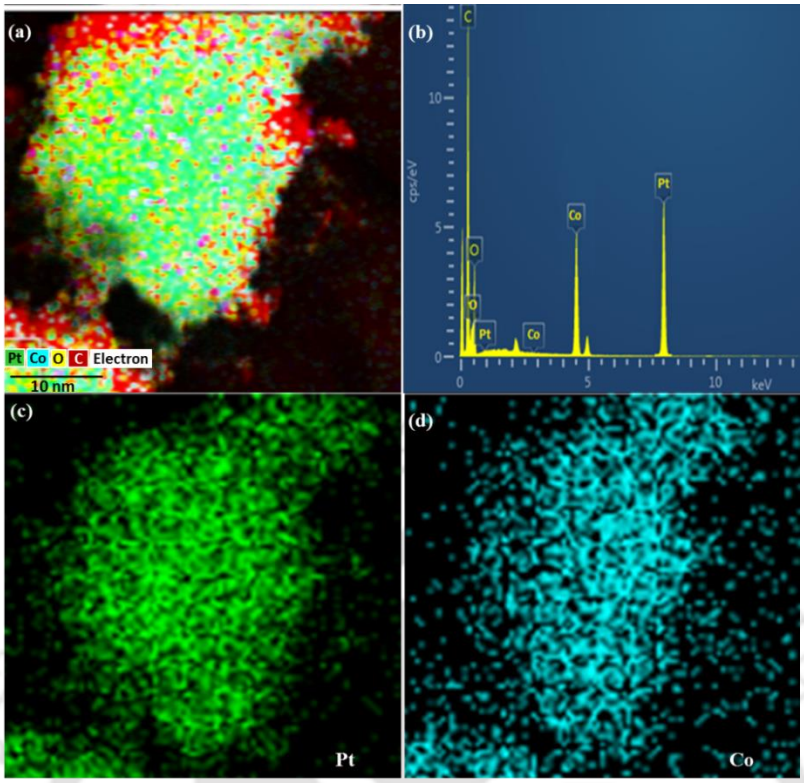

Figure 4.4. EDX analysis of PtCoNPs(1:1) (a) composite image of Pt vs Co, (b) EDX spectra, and (c-d) 2D electron energy loss spectroscopic mapping of Pt (green) and Co (blue).

OH^- ions reacted with Co^{2+} yielding $Co(OH)_2$ particles (Eq. 4.1) and, it was further reduced to Co^0 in the presence of ascorbic acid (AA). In the alkaline media, AA is reversibly oxidized (Eq. 4.2) to dehydro-AA (E^0 = 0.535 V vs. standard hydrogen electrode, SHE), and it is then irreversibly converted to 2,3 diketo-gulonic acid and oxalic acid. The tiny clusters of Co^0 would migrate onto the $Co(OH)_2$ surface and with time it grow to tiny CoNPs. Similarly, Pt^{2+} was reduced to PtNPs in the presence of AA in an alkaline medium (Eq. 4.3).

For the bimetallic system, Pt^{2+} ions were easily reduced than $Co(OH)_2$ due to a more positive reduction potential (Pt^{2+}/Pt^0: E^0 =1.18 V; $Co(OH)_2/Co^0 + OH^-$: E^0 =-0.73 V, Eqs. 4.4 and 4.5) (Podlovchenko and Maksimov, 2013). So, Pt^0 was formed quickly as a core then CoNPs surrounded as skin over PtNPs. Pt has a strong adsorption affinity towards hydrogen and splits it to form metal hydrides on the metal surface. Hydrogen atoms are first adsorbed on Pt. Consequently, $Co(OH)_2$ is easily reduced to Co^0 by the hydrogen atoms adsorbed on the Pt NPs due to a low reduction potential. So, Co^0 atoms are deposited on the surface of the PtNPs forming bimetallic PtCoNPs with core-shell structures (Corain et al., 2011).

$$Co^{2+} + 2NaOH \rightarrow Co(OH)_2 + 2Na^+ \quad (4.1)$$

$$Co(OH)_2 + C_6H_8O_6 \rightarrow Co + C_6H_6O_6 + 2H_2O \quad (4.2)$$

$$H_2PtCl_6 + 2C_6H_8O_6 + 6NaOH \rightarrow Pt + 2C_6H_6O_6 + 6NaCl + 6H_2O \quad (4.3)$$

$$Pt^{2+} + 2e^- \rightarrow Pt \quad (4.4)$$

$$Co(OH)_2 \rightarrow Co + 2OH^- \quad (4.5)$$

The yield of Pt and Co nanostructures at different initial concentrations are shown in **Figure 4.5**. About 97.7 and 94.1 % Pt^{2+} and Co^{2+} were converted to Pt^0 and Co^0 in 24 h reaction time and remained almost invariant even after that at 1 mM total concentration. However, both higher and lower concentration than 1 mM had a detrimental effect on the conversion for both the NPs. In the case of bimetal NPs, it was observed that the yield of PtNPs was higher than CoNPs for all the doses (**Figure 4.6**). These results are in consistent with the EDX analysis.

The reaction mixture (PtCoNPs(1:1)) color was also varied with time. Initially, it was light orange color and turned to light red after 3 h of reaction and became dark red after 24 h (**Figure 4.7**). There was no change in solution color after 24 h of reaction with PtCoNPs.

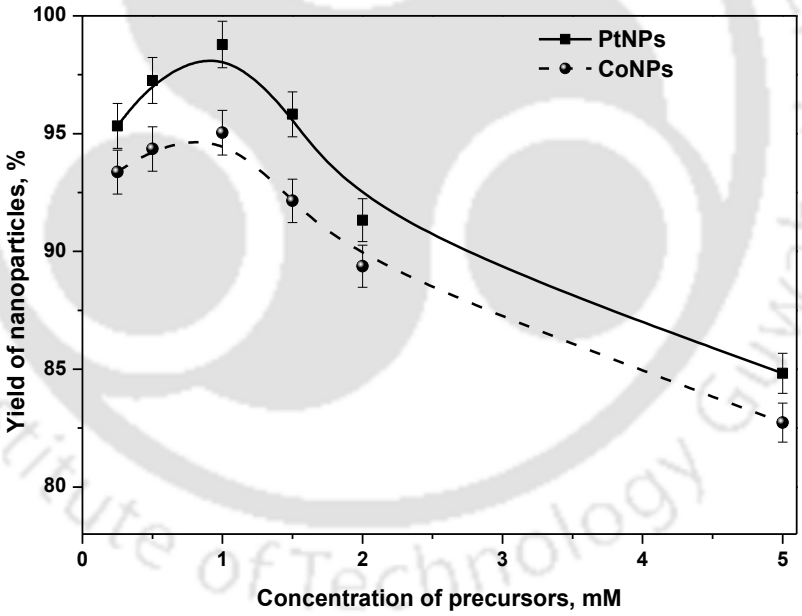

Figure 4.5. Yield of Pt and Co NPs at different initial concentrations.

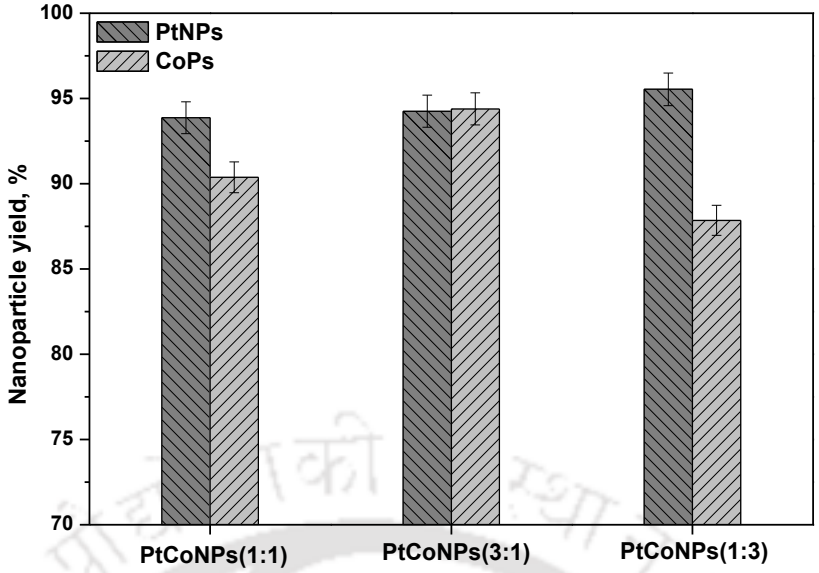

Figure 4.6. Yield of PtNPs and CoNPs in the case of PtCoNPs.

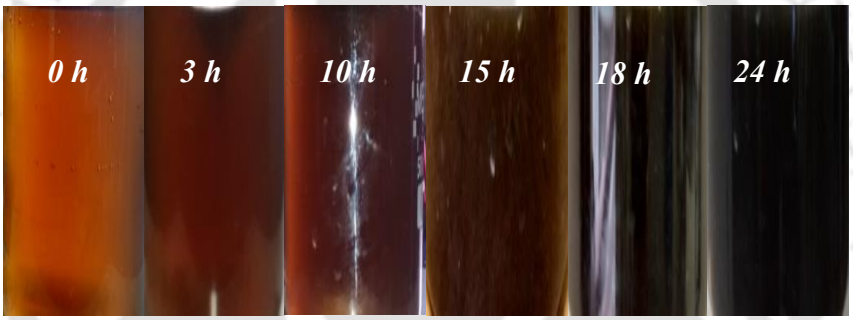

Figure 4.7. Variation of PtCoNPs(1:1) color intensity with synthesis time.

The existence of biomolecules on the surface of NPs was confirmed by TGA (**Figure 4.8**). The derivative mass losses occurred in three distinct temperature regions (**Figure 4.9**). A similar explanation as in **Section 3.2.2.3** is also applicable here. There was about 26, 27, and 51 % mass loss at 150–360 ºC for PtNPs, CoNPs and PtCoNPs(1:1) from the decomposition of organic compounds, like AA, carbohydrates, lignin molecules, ferulic acid, and quercetins (Sun et al., 2014). The third steady weight loss was found to be 25, 38, and 41 % at 370–900 ºC was due to the degradation of resistive aromatic complexes and bio-organic salt like carbonates removal (Sun et al., 2014). An average overall mass loss of 87, 76 and 77 % was observed within the whole temperature range. PtNPs showed the maximum mass loss as more capping agent surrounded the particles having a high surface area due to smaller size.

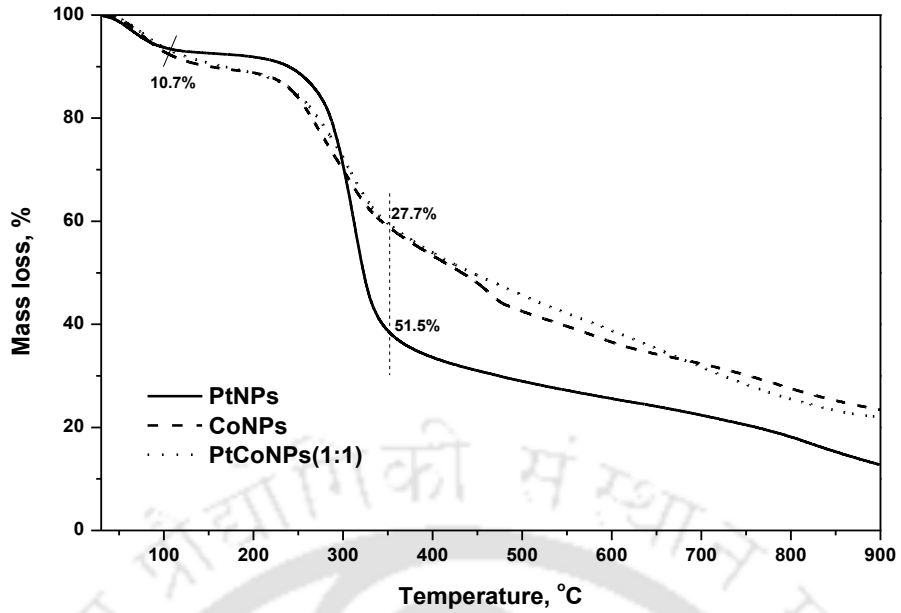

Figure 4.8. TGA profile of mono and bimetallic Pt and Co NPs.

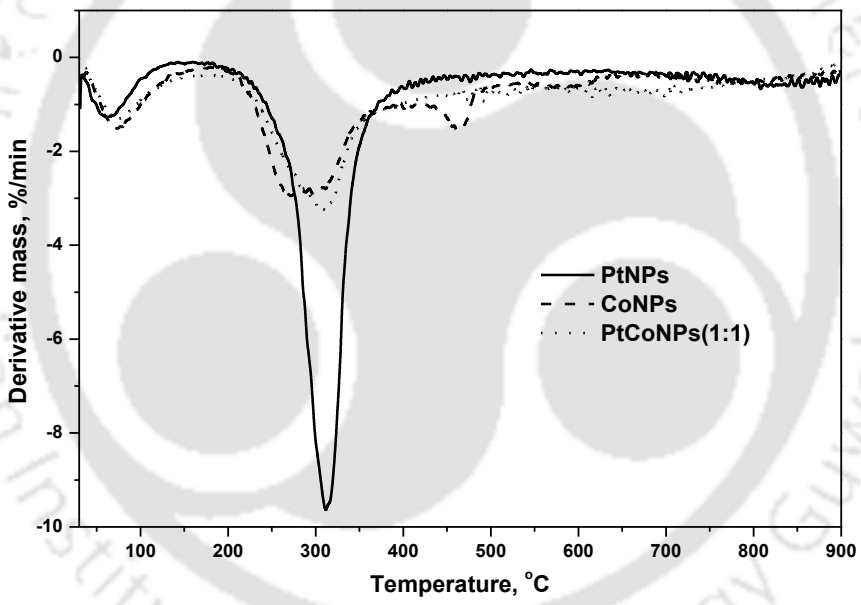

Figure 4.9. First derivative mass loss from Figure 4.7 vs. temperature.

FTIR spectra of bio-extract showed strong peaks at 1727, and 3329 cm^{-1} correspond to the hydroxyl group (**Figure 4.10**). The sharp peaks at 1062, 1377, and 1634 cm^{-1} was associated with the stretching vibration of O–C–C, C–O, and C=O bonds probably of AA (Oluwafemi et al., 2010). The existence of almost all the characteristic peaks of bio-extract in the NPs indicated that the stabilization of NPs was caused by the biomolecules present in the extract. The peak intensity was decreased in the case of NPs indicating a relatively lower concentration of biomolecules present on the NPs. The peak at 1135 cm^{-1} assigned to carboxylate group was found to diminish in the NPs indicating the possible conjugation of the

metal NPs with the biomolecules through the carboxylate group (Oluwafemi et al., 2010). It supports that AA in the bio-extract plays a key role in reducing the metal ions for the formation of metallic NPs and further, it could stabilize through conjugation with the NPs.

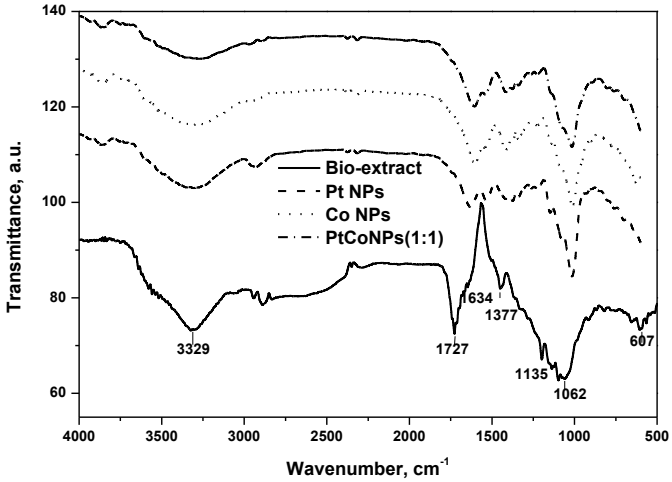

Figure 4.10. FTIR spectra of bio-extract, mono, and bimetal Pt and Co nanoparticles.

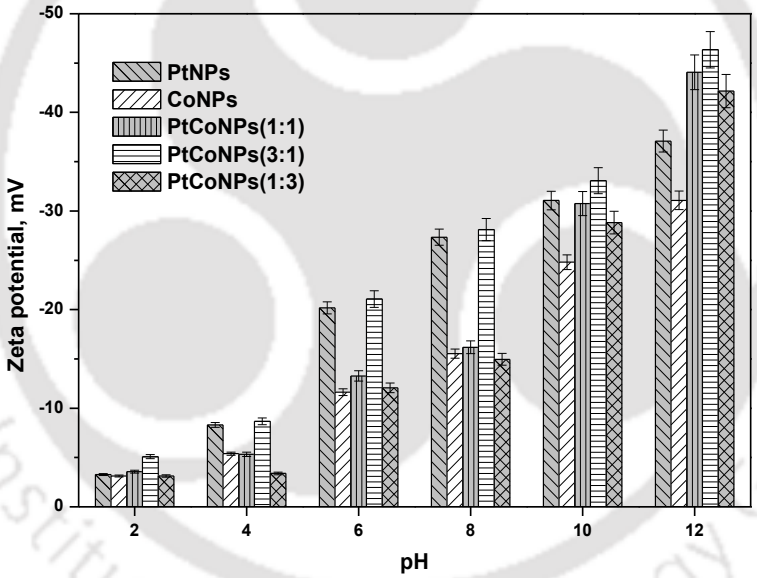

Figure 4.11. Zeta-potential of synthesized PtCoNPs with pH variation.

The change in zeta-potential (ζ) of Pt and Co NPs was measured to observe its destabilization tendency in the aqueous colloidal medium (**Figure 4.11**). ζ was negative for all the metal NPs which was caused by the adsorption of biomolecules such as the formation of the NPs–ascorbate layer (**Chapter 3, Section 3.2.2**). ζ was gradually reduced with the increment in pH from 2 to 12. In the case of PtNPs and CoNPs, ζ was decreased from ~ -3.2 to -37.1 and -31.1 mV between pH 2 and 12, and it varied from -5.1 to -46.2 mV for PtCo bimetallic NPs. It indicates that PtCoNPs promoted better destabilization compared to the

mono metal particles. Moreover, the concentration of metal–ascorbate layer increases with the rise in pH. Hence, the nanocrystal surface may be passivated more at a higher pH.

4.2.2 Effect of PtCoNPs on antimicrobial activity

The antibacterial activity of Pt and Co NPs was examined by the disk diffusion method with 25 µg mL^{-1} NPs. The results were compared with ciprofloxacin and cefprozil with 30 µg mL^{-1} concentration as the controls for the inactivation study. It was found that the bio-extract alone inhibited the growth of both *B. subtilis* and *E. coli* with 25 and 24 mm zone diameters (**Figures 4.12(a)** and **4.12(b)**). The ciprofloxacin control media exhibited the maximum inhibition zone of 48 mm against *B. subtilis* zone diameter (**Figures 4.12(a)** and **4.12(b)**). However, both the bacterial strains were resistant to cefprozil control and, the growth was quite less (28 mm inhibition zone). Babu et al. reported that ciprofloxacin (10 µg/mL) could inactivate *B. subtilis* and *E. coli* with the inhibition zone diameters of 26 and 20 mm, respectively. The reduction in the antimicrobial activity compared to the present was for a lower ciprofloxacin concentration (Babu et al., 2016). Whereas as cefprozil (5×10^5 cfu/mL) could inactivate 98% of *E. coli* (Pistiki et al., 2015).

Both mono and bimetallic PtCoNPs also showed notable variation in inhibition behavior. The inhibition efficiency was more with bimetal NPs. The antimicrobial activity of CoNPs was the lowest with 28 and 29 mm zone diameter against *B. subtilis* and *E. coli* and, after that, it increased with bimetal NPs for both the strains (**Figures 4.12(c)** and **4.12(d)**). PtNPs showed 31 and 33 mm inhibition diameters against *B. subtilis* and *E. coli*. In the case of PtCoNPs, the zone diameter increased gradually to a maximum of 37 and 40 mm with PtCoNPs (1:3) (**Figures 4.12(c)** and **4.12(d)**). The core-shell NPs possesses synergistic effects such as ligand interaction between the core and shell, and the geometric effect is originating from the difference reactivity between core and shell enabling them for the higher efficiency of bacterial inhibition (Gawande et al., 2015). Boomi et al. (2014) reported the maximum inhibition zone for polyaniline/Pt–Pd nanocomposite against *Staphylococcus* sp. (28 ± 0.70 mm) followed by *E. coli* (22 ± 0.36 mm) (Boomi et al., 2014). Fakhri et al. (2017) synthesized Ag/Au core-shell NPs and showed 15 ± 0.2, 13 ± 0.2 and 9 ± 0.2 mm zone of inhibition against *E. coli*, *M. luteus*, and *S. aureus* (Fakhri et al., 2017).

Smaller particles easily penetrate into the bacterial cell membrane and interrupt the metabolic pathway of the pathogen by initiating reactive oxygen species (ROS) uptake and early phagocytosis, and the generation of ROS is enhanced due to the presence of platinum atoms (Zhang et al., 2010). Moreover, the cytotoxic effect of Co component synergized the

antimicrobial activity (Chohan and Supuran, 2005; Fu et al., 2014). The metal NPs owning to a free radical character could rapture the membrane lipids causing in the destruction of cellular materials (Figure 9) (Sunada et al., 2003). Whereas *B. subtilis* lacks the monolayer of peptidoglycan and the protective membrane (Konwarh et al., 2011). The g-factor recorded from the ESR analysis (Figure 9), varied from 2.0052 to 2.0058 which corresponds to the existence of ascorbate free radicals (0.282 V vs. SHE) (Buettner and Jurkiewicz, 1993).

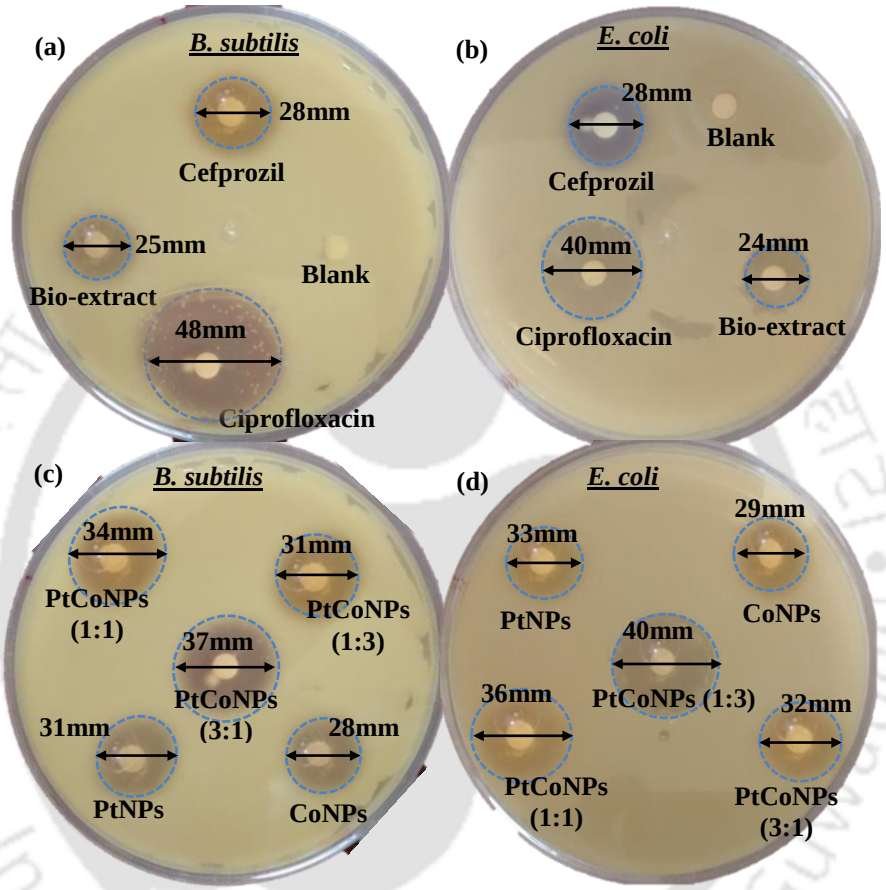

Figure 4.12. Pictorial images showing growth inhibition of *B. subtilis* and *E. coli* in the presence of (a and b) antibiotic control and bio-extract, and (c and d) Co and Pt mono and bimetal NPs. Experimental conditions: Concentration of ciprofloxacin and cefprozil: 30 mg mL^{-1}, AgNPs concentration 20 mg mL^{-1}, incubation temperature 37ºC and reaction time 24 h.

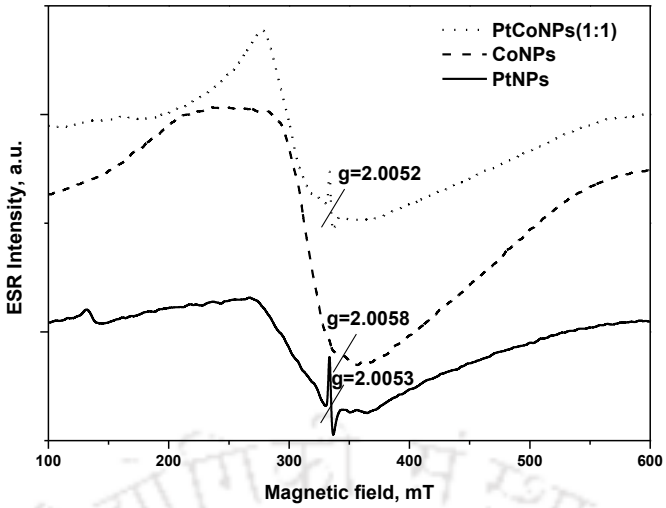

Figure 4.13. ESR spectra of Pt and Co NPs at room temperature (28±2 °C).

4.3 Major Findings

A bio-mediated process using the analytes such as ascorbic acid present in *S. edule* fruit extract could successfully synthesize Co, Pt, and PtCo nanoparticles of prismoidal, spherical, and core-shell structures with a mean diameter of 47.3, 25.4, and 28.6 nm. The yield of the NPs was as high as 98 % within 24 h of reaction. The analytes served the purpose of metal ions reduction leading to the formation of face-centered cubic crystals and NPs stabilization through conjugation such as intermolecular attractions. The formation of Pt^0 was thermodynamically more favorable than Co^0. So, a dense core of Pt or PtCo alloy was formed followed by a shell consisting of mostly Co with an average core-shell diameter of 13.2 nm–28.6 nm. PtCo core-shell structures exhibited a better colloidal stability (zeta potential –46.2 mV at pH 12) and antimicrobial activity compared to prismoidal and spherical Co and Pt counterparts. TGA confirms the existence of capping agent from the decomposition of organic compounds with 26, 27, and 51 % for PtNPs, CoNPs and PtCoNPs(1:1). The activity of core-shell particles and ciprofloxacin control was comparable for the inhibition of the growth of *E. coli*, but it outperformed cefprozil control for both *E. coli* and *B. subtilis.* The formation of ascorbate free radicals (g-factor 2.0052 to 2.0058) also caused the synergistic effect for the antimicrobial functionality of the NPs. So, it can be summarised as that synthesis of such tailor made structures using a bio-inspired cost-effective route opens up a vast scope of future research in catalysis, electrocatalysis, biomedical and biosensor applications.

References

Babu, B.G., Kumar, A.D.., Badana, A., Kumari, S., Jha, A., Malla, R.., 2016. Effect of C-glycosyl flavone from Urginea indica on antibiotic induced microbial cell death. Int. J. Pharm. Pharm. Sci. 8, 296–305.

Boomi, P., Prabu, H.G., Mathiyarasu, J., 2014. Synthesis, characterization and antibacterial activity of polyaniline/Pt-Pd nanocomposite. Eur. J. Med. Chem. 72, 18–25.

Buettner, R.G., Jurkiewicz, B.A., 1993. Ascorbate free radical as a marker of oxidative stress: An EPR study. Free Radic. Biol. Med. 14, 49–55.

Chohan, Z.H., Supuran, C.T., 2005. In-vitro antibacterial and cytotoxic activity of cobalt (ii), copper (ii), nickel (ii) and zinc (ii) complexes of the antibiotic drug cephalothin (keflin). J. Enzyme Inhib. Med. Chem. 20, 463–468.

Corain, B., Schmid, G., Toshima, N., 2011. Metal nanoclusters in catalysis and materials science: The issue of size control. Elsevier Science.

Fakhri, A., Tahami, S., Naji, M., 2017. Synthesis and characterization of core-shell bimetallic nanoparticles for synergistic antimicrobial effect studies in combination with doxycycline on burn specific pathogens. J. Photochem. Photobiol. B Biol. 169, 21–26.

Gawande, M.B., Goswami, A., Asefa, T., Guo, H., Biradar, A. V., Peng, D.-L., Zboril, R., Varma, R.S., 2015. Core–shell nanoparticles: synthesis and applications in catalysis and electrocatalysis. Chem. Soc. Rev. 44, 7540–7590.

Konwarh, R., Gogoi, B., Philip, R., Laskar, M.A., Karak, N., 2011. Biomimetic preparation of polymer-supported free radical scavenging, cytocompatible and antimicrobial "green" silver nanoparticles using aqueous extract of Citrus sinensis peel. Colloids Surfaces B Biointerfaces 84, 338–345.

Kovács, G., Kozlov, S.M., Matolínová, I., Vorokhta, M., Matolín, V., Neyman, K.M., 2015. Revealing chemical ordering in Pt–Co nanoparticles using electronic structure calculations and X-ray photoelectron spectroscopy. Phys. Chem. Chem. Phys. 17, 28298–28310.

Kuehner, D.E., Heyer, C., Rämsch, C., Fornefeld, U.M., Blanch, H.W., Prausnitz, J.M., 1997. Interactions of lysozyme in concentrated electrolyte solutions from dynamic light-scattering measurements. Biophys. J. 73, 3211–24.

Oluwafemi, O.S., Revaprasadu, N., Adeyemi, O.O., 2010. A facile "green" synthesis of ascorbic acid-capped ZnSe nanoparticles. Colloids Surfaces B Biointerfaces 79, 126–130.

Pistiki, A., Tsaganos, T., Galani, I., Giamarellos-Bourboulis, E.J., 2015. In vitro activity of oral cephalosporins (cefprozil and cefixime) against ciprofloxacin-resistant enterobacteriaceae from community-acquired urinary-tract infections. Infect. Dis. Ther. 4, 425–432.

Podlovchenko, B.I., Maksimov, Y.M., 2013. Open-circuit potentials established on platinum and gold electrodes in PtCl2–4 solutions after the displacement of copper adatoms. Mendeleev Commun. 23, 157–159.

Sunada, K., Watanabe, T., Hashimoto, K., 2003. Studies on photokilling of bacteria on TiO_2 thin film. J. Photochem. Photobiol. A Chem. 156, 227–233.

Vigneshwaran, N., Arati, K.A., Perianambi, V. V, Rajan, N.P., Rudrapatna, B.H., 2007. Silver − Protein (Core − Shell) Nanoparticle Production Using Spent Mushroom Substrate. Langmuir 23, 7113–7117.

Yu, X., Yu, W., Li, H., Tu, S.T., Han, Y.F., 2013. Preparation, characterization and application of K-PtCo/Al_2O_3 catalyst coatings for preferential CO oxidation. Appl. Catal. B Environ. 140–141, 588–597.

Zhang, B.-W., Sheng, T., Wang, Y.-X., Qu, X.-M., Zhang, J.-M., Zhang, Z.-C., Liao, H., Zhu, F., Dou, S.X., Jiang, Y., Sun, S.-G., 2017. Platinum–Cobalt bimetallic nanoparticles with Pt skin for electro-oxidation of ethanol. ACS Catal. 7, 892–895.

Zhang, L., Laug, L., Münchgesang, W., Pippel, E., Gösele, U., Brandsch, M., Knez, M., 2010. Reducing stress on cells with apoferritin-encapsulated platinum nanoparticles. Nano Lett. 10, 219–223.

Zhang, X., Chan, K.-Y., 2002. Microemulsion synthesis and electrocatalytic properties of platinum–cobalt nanoparticles. J. Mater. Chem. 12, 1203–1206.

Chapter 5

Development of a Technique of Silver-doping on Semiconductor Supports

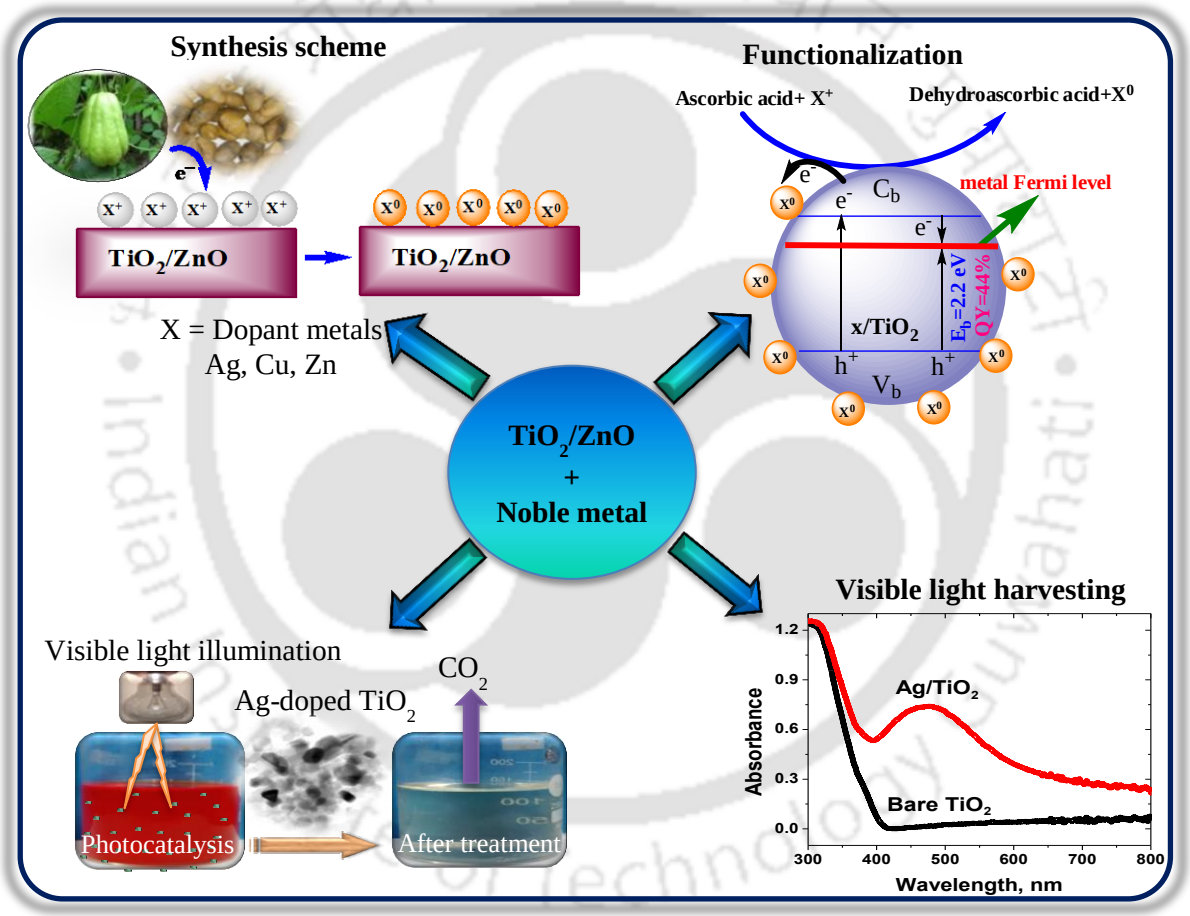

This chapter contains two parts. In the first part, the role of the primary analyte present in the bio-extract was explored for its potential functionality for proper Ag-doping on TiO_2 (Ag/TiO_2). The photocatalytic performance of this doped catalyst is investigated in terms of its physicochemical properties and dye-sensitization effect, along with its comparison with the control catalyst doped, if any, without bio-extract and doped catalyst using commercial ascorbic acid (AA). The photocatalytic activity of Ag/TiO_2 was tested for the degradation of

Congo red dye under visible light irradiation. The second part covers the physicochemical and photoelectrochemical attributes of Ag/ZnO photocatalyst as well as the degradation study of dipyrone drug under visible light irradiation.

5.1 Silver-doping on Semiconductor Material

The versatile applications of semiconductor photocatalysts such as TiO_2 and ZnO include water purification, self-cleaning, sterilization, removal of odor, and harmful constituents (Sunada et al., 2003). Easy availability, high chemical stability, high catalytic activity, low cost, non-toxicity, and high oxidation power of these materials have made them as candidates photocatalyst even for the industrial uses (Sobana et al., 2006). Both the TiO_2 and ZnO are active in the UV region (λ<387 nm). Under the photo-excitation (band gap ≥ photo energy), electron (e^-) jumps to the conduction band (C_b) generating the hole (h^+) in the valence band (V_b). Both the oxidation and reduction reaction occur owing to the generation of e^- and h^+ on the catalyst surface. e^- and h^+ react with O_2 and H_2O or HO^-, adsorbed on the catalyst surface, and, subsequently the superoxide ($O_2^{\bullet-}$, -0.16 V vs. NHE) and hydroxyl ($^{\bullet}OH$, 2.73 V vs. NHE) radicals are formed (Etacheri et al., 2015). One of the significant limitations with semiconductor photocatalysts is that the photogenerated e^- and h^+ can recombine very quickly (~20 ns), and the quantum efficiency of the overall reaction reduces. The metal-loaded TiO_2 has a high Schottky barrier, which acts as e^- traps at a metal–semiconductor junction, facilitating e^- and h^+ separation and promotes the interfacial e^- transfer process (Aysin et al., 2013). It could significantly improve the chemical sensing performance of TiO_2 and also enhance the catalytic activity of the material (Lu et al., 2008). Ag is one of the best dopants because of its excellent electrical conductivity and chemical stability. The photo-excited e^-/h^+ carriers are first generated in Ag with the visible light absorption and, the produced charge carriers are instantly introduced from the optically stimulated surface plasmon resonance (SPR) of the nanomaterials on the semiconductor (Patil et al., 2016). This exclusive characteristic along with its electrical and optical properties establishes Ag-doped semiconductor (Ag/TiO_2 or Ag/ZnO) as an essential nanomaterial for photocatalysis and special applications like gas-sensing, antimicrobial (Michael et al., 2014), and surface-enhanced Raman scattering activities (Shan et al., 2007). The detailed literature survey on metal doping on semiconductor supports in conventional route is provided in C**hapter 1** (**Section 1.9.1**).

There are no existing studies on bio-mediated doping (BMD) using metal dopants for the functionalization of semiconductor photocatalysts to reduce the band gaps. The utilization of bio-extracts is often compromised by the longer reaction time and availability of the reducing agents. In this respect, the *Sechium edule* extract exhibited an excellent performance for the reduction of various metal ions (Chapter 3 and Chapter 4). This work develops a new method of Ag-doping onto the TiO_2 support using the aqueous *S. edule* extract to make it active in the visible light. The reducing agents such as AA were utilized for the doping of pre-immobilized Ag^+ onto the TiO_2 surface. The photocatalytic activity of thus functionalized TiO_2 was tested for the degradation of Congo red (CR) dye under the visible light illumination.

The second part of this work (**Chapter 5**) investigates the physicochemical and photoelectrochemical attributes of Ag/ZnO, catalyst reusability, and quantum yield of the reaction for the degradation study of dipyrone drug, a colorless compound as a model contaminant under visible light irradiation.

Dipyrone is an analgesic and antipyretic drug and, about 33 % of dipyrone consumed does not absorb by the body and, it is mostly excreted in urine (Giri and Golder, 2014). The metabolites of dipyrone get into the surroundings from various sources like clinical, pharmaceutical, and production sites. Such compounds are also not entirely removed by the conventional biological methods (Giri and Golder, 2014). Thus, their existence is detected in surface water and sludge treatment plant effluents. Therefore, dipyrone was selected as a model contaminant.

5.2 Results and Performance of Ag doped TiO_2

5.2.1 Optimal pH for Ag^+ binding onto TiO_2

The solution pH has a major role on the immobilization of Ag^+ on the surface of TiO_2 (Mehrani et al., 2011) in the absence of bio-extract. To study the influence of pH on Ag^+ adsorption, pH was adjusted in the range of 3 to 11 with 1 % (w/w) Ag^+ (per 100 g catalyst). The data was graphed as a function of pH after 60 min of contact time as there was no further improvement of Ag^+ adsorption beyond 60 min. As it can be seen from **Figure 5.1**, the optimum quantitative retention of Ag^+ ions on the TiO_2 was obtained at pH 7. Thus, all the further studies experiments were conducted at this pH. The presence of Ag^+ in bio-extract if any also determined (**Chapter 2, Section 2.5.2**). There was an insignificant amount (<4 mg L^{-1}) of Ag^+ ions found in the solution which says that the Ag^+ was completely immobilized

on TiO_2. There is a similar report on the optimum retention of Cu-Ag nanoparticles on TiO_2 support at pH 7 (Behbahani et al., 2013). The efficiency of Ag-doping was found to be 83.2 %. It implies that the true Ag-loading, Ag onto TiO_2 was about 0.83 % (w/w). The same procedure applied with different Ag-loadings as well, and the true Ag-loading was 0.21, 0.42, 0.63, 0.83, 1.18 and 1.43 % for 0.25, 0.5, 0.75, 1, 1.5 and 2 % (w/w) per 100 g catalyst initial Ag-concentration, respectively. So, the doped catalyst is denoted as X-Ag/TiO_2, where X is the amount of Ag actually doped.

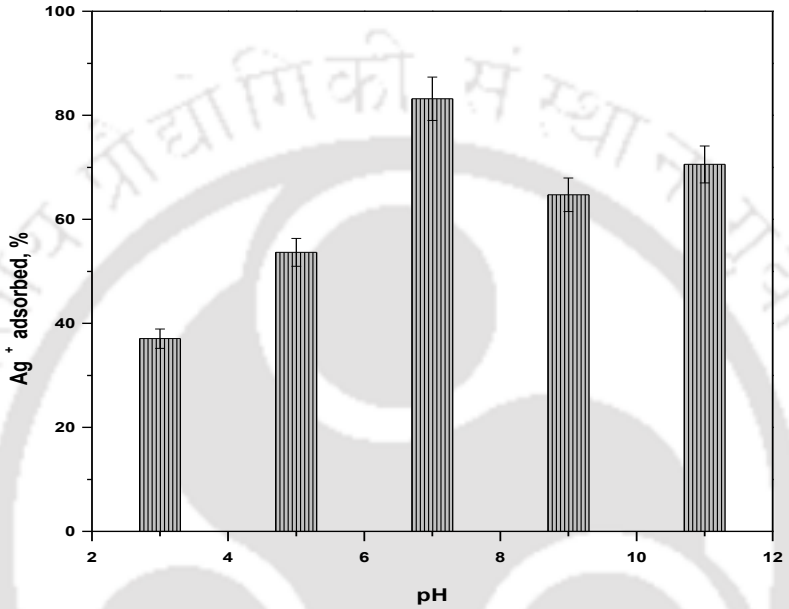

Figure 5.1. Effect of solution pH on the quantitative retention of Ag^+ ions onto TiO_2 in absence of bio-extract. Experimental conditions: initial 1 % (w/w) Ag^+ concentration, stirring speed 300 rpm and reaction time 60 min.

Figure 5.2 depicts the H_2-TPR of 0.83 % (w/w) Ag/TiO_2 catalyst to determine the existence of un-converted Ag^+ if any. There was no significant reduction peak observed up to 700 °C. The bare TiO_2 also didn't show any reduction peaks (Lenzi et al., 2011). It signifies that the amount of unreduced Ag^+ ion as well as Ag_2O clusters on TiO_2 were insignificant owing to complete Ag-doping.

Ascorbic acid (AA) was found to be the most abundant compound (176.92 *m/z*) (**Figure 5.3**). *S. edule* was consisting of 294 mg AA/kg which was close to the earlier reports (Bellur Nagarajaiah and Prakash, 2015; Cadena-Iniguez et al., 2006) (**Chapter 3, Section 3.2.5**). AA is an ideal e^- donor among the various e^- donor species with the redox potential of (0.059 V vs. NHE) and, it can be easily oxidized by h^+ (Zhao et al., 2012). Ag^+ ions are reduced to Ag^0 by AA (Eq. 5.1) (Velikov et al., 2003). The nucleation-burst take place on the

surface of TiO_2 and small Ag^0 aggregates (AgNPs) were formed with the nearby atoms. e^- would effectively transfer to Ag-cluster when the number of Ag^0 aggregates is small.

$$C_6H_8O_6 + 2Ag^+ \rightarrow 2Ag^0 + C_6H_6O_6 + 2H^+ \quad (5.1)$$

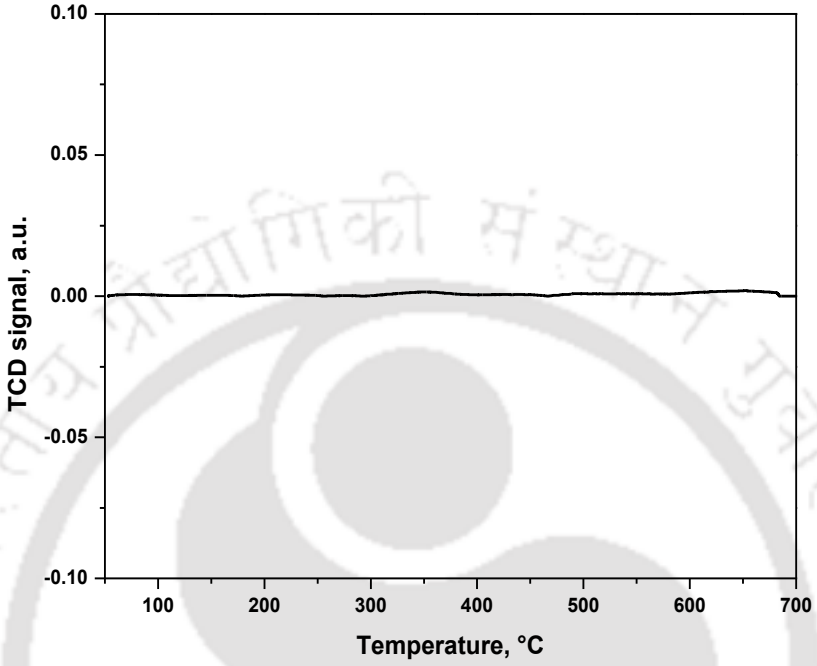

Figure 5.2. TPR profile of 0.83 % (w/w) Ag/TiO_2 catalyst.

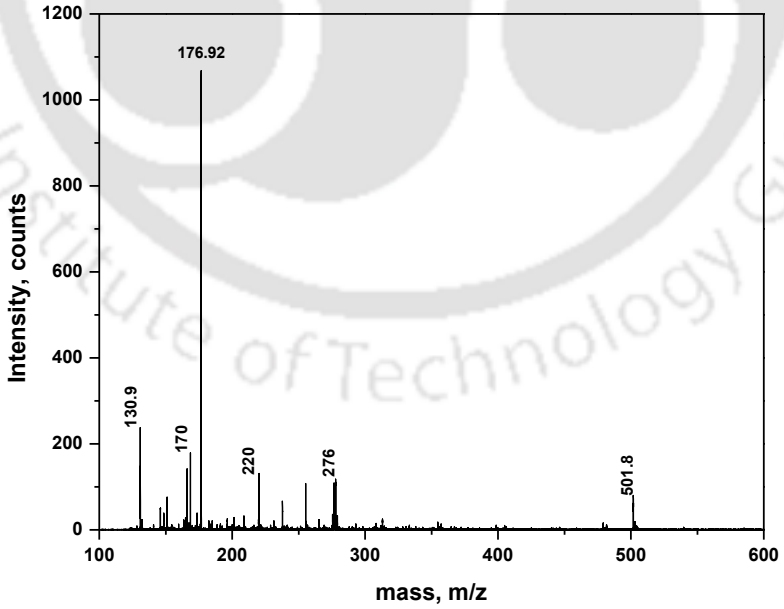

Figure 5.3. Mass spectra of *Sechium edule* fruit aqueous extract.

5.2.2 Characteristics of Ag/TiO_2

5.2.2.1 X-ray diffractogram

The XRD patterns of the bare TiO_2 and Ag/TiO_2 particles are shown in **Figure 5.4.** It confirms that the synthesized Ag/TiO_2 exists in the crystalline phases. The majority of peaks at 25.3, 37.8, 48.1 and 62.7° 2θ values were due to the reflections from the (1 0 1), (0 0 4), (0 2 0) and (0 2 4) planes for anatase, and 27.4, 36.06 and 54.3° 2θ values for rutile, respectively (Ramakrishnan et al., 2012). The bare TiO_2 shows the existence of pure phases. 0-Ag/TiO_2 (**Figure 5.4)** was obtained using the same method of Ag-doping, however without Ag^+ precursor. It exhibits the similar crystallinity as the bare TiO_2. In the case of Ag-loaded TiO_2, no additional peaks assigned to Ag^0 were detected, possibly due to high dispersity and its low content. However, at higher Ag-loading (i.e., 1.43 % w/w), two additional peaks at 38.1 and 64.5° were likely due to the crystalline phases of AgNPs. It matches well with the (1 1 1) and (2 2 0) planes of FCC structured Ag (JCPDS No. 89-3722, a = 4.085 Å) (Wang et al., 2013).

The content of rutile phase was determined by the following relation (Eq. 5.2) (Ramakrishnan et al., 2012). The results are given in **Table 5.1**.

$$\text{Rutile content}\,(\%) = \frac{A_R}{0.884(A_A + A_R)} \qquad (5.2)$$

Where, A_A and A_R indicate the anatase and rutile phases integrated intensity of (1 0 1) and (1 1 0) peaks, respectively. There was a slight decrease in percentage anatase content with Ag-doping from 79.8 to 70.6 %. Ag^+ ions would tie up with TiO_2 through the coordination reaction or an ion-exchange (Li et al., 2003) which could act as a nucleation precursor. Hence, a little phase transformation was noted.

The crystallite size was calculated from the highest peak, i.e., at 2θ = 25.35° for the anatase phase, and 27.46° for the rutile phase, using the Scherer's formula. They are summarized in **Table 5.1**. The crystallite size increased gradually with Ag-loading from 16.26 to 32.31 nm in the anatase phase, and 17.32 to 51.36 nm in the rutile phase. The interplanar spacing (d-spacing) also increased gradually with Ag-loading from 3.5135 to 3.541 Å. Ag^+ ions may be incorporated into TiO_2 crystal lattice and substituted titanium ions to Ti–O–Ag bonds or placed at the interstitial sites (Behnajady and Eskandarloo, 2013; Zhang et al., 2011).

The lattice strains of bare TiO_2 and 1.18Ag/TiO_2 NPs were determined from FWHM of the diffraction lines observed at different 2θ angles (20 to 80°) according to the Williamson-Hall's equation (Eq. 5.3) (Riazian et al., 2013).

$$\beta\cos\theta = \frac{k\lambda}{L} 4\varepsilon\sin\theta \qquad (5.3)$$

Where, β is the FWHM, ε is the lattice strain, and the shape factor *k* is assumed to be 0.9 similar to Scherrer's equation. λ is the wavelength of Kα(Cu) radiation). It was found that βcosθ was varied almost linearly with 4sinθ (**Figure 5.5**). The lattice strain (ε) was determined from the slope of the best fit line. The lattice strain was decreased from 0.038 to 0.0363 with Ag-doping as it caused the partial transformation of the anatase phase to rutile phase. These results are also in line with the increase in crystalline size due to Ag-doping (Inagaki et al., 2006; Moghaddam and Nasirian, 2012). The interplanar spacing (d-spacing) was increased gradually with Ag-doping from 3.5135 to 3.541 Å. Ag^{+} ions were incorporated into the TiO_2 crystal lattice and substituted titanium ions forming Ti–O–Ag bonds or placed at the interstitial sites (Behnajady and Eskandarloo, 2013; Zhang et al., 2011).

To investigate this observation further, the elemental EDX image mapping of Ti, O, and Ag was undertaken (**Figure 5.6).** The numerous nanocrystals are accumulated by the structural configuration that comprises of Ti, O, and Ag elements. The weight percent of Ag deposited on TiO_2 is 0.6 ± 0.3. Ti and O showed the weight percent of 43.5±0.7 and 55.9±0.7. The high dispersity of Ag is evident from the images as that O and Ti.

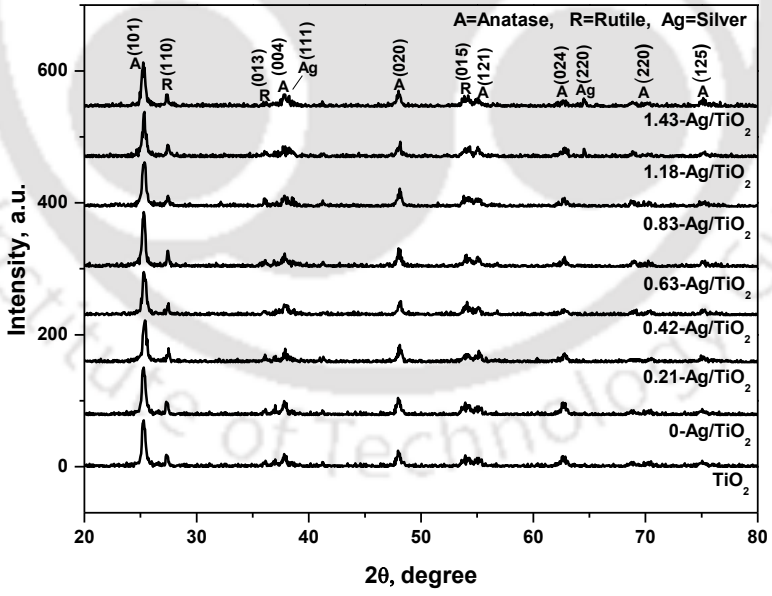

Figure 5.4. XRD patterns of undoped and bio-mediated doped Ag/TiO_2 nanostructures.

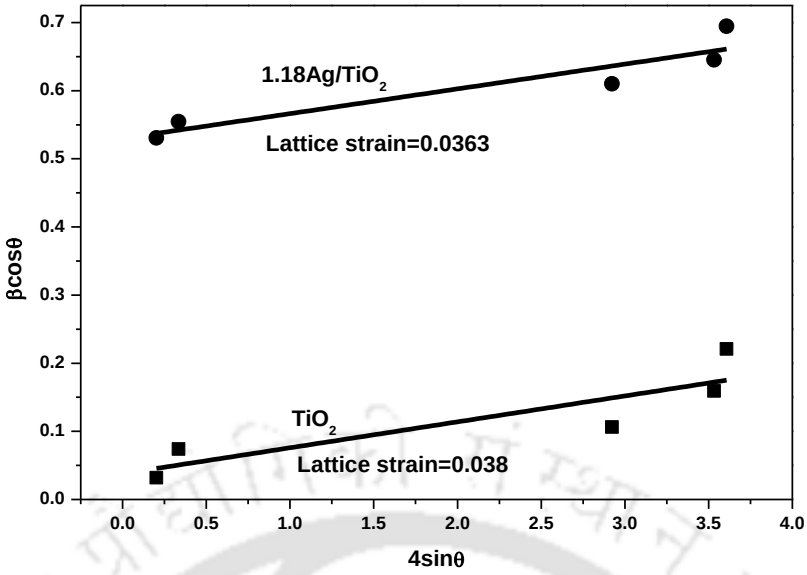

Figure 5.5. Vraition of $\beta\cos\theta$ with $4\sin\theta$ (Williamson-Hall plots) with TiO_2 and 1.18-Ag/TiO_2 NPs.

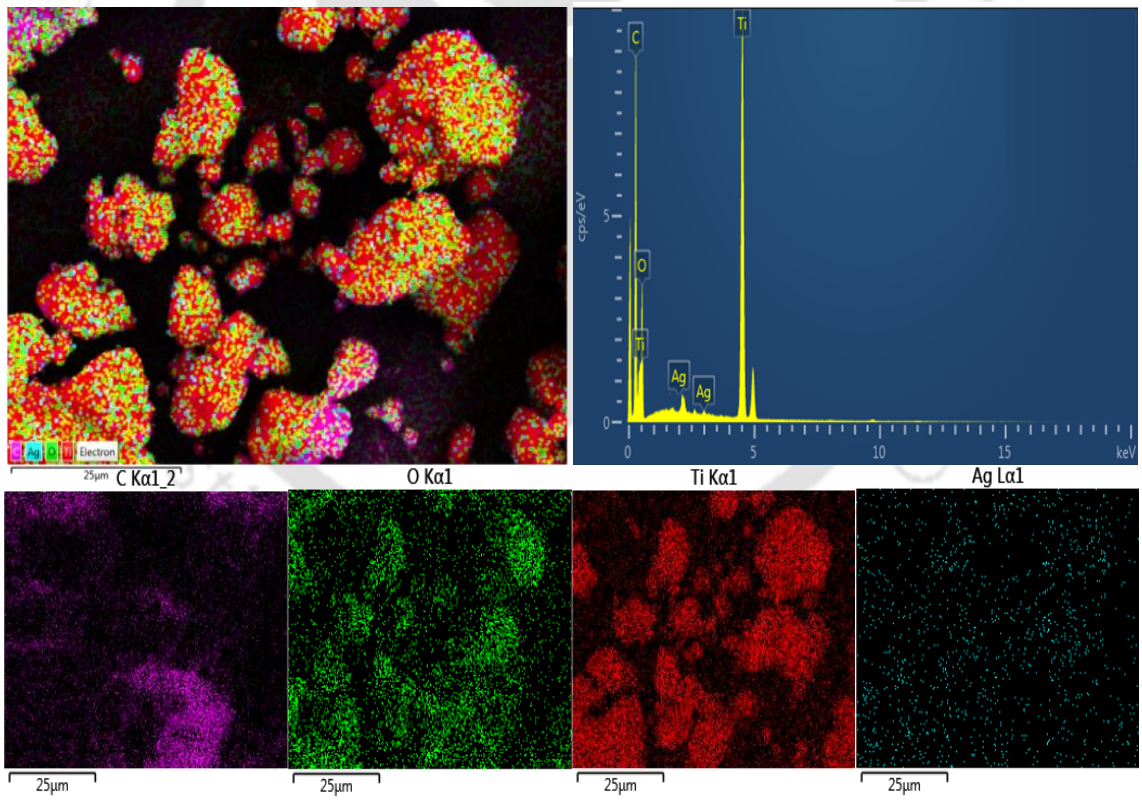

Figure 5.6. EDX analysis of 1.18-Ag/TiO_2 particles ((i): relative dispersity of C, O, Ti and Ag elements, (ii): EDX spectra, (iii) C dispersity, (iv) O dispersity, (v): Ti dispersity, and (vi): Ag dispersity).

Table 5.1. Anatase and rutile crystalline phases and sizes for bare and ag-doped TiO_2 nanostructures.

Catalyst type	d-spacing, Å	Crystalline phase, %		Crystallite size, nm	
		Anatase, 25.3°	Rutile, 27.4°	Anatase, 25.3°	Rutile, 27.4°
TiO_2	3.5135±0.75	79.78±0.33	20.22±0.65	16.26±0.02	17.32±0.18
0.21-Ag/TiO_2	3.5152±0.13	77.01±0.75	22.99±0.85	16.35±0.12	18.59±0.23
0.42-Ag/TiO_2	3.5203±0.2	75.68±0.85	24.32±0.94	21.57±0.09	24.88±0.41
0.63-Ag/TiO_2	3.5272±0.67	75.14±0.36	24.86±1.23	23.01±0.11	32.24±0.25
0.83-Ag/TiO_2	3.5341±0.7	73.45±0.21	26.55±0.2	24.05±0.24	37.88±0.35
1.18 -Ag/TiO_2	3.5391±0.54	72.39±0.82	27.61±0.1	29.74±0.31	48.74±0.13
1.43-Ag/TiO_2	3.5410±0.71	70.55±0.79	29.41±0.24	32.31±0.22	51.36±0.75

5.2.2.2 Spectral absorbance of Ag/TiO_2 and band gap calculation

The color intensity of the Ag/TiO_2 particles was found to depend on the content of Ag-dopant. The bare TiO_2 is milky white. While Ag-doped TiO_2 showed light brown color which was turned to dark brown at higher Ag-loading (1.43-Ag/TiO_2). UV-DR spectra at different Ag-loading are illustrated in **Figure 5.7**. Bare TiO_2 showed strong absorption peak in the UV region and almost no absorption in the visible region. In the case of Ag/TiO_2, the absorption peaks were shifted to the visible-light region (~500 nm), and the intensity of the peak gradually increased with the increase in Ag-doping. The surface plasmon resonance (SPR) scattering into the TiO_2 layer increases with the rise in Ag-loading. The increase in the SPR can raise the electric fields (Dong et al., 2015), which can facilitate e^- and h^+ generation. It causes the increment of visible light absorption. There was no further increase in the absorbance beyond 1.18 % (w/w) Ag-loading. The number of active-site located capturing e^- was decreased at higher Ag-loading. There was no increment in the absorption of photogenerated charge carrier. Hence, the photocatalytic performance may reduce (Suwarnkar et al., 2014). The e^- and h^+ pair yield depends on the intensity of the incident photons with the energy equalling or exceeding the band gap energy. As it can be seen with 1.43 % (w/w) Ag-loading, the new broad absorption band belongs to the metal-ligand charge transfer in TiO_2. In the case of 1.18 % (w/w) Ag-loading, there was a sharp peak. However, exceeding the 1.43 % Ag-loading resulted in a narrower space charge layer such that the penetration depth exceeds the width of this space charge layer. Consequently, the recombination rate increases due to the lack of a driving force to separate out them (Ola and Maroto-Valer, 2015).

The band gap energy (E_g) was found by the linear extrapolation of the absorption onsets, from the point of inflection of curve to the baseline (Eq. 5.4). E_g values were calculated from a linear regression of $(\alpha E)^{1/2}$ vs. E with the extrapolation to zero called, Tauc plot (Barajas-Ledesma et al., 2010).

$$(\alpha E)^{1/2} = A(E - E_g) \quad (5.4)$$

Where, $E=hc/\lambda$, h is Planck's constant (4.135667×10^{-15} eV s), c is the velocity of light (3×10^8 m s^{-1}), λ is the wavelength (nm), α is absorbance (a.u), A is photon energy, an independent parameter for the respective transitions (eV), and E_g is in eV.

The E_g values at different Ag-loading are presented in **Figure 5.8** calculated from the Tauc plot **(Figure 5.9**). The variation in the band gap clearly indicates the difference in absorption edge for various Ag-loaded TiO_2 particles. E_g of the bare TiO_2 is found to be 3.1 eV. The presence of Ag in the TiO_2 nanoparticle greatly enhanced the visible light transmission (increase absorption) (**Figure 5.7**), while with the rise in the Ag-content, E_g was gradually decreased to 2.53 eV with 1.18-Ag/TiO_2 (**Figure 5.8**). The reason for the decrease in E_g could be the localized SPR effect that was attributed by the AgNPs (Doudrick et al., 2013). Therefore, the actual E_g of TiO_2 was the same, but the SPR added visible light absorbance (Kobwittaya and Sirivithayapakorn, 2014). However, E_g raised with 1.43 % (w/w) Ag-loading may be due to the bulk defects in the C_b edge that causes the molecular orbitals delocalization and generate deep or shallow in electronic energy. It caused E_g increment in absorption spectra in red-shift (Yan et al., 2013).

Ag was doped onto TiO_2 following the proposed procedure where the solution of AA was used instead of bio-extract. The concentration of AA was same as that of in the bio-extract. The UV-vis spectra are shown in **Figure 5.10**. The bio-mediated Ag-doped TiO_2 showed a superior performance for the shifting of the absorption band to visible light.

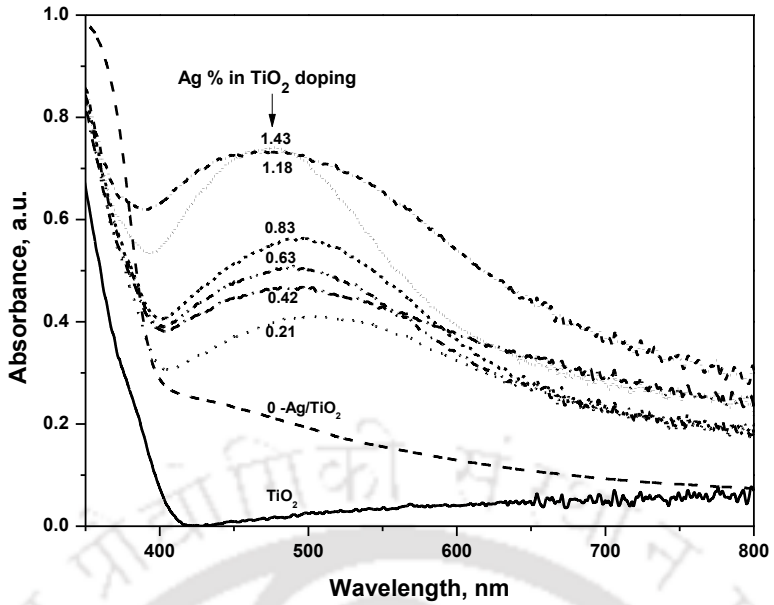

Figure 5.7. UV–vis DR spectra of bare TiO_2 and doped TiO_2 at different Ag-loadings.

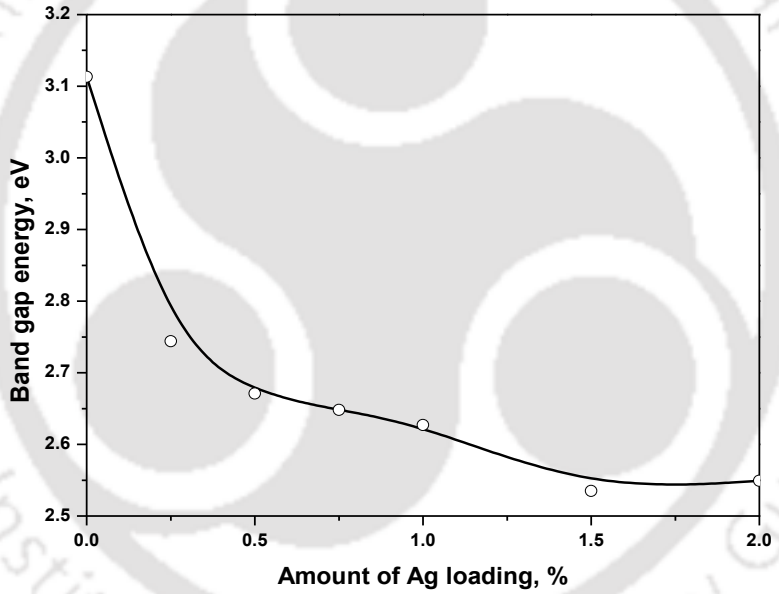

Figure 5.8. Band gap values with different Ag-loading.

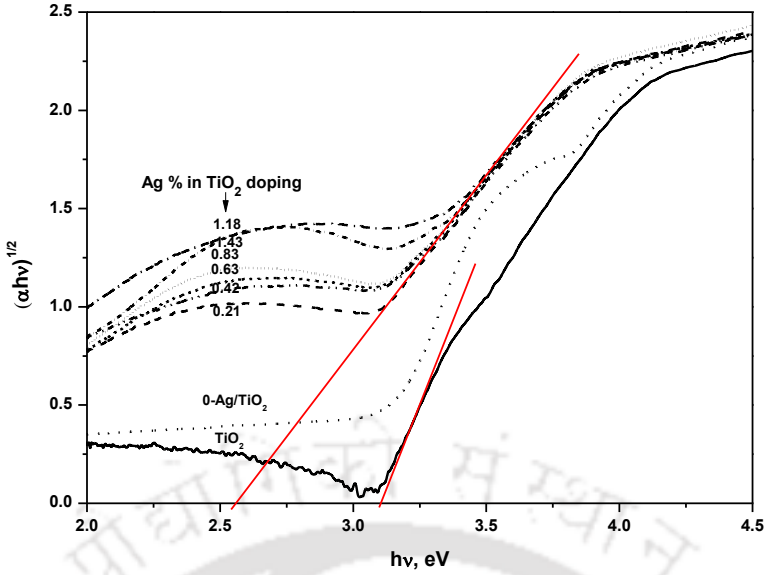

Figure 5.9. Optical direct band gaps (Tauc plot) of the bare and doped TiO_2.

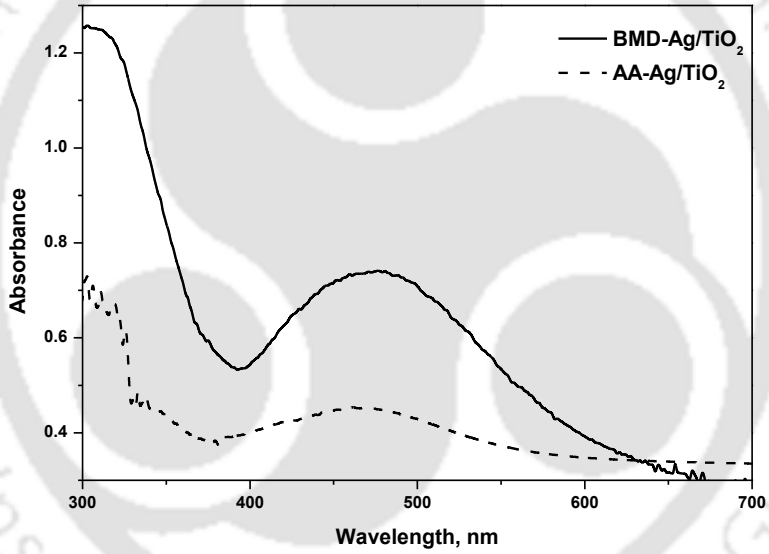

Figure 5.10. UV-vis-DR spectra of AA-Ag/TiO_2 and BMD-Ag/TiO_2.

5.2.2.3 BET surface area of Ag/TiO_2

The BET surface area of the bare TiO_2 and Ag/TiO_2 particles are shown in **Table 5.2**. The surface area was decreased with the Ag-loading (Cheng et al., 2010; Grover et al., 2013) from 66.48 to 55.59 m^2g^{-1}. It was due to the incorporation of Ag into TiO_2 lattice which is in accordance to the increase in crystallite size with Ag-doping (Table 5.1). **Table 5.2** indicates nearly a linear decrement in the surface area with various Ag-loadings. The surface area of TiO_2 was reduced by around 16.4 % with 1.43 % (w/w) Ag-loading. The pore volume and pore radius were increased with the increase in Ag-loading (**Table 5.2**). The average pore

diameter was found to be around 18 nm for the bare TiO_2. It increased to 35 and 38 nm with 1.18 and 1.43 % (w/w) Ag-loadings. The enhancement of average pore size in Ag-doped TiO_2 is due to the increase in crystallite size which gives the higher porosity of the nanoparticles. Also, Ag-doping into TiO_2 crystal lattice may be the reason for the increase in the lattice tension. Therefore, the particle size became larger after doping, which is in agreement with the XRD results (Chen et al., 2013). The reduction in the surface area in the case of BMD was lower than TiO_2 doped by different conventional doping techniques (Behera et al., 2016; Sobana et al., 2006; Zhang et al., 2009).

Table 5.2. BET surface area, pore radius and pore volume of catalyst particles.

Catalyst type	Surface area, $m^2 g^{-1}$	Pore diameter, nm	Pore volume, $cm^3 g^{-1}$
TiO_2	66.475	17.68	0.293945
0.21-Ag/TiO_2	64.828	19.90	0.311594
0.42-Ag/TiO_2	62.128	22.52	0.360546
0.63-Ag/TiO_2	59.342	26.26	0.414546
0.83-Ag/TiO_2	57.027	32.40	0.466446
1.18 -Ag/TiO_2	56.011	35.24	0.499902
1.43-Ag/TiO_2	55.595	37.86	0.539617

5.2.2.4 Particle size and morphology of Ag/TiO_2

The TEM micrograph of 1.18-Ag/TiO_2 is illustrated in **Figure 5.11(a).** A slight agglomeration was taken place in some of the clustered particles. The SAED pattern is shown in **Figure 5.11(b).** The intense rings represent to the anatase phase of standard polycrystalline diffraction rings (Gharagozlou and Naghibi, 2015). According to the SAED patterns, the d-values representing to the sharpest rings were in agreement with the standard d-values for the anatase (h k l) planes of (1 0 1), (0 0 4) and (2 0 0). It is also supported by the XRD patterns (Fu et al., 2015). From the locally magnified image, we can thus determine the interplanar spacing of fringe separation of 0.354 and 0.353 nm. They correspond to the lattice face of (1 0 1) of the anatase structure **(Figure 5.11(c)).** The sizes of the particles were not uniform and ranged between 17 and 80 nm in diameter (**Figure 5.11(d)**) which was measured from TEM micrograph using ImageJ software.

The particle size measured by DLS is shown in **Figure 5.12.** The particle size distribution was shifted towards the larger mean size as increasing the Ag-loading and has a lower covering intensity with a wider size arrange. In fact, TiO_2 particles show a tendency to aggregate due to the hydroxyl groups on the TiO_2 surface. The change in size distribution of various Ag-loaded TiO_2 was caused by clustering of the particles. At higher Ag-loading, the

lower uniformity in the particle size distribution and the enhancement in polydispersity as a consequence of the size diversity and the differences in hindrance effects of suspended particles in the aqueous solution took place. The difference was found in the particles size appeared in TEM image, and in DLS studies. **Table 5.3** shows the mean diameter of bare and Ag-loaded TiO_2. The particle size was more with DLS measurement due to the aggregation of particles as well as a hydrodynamic layer is involved in the case of DLS (Schmitt Pauly et al., 2015) where TEM provided the size of the dry particles.

One of the challenging tasks is to avoid Ag^0 coating on the surface of TiO_2. If the test was carried out without pre-immobilization of Ag^+ onto TiO_2, Ag^0 was coated on the surface. The evidence is shown in the TEM micrograph **(Figure 5.13)**. The band gap of Ag/TiO_2 without Ag^+ pre-immobilization was found to be 2.72 eV in comparison to 2.53 eV with 1.18-Ag/TiO_2. In fact, initially, Ag-doping was conducted without Ag^+ pre-immobilization. It was found that Ag^0 is coated onto TiO_2 rather than doping. After that, the whole doping methodology was re-designed to have successful Ag-doping as reported in the manuscript.

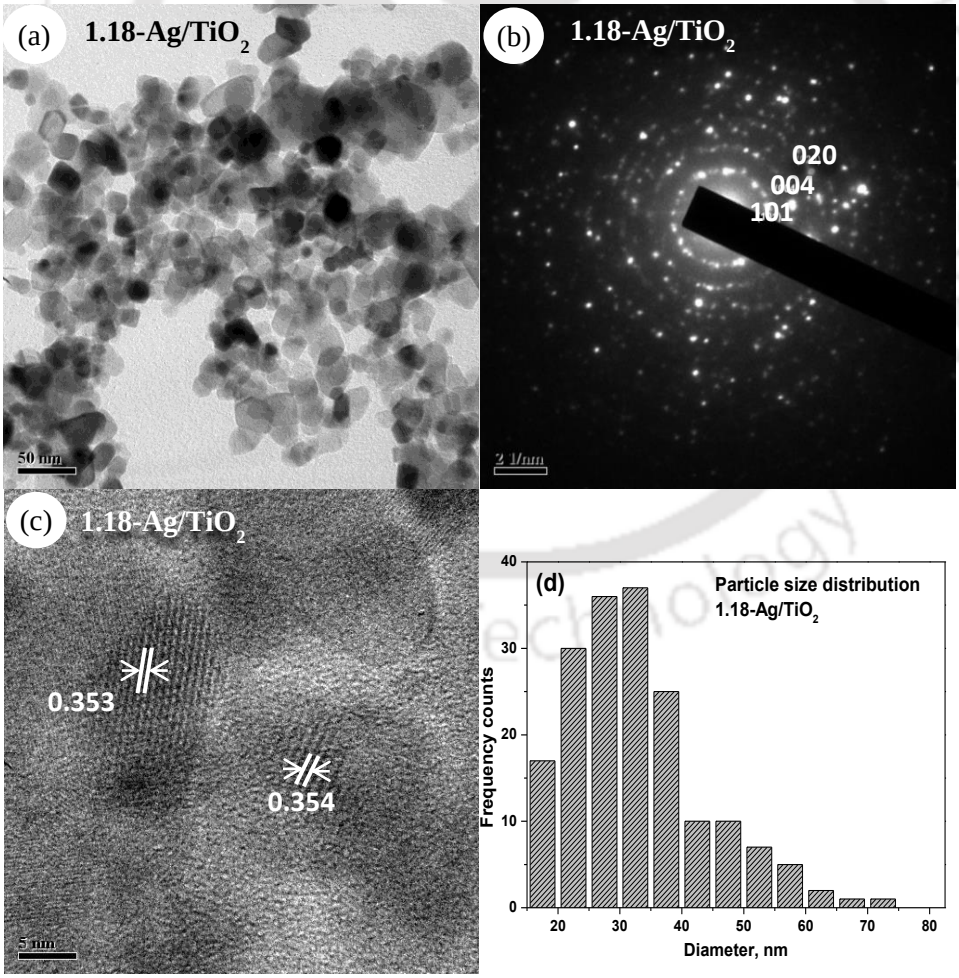

Figure 5.11. (a) TEM image, (b) SAED pattern, (c) HRTEM and, (d) Particles size distribution from TEM micrograph of 1.18-Ag/TiO_2.

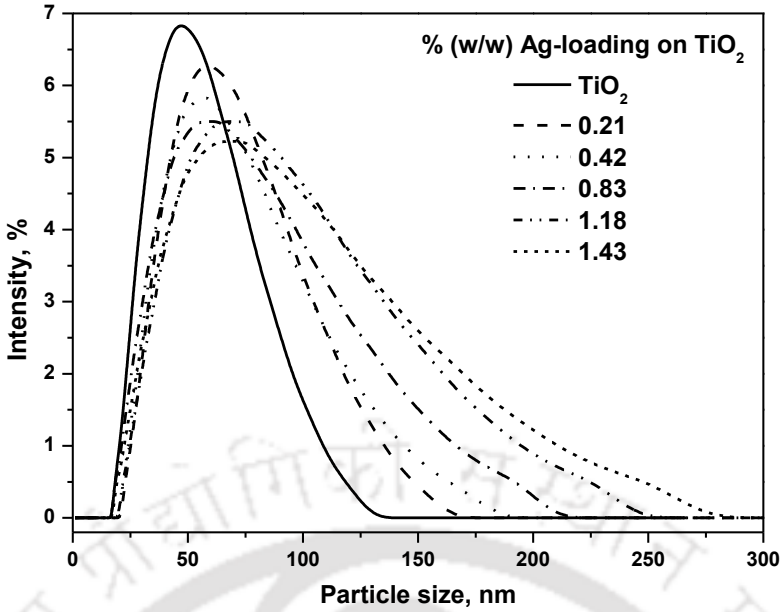

Figure 5.12. Particles size distribution using DLS.

Table 5.3. Comparison of mean diameter of Ag/TiO_2 with different analysis

Catalyst type	Mean particle diameter, nm	
	DLS	TEM
TiO_2	48.61±0.15	29.15±0.96
0.21-Ag/TiO_2	52.16±0.55	
0.42-Ag/TiO_2	63.02±0.81	
0.83-Ag/TiO_2	67.43±0.94	
1.18-Ag/TiO_2	72.02±1.01	39.06±1.04
1.43-Ag/TiO_2	77.41±0.79	

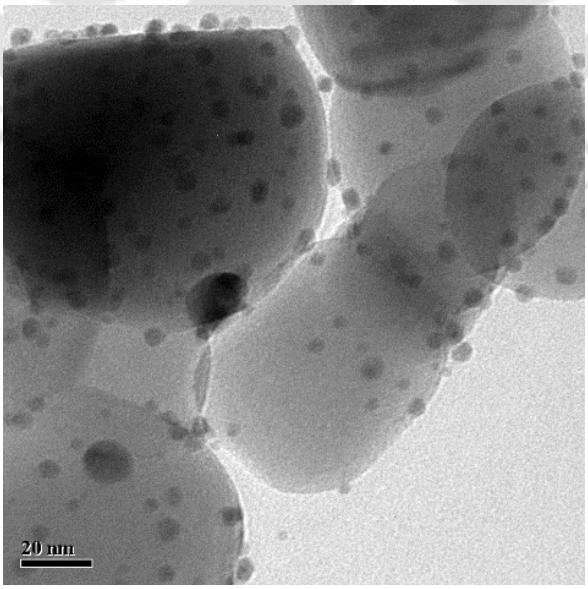

Figure 5.13. Evidence of Ag^0 from TEM micrograph in the case of improper doping methodology.

5.2.2.5 Thermal and colloidal stability of TiO_2 and Ag/TiO_2

The influences of temperature on bare and Ag-doped TiO_2 particles are shown in **Figure 5.14**. For the bare TiO_2, the mass loss extended up to 525 °C, and it was about 2.28 % in this temperature range. It was because of the small amount of organic residues (Ramasamy et al., 2012). However, 1.18-Ag/TiO_2 showed mass losses in two steps. In the first step, the mass loss extended to a temperature of 370 °C was due to the loss of water from the hydrated TiO_2 and the hydrated part was converted to TiO_2 (Ramasamy et al., 2012). The melting of Ag NPs core within the shell was started at 640 °C causing the loss of silver due to diffusion.

The surface potential significantly influences the adsorption of organic components and its intermediates on the surface of the photocatalyst during photoreaction. The variation of zeta-potential (ζ) is shown in **Figure 5.15**. The zero point charge (pH_{zpc}) of bare TiO_2 was found to be 6.49±0.6 and, ζ varied from 20.1±0.8 to −23.6±1 mV between pH 3 and 10. With the increase in pH, ζ was more negative and, similarly with the decrease in pH, ζ turned more positive. The pH_{zpc} of different Ag-loaded TiO_2 varied from 6.44±0.4 to 6.13±0.5. The colloidal stability of particles increases with higher negative ζ (Popa et al., 2009), i.e., at higher pH, Ag/TiO_2 particles were more stable than bare TiO_2. At pH 10, ζ varied between −23.6±0.7 and −44.26±1 mV signifying that in the aqueous medium, the particles were well dispersed. The negatively charged particles prevent from the formation of aggregates because of electrostatic repulsion at higher pH (Behera et al., 2016). It implies that at lower pH, Ag/TiO_2 particles opposed destabilization. As a result at lower pH, ζ did not increase much as compared to the higher pH. The growth of the surface charge on TiO_2 based materials usually follows as shown in Eqs. 5.5 and 5.6. The higher valency of the support material than the dopant metal induces the more oxygen vacancies (Yang et al., 2015). It gets stability by trapping more -OH groups or H_2O onto the surface of Ag/TiO_2. Therefore, the absolute value of ζ was more for Ag/TiO_2 both at lower and higher pH.

$$Ti\text{-}OH + H^+ \leftrightarrow Ti\text{-}OH_2^+ \quad (5.5)$$

$$Ti\text{-}OH + OH^- \leftrightarrow Ti\text{-}O^- + H_2O \quad (5.6)$$

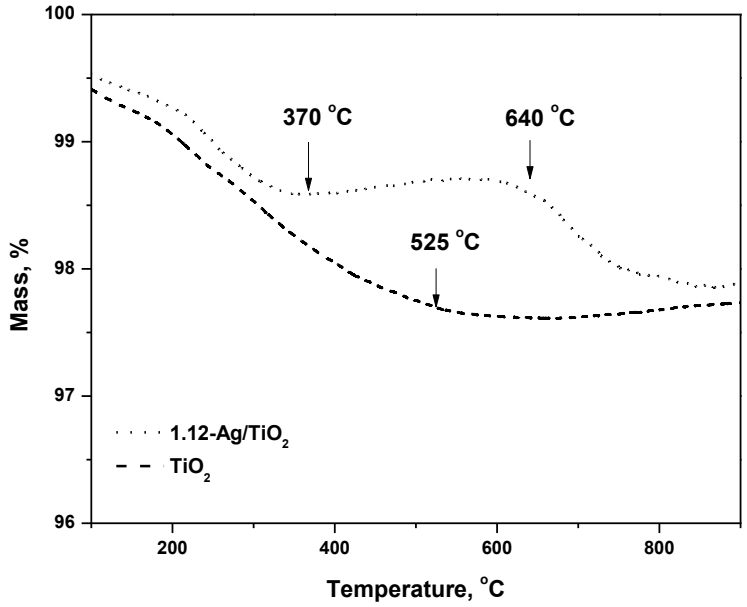

Figure 5.14. TGA analysis of bare and 1.18-Ag/TiO_2.

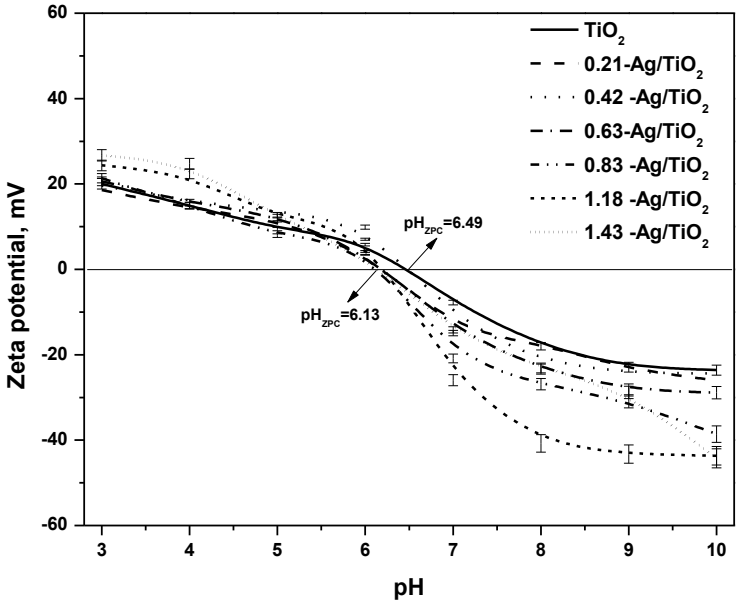

Figure 5.15. Variation of zeta-potential of bare and Ag-doped TiO_2 by BMD at various pH.

5.2.3 Ag/TiO_2 photocatalytic activity under visible light

The photocatalytic activity of the bio-mediated Ag-doped TiO_2 catalyst was examined for the degradation of CR dye. **Figure 5.16** shows the plot of dye color removal as a function of reaction time catalyzed with bare TiO_2 and Ag/TiO_2 particles under visible light. It can be seen that CR dye was very stable by itself, and almost no decomposition was noted after 120 min of illumination under visible light. There was about 7 % CR dye removal in the case of bare TiO_2 in the first 60 min, and it reached 13 % after 120 min reaction. BMD Ag/TiO_2 exhibited a dramatic performance of CR dye degradation. There was about 69 to 78 % dye

removal in 120 min using 0.21 to 0.63 % (w/w) Ag-doped TiO_2. In the case of 0.83 % (w/w) Ag-loading, almost 93 % dye removal was observed. The highest degradation was noted with 1.18-Ag/TiO_2 (98 %) in 120 min. The photocatalytic activity enhanced with Ag/TiO_2 was due to the improvement of separation of e^- and h^+ through e^- trapping of AgNPs with the induction of higher oxygen vacancies (Yang et al., 2015). However, 1.43-Ag/TiO_2 gave a recombination rate (Ola and Maroto-Valer, 2015) resulting in the decrease in dye decomposition at higher Ag-loading. The performance of BMD TiO_2 showed a clear superiority over the many conventional doping methods for the faster degradation of azo dyes (Hu et al., 2006; Sangpour et al., 2010; Sobana et al., 2006).

The above results clearly show that there is no effect of photosensitization and, that is why there was almost no dye degradation with bare TiO_2. Nevertheless, the experiments were conducted for the degradation of phenol, a colorless compound. 1.18-Ag/TiO_2 exhibited about 80 % phenol decomposition from a solution of 100 mg L^{-1} under the identical test condition after 2 h of reaction time. Likewise, the effect of photosensitization can be ignored. The formation of reactive oxygen species on bare TiO_2 and Ag/TiO_2 was detected by ESR spectra which were recorded at room temperature (**Figure 5.17**). The g-value for TiO_2 and Ag/TiO_2 of 0.21 to 1.43 % was 2.021, 2.023, 2.011, 2.043, 2.037, 2.042 and 2.025, respectively. The g-value corresponds to the most intense peak (~310 mT) attributed to the formation of superoxide ($O_2^{\bullet-}$) radicals (Sobana et al., 2006). $O_2^{\bullet-}$ radicals can be generated from the reduction of O_2 adsorbed on the TiO_2 surface by the electron in conduction band of TiO_2. It can also yield perhydroxyl radical ($^{\bullet}OOH$) by reacting with H^+. At higher Ag-loading (1.18 and 1.43 % w/w), a small peak (~337 mT) gives g=1.96 which corresponds to Ti^{3+} at the TiO_2 surface. Ag particle could transfer e^- to react with a Ti^{4+} or O_2 molecule to form reactive surface center like Ti^{3+} and $O_2^{\bullet-}$ radical. Ti^{3+} surface defects serve as traps for e^- and consequently, prolong the lifetime of h^+. It also extends uniquely locate for oxygen-chemical adsorption (Liu et al., 2004). The maximum intensity was with 1.18-Ag/TiO_2. It implies that the intensities of signals of $O_2^{\bullet-}$ radical increased considerably which may explain the high photocatalytic activity of 1.18-Ag/TiO_2. The ESR analysis was carried out with the solid samples. So, it could not detect the formation of $^{\bullet}OH$ radicals using Ag/TiO_2 photocatalysts (Hu et al., 2006). Ag causes a change in the chemical state of TiO_2 leading to the reduction of Ti^{4+} into Ti^{3+}, and the oxygen vacancies are induced in the TiO_2 lattice (Atla et al., 2012). Ti^{4+} ions also could be reduced to Ti^{3+}, Ti^{2+}, and Ti^+ due to metal doping (Xiong et al., 2012).

Ag^+ ions are adsorbed on the hydroxylated TiO_2 surface, and anchored to the external-surface forming Ti-O-Ag bonds (Eq. 5.7).

$$Ag^+ + Ti - OH \rightarrow Ti - O - Ag + H^+ \quad (5.7)$$

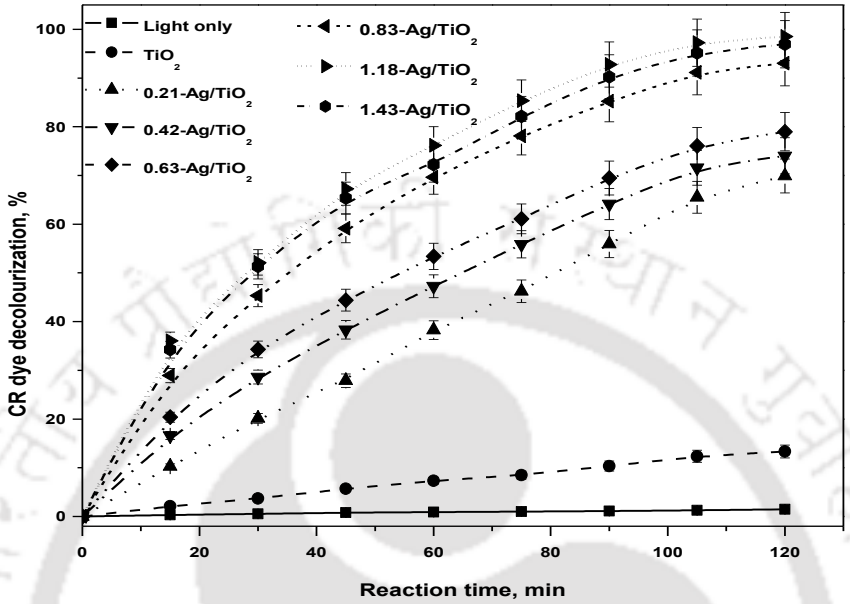

Figure 5.16. CR dye decolorization with reaction time under visible light illumination Experimental conditions: CR dye 100 mg L^{-1}, catalyst dose 100 mg L^{-1}, pH 7, reaction volume 100 mL, stirring speed 300 rpm, and reaction temperature 25 ± 2 °C.

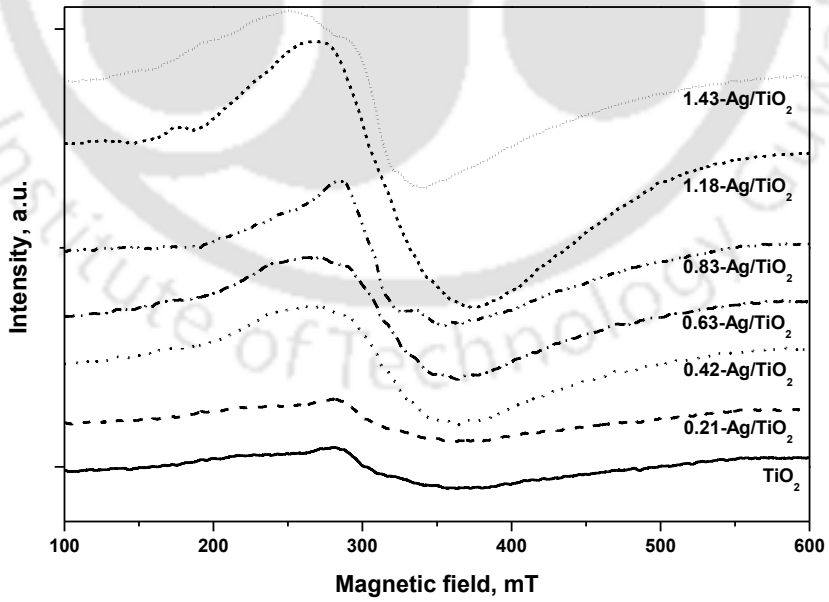

Figure 5.17. EPR spectra for pristine TiO_2, and Ag/TiO_2 at different Ag-loading.

5.3 Ag/ZnO for Dipyrone Drug Degradation

5.3.1 Optimal pH for Ag^+ binding onto ZnO

The highest immobilization efficiency of 80.7 % was found at pH 8 (**Figures 5.18 and 5.19**). Likewise, the amount of Ag^+ immobilized was 0.203, 0.403, 0.598, 0.807, 1.188, and 1.576 % for 0.25, 0.5, 0.75, 1.0, 1.5, and 2 % (w/w) with respect to 100 g ZnO support which was taken initially at pH 8 (**Figure 5.18**). A similar explanation as in **Section 5.2.1** is also applicable here. It displays a fairly linear trend of Ag^+ immobilization even at a higher initial Ag^+ concentration of 2 %. So, the doped catalyst is denoted as x-Ag/ZnO (x is the amount of Ag doped). The presence Ag^+ ions in the bio-extract could lead to Ag^0 ridge formation on ZnO surface rather than doping which could inhibit the visible light harvesting. It also could happen when Ag^+ is not immobilized properly on ZnO (**Figure 5.20**).

A mechanistic scheme of bio-mediated Ag-doping on ZnO is shown in **Figures 5.21(a)** and **5.21(b)**. AA, as a sacrificial e^- donor, reduces Ag_2O and, dehydro-AA is formed (**Figure 5.19(a)**). Under an alkaline medium, an intermolecular reaction between Zn-O and $Ag(OH)_2$ may occur and the Ag_2O/ZnO nuclei is formed through a Zn–O–Ag bond (Gao et al., 2011). In fact, Ag_2O particles are reduced favorably than Ag^+ due to a lower electrode potential (**Chapter 3, Section 3.2.2.1**). So, Ag_2O is reduced by AA leading to the formation of Ag^0 nuclei on ZnO surface and, AA is oxidized to dehydro-AA. At the growth stage, a Zn–O–Ag bond can be formed between Ag and ZnO, and further, it could act as the nucleation sites for the growth of particles leading to the formation of Ag/ZnO nanocomposites.

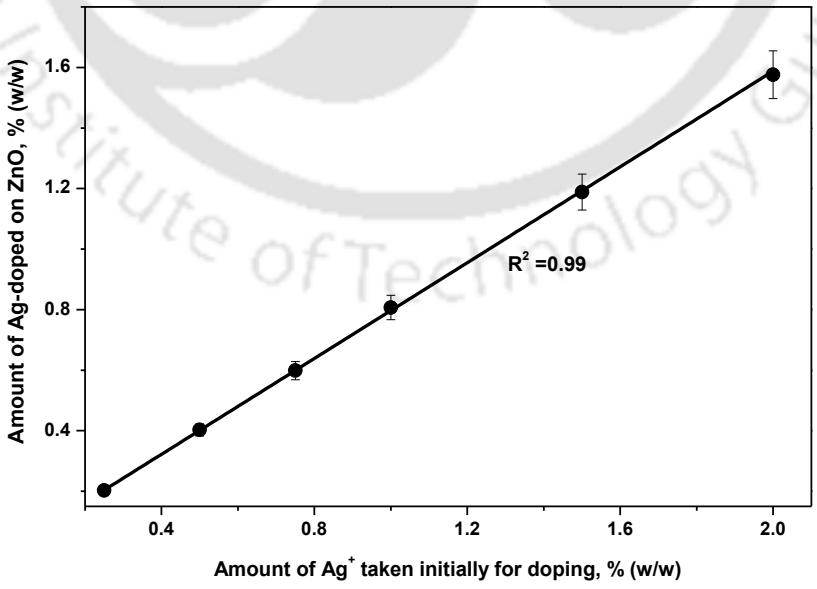

Figure 5.18. Ag^+ solution concentration and quantitative retention of Ag onto ZnO. Experimental conditions: Stirring speed 300 rpm, temperature 28±2 °C, and reaction time 1 h.

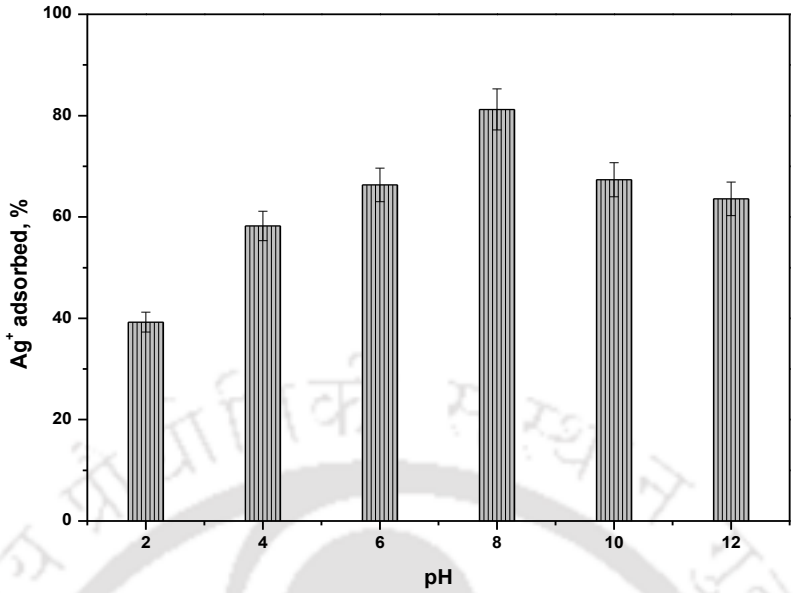

Figure 5.19. Effect of solution pH on Ag^{+} immobilization on ZnO without bio-extract. Experimental conditions: Ag^{+} concentration 1 %, stirring speed 300 rpm, and contact time 60 min.

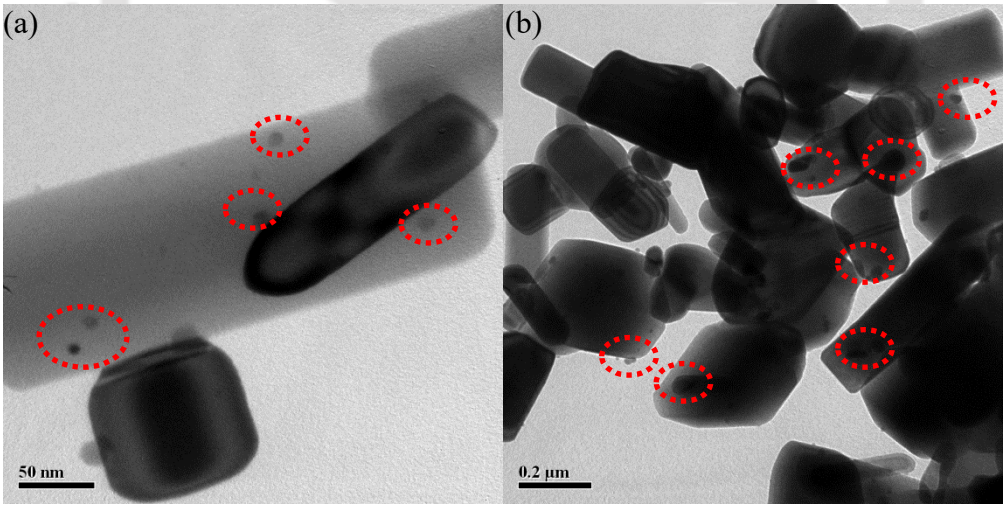

Figure 5.20. Evidence of Ag^{0} from TEM micrograph in the case of improper doping methodology at different magnification: (a) 50 nm and (b) 200 nm.

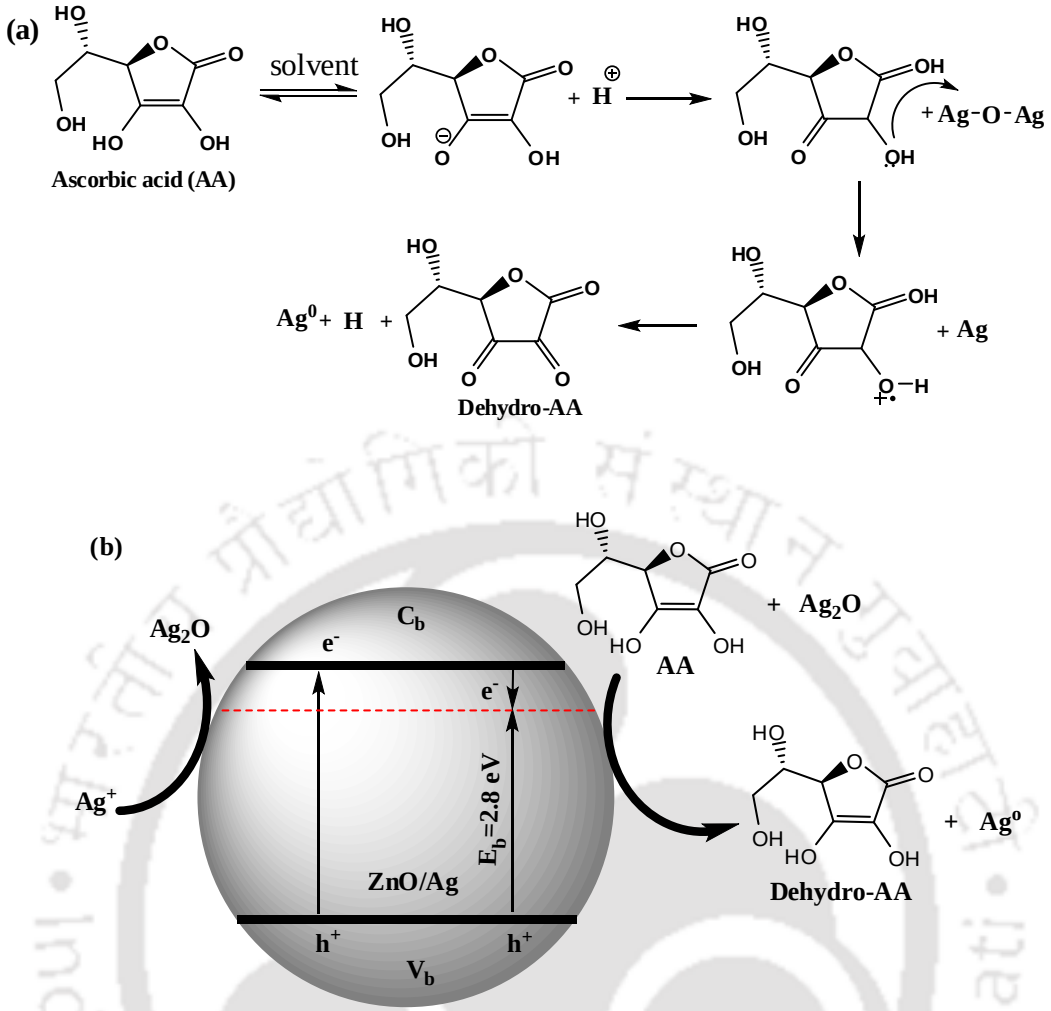

Figure 5.21. (a) Proposed mechanism showing the reduction of Ag ions by AA, and (b) bio-mediated Ag-doping on ZnO.

5.3.2 Characteristics of Ag/ZnO

5.3.2.1 XRD patterns of Ag/ZnO

Figure 5.22 illustrates the XRD patterns of pristine ZnO and Ag/ZnO particles. The peaks at 31.8, 34.4, 36.3, 47.5, 56.6, 62.9, 67.9, and 69.1° 2θ values are for the reflections from the (1 0 0), (0 0 2), (1 0 1), (0 1 2), (1 1 0), (0 1 3), (1 1 2), and (2 0 1) planes for ZnO, respectively (Vivekanandhan et al., 2014). The pristine ZnO showed the presence of pure phases. 0-Ag/ZnO without Ag^+ precursor showed the similar crystallinity as with the pristine ZnO. No additional peaks were detected for Ag^0 in the case of Ag-loading <1.18 % due to its low content and high dispersity. However, at 1.58 % loading, two peaks at 38.4 and 64.4° were of the crystalline phases of AgNPs (Wang et al., 2013) (**Section 5.2.2.1**).

The crystallite size of Ag/ZnO was calculated at 2θ = 36.3° (**Table 5.4**). The interplanar d-spacing and crystallite size were increased with the increase in Ag-loading. This is due to

the induction of Ag^{+} ions into ZnO crystal lattice which could be placed in the interstitial sites or substituted zinc ions to Ag–O–Zn bonds (Zhang and Zeng, 2011) (**Section 5.2.2.1**).

The elemental EDX image mapping of 1.18-Ag/ZnO is illustrated in **Figure 5.23(a)**. The number of nanocrystals identified by the structural configuration included of Zn, O, and Ag elements. The weight percent of Ag-loading on ZnO was 0.7 ± 0.1 against 78.9±0.6 and 20.5±0.6 for Zn and O (**Figure 5.23(b)**). High dispersity of Ag is evident as that of C, O, and Zn (**Figures 5.23(c) – 5.23(f)**). The carbon tape used for the analysis caused the source of C.

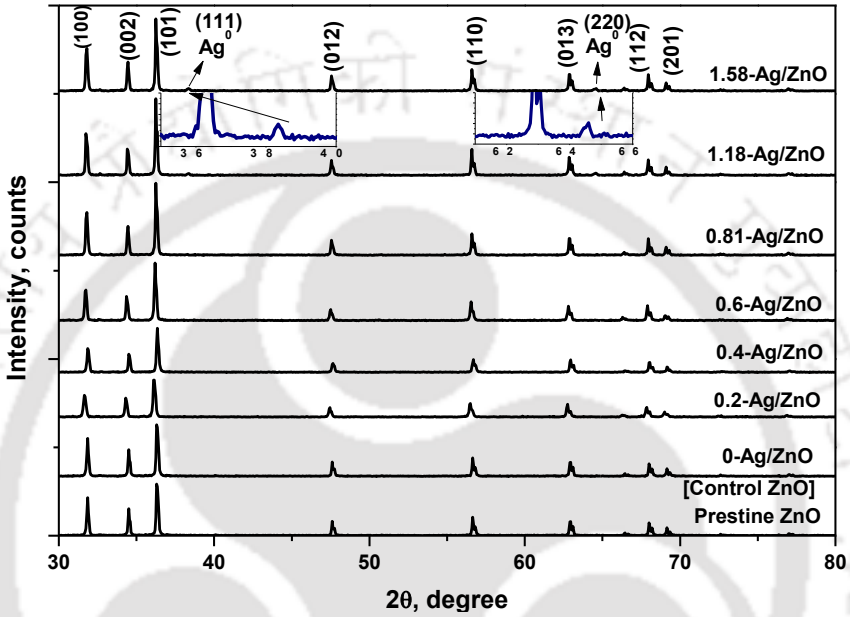

Figure 5.22. XRD patterns of undoped and bio-mediated doped Ag/ZnO nanostructures.

Table 5.4. Interplanar d-spacing, crystallite size, and band gap of support and Ag-doped ZnO particles.

Catalyst	d-spacing, A°	Crystallite size, nm	Band gap energy, eV
Pristine ZnO	2.4753±0.15	43.509±0.75	3.136±0.74
0.2-Ag/ZnO	2.4757±0.99	49.641±0.71	3.131±0.14
0.4-Ag/ZnO	2.4757±0.25	52.138±0.35	3.117±0.93
0.6-Ag/ZnO	2.4759±0.17	52.364±046	2.941±0.22
0.81-Ag/ZnO	2.4762±0.93	57.318±0.18	2.878±0.81
1.18-Ag/ZnO	2.4767±0.16	58.616±0.79	2.839±0.62
1.58-Ag/ZnO	2.4765±0.07	57.597±0.25	2.847±0.78

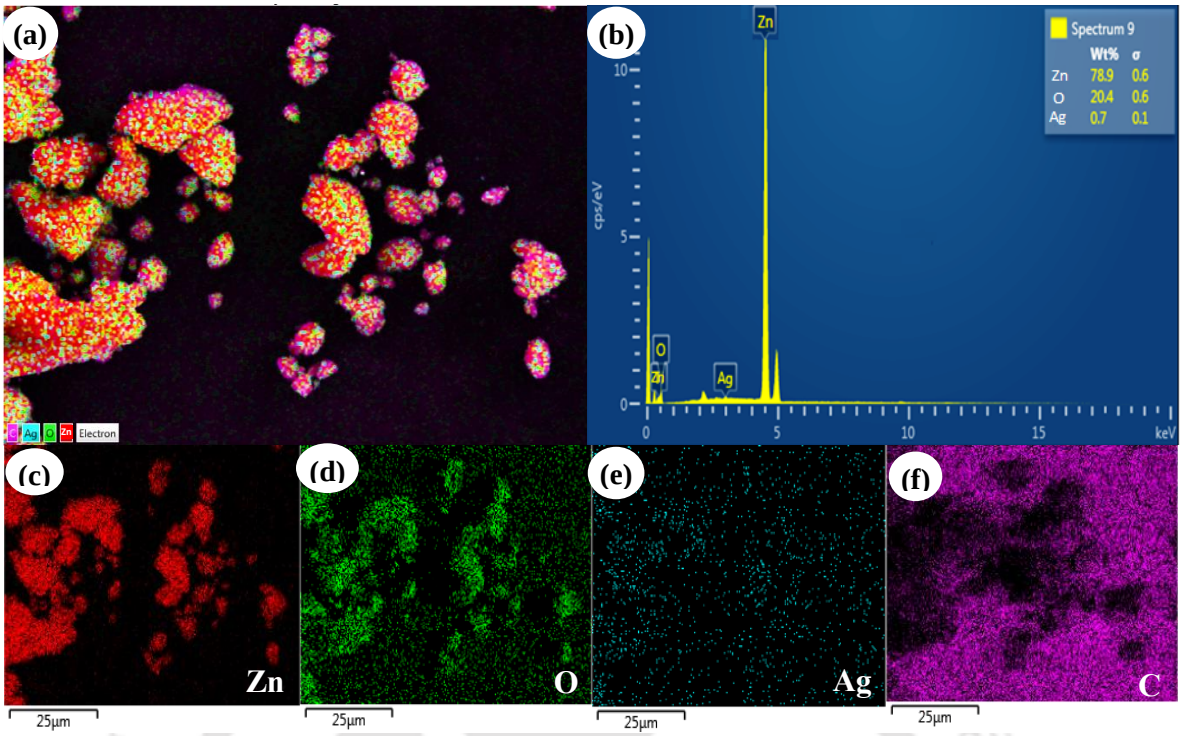

Figure 5.23. EDX image mapping of 1.18-Ag/ZnO particles ((a): relative dispersity of C, O, Zn, and Ag elements, (b): Dispersity of individual element (c-f) Zn, O, Ag and C dispersity).

5.3.2.2 UV-vis DR spectra and repeatability test

The UV-vis DR spectra at various Ag-loadings are shown in **Figure 5.24**. The pristine ZnO didn't show any absorption peak in the visible region. In the case of Ag/ZnO, a broad absorption peak appeared to the visible region (~475 nm) and, the peak intensity was enhanced gradually with the increase in Ag-loading up to 1.18 % (w/w) thereafter it was reduced with 1.58 % (w/w). The E_g was calculated by the Tauc plot (**Figure 5.25**) (**Section 5.2.2.2**). With the increase in Ag-loading, E_g was gradually reduced to 2.85 eV with 1.18-Ag/ZnO and increased slightly and 1.58-Ag/ZnO. A similar explanation of UV-vis DR spectra, change in absorption band with Ag-loading as well as band gap reduction as in **Section 5.2.2.2** is also applicable here.

The experiment was triplicated and, the results with 1.18-Ag/ZnO are only shown in **Figures 5.26** and **5.27**. The absorption band closely overlapped and, the standard deviation of band gap energy was found to be 0.00439 eV. The Ag^+ precursor and the bio-extract were directly mixed with ZnO support. The band of direct Ag^+ doping without immobilization was found to be 2.88 eV.

Ag was also doped using pure AA by maintaining the concentration as it was found in the bio-extract. The UV-vis DR spectra of AA and bio-extract mediated-Ag/ZnO are

presented in **Figure 5.28**. The shift of the absorption band in the visible light for Ag/ZnO (bio-extract) was significantly higher compared to AA-Ag/ZnO. The band gap with AA-Ag/ZnO was found to be 2.91 eV. *S. edule* contains about 19.3, 5.58 and 53.2 mg per 100 g fruit flavonoids, aglycone, and reducing sugars along with other secondary analytes which could help for the efficient Ag-doping (Modgil et al., 2004; Siciliano et al., 2004). Moreover, the bio-extract could prevent the particle aggregation. So, it helps particles destabilization.

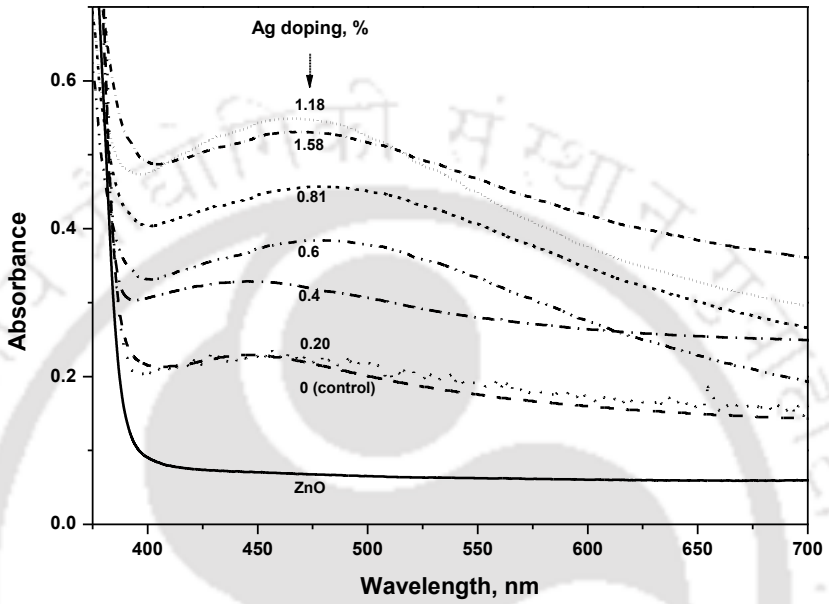

Figure 5.24. UV-vis DR spectra of pristine ZnO, control ZnO, and Ag/ZnO with variation of dopant loading.

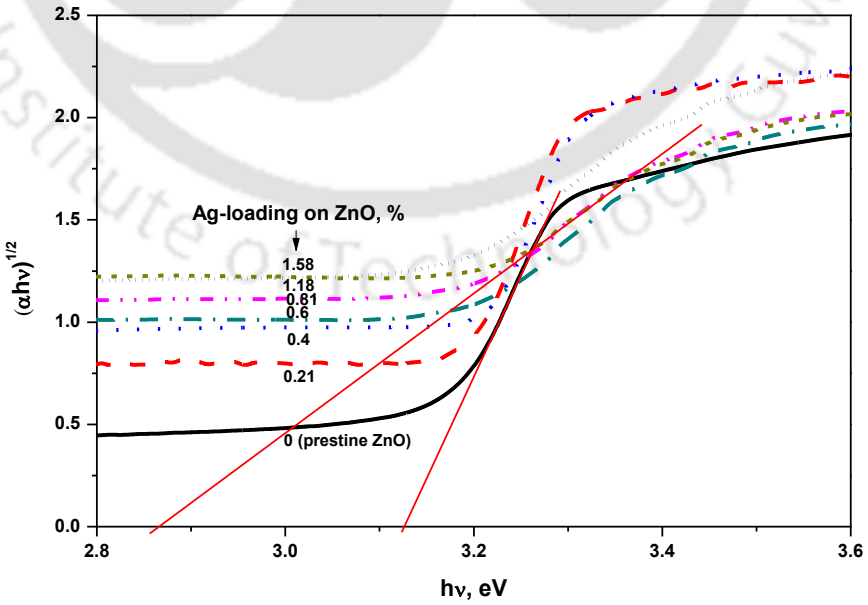

Figure 5.25. Optical direct band gaps (Tauc plot) of the pristine and Ag-doped ZnO.

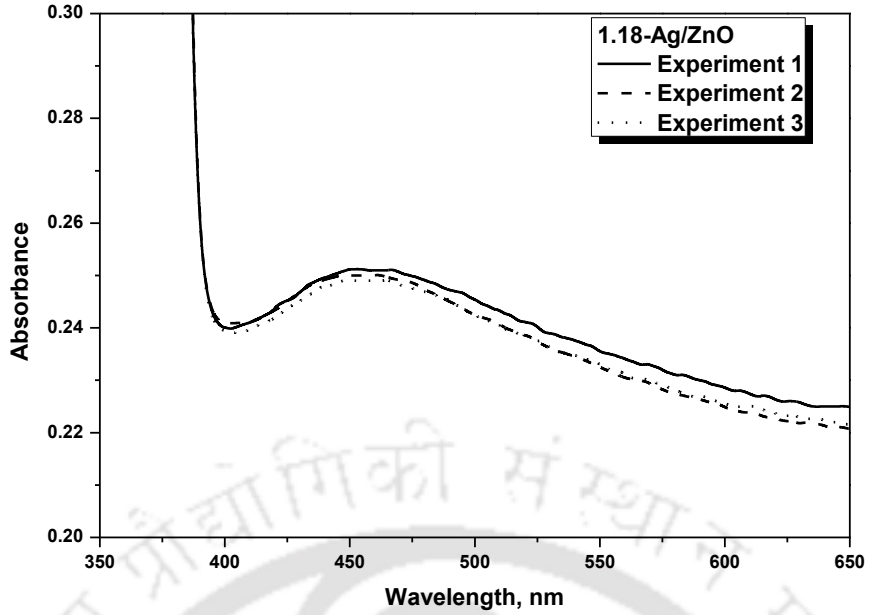

Figure 5.26. Consistency of Ag/ZnO in terms of UV-vis DRS spectra from triplicate doping tests (shown only with 1.18-Ag/ZnO).

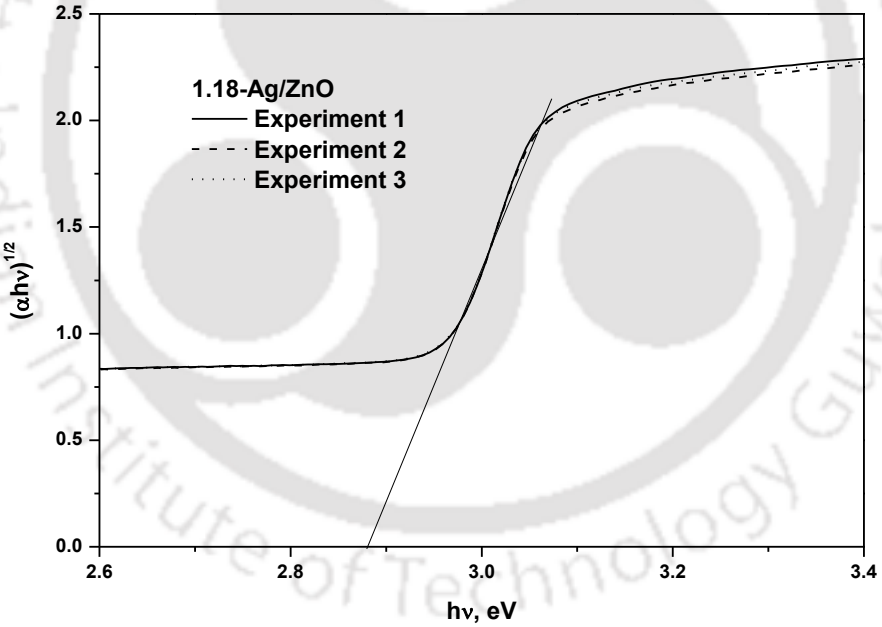

Figure 5.27. Consistency of Ag/ZnO in terms of optical direct band gaps (Tauc plot) from triplicate doping tests (Figure 5.23).

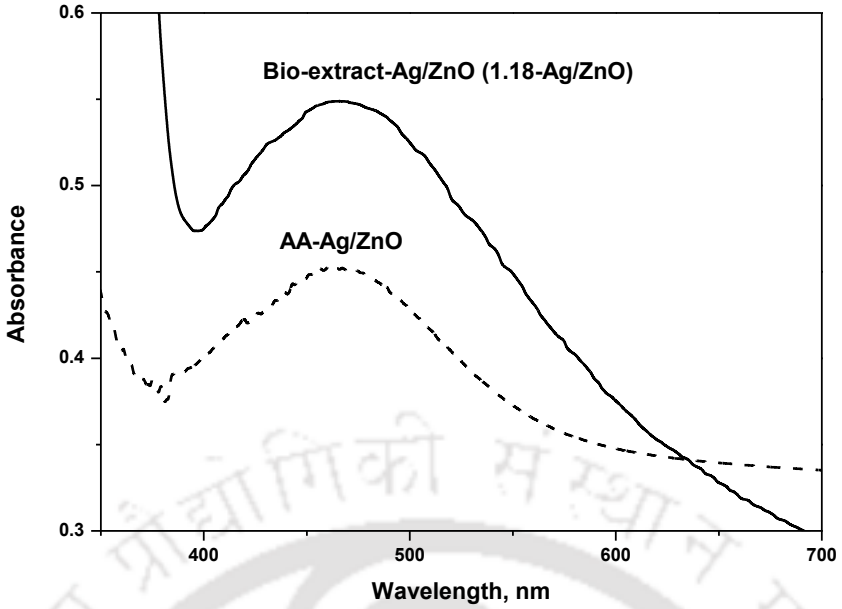

Figure 5.28. UV-vis-DR spectra of bio-extract-Ag/ZnO and AA-Ag/ZnO. Experimental conditions: AA concentration 0.6 mM, pH 8, temperature 28±2 °C, and reaction time 24 h.

5.3.2.3 BET surface area, particle size and morphology of Ag/ZnO

Table 5.5 shows the BET surface area of pristine ZnO and Ag-doped ZnO. The surface area was decreased from 15.4 to 11.9 $m^2 g^{-1}$, i.e., by 22.3 % reduction at the highest dopant concentration of 1.58 %. The reduction in surface area was for the induction of Ag into ZnO lattice (**Section 5.2.2.3**). Nearly a linear reduction in surface area was observed (R^2= 0.90). The pore diameter and pore volume of pristine ZnO were increased from 31.8 to 58.1 nm and 0.059 to 0.09 $cm^3 g^{-1}$ for 1.58-Ag/ZnO. The increase in the average pore size of Ag/ZnO is due to the rise in crystallite size (**Section 5.2.2.3**). The surface area decrement with the bio-mediated Ag/ZnO was relatively lesser than ZnO doped using Ag by hydrothermal, photodeposition, and impregnation methods (Jasso-Salcedo et al., 2014; Wang et al., 2016).

Figure 5.29 shows 2D and 3D surface morphologies of Ag/ZnO nanocrystals. The surface of ZnO appeared as a grain like structures of around 25–95 nm and, the RMS roughness was found to be 3.5054 (**Figures 5.29(a)** and **5.29(b)**) (Garcia-alamo et al., 2013). These results are in agreement with the TEM micrograph for 1.18-Ag/ZnO (**Figure 5.29(c)**). The sizes of the particles were not uniform and, it ranged between 17 and 135 nm. A minor agglomeration was seen in some of the clustered particles. Since it is hard to see the Ag deposition on ZnO in TEM micrograph that it may be because of Ag^+ ions would tie up with TiO_2 through the coordination reaction or an ion-exchange (Li et al., 2003) which could act as a nucleation precursor. The SAED patterns are presented in **Figure 5.29(d)** which shows

the polycrystallinity nature (Patil et al., 2016). The sharp lattice fringes with an interplanar spacing of 0.247 nm was observed from the high-resolution TEM micrograph which attributes to the d-spacing of the (101) of hexagonal ZnO wurtzite structure (**Figure 5.29(e)**).

Figure 5.29(f) shows the particle size measured by DLS. The size distribution of nanoparticles moved to a higher mean with the increase in dopant concentration (S**ection 5.3.2.3**). ZnO nanocrystals exhibit an affinity to agglomerate due to the presence of OH^- groups on the surface. The polydispersity index was increased from 0.179 to 0.343 owing to Ag-doping in the case of TiO_2/Ag-1.18 (**Table 5.6**). The variation in the mean particle size in TEM, AFM, and DLS studies are shown in **Table 5.6** (**Section 5.2.2.4**).

Table 5.5. Surface area, pore diameter, and volume of ZnO and Ag/ZnO.

Catalyst type	Surface area, $m^2 g^{-1}$	Pore diameter, nm	Pore volume, $cm^3 g^{-1}$
ZnO	15.42	31.82	0.0587
0.2-Ag/ZnO	14.21	35.82	0.0628
0.4-Ag/ZnO	13.57	40.53	0.0721
0.6-Ag/ZnO	13.38	47.26	0.0829
0.81-Ag/ZnO	12.86	58.28	0.0933
1.18-Ag/ZnO	11.88	58.36	0.0929
1.58-Ag/ZnO	11.97	58.05	0.0921

Table 5.6. Mean diameter of Ag/ZnO.

Catalyst type	Polydispersity index in case of DLS	Mean particle diameter, nm		
		DLS	TEM	AFM
0.2-Ag/ZnO	0.179±0.091	82.92±0.11	29.75±0.91	26.93±0.91
0.4-Ag/ZnO	0.181±0.006	85.13±0.91		
0.6-Ag/ZnO	0.198±0.082	88.84±0.24		
0.81-Ag/ZnO	0.213±0.007	89.49±0.82		
1.18-Ag/ZnO	0.274±0.09	93.24±1.04		
1.58-Ag/ZnO	0.283±0.039	95.03±1.01	50.34±1.21	48.88±1.05
0.2-Ag/ZnO	0.343±0.086	95.81±0.73		

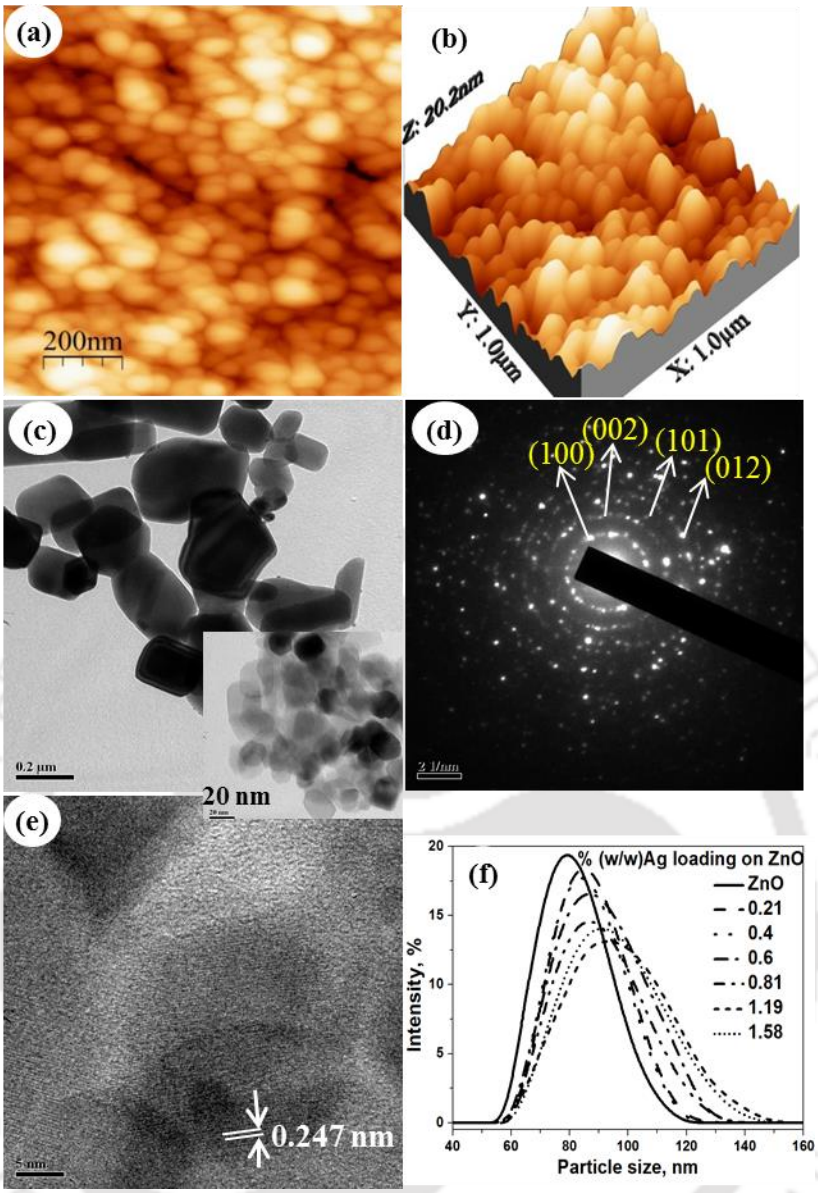

Figure 5.29. (a) AFM 2D and (b) 3D micrographs, (c) TEM micrograph, (d) SAED pattern, (e) High-resolution TEM, and (f) Particles size distribution from DLS for 1.18-Ag/ZnO.

5.3.2.4 Thermal and colloidal stabilities

The influence of temperature on the catalyst support and Ag/ZnO nanocrystals is shown in **Figure 5.30**. The pristine ZnO showed a steady mass loss of about 1.21 % up to 950 °C. Water removal by drying was found between 50 and 150 °C for 1.18-Ag/ZnO. There was mass loss of 4.9 % within 200 to 540 ºC due to decomposition of organic compounds like ascorbic acid, quercetins, ferulic acid, carbohydrates, and lignins (Carballo et al., 2008; Sun et al., 2014). Most of these constituents act as the capping agents. After that, 3.95 % mass loss was observed at 540-950 ºC due to thermal degradation of bioorganic salts like carbonates and resistive aromatic complexes (Carballo et al., 2008).

The adsorption of organic compounds on the catalyst surface was highly controlled by the surface potential. So, the Zeta-potential (ζ) was determined and, the variation of ζ with respect to the solution pH was shown in **Figure 5.31**. The point of zero charge (pHzpc) of pristine ZnO was found to be 9.37±0.4 mV and, it decreased to 8.21±0.3 mV for Ag/ZnO. ζ varied from 18±0.5 to −24.8±0.6 mV for pH between 3 and 12 with ZnO. For Ag/ZnO, ζ was found between −24.8±0.5 and −47.13±0.8 mV at pH 12. At a higher pH, the formation of agglomerates is prevented because of electrostatic repulsion (Behera et al., 2016). A similar explanation of surface charge difference in lower and higher pH as in **Section 5.2.2.4** is also applicable here. The surface charge on ZnO surface is developed both in acidic and basic pH as shown in Eqs. 5.8 and 5.9 (Bian et al., 2011). Moreover, the higher valency of the support metal than the dopant metal induces the oxygen vacancies (Yang et al., 2015). It gives the particles stability by trapping more H_2O or –OH groups on Ag/ZnO surface.

$$ZnO + H^+ \leftrightarrow ZnOH^+ \quad (5.8)$$

$$ZnO + H_2O + 2OH^- \rightarrow Zn(OH)_4^{2-} \quad (5.9)$$

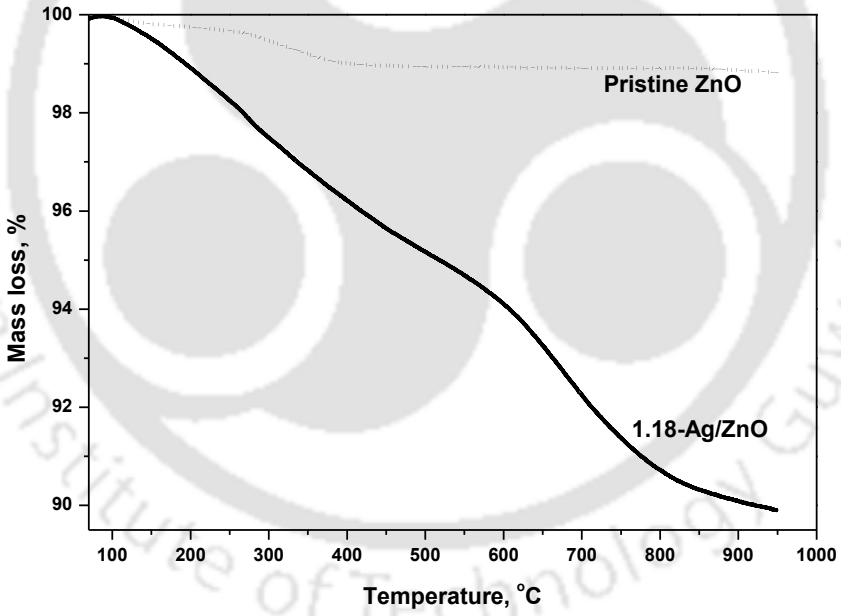

Figure 5.30. TGA of ZnO and 1.18-Ag/ZnO nanostructures.

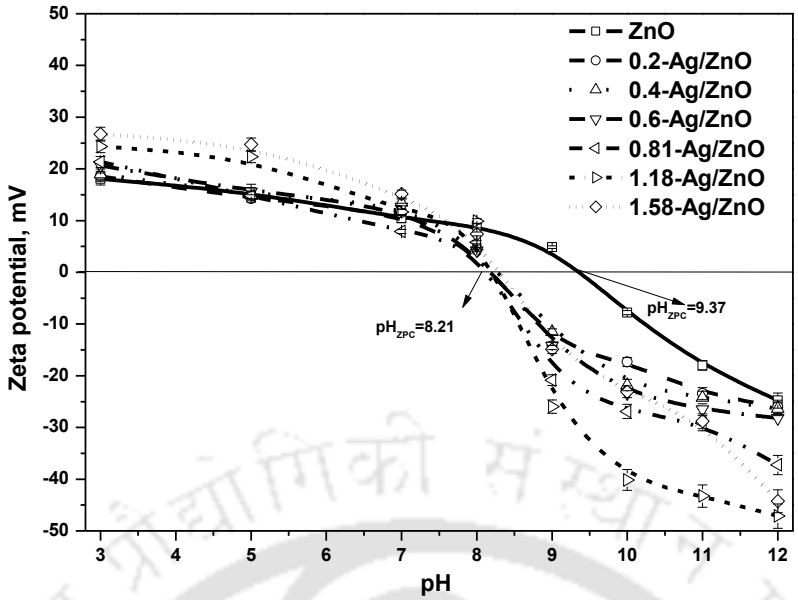

Figure 5.31. Variation of zeta-potential of pristine ZnO and Ag/ZnO at different pH. Experimental conditions: Temperature 28±2 °C, and sample volume 10 mL.

5.3.3 ZnO/Ag photocatalytic performance under visible light

Almost no dipyrone decomposition was observed after 120 min of illumination without any catalyst. In the case of pristine ZnO, 12 % drug removal was achieved after 120 min (**Figure 5.32**). As expected, dipyrone degradation was increased to 52.9-79.5 % in 120 min for 0.2-Ag/ZnO to 1.18-Ag/ZnO. However, 1.58-Ag/ZnO showed a little reduction in drug degradation as compared to 1.18-Ag/ZnO. A similar explanation as in **Section 5.2.3** is also applicable here.

The photosensitization effect in the presence of color compound also could be functioning (Behera et al., 2016). Such effect with dipyrone can be neglected being a colorless compound. Ag/ZnO (AA) was prepared with 1.18 % Ag^{+} loading using 44.1 mg L^{-1} AA which was same as AA concentration in the bio-extract (**Figure 5.32**). It showed only 17.6 % dipyrone decomposition.

Figure 5.33 presents the comparative drug and COD reduction at 120 min of reaction. There was maximum 71 % COD removal with 1.18-Ag/ZnO. The organic fragments formed were not completely decomposed under these oxidation conditions, but the difference between drug and COD removal was minimal.

The loss of the catalytic activity performance was found to be only 9 % in terms of dipyrone degradation after the fourth cycle (**Table 5.7**) and, the amount of catalyst loss was 6 % (Hu et al., 2017). Quantum yield (QY) is a very important factor in assessing the reaction

efficiency as a whole, which is controlled by the effectiveness of suppression of e^-/h^+ recombination. The QY for the degradation of dipyrone was calculated by using Eq. 5.10 (Shidpour, 2015).

$$QY = \frac{DV_0hc}{Pt\lambda_m} \times 100, \% \quad (5.10)$$

Where, D is the degradation fraction ($1\text{-}C/C_0$) from **Figure 5.32**, V_0 is the volume of dipyrone solution (cm^3), h is the Planck's constant, c is the speed of light, λ_m is in cm, P is the power of accident light in (here 200 W), and t is the reaction time (min). QY was increased with the increase in dopant concentration (**Figure 5.33**). The maximum QY was determined to be 35.77 % in 120 min of reaction time for 1.18-Ag/ZnO. So, the QY of bio-mediated Ag-doped ZnO was more than many earlier reports (**Table 5.8**). In fact, this comparison should be made on similar experimental conditions i.e., same analyte, analyte concentration, photocatalyst concentration, and same wavelength. Since such literatures are not available with the same analyte, the comparison of photocatalytic degradation and quantum yield efficiency were made for visible light assisted process using doped TiO_2.

The photogenerated e^- of AgNPs are induced to the CB of ZnO (**Figure 5.34**) and form the free radicals (Patil et al., 2016; Subash et al., 2012). The potential–photocurrent profiles of pristine ZnO and 1.18-Ag/ZnO coated ITO electrodes are shown in **Figure 5.35**. Both ZnO and 1.18-Ag/ZnO coated electrodes exhibited quite low current densities (-0.0647-0.828 µA cm^{-2}) for E_{anode}= -0.161 to 0.601 V (vs. Ag/AgCl) in dark. h^+ moved at the electrolyte/electrode interface and, e^- is carried to the ITO-coated glass substrate through the AgNPs in connection with an external circuit to generate the photocurrent. The current density starts to onset at E_{anode}= 0.2 V and proceeds to saturation at E_{anode}= 0.3 V for 1.18-Ag/ZnO coated electrode (Patil et al., 2016). The current density was 46.68 µA cm^{-2} against 23.28 µA cm^{-2} for pristine ZnO coated electrode. The increase in current density for 1.18-Ag/ZnO coated electrode are due to the raise in optical absorption of ZnO by the AgNPs SPR effect resulting in enhanced local field strength and a lower charge resistance with the greater separation of e^-–h^+ pairs (Patil et al., 2016). The successful transport of charge carriers has resulted in the increased PEC activity of the 1.18-Ag/ZnO photoanode.

So, O_2 in water and the CB electrons from the bulk ZnO can easily synchronize to obtain $^{\bullet}OH$, $O_2^{\bullet-}$ or $^{\bullet}OOH$ radicals under the visible light illumination. The formation of oxygen vacancies and the effect of Ag-doping for the development of the charge trapping centers and other possible paramagnetic sites in ZnO and 1.18-Ag/ZnO were further investigated by ESR spectroscopy. Pristine ZnO gave four discrete resonances at g = 2.0024,

2.0035, 2.005, and 2.017 while 1.18-Ag/ZnO exhibited five separate signals at g = 2.003, 2.004, 2.008, 2.014, and 2.020 (**Figure 5.34**). The signals at g = 2.002 to 2.008 are attributed to the surface-absorbed $O_2^{\bullet-}$, while the resonances at g = 2.014 and 2.017 are for the zinc vacancies (Wang et al., 2016). A signal at g =2.020 with 1.18-Ag/ZnO could be attributed to the presence of paramagnetic oxygen vacancies which could inhibit e^-/h^+ pair recombination (Su et al., 2013; Wang et al., 2016). So, Ag/ZnO could promote a better e^-/h^+ pair separation for an enhanced photocatalytic activity.

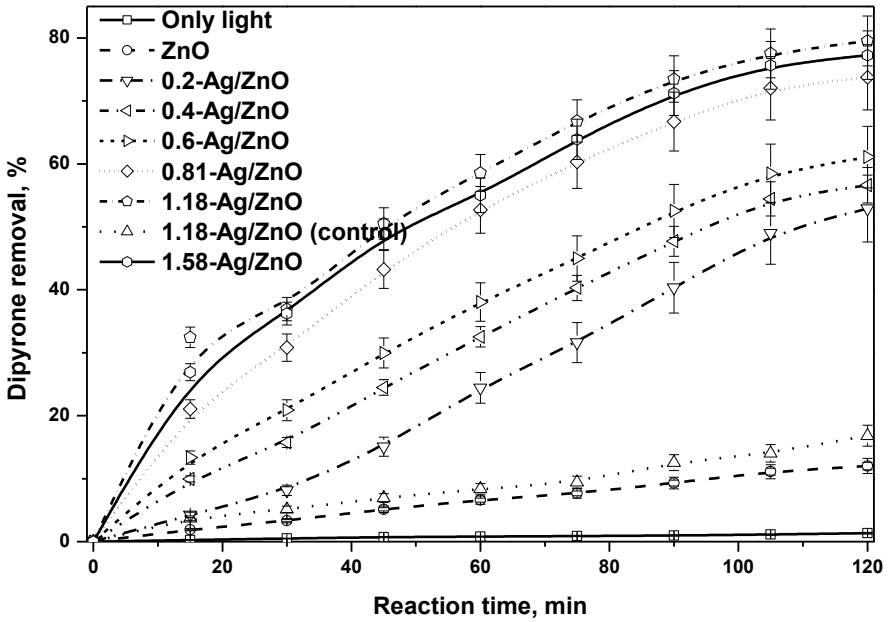

Figure 5.32. Dipyrone drug degradation using ZnO and Ag/ZnO catalysts under visible light irradiation. Experimental conditions: Dipyrone concentration 100 µg L^{-1}, catalyst dose 100 mg L^{-1}, pH 7, reaction volume 100 mL, light intensity 18 K lux, stirring speed 300 rpm, and reaction temperature 25 ± 2 ºC.

Table 5.7. Reusability of 1.18-Ag/ZnO catalyst for dipyrone degradation after 120 min of photocatalysis.

Experiment	Dipyrone degradation, %	Catalyst loss, %
First run	79.5±0.7	Insignificant
Second run	74.2±0.91	Insignificant
Third run	72.4±1.31	5±0.093
Fourth run	70.8±0.83	6±0.07

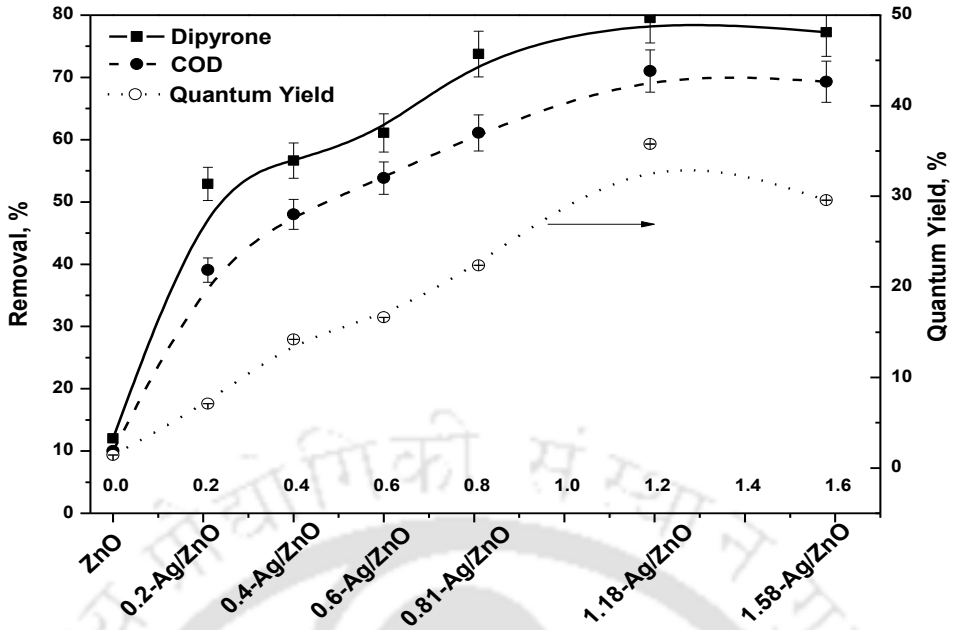

Figure 5.33. Removal of dipyrone drug and COD, and quantum yield variation with different catalysts. Experimental conditions: Dipyrone 100 µg L^{-1}, catalyst dose 0.1 g L^{-1}, pH 7, light intensity 18 K lux, reaction volume 100 mL, stirring speed 300 rpm, and reaction temperature 25±2 °C.

Table 5.8. Comparison of QY in various photocatalytic systems with point light source and particulate photocatalyst.

Photocatalyst	**Pollutant**	**C_0 pollutant (mg L^{-1})**	**$C_{photocatalyst}$ (mg L^{-1})**	**λ_m (nm)**	**P (W)**	**D (%)**	**t (min)**	**QY (%)**	**Reference**
S/TiO_2	Methylene blue (MB)	5000	20000	470	250	99	50	20.9	Ohno et al., 2004
ZnO nanotubes	Ciprofloxacin	0.7	14	420	300	12	120	1.48	Bojer et al., 2017
Ag/ZnO	MB	32	1200	340	1000	98	40	8.94	Georgekutty et al., 2008
Ag/ZnO	MB	5	200	470	300	10	20	4.39	(Whang et al., 2012)
C/TiO_2	MB	5	200	550	100	36	240	3.38	(Kusiak-Nejman et al., 2011)
Ag/ZnO/CNT	Acid Orange 7	1000	100	485	400	98	120	12.1	(Moradi et al., 2017)
ZnO/ Graphene oxide	MB	15	800	420	300	90	25	35.4	(Li et al., 2012)
ZnO/reduced grapheme oxide	MB	5	1500	365	500	60	150	2.72	(Lv et al., 2011)
ZnO/C/CdS	4-	10	500	420	60	98	120	12.1	(Lavand

	chlorophenol								and Malghe, 2015)
TiO_2/CuO	MB	10	2222	656	300	92	120	4.83	Simamora et al., 2012
N/TiO_2	MB	5	1000	400	500	90	120	4.65	Elghniji et al., 2012
1.18-Ag/ZnO	Dipyrone	0.1	100	525	200	78	120	35.8	**Present work**

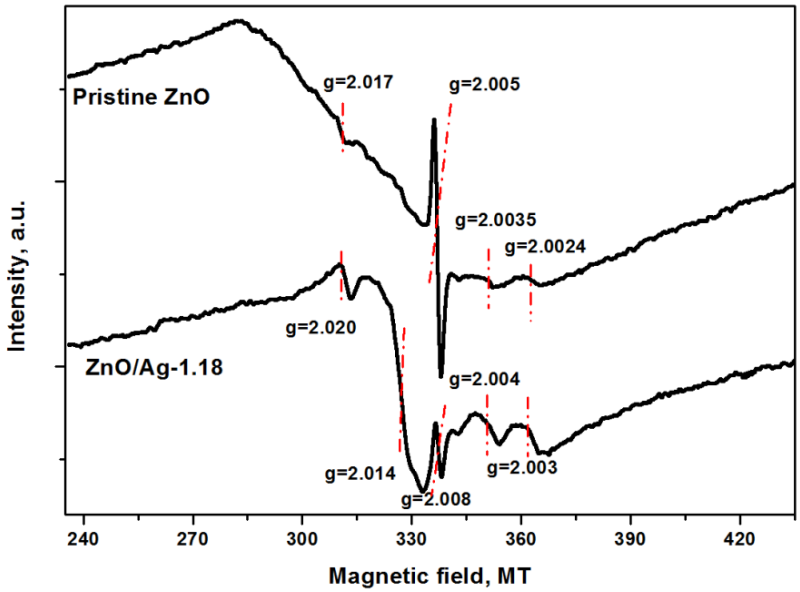

Figure 5.34. ESR spectra of pristine ZnO and 1.18-Ag/ZnO.

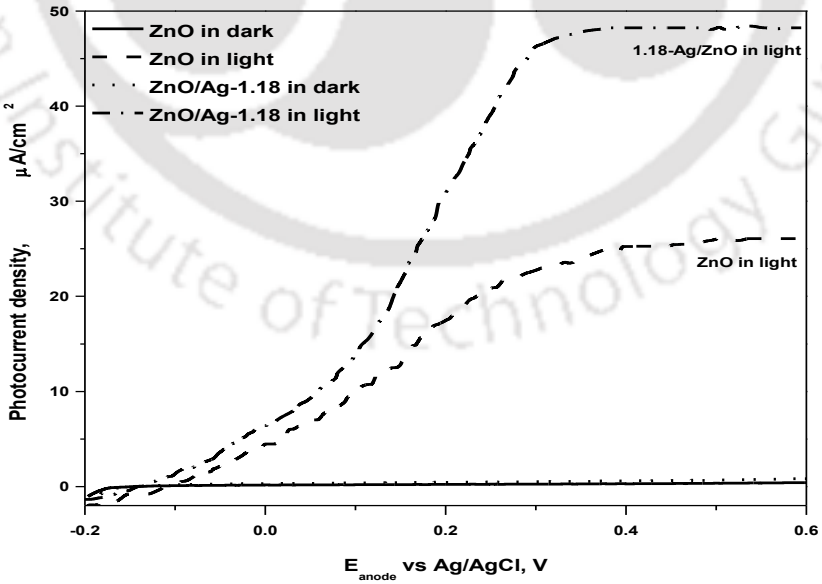

Figure 5.35. Photocurrent density vs. voltage curves for ZnO and Ag/ZnO (measured in 0.5 M Na_2SO_4 at 200 W visible light).

5.3.4 Effect of Ag/ZnO on antimicrobial activity

The growth kinetics of bacterial strains was examined using the spectrophotometric technique (**Chapter 2, Section 2.4.15**) at various doses of 1.18-Ag/ZnO using the same light sourse. *E. coli* and *B. subtilis* bacterial growth kinetics were tested in the presence of Ag/ZnO which is showed in **Figures 5.36** and **5.37**. As increase in 1.18-Ag/ZnO concentration, the inhibition rate increased gradually. Both *E. coli* and *B. subtilis* showed complete inhibition at Ag/ZnO of ≥30 μg mL^{-1}.

E. coli does not show growth propagation, so the lag phase observed clearly. However, with *B. subtilis* the stationary phase can't find so clearly. The growth phase was clearly visible with *E. coli* because of more suppression of strain growth. 10 μg mL^{-1} Ag/ZnO showed about 32 % suppression in *B. subtilis* growth compared to the control media. Interestingly, *E. coli* at the same concentration exhibited 51 % decrease in the cell density. The gram-positive bacteria were less susceptible to Ag/ZnO particles than the gram-positive bacteria. A similar trend of bacterial growth inhibition with ZnO is also reported before (Agnihotri et al., 2014; Ruparelia et al., 2008).

The antibacterial activity of ZnO and Ag/ZnO were also examined by the disk diffusion method at 30 mg L^{-1} AgNPs (**Figure 5.38**). 1.18-Ag/ZnO exhibited an effective inhibition zone of 44 and 42 mm against *E. coli* and *B. subtilis*, whereas ZnO showed very less inhibition (14 mm) against both the bacteria.

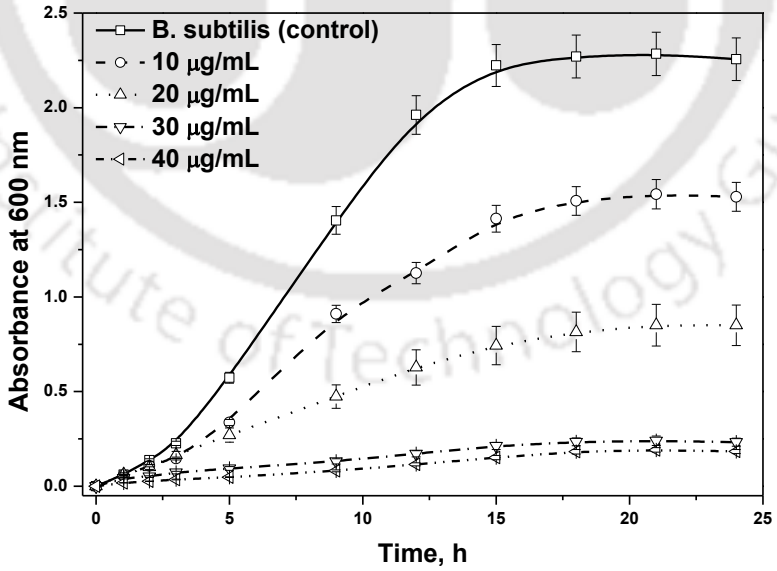

Figure 5.36. The optical density measurements at a wavelength of 600 nm for the bacterial growth kinetics for *B. subtilis* against doses of 1.18-Ag/ZnO. Experimental conditions: Incubation temperature 37 ºC, and reaction time 24 h.

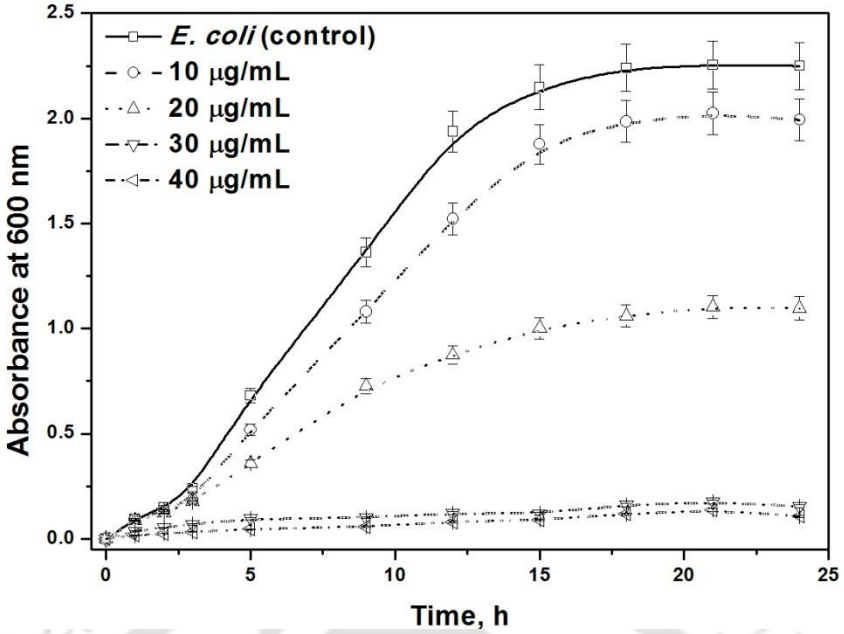

Figure 5.37. The optical density measurements at 600 nm wavelength for the growth kinetics of *E. coli* at different doses of 1.18-Ag/ZnO. Experimental conditions: Incubation temperature 37 ºC, and reaction time 24 h.

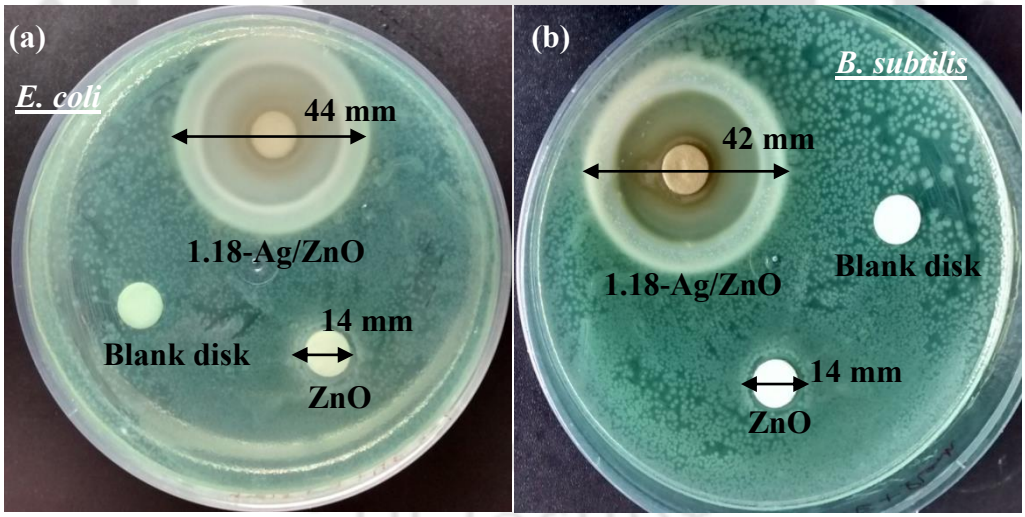

Figure 5.38. Antimicrobial activity of ZnO and 1.18-Ag/ZnO against (a) *E. coli* and (b) *B. subtilis*. Experimental conditions: ZnO or Ag/ZnO concentration 30 mg mL^{-1}, pH 5.8, incubation temperature 37 ºC, and reaction time 24 h.

5.4 Major Findings

Bio-mediated doping method is rather simple, eco-friendly, and cost effective as compared to the conventional doping techniques in terms of bandgap energy reduction and quantum yield for the pollutant degradation. Doping of Ag onto TiO_2 using *Sechium edule* fruit extract was found to be effective to make it active in the visible light and also comparable with the typical doping techniques. The immobilized Ag^+ (71 to 84 % of the initial amount) was suitably doped on TiO_2 because the amount of unreduced Ag^+ ion, as well as Ag_2O clusters, was insignificant. The BMD method increased the crystallite size of TiO_2 with Ag-doping because of a higher ionic radius of Ag^+ compared to Ti^{4+}, and there was also small phase transformation. The Diffuse Reflectance Spectra of Ag/TiO_2 gave a distinct absorption band in the visible region, and the band gap of bare TiO_2 reduced dramatically with Ag-doping to 2.5 eV. BMD caused a significant reduction in zeta potential both at above and below the pH_{zpc} due to the induced oxygen vacancies and that provided Ag/TiO_2 more stability in its aqueous colloidal solution. Ag/TiO_2 showed an intermediate mass loss starting at about 640 °C, due to the melting of Ag nanoparticles. However, the mass loss of bare and doped TiO_2 was comparable at the final temperature (900 °C) indicating insignificant adsorption of biomolecules during bio-doping. $O_2^{\bullet-}$ radical (g varies from 2.01 to 2.04) formed on the surface of TiO_2, was the most reactive species for degradation of CR dye with 98 % efficiency.

Like Ag-doping on TiO_2, the formation of AgNPs, in the bulk media should be avoided to minimize the growth of AgNPs ridges on ZnO surface and, the commercial AA led to AgNPs ridge formation (improper doping) on the supports. So, the bandgap of ZnO didn't reduce as effectively as for the commercial AA in comparison with the bio-inspired Ag-doped ZnO. It is also evidenced from photocurrent with Ag/ZnO modified indium coated tinoixe (ITO) glass substrate electrode and electron-spin resonance spectra. The quantum yield of Ag-doped catalyst for the degradation of dipyrone showed a clear superiority over many existing studies using conventional doping methods. The effects of dye-sensitization resulted from the adsorption of pigments present in the bio-extract and dipyrone didn't contribute with the photocatalytic performance of Ag/ZnO. The proposed doping process can be further applied for the doping of other metals like platinum, gold, copper, nickel or palladium for the functionalization of advanced semiconductor materials. This doping technique can be further applied for the development of high-efficiency solar cells and electrochemical sensors.

References

Agnihotri, S., Mukherji, S., Mukherji, S., 2014. Size-controlled silver nanoparticles synthesized over the range 5–100 nm using the same protocol and their antibacterial efficacy. RSC Adv. 4, 3974–3983.

Atla, B.S., Chen, C., Chen, C., Lin, P., Pan, W., Cheng, K., Ming, Y., Chang, Y., Jean, J., 2012. Visible light response of Ag^{+}/TiO_2–Ti_2O_3 prepared by photodeposition under foam fractionation. "Journal Photochem. Photobiol. A Chem. 236, 1–8.

Aysin, B., Ozturk, A., Park, J., 2013. Silver-loaded TiO_2 powders prepared through mechanical ball milling. Ceram. Int. 39, 7119–7126.

Barajas-Ledesma, E., García-Benjume, M.L., Espitia-Cabrera, I., Ortiz-Gutiérrez, M., Espinoza-Beltrán, F.J., Mostaghimi, J., Contreras-García, M.E., 2010. Determination of the band gap of TiO_2–Al_2O_3 films as a function of processing parameters. Mater. Sci. Eng. B 174, 71–73.

Behbahani, M., Babapour, M., Amini, M.M., Sadeghi, O., Bagheri, A., Salarian, M., Rafiee, B., 2013. Separation/enrichment of copper and silver using titanium dioxide nanoparticles coated with poly-thiophene and their analysis by flame atomic absorption spectrophotometry. Am. J. Anal. Chem. 04, 90–98.

Behera, A.K., Rao, C.V., Das, R.K., Giri, A.S., Golder, A.K., 2016. Fabrication and characterization of Ag-doped titania: impact of dye-sensitization, phenol decomposition kinetics and biodegradability index. Desalin. Water Treat. 57, 9488–9497.

Behnajady, M.A., Eskandarloo, H., 2013. Silver and copper co-impregnated onto TiO_2-P25 nanoparticles and its photocatalytic activity. Chem. Eng. J. 228, 1207–1213.

Bellur Nagarajaiah, S., Prakash, J., 2015. Chemical composition and bioactive potential of dehydrated peels of benincasa hispida, luffa acutangula, and sechium edule. J. Herbs. Spices Med. Plants 21, 193–202.

Bian, S.W., Mudunkotuwa, I.A., Rupasinghe, T., Grassian, V.H., 2011. Aggregation and dissolution of 4 nm ZnO nanoparticles in aqueous environments: Influence of pH, ionic strength, size, and adsorption of humic acid. Langmuir 27, 6059–6068.

Bojer, C., Schöbel, J., Martin, T., Ertl, M., Schmalz, H., Breu, J., 2017. Clinical wastewater treatment: Photochemical removal of an anionic antibiotic (ciprofloxacin) by mesostructured high aspect ratio ZnO nanotubes. Appl. Catal. B Environ. 204, 561–565.

Cadena-Iniguez, J., Arevalo-Galarza, L., Ruiz-Posadas, L.M., Aguirre-Medina, J.F., Soto-Hernandez, M., Luna-Cavazos, M., Zavaleta-Mancera, H.A., 2006. Quality evaluation and influence of 1-MCP on *Sechium edule* (Jacq.) Sw. fruit during postharvest. Postharvest Biol. Technol. 40, 170–176.

Carballo, T., Gil, M.V., Gomez, X., Gonzalez-Andres, F., Moran, A., 2008. Characterization of different compost extracts using Fourier-transform infrared spectroscopy (FTIR) and thermal analysis. Biodegradation 19, 815–830.

Chen, Y., Xie, Y., Yang, J., Cao, H., Liu, H., Zhang, Y., 2013. Double layered, one-pot hydrothermal synthesis of M-TiO_2 (M = Fe^{3+}, Ni^{2+}, Cu^{2+} and Co^{2+}) and their application in photocatalysis. Sci. China Chem. 56, 1783–1789.

Cheng, B., Le, Y., Yu, J., 2010. Preparation and enhanced photocatalytic activity of Ag@TiO_2 core–shell nanocomposite nanowires. J. Hazard. Mater. 177, 971–977.

Dong, F., Zhao, Z., Sun, Y., Zhang, Y., Yan, S., Wu, Z., 2015. An advanced semimetal–organic bi spheres–g-C_3N_4 Nanohybrid with SPR-enhanced visible-light photocatalytic performance for NO purification. Environ. Sci. Technol. 49, 12432–12440.

Doudrick, K., Yang, T., Hristovski, K., Westerhoff, P., 2013. Photocatalytic nitrate reduction in water: Managing the hole scavenger and reaction by-product selectivity. Appl. Catal. B Environ. 136–137, 40–47.

Elghniji, K., Ksibi, M., Elaloui, E., 2012. Sol–gel reverse micelle preparation and characterization of N-doped TiO_2: Efficient photocatalytic degradation of methylene blue in water under visible light. J. Ind. Eng. Chem. 18, 178–182.

Etacheri, V., Di Valentin, C., Schneider, J., Bahnemann, D., Pillai, S.C., 2015. Visible-light activation of TiO_2 photocatalysts: Advances in theory and experiments. J. Photochem. Photobiol. C Photochem. Rev. 25, 1–29.

Fu, N., Huang, C., Liu, Y., Li, X., Lu, W., Zhou, L., Peng, F., Liu, Y., Huang, H., 2015. Organic-free anatase TiO_2 paste for efficient plastic dye-sensitized solar cells and low temperature processed perovskite solar cells. ACS Appl. Mater. Interfaces 7, 19431–19438.

Gao, S., Jia, X., Yang, S., Li, Z., Jiang, K., 2011. Hierarchical Ag/ZnO micro/nanostructure: Green synthesis and enhanced photocatalytic performance. J. Solid State Chem. 184, 764–769.

Garcia-alamo, M., Rodriguez-nava, O., Morales-ramírez, A.D.J., 2013. Synthesis and antibacterial properties of ZnO : Ag films prepared from a Triton containing solution. Materials (Basel). 6, 1–10.

Georgekutty, R., Seery, M.K., Pillai, S.C., 2008. A highly efficient Ag-ZnO photocatalyst : Synthesis, properties, and mechanism. J. Phys. Chem. C 112, 13563–13570.

Gharagozlou, M., Naghibi, S., 2015. Preparation of vitamin B12–TiO_2 nanohybrid studied by TEM, FTIR and optical analysis techniques. Mater. Sci. Semicond. Process. 35, 166–173.

Giri, A.S., Golder, A.K., 2014. Fenton, photo-Fenton, H_2O_2 photolysis, and TiO_2 photocatalysis for dipyrone oxidation: Drug removal, mineralization, biodegradability, and degradation mechanism. Ind. Eng. Chem. Res. 53, 1351–1358.

Grover, I.S., Singh, S., Pal, B., 2013. The preparation, surface structure, zeta potential, surface charge density and photocatalytic activity of TiO_2 nanostructures of different shapes. Appl. Surf. Sci. 280, 366–372.

Hu, C., Lan, Y., Qu, J., Hu, X., Wang, A., 2006. Ag/AgBr/TiO_2 visible light photocatalyst for destruction of azodyes and bacteria. J. Phys. Chem. B 110, 4066–4072.

Hu, Q., Liu, X., Tang, L., Min, D., Shi, T., Zhang, W., 2017. Pd–ZnO nanowire arrays as recyclable catalysts for 4-nitrophenol reduction and Suzuki coupling. RSC Adv. 7, 7964–7972.

Inagaki, M., Nonaka, R., Tryba, B., Morawski, A.W., 2006. Dependence of photocatalytic activity of anatase powders on their crystallinity. Chemosphere 64, 437–445.

Jasso-Salcedo, A.B., Palestino, G., Escobar-Barrios, V.A., 2014. Effect of Ag, pH, and time on the preparation of Ag-functionalized zinc oxide nanoagglomerates as photocatalysts. J. Catal. 318, 170–178.

Kobwittaya, K., Sirivithayapakorn, S., 2014. Photocatalytic reduction of nitrate over TiO_2 and Ag-modified TiO_2. J. Saudi Chem. Soc. 18, 291–298.

Kusiak-Nejman, E., Janus, M., Grzmil, B., Morawski, A.W., 2011. Methylene Blue decomposition under visible light irradiation in the presence of carbon-modified TiO_2 photocatalysts. J. Photochem. Photobiol. A Chem. 226, 68–72.

Lavand, A.B., Malghe, Y.S., 2015. Visible light photocatalytic degradation of 4-chlorophenol using C/ZnO/CdS nanocomposite. J. Saudi Chem. Soc. 19, 471–478.

Lenzi, G.G., Fávero, C.V.B., Colpini, L.M.S., Bernabe, H., Baesso, M.L., Specchia, S., Santos, O. a a, 2011. Photocatalytic reduction of Hg(II) on TiO_2 and Ag/TiO_2 prepared by the sol-gel and impregnation methods. Desalination 270, 241–247.

Li, B., Liu, T., Wang, Y., Wang, Z., 2012. ZnO/graphene-oxide nanocomposite with remarkably enhanced visible-light-driven photocatalytic performance. J. Colloid Interface Sci. 377, 114–121.

Li, W., Liang, C., Zhou, W., Qiu, J., Zhou, Z., Sun, G., Xin, Q., 2003. Preparation and characterization of multiwalled carbon nanotube-supported platinum for cathode catalysts of direct methanol fuel cells. J. Phys. Chem. B 107, 6292–6299.

Liu, S.X., Qu, Z.P., Han, X.W., Sun, C.L., 2004. A mechanism for enhanced photocatalytic activity of silver-loaded titanium dioxide. Catal. Today 93–95, 877–884.

Lu, W., Gao, S., Wang, J., 2008. One-Pot Synthesis of Ag/ZnO Self-Assembled 3D Hollow Microspheres with Enhanced Photocatalytic Performance. J. Phys. Chem. C 112, 16792–16800.

Lv, T., Pan, L., Liu, X., Lu, T., Zhu, G., Sun, Z., 2011. Enhanced photocatalytic degradation of methylene blue by ZnO-reduced graphene oxide composite synthesized via microwave-assisted reaction. J. Alloys Compd. 509, 10086–10091.

Mehrani, K., Mehrani, A., Amini, M.M., Sadeghi, O., Tavassoli, N., 2011. Dipyridylamine-modified nanoporous silicas as new sorbents for the separation and pre-concentration of palladium. Microchim. Acta 173, 521–527.

Michael, R.J.V., Sambandam, B., Muthukumar, T., Umapathy, M.J., Manoharan, P.T., 2014. Spectroscopic dimensions of silver nanoparticles and clusters in ZnO matrix and their role in bioinspired antifouling and photocatalysis. Phys. Chem. Chem. Phys. 16, 8541–8555.

Modgil, M., Modgil, R., Kumar, R., 2004. Carbohydrate and mineral content of chayote (Sechium

edule) and bottle gourd (*Lagenaria Siceraria*). J. Hum. Ecol. 15, 157–159.

Moghaddam, H.M., Nasirian, S., 2012. Dependence of activation energy and lattice strain on TiO_2 nanoparticles, Nanosci. Methods 1, 201–212.

Moradi, M., Haghighi, M., Allahyari, S., 2017. Precipitation dispersion of Ag–ZnO nanocatalyst over functionalized multiwall carbon nanotube used in degradation of Acid Orange from wastewater. Process Saf. Environ. Prot. 107, 414–427.

Ohno, T., Akiyoshi, M., Umebayashi, T., Asai, K., Mitsui, T., Matsumura, M., 2004. Preparation of S-doped TiO_2 photocatalysts and their photocatalytic activities under visible light. Appl. Catal. A Gen. 265, 115–121.

Ola, O., Maroto-Valer, M.M., 2015. Review of material design and reactor engineering on TiO_2 photocatalysis for CO_2 reduction. J. Photochem. Photobiol. C Photochem. Rev. 24, 16–42.

Patil, S.S., Tamboli, M.S., Patil, D.R., Kulkarni, M. V, Yoon, H., Kim, H., Al-deyab, S.S., Yoon, S.S., Kolekar, S.S., Kale, B.B., 2016. Green approach for hierarchical nanostructured Ag-ZnO and their photocatalytic performance under sunlight. Catal. Today 260, 126–134.

Popa, I., Gillies, G., Papastavrou, G., Borkovec, M., 2009. Attractive electrostatic forces between identical colloidal particles induced by adsorbed polyelectrolytes. J. Phys. Chem. B Lett. 113, 8458–8461.

Ramakrishnan, R., Kalaivani, S., Amala Infant Joice, J., Sivakumar, T., 2012. Photocatalytic activity of multielement doped TiO_2 in the degradation of congo red. Appl. Surf. Sci. 258, 2515–2521.

Ramasamy, P., Seo, D.-M., Kim, S.-H., Kim, J., 2012. Effects of TiO_2 shells on optical and thermal properties of silver nanowires. J. Mater. Chem. 22, 11651–11657.

Riazian, M., Rad, S.D., Azinabadi, R.R., 2013. Fabrication of pure and Ag-doped TiO_2 nanorods and study of the lattice strain and the activation energy of the crystalline phases. J. Korean Phys. Soc. 62, 459–468.

Ruparelia, J.P., Chatterjee, A.K., Duttagupta, S.P., Mukherji, S., 2008. Strain specificity in antimicrobial activity of silver and copper nanoparticles. Acta Biomater. 4, 707–716.

Sangpour, P., Hashemi, F., Moshfegh, A.Z., 2010. Photoenhanced degradation of methylene blue on cosputtered M:TiO_2 (M = Au, Ag, Cu) nanocomposite systems: A comparative study. J. Phys. Chem. C 114, 13955–13961.

Schmitt Pauly, C., Genix, A.-C., Alauzun, J.G., Guerrero, G., Appavou, M.-S., Pérez, J., Oberdisse, J., Mutin, P.H., 2015. Simultaneous phase transfer and surface modification of TiO_2 nanoparticles using alkylphosphonic acids: Optimization and structure of the organosols. Langmuir 31, 10966–10974.

Shan, G., Xu, L., Wang, G., Liu, Y., 2007. Enhanced raman scattering of ZnO quantum dots on silver colloids. J. Phys. Chem. C 111, 3290–3293.

Shidpour, R., 2015. A Power-law relationship between characteristics of light source and quantum yield in photocatalytic systems. J. Phys. Chem. C 119, 22425–22431.

Siciliano, T., Tommasi, D.N., Morelli, I., Braca, A., 2004. Study of flavonoids of sechium edule (Jacq) swartz (Cucurbitaceae) different edible organs by liquid chromatography photodiode array mass spectrometry. J. Agric. Food Chem. 52, 6510–6515.

Simamora, A.J., Hsiung, T.L., Chang, F.C., Yang, T.C., Liao, C.Y., Wang, H.P., 2012. Photocatalytic splitting of seawater and degradation of methylene blue on CuO/nano TiO_2. Int. J. Hydrogen Energy 37, 13855–13858.

Sobana, N., Muruganadham, M., Swaminathan, M., 2006. Nano-Ag particles doped TiO_2 for efficient photodegradation of Direct azo dyes. J. Mol. Catal. A Chem. 258, 124–132.

Su, Y., Lang, J., Li, L., Guan, K., Du, C., Peng, L., Han, D., Wang, X., 2013. Unexpected catalytic performance in silent tantalum oxide through nitridation and defect chemistry. J. Am. Chem. Soc. 135, 11433–11436.

Subash, B., Krishnakumar, B., Velmurugan, R., Swaminathan, M., Shanthi, M., 2012. Synthesis of Ce co-doped Ag–ZnO photocatalyst with excellent performance for NBB dye degradation under natural sunlight illumination. Catal. Sci. Technol. 2, 2319.

Sun, Q., Cai, X., Li, J., Zheng, M., Chen, Z., Yu, C.P., 2014. Green synthesis of silver nanoparticles using tea leaf extract and evaluation of their stability and antibacterial activity. Colloids Surfaces A Physicochem. Eng. Asp. 444, 226–231.

Sunada, K., Watanabe, T., Hashimoto, K., 2003. Studies on photokilling of bacteria on TiO_2 thin film. J. Photochem. Photobiol. A Chem. 156, 227–233.

Suwarnkar, M.B., Dhabbe, R.S., Kadam, A.N., Garadkar, K.M., 2014. Enhanced photocatalytic activity of Ag doped TiO_2 nanoparticles synthesized by a microwave assisted method. Ceram. Int. 40, 5489–5496.

Velikov, K.P., Zegers, G.E., Blaaderen, A. Van, 2003. Synthesis and characterization of large colloidal silver particles. Langmuir 19, 1384–1389.

Vivekanandhan, S., Schreiber, M., Mason, C., Kumar, A.M., Misra, M., 2014. Biointerfaces Maple leaf (Acer sp.) extract mediated green process for the functionalization of ZnO powders with silver nanoparticles. Colloids Surfaces B Biointerfaces 113, 169–175.

Wang, H., Liu, X., Han, S., 2016. The synthesis of a Ag–ZnO nanohybrid with plasmonic photocatalytic activity under visible-light irradiation: the relationship between tunable optical absorption, defect chemistry and photocatalytic activity. CrystEngComm 18, 1933–1943.

Wang, S., Qian, H., Hu, Y., Dai, W., Zhong, Y., Chen, J., Hu, X., 2013. Facile one-pot synthesis of uniform TiO_2-Ag hybrid hollow spheres with enhanced photocatalytic activity. Dalt. Trans. 42, 1122–1128.

Whang, T.-J., Hsieh, M.-T., Chen, H.-H., 2012. Visible-light photocatalytic degradation of methylene blue with Fe doped CdS nanoparticles. Appl. Surf. Sci. 258, 2796–2801.

Xiong, L. Bin, Li, J.L., Yang, B., Yu, Y., 2012. Ti^{3+} in the surface of titanium dioxide: Generation, properties and photocatalytic application. J. Nanomater. 2012, 1–13.

Yan, H., Wang, X., Yao, M., Yao, X., 2013. Band structure design of semiconductors for enhanced photocatalytic activity: The case of TiO_2. Prog. Nat. Sci. Mater. Int. 23, 402–407.

Yang, X., Wang, S., Sun, H., Wang, X., Lian, J., 2015. Preparation and photocatalytic performance of Cu-doped TiO_2 nanoparticles. Trans. Nonferrous Met. Soc. China 25, 504–509.

Zhang, D., Zeng, F., 2011. Photocatalytic oxidation of organic dyes with nanostructured zinc dioxide modified with silver metals. Russ. J. Phys. Chem. A 85, 1077–1083.

Zhang, X., Liu, F., Huang, Q.L., Zhou, G., Wang, Z.S., 2011. Dye-sensitized W-doped TiO_2 solar cells with a tunable conduction band and suppressed charge recombination. J. Phys. Chem. C 115, 12665–12671.

Zhang, X., Zhang, L., Xie, T., Wang, D., 2009. Low-temperature synthesis and high visible-light-induced photocatalytic activity of BiOI/TiO_2 heterostructures. J. Phys. Chem. C 113, 7371–7378.

Zhao, W., Yan, D., Xu, J., Chen, H., 2012. In situ enzymatic ascorbic acid production as electron donor for CdS quantum dots equipped TiO_2 nanotubes: A general and efficient approach for new photoelectrochemical immunoassay. Anal. Chem. 84, 10518–10521.

Chapter 6

Synergistic Effects of Cu/Zn Bimetal Doping on TiO_2 for Photocatalytic Water Treatment

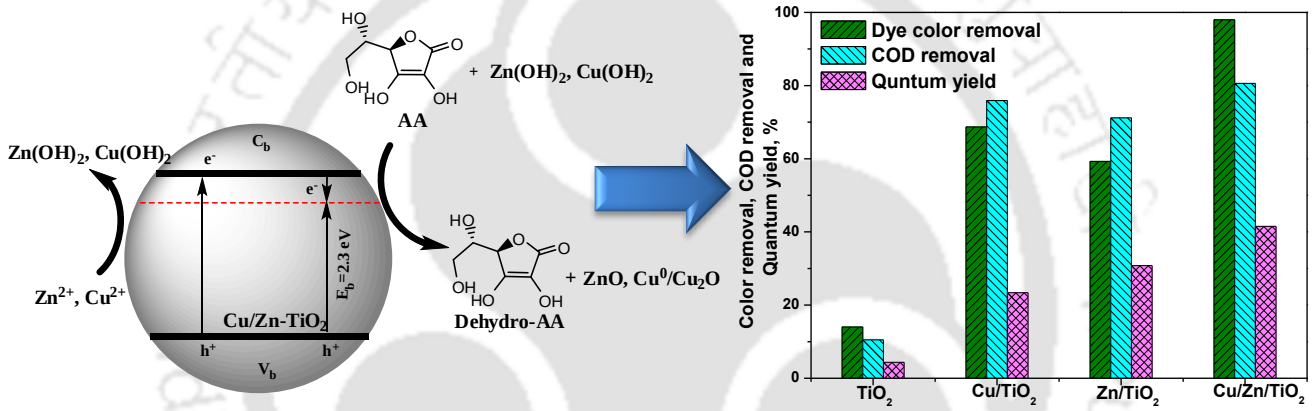

*This chapter investigates the use of cheaper and easily available dopants, such as Cu and Zn for TiO_2 doping following the bio-inspired technique developed for Ag-doping (**Chapter 5**). The focus was to explore the performance of bimetal doped TiO_2 and its comparison to the bare and mono-metal doped systems.*

6.1 Introduction

The heterogeneous photocatalysis using TiO_2 is one of the most preferred advanced oxidation processes (AOPs) for the treatment of both aqueous and non-aqueous effluents (Riaz et al., 2013). Many times, it can be seen that bimetal doped photocatalysts show a better catalytic activity than the mono-metal doped systems (Malika et al., 2016; Riaz et al., 2013; Tobaldi et al., 2016). Doping techniques and dopant metal composition also could considerably alter the activity of photocatalysts (Malika et al., 2016). The visible light absorption could enhance with bimetal doping and stimulate a faster photo-generated

electron (e^-) transfer to dopant metal from TiO_2 owing to increase the separation of e^- and hole (h^+) (Malika et al., 2016). The recombination of e^-/h^+ and its separation, plays a key role in the photocatalytic activity. Cu and Zn are low-cost and easily available than many transition metals.

Therefore, the earlier work (**Chapter 5**) was further deepened to study the performance of Cu/Zn bimetal-doped TiO_2 functionalized using the same bio-analytes present in *S. edule* leaf-extract. The doped catalysts were characterized by using XRD, DR-UV–vis spectroscopy, FTIR spectroscopy, Transmission electron microscopy, and zeta-potential measurements. The catalytic activity of Cu/TiO_2, Zn/TiO_2, and $Cu/Zn/TiO_2$ was tested for the degradation of CR dye in terms of chemical oxygen demand and quantum yield for the cleavage of CR dye. The kinetics of dye degradation was studied using the Langmuir–Hinshelwood model at a lower dye concentration.

6.2 Results and Discussion

6.2.1 Determination of Cu and Zn loading onto TiO_2

Cu^{2+} and Zn^{2+} uptake efficiency of TiO_2 with the equilibrium (after 1 h of adsorption) Cu^{2+} and Zn^{2+} concentration are illustrated in **Table 6.1**. The initial concentration of Cu^{2+} and Zn^{2+} was maintained 2 % (w/w) for the mono-metal system and, it was half (w/w) in the case of bimetal doping per 10 g TiO_2. The time of doping test was set to 24 h. It was selected from a trial run of only Cu^{2+} and Zn^{2+} precursor and bio-extract without TiO_2 and, the formation of Cu and Zn-nanoparticle were complete in 24 h. The efficiency of Cu and Zn-doping was found to be 80.7 and 74.2 % with 2 % (w/w) individual metal concentration which was obtained in the pre-immobilization (adsorption) study. It implies that the true loading of Cu and Zn onto TiO_2 was about 1.61 and 1.48 (w/w w.r.t. Cu/TiO_2 and Zn/TiO_2). There was an insignificant amount of Cu^{2+}, and Zn^{2+} ions leached out in the solution during the doping test.

Table 6.1. Quantitative retention of Cu^{2+} and Zn^{2+} ions onto TiO_2. Experimental conditions: room temperature (25±2ºC) and normal pH of 5.8 at 320 rpm.

Catalyst	Ionic matter	Initial loading, % (w/w)	True loading, % (w/w) on TiO_2	Residual concentration, %	
				After 1 h adsorption	After 48 h reaction
Cu/TiO_2	Cu^{2+}	2	1.614	19.3±0.73	1.43±0.3
Zn/TiO_2	Zn^{2+}	2	1.484	25.8±0.22	1.76±0.93
$Cu/Zn/TiO_2$	Cu^{2+}	1	0.938	6.2±0.89	0.5±0.81
	Zn^{2+}	1	0.792	20.8±1.2	0.9±1.12

6.3 Characteristics of Cu/Zn/TiO_2

6.3.1 X-ray diffractogram

The XRD patterns of pristine, mono- and bi-metal doped Cu/Zn/TiO_2 are shown in **Figure 6.1**. It exhibited the major characteristic peaks of highly crystalline TiO_2. A similar explanation as in **Chapter 5, Section 5.2.2.1**, is also applicable here. Three additional characteristic peaks appeared at 41.8, 50.1 and 73.9º were corresponding to the (1 1 1), (2 0 0), and (2 2 0) crystalline planes of FCC crystals of Cu nanoparticles (JCPDS No. 04-0836, a = 3.609 Å) and, a small peak observed at 61.1º was associated to (2 2 0) plane of Cu_2O (Cuya Huaman et al., 2011). Similarly, two more peaks were found at 31.6 and 67.9º corresponding to (1 0 0) and (1 1 2) planes of ZnO nanoparticles (JCPDS No. 361451) (Bala et al., 2015). The existence of Cu/Zn species also was confirmed by the EDX image mapping (**Figure 6.2**). It displays the assemblies of numerous nanocrystals by the structural configuration that comprises of Ti, O, Cu, and Zn elements. Highly homogeneous distribution of Cu and Ni resulted from an enhanced interaction between metal and TiO_2 and could lead to higher phtocatalytic activity. The crystallite size was determined by using the Scherrer's equation (**Chapter 5, Section 5.2.2.1**). The crystallite size for the intense peak of anatase phase at (1 1 1) plane was found to be 16.66, 22.38, 38.2, and 24.84 nm for TiO_2, Cu/TiO_2, Zn/TiO_2, Cu/Zn/TiO_2, respectively. The same for the rutile phase at (1 1 0) plane was calculated as 28.21, 29.46, 32.75 and 65.68 nm, respectively. The variation in the size of the crystal lattice is dependent on the ionic radius of the metal dopants (Malika et al., 2016). The induction of larger ionic radius metal dopants into the Ti^{4+} lattice resulted in higher crystallite size. The anatase phase was found as 80.06, 81.38, 70.47, and 76.54 % for TiO_2, Cu/TiO_2, Zn/TiO_2, Cu/Zn/TiO_2, respectively, from the integrated peak intensities at (1 0 1) and (1 1 0) planes. It indicates a maximum of 12 % phase change from anatase to rutile. A similar trend for the increase in crystallite size was also reported by Behnajady and Eskandarloo (2013) in the case of bimetal doped TiO_2 using the impregnation technique (Behnajady and Eskandarloo, 2013).

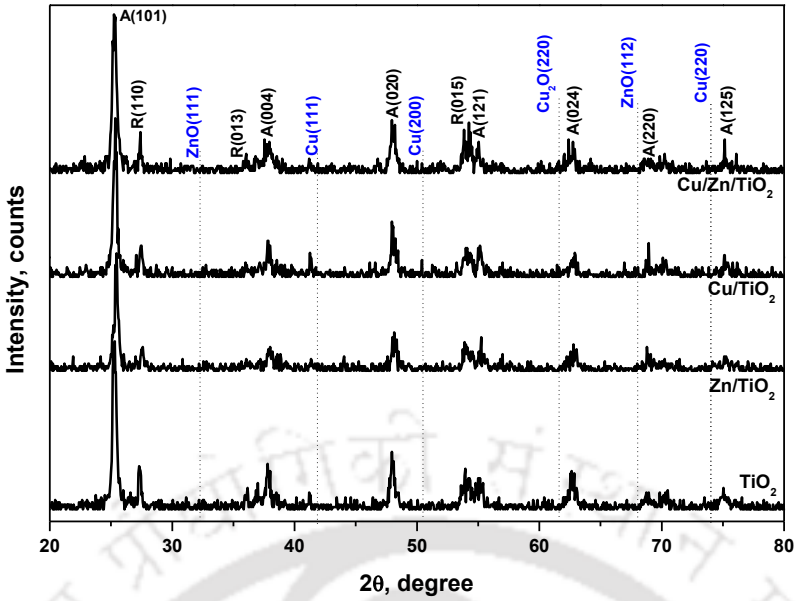

Figure 6.1. XRD patterns of bare, mono and Cu/Zn bimetal doped TiO_2 nanostructures.

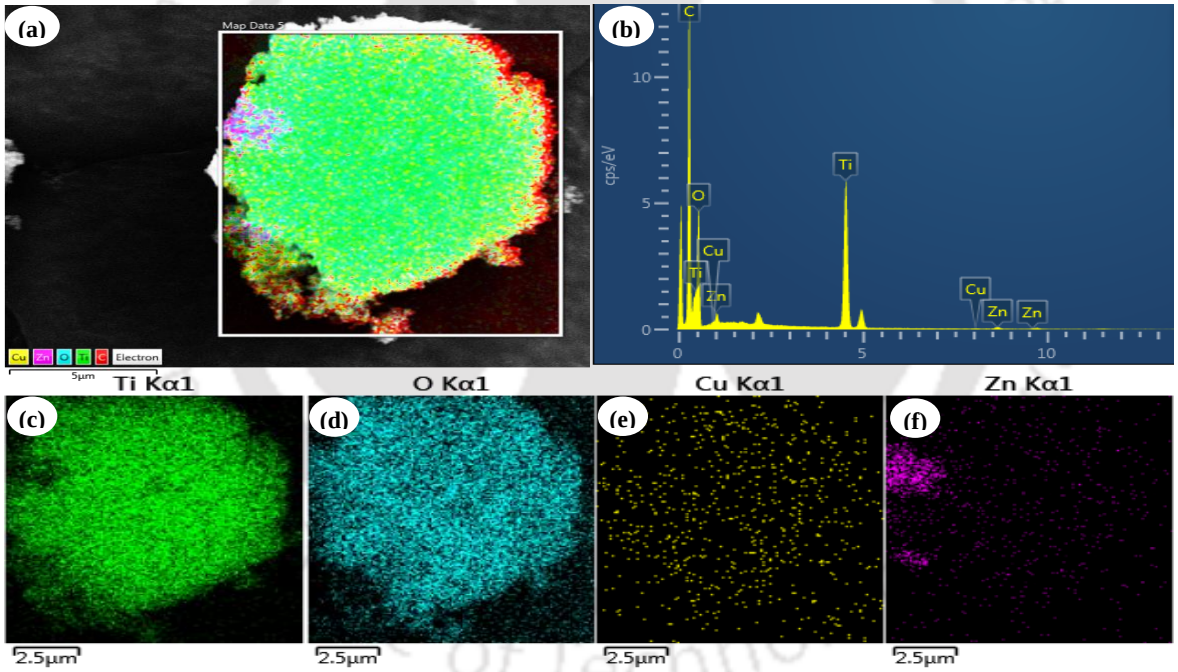

Figure 6.2. (a) EDX image mapping, (b) Relative dispersity of Ti, O, Cu, and Zn elements, (c-f) Dispersity of individual element Ti, Cu and Zn in the case of $Cu/Zn/TiO_2$.

6.3.2 Spectral absorbance of bio-mediated doped $Cu/Zn/TiO_2$

An intense absorption peak in the UV domain (**Figure 6.3**) can be noticed for pristine TiO_2, which is assigned to the band-to-band transition (Malika et al., 2016). A maximum absorption band around 315 nm in the TiO_2 spectrum is related to the route of charge transferring from O^{2-} (2p) to Ti^{4+} (3d) (Paulino et al., 2016a). Cu doping displayed an

important absorption tail in the visible domain from 400 to 800 nm. The band at 250–310 nm is assigned to the ligand-to-dopant charge transfer formation of Cu^{2+}(3d) from O^{2-}(2p), happening in separated Cu^{2+} locates (Paulino et al., 2016a). Also, the band at 340 nm evidences the existence as well as large distribution of $(Cu–O–Cu)^{2+}$ assembles. In the case of Zn-doping, the energy absorption spectrum possesses a maximum wavelength near to 400 nm (little above to TiO_2). $Cu/Zn/TiO_2$ absorption spectrum exhibited a broader band than the other photocatalysts spectra, indicating a greater photocatalytic activity (Malika et al., 2016).

The band gap energy of doped catalysts was determined using the indirect transition model (Touc plot) (**Chapter 5**, **Section 5.2.2.2**) (**Figure 6.4**). E_g of 3.05 eV was found for TiO_2, whereas Zn doping (2 %, w/w) alone did not reduce the band gap significantly. However, Cu-doping showed superior performance in the band gap reduction with 2.397 eV. The change in E_g suggests that the induction of Cu changes the material functionalization, owing to a reallocation of its electrical charge. Cu acts as a h^+ scavenger leading to a lengthier isolation between the e^-/h^+ pairs produced by the enhanced material photoefficiency. As it was expected that, Zn-doping did not stimulate a reduction in E_g for $Cu/Zn/TiO_2$ and, E_g of 2.79 eV was obtained. Paulino et al. (2016) also reported the band gaps of 3.17, 2.95 and 3.02 eV with TiO_2, Cu/TiO_2, $Cu/Zn/TiO_2$, respectively (Paulino et al., 2016b). They used impregnation method for the doping experiment.

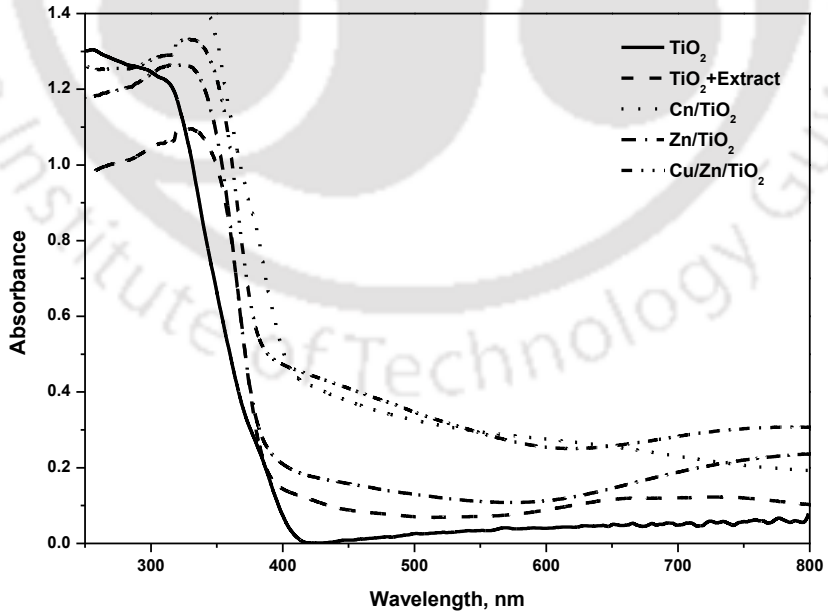

Figure 6.3. UV–vis DR spectra of pristine, mono and bimetal-doped TiO_2.

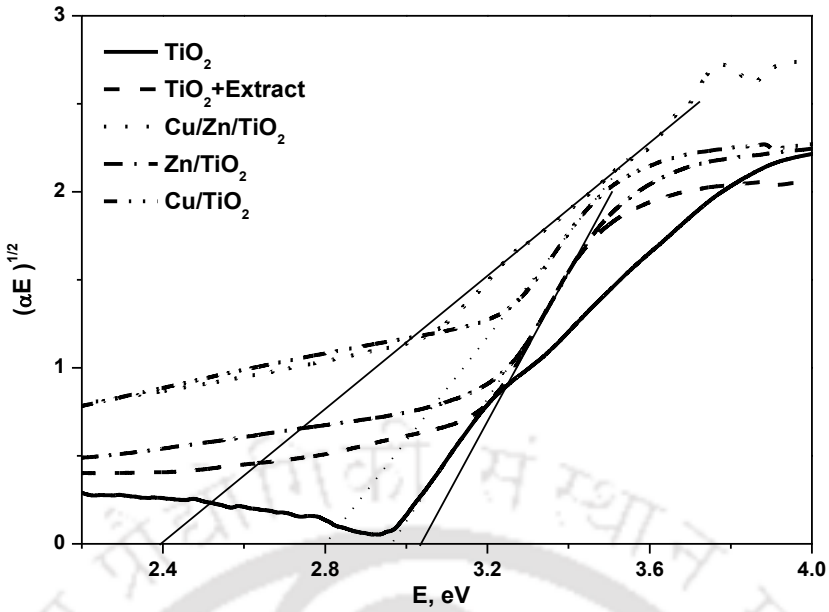

Figure 6.4. Optical direct band gaps (Tauc plot) from Figure 6.3.

6.3.3 Particle size and morphology of Cu/Zn-doped TiO_2

The TEM micrograph of Cu/Zn/TiO_2 is illustrated in **Figure 6.5**. The sizes of the particles were not uniform and, particles diameters ranged between 22 and 84 nm. A slight agglomeration was taken place in some of the clustered particles. The SAED pattern is shown in **Figure 6.5(b).** The intense rings represent to the anatase phase of standard polycrystalline diffraction rings (Gharagozlou and Naghibi, 2015). According to SAED patterns, the d-values representing to the sharpest rings were in agreement with the standard d-values for the (1 0 1), (0 0 4) and (0 2 0) planes of anatase phase. It is also supported by the XRD patterns. From the locally magnified image, we determine the interplanar spacing of lattice fringe separation of 0.353 nm which corresponds to the lattice face of (1 0 1) plane of the anatase structure (**Figure 6.5(c)**). The particle size measured by DLS is shown in **Figure 6.5(d)**. The particle size distribution was shifted at a larger mean size with Cu/Zn doping and exhibited a lower covering intensity with a wider size arranges. The explanation is already provided in **Chapter 5**, **Section 5.2.2.4**. **Table 6.2** shows the mean diameter of bare and doped TiO_2 particles.

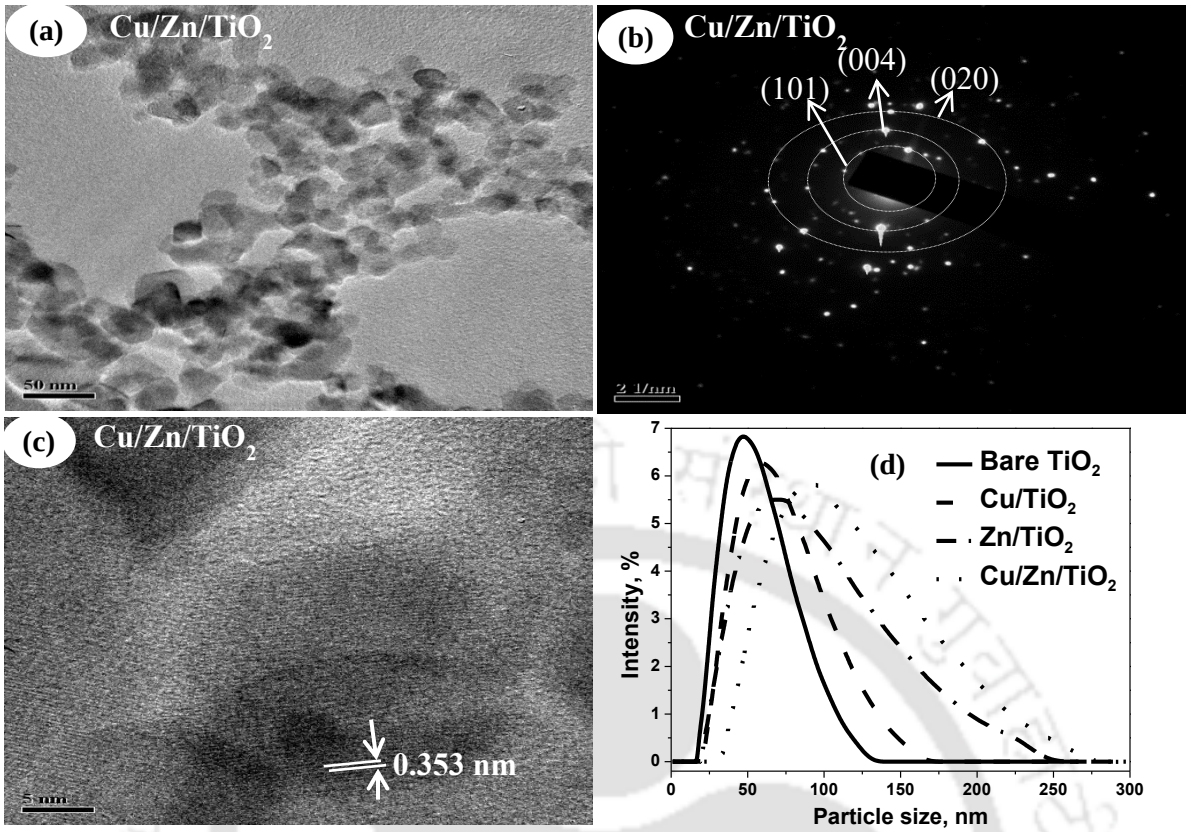

Figure 6.5. (a) TEM, (b) SAED, (c) HRTEM micrograph of $Cu/Zn/TiO_2$ and, (d) Particle size distribution using DLS.

Table 6.2. Comparison of mean diameter of catalyst particles in DLS and TEM measurements.

Catalyst type	Mean particle diameter, nm	
	DLS	TEM
TiO_2	48.61±0.89	29.1548.61±1.12
Cu/TiO_2	52.16±1.12	
Zn/TiO_2	79.02±2.01	
$Cu/Zn/TiO_2$	68.43±1.82	43.2548.61±1.74

6.3.4 FTIR spectra of $Cu/Zn/TiO_2$

FTIR spectra of pristine, mono and bimetal doped TiO_2 particles are shown in **Figure 6.6**. The bands at 3460 and 1600 cm^{-1} are attributed to the OH–stretching and OH–bending modes of physically absorbed moisture. A small band observed at 2891 cm^{-1} can be assigned to dimer –OH (Behera et al., 2016). The metal-doped TiO_2 enhanced the surface adsorption of –OH and water groups. Ti^{4+} in TiO_2 lattice was substituted by Cu^{2+} and Zn^{2+} ions and formed Cu–O or Zn–O bond. It enhances the oxygen vacancies that are equilibrated by the adsorption of more H_2O or –OH groups (Malika et al., 2016). The peaks identified at 472,

523, and 482 cm^{-1} are for the stretching mode of Ti–O, Cu–O, and Zn–O, respectively (Malika et al., 2016; Tobaldi et al., 2016). A wide peak observed at 1184 cm^{-1} can be attributed to the scissoring mode of the H_2O molecule. A band at 783 cm^{-1} corresponding to Ti-O was shifted to 727 and 732 cm^{-1} after doping because of Cu–O–Ti and Zn–O–Ti stretching asymmetric vibrations. These changes were identified due to the defects raised by the induction of metal dopants into TiO_2 lattice (Behera et al., 2016).

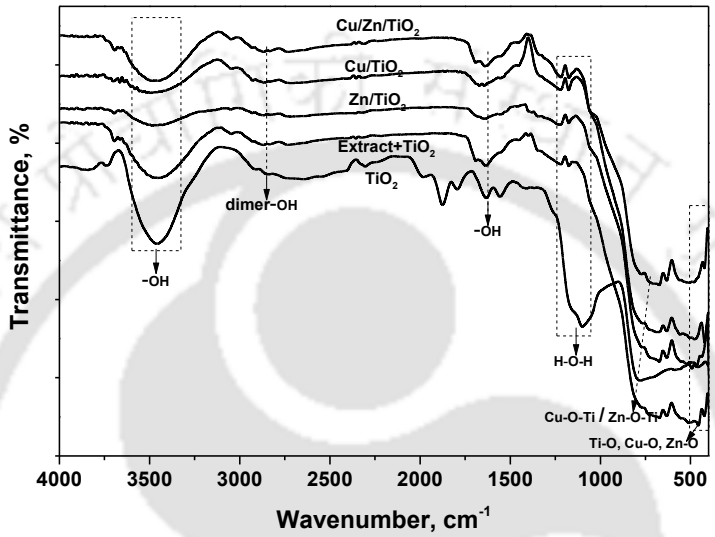

Figure 6.6. FTIR spectra of bare and metal-doped catalysts.

6.3.5 Colloidal stability of TiO_2 and Cu/Zn/TiO_2

The ξ of bare TiO_2 and doped Cu-Zn/TiO_2 are presented in **Figure 6.7**. ξ was measured at different pH (3 to 10) to understand the behaviour of surface charge of modified TiO_2 in the aqueous solution. The zero point charge (pH_{zpc}) of TiO_2 was dropped from 6.42 to 5.91 after metal doping. The pH_{zpc} is potentially affects the adsorption behavior of organic compounds on the photocatalyst surface during the photocatalytic reaction (Malika et al., 2016). The surface of the photocatalyst is positively charged below pH_{zpc} and carries a net negative charge above it. A similar explanation as in **Chapter 5**, **Section 5.2.2.5** is also applicable here. So, the higher electrostatic repulsion of Cu-Zn/TiO_2 particles at the same pH compared to bare and mono-metal doped TiO_2 causes greater stability (Behera et al., 2016).

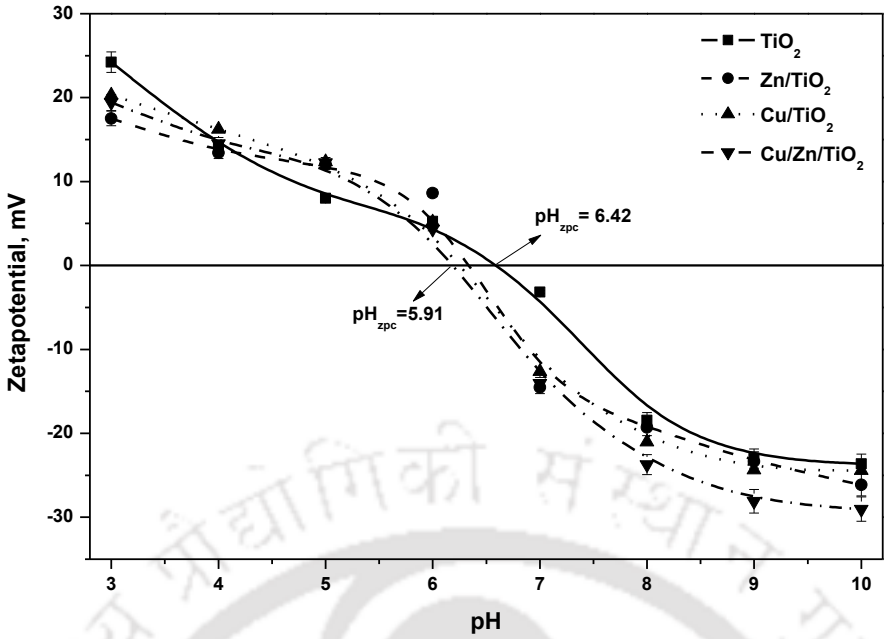

Figure 6.7. Effect of pH on the zeta-potential (ξ) for bare and doped TiO_2 particles.

6.3.6 Mono and bimetal doped TiO_2 for dye decomposition

The optimal condition of CR dye degradation was determined at different solution pH and Cu/Zn/TiO_2 doses. The results are shown in **Figures 6.8** and **6.9**. The dye degradation was the highest at initial pH 7.0. It was decreased both with the fall and rise of solution pH from 7. pH_{zpc} varied from 5.91 to 6.42 (**Figure. 6.7**). The concentration TiO− group increases with the increase in pH above it (Roy and Mondal, 2017). So, the affinity of CR dye being adsorbed on the surface reduces at higher pH because of the charge repulsion (Roy and Mondal, 2017). It has resulted in a lower rate of dye degradation at higher pH. H^+ is a scavenger of $^{\bullet}OH$ and $O_2^{\bullet-}$ radicals at lower pH (Giri and Golder, 2014) and, also the strong interaction between the dye molecule and the catalyst surface could delay the rate of the reaction.

Dye degradation was increased with the increase in Cu/Zn/TiO_2 dose up to 0.1 g L^{-1} with 98 % removal. The increase in catalyst concentration beyond 0.1 g L^{-1} did not have much effect on dye removal. Ramakrishnan et al. (2012) reported similar results for the CR dye removal using multi-elements (C/N/B/F) doped TiO_2 by wet impregnation technique. They achieved the maximum dye removal of 100 % at the optimal condition as pH 7.0, catalyst dose 2.5 g L^{-1}, reaction time 4 h, and CR concentration17.4 mg L^{-1} using UV light of 365 nm wavelength (Ramakrishnan et al., 2012).

Figure 6.10 shows the plot of CR dye color removal as a function of reaction time catalyzed by the bare and doped TiO_2 particles with at the optimal condition under visible

light illumination (**Chapter 5, Section 5.2.3**). In the case of bare TiO_2, the dye removal was found as 14 % after 120 min of reaction. Cu and Zn doping exhibited a dramatic improvement in the performance of CR dye degradation. There were about 68.7, 59.3, and 98 % dye removal in 120 min using Cu/TiO_2, Zn/TiO_2, and $Cu/Zn/TiO_2$ with the similar experimental condition. The results are line with the optical response of the photocatalysts in the visible region (**Figure 6.3**). It indicates that the bimetal doped TiO_2 was more efficient than mono-metal doping under the visible light irradiation.

The activity of Cu/TiO_2 was also better than Zn/TiO_2 as Cu doping could enhance the charge separation efficiency with a low recombination rate (**Figure 6.3**). O 2p orbitals of TiO_2 share to the occupied valence band (VB), whereas the Ti 3d, 4s, 4p orbitals contribute to the vacant conduction band (CB). The lower position of CB is dominated by Ti 3d orbitals (Scrocco, 1979). An impurity level could be introduced in the forbidden band with Zn^{2+} and Cu^{2+} doping with the substitution of Ti^{4+}. Therefore, the doped catalyst absorbs visible light as this intermediate energy level can act either as an e^- acceptor or a donor (Ma et al., 2014). In the case of bi-metal doping using metals with different charges, the synergistic effect plays a key role in the increment of stability of the photocatalyst due to the charge balancing effect.

The enhanced photocatalytic activity with $Cu/Zn/TiO_2$ was due to the improvement of separation of e^- and h^+ through e^- trapping of Cu/Zn NPs with the induction of higher oxygen vacancies (Yang et al., 2015).

At the low concentration of the substrates (KC_e<<1), the Langmuir–Hinshelwood model (Eq. 6.1) for the photocatalytic degradation essentially obeys the pseudo-first-order kinetics (Eq. 6.2) (Lazar et al., 2012).

$$r = -\frac{dC}{dt} = \frac{k_r\, KC_e}{1 + KC_e} \tag{6.1}$$

$$-\ln\left(\frac{C_{CR}}{C_{CR}^0}\right) = kt \tag{6.2}$$

Where, r represents the rate of reaction that changes with time, mg L^{-1} min^{-1}; t is the reaction time, s; K is the equilibrium constant for adsorption of the substrate (here CR dye) on the catalyst; k_r is the limiting rate constant of reaction with the maximum coverage under given experimental conditions; C_e is the equilibrium concentration at any time t during degradation, mg L^{-1}. k is the apparent rate constant and C_e is essentially the initial

CR concentration as the reaction was carried out after the equilibrium CR adsorption (Eq. 6.2).

The rate of CR degradation well fitted to the pseudo-first-order kinetic model (**Figures 6.11** and **6.12**). The best-fit parameters are listed in **Table 6.3.** The correlation coefficient (R^2) was above 0.98 for test runs. The apparent rate constant determined with bare TiO_2 was found to be the lowest followed by Zn/TiO_2, Cu/TiO_2 and then $Cu/Zn/TiO_2$. It was around 2.1–16.2 % lower compared to doped TiO_2. The results imply that $Cu/Zn/TiO_2$ at pH 7 displayed a rate constant of 16.2, 7.6, and 5.8 times higher than TiO_2, Zn/TiO_2, and Cu/TiO_2. The kinetic parameters using $Cu/Zn/TiO_2$ at different pH values are also shown in **Table 6.3**. The rate constant varied from 0.25×10^{-3} to 0.647×10^{-3} s^{-1}. The rate constant was found to the highest at pH 7.0, and apparently it falls (**Figure 6.8**) at lower and higher pH values. The rate constants for the decomposition of azo dyes such as Methylene blue and Acid Orange 7 using bimetal doped $Au/Pd/TiO_2$ (Quiñones et al., 2010) and $Cu/Ag/TiO_2$ (Ramakrishnan et al., 2012) photocatalysts exhibited similar results as obtained with $Cu/Zn/TiO_2$ in the study.

The bimetal doped catalyst showed the maximum COD removal of 80.6 % (**Figure 6.13**). The COD removal was found to be 10.5, 75.9, and 71.2 % for TiO_2, Cu/TiO_2, and Zn/TiO_2, respectively, which is following the similar trend of CR dye color removal.

The QY for the degradation of CR dye was also determined (**Chapter 5**, **Section 5.3.3**) (**Figure 6.13**). The maximum QY was found to be 41.5 % in 120 min of reaction time for $Cu/Zn/TiO_2$. The QY of bio-mediated Cu/Zn-doped TiO_2 was more than many earlier reports (Kusiak-Nejman et al., 2011, Li et al., 2012). **Figure 6.14** showed the ESR spectra of bare and doped TiO_2 where g-value at 310 mT attributes to the formation of $O_2^{\bullet-}$ radicals (**Chapter 5**, **Section 5.2.3**). The intensities of signals of $O_2^{\bullet-}$ radical was increased considerably which may explain the high photocatalytic activity of $Cu/Zn/TiO_2$. Thus, the $O_2^{\bullet-}$ radicals were mostly responsible for the degradation of CR dye as evidenced from the ESR spectra (**Chapter 5**, **Section 5.2.3**).

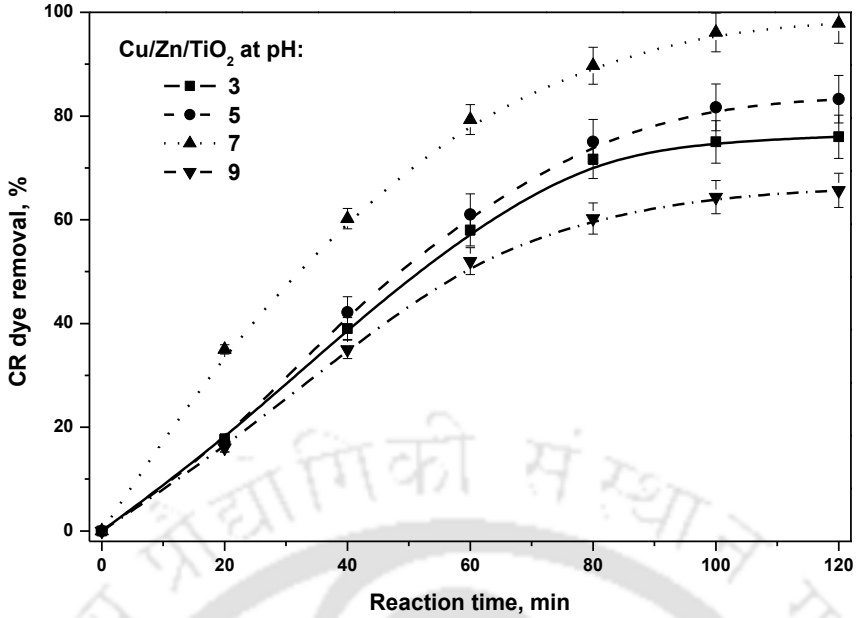

Figure 6.8. Influence of initial pH on the variation of CR dye degradation with reaction time. Initial dye 100 mg L^{-1}, catalyst dose 0.1 g L^{-1}, agitation speed 400 rpm, temperature 27 °C, and solution volume 200 mL.

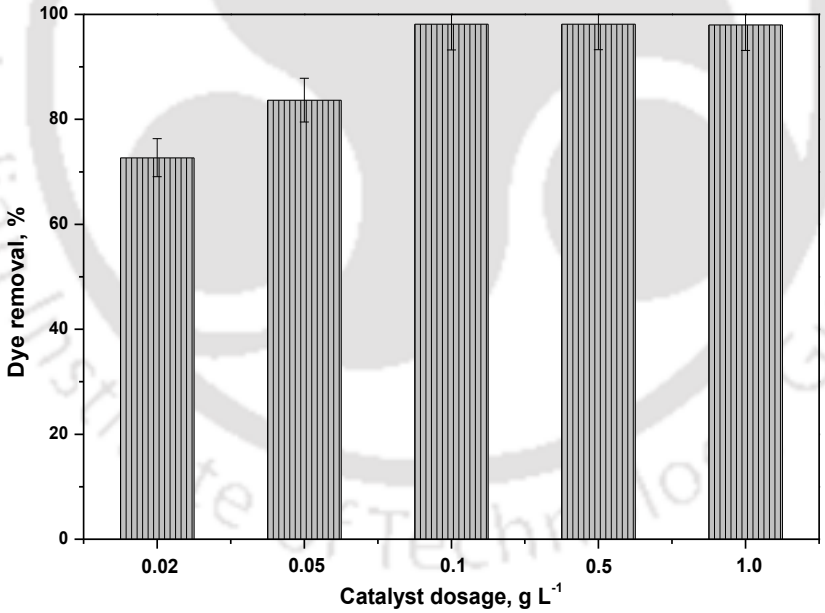

Figure 6.9. Effect of catalyst dose on dye degradation at optimal pH of 7.0 at reaction time of 120 min. Initial dye 100 mg L^{-1}, agitation speed 400 rpm, temperature 27 °C, and solution volume 200 mL.

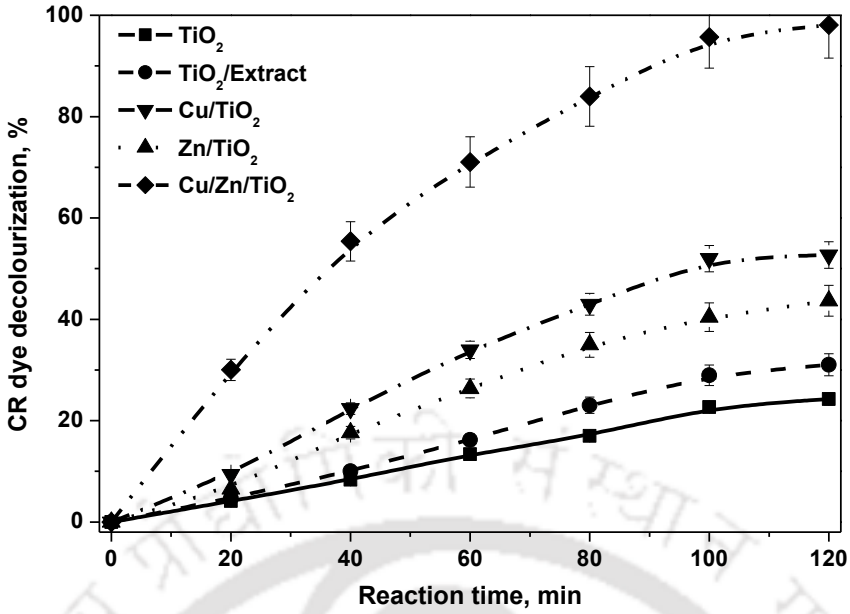

Figure 6.10. Congo red dye degradation with reaction time for mono and bimetal doped TiO_2. Initial dye 100 mg L^{-1}, catalyst dose 0.1 g L^{-1}, pH 7.0, agitation speed 400 rpm, temperature 27 °C, and solution volume 200 mL.

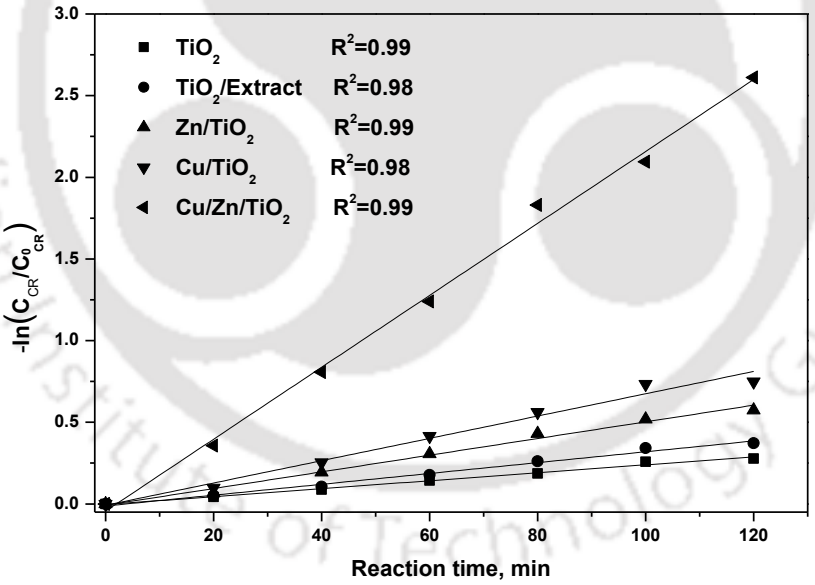

Figure 6.11. Pseudo-first order model fitting to CR dye degradation (Figure 6.10) in the presence of bare and doped TiO_2 photocatalysts.

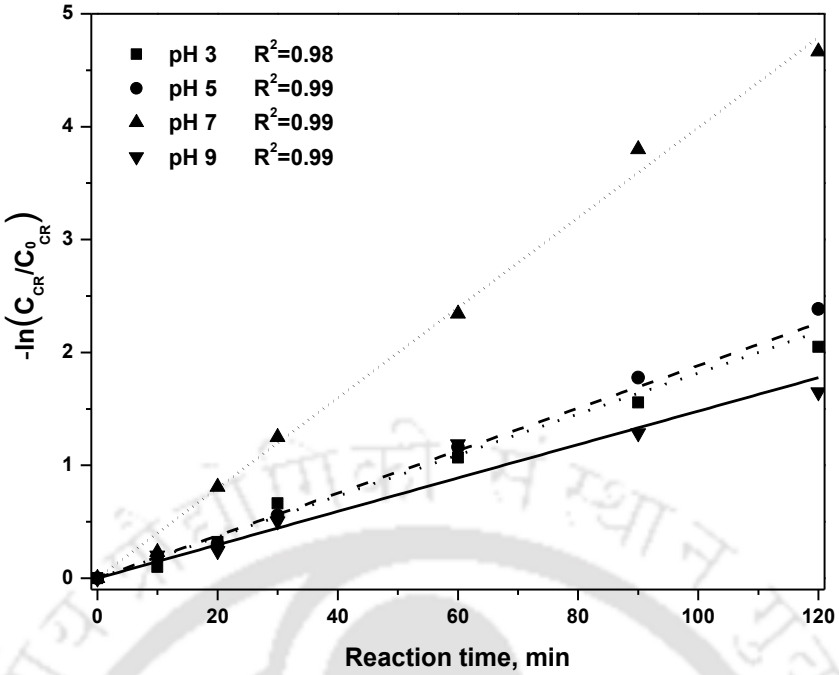

Figure 6.12. Pseudo-first order model fitting to CR dye decomposition (Figure 6.8) using Cu/Zn/TiO_2 catalyst at different pH.

Table 6.3. Pseudo-first order kinetic parameters for the degradation of CR dye using mono- and bi-metal doped TiO_2 with a dose of 0.1 g L^{-1}.

Catalyst type	Reaction pH	$k\times10^3$ (s^{-1})	R^2
TiO_2	7±0.2	0.0448±0.001	0.991±0.01
TiO_2+Extract	7±0.2	0.0533±0.005	0.986±0.01
Zn/TiO_2	7±0.2	0.0854±0.001	0.994±0.02
Cu/TiO_2	7±0.2	0.1124±0.003	0.982±0.01
Zn/Cu/TiO_2	3±0.2	0.3044±0.02	0.985±0.02
	5±0.2	0.3138±0.008	0.994±0.05
	7±0.2	0.6472±0.005	0.994±0.01
	9±0.2	0.2514±0.02	0.989±0.02

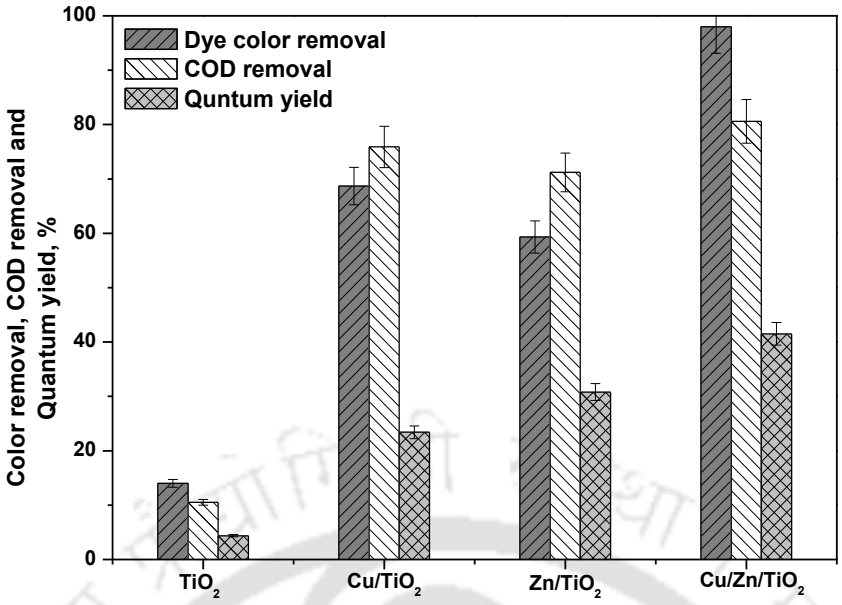

Figure 6.13. Congo red dye color, COD removal, and quantum yield for bare and doped catalysts with a dose of 0.1 g L^{-1}, initial dye concentration 100 mg L^{-1}, pH 7.0, agitation speed 400 rpm, temperature 27 °C, and solution volume 200 mL.

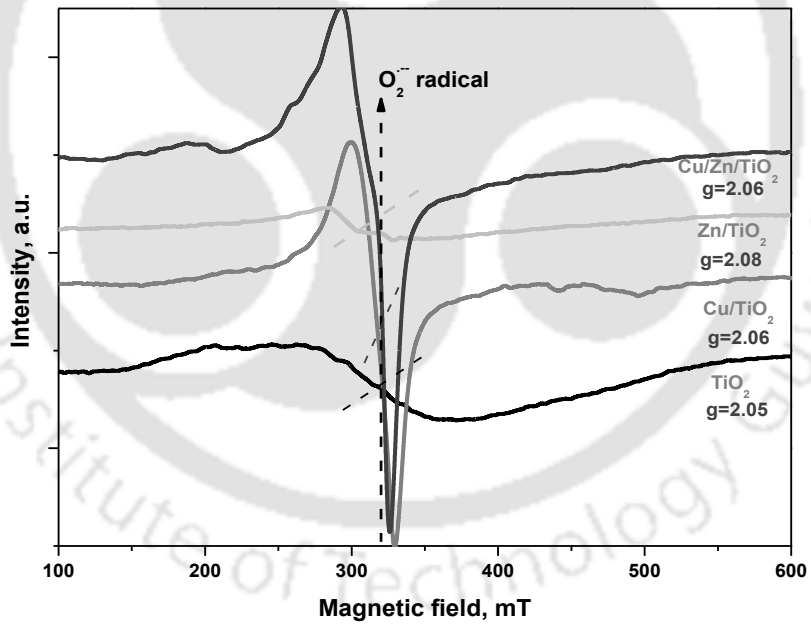

Figure 6.14. ESR spectra of bare, mono and bimetal Cu/Zn-doped TiO_2 particles recorded at room temperature (28±2 °C).

6.4 Major Findings

The bio-mediated co-metal doping using Cu and Zn onto TiO_2 showed a significant decrease in the band gap energy than the mono-metal doping at the same dopant concentration. The proposed doping technique increased the crystallite size for both anatase and rutile phases. The absolute zeta potential value was more with the bimetal doped catalyst which is indicative of a strong tendency to oppose the destabilization. The visible light aided the degradation of CR dye with Cu/Zn/TiO_2 was significantly higher and could cause almost complete decolorization in 2 h with the significant reduction in COD (difference is only 18 %). The improvement of photocatalytic activity of Cu/Zn/TiO_2 compared with that of the monometallic samples is attributed to a synergetic effect between Cu and Zn acting for a better charge separation with a low e^-/h^+ recombination rate than the monometallic samples. The pseudo-first order model well fitted the dye decolorization kinetics and, there was about the sixteen-fold increase in the rate constant with Cu/Zn/TiO_2 compared to bare TiO_2. The quantum yield (23 – 41 %) of bimetal doped TiO_2 catalyst in the present study exhibited a clear superiority over many existing studies using conventional doping methods.

References

Bala, N., Saha, S., Chakraborty, M., Maiti, M., Das, S., Basu, R., Nandy, P., 2015. Green synthesis of zinc oxide nanoparticles using Hibiscus subdariffa leaf extract: effect of temperature on synthesis, anti-bacterial activity and anti-diabetic activity. RSC Adv. 5, 4993–5003.

Behera, A.K., Rao, C.V., Das, R.K., Giri, A.S., Golder, A.K., 2016. Fabrication and characterization of Ag-doped titania: impact of dye-sensitization, phenol decomposition kinetics and biodegradability index. Desalin. Water Treat. 57, 9488–9497.

Behnajady, M.A., Eskandarloo, H., 2013. Silver and copper co-impregnated onto TiO_2-P25 nanoparticles and its photocatalytic activity. Chem. Eng. J. 228, 1207–1213.

Cuya Huaman, J.L., Sato, K., Kurita, S., Matsumoto, T., Jeyadevan, B., 2011. Copper nanoparticles synthesized by hydroxyl ion assisted alcohol reduction for conducting ink. J. Mater. Chem. 21, 7062–7069.

Gharagozlou, M., Naghibi, S., 2015. Preparation of vitamin B12–TiO_2 nanohybrid studied by TEM, FTIR and optical analysis techniques. Mater. Sci. Semicond. Process. 35, 166–173.

Giri, A.S., Golder, A.K., 2014. Chloramphenicol degradation in fenton and photo-fenton: Formation of Fe^{2+}-chloramphenicol chelate and reaction pathways. Ind. Eng. Chem. Res. 53, 16196–16203.

Kusiak-Nejman, E., Janus, M., Grzmil, B., Morawski, A.W., 2011. Methylene Blue decomposition under visible light irradiation in the presence of carbon-modified TiO_2 photocatalysts. J. Photochem. Photobiol. A Chem. 226, 68–72.

Lazar, M.A., Varghese, S., Nair, S.S., 2012. Photocatalytic water treatment by titanium dioxide: recent updates. Catalysts 2, 572–601.

Li, B., Liu, T., Wang, Y., Wang, Z., 2012. ZnO/graphene-oxide nanocomposite with remarkably enhanced visible-light-driven photocatalytic performance. J. Colloid Interface Sci. 377, 114–121.

Ma, Y., Wang, X., Jia, Y., Chen, X., Han, H., Li, C., 2014. Titanium dioxide-based nanomaterials for photocatalytic fuel generations. Chem. Rev. 114, 9987–10043.

Malika, M., Rao, C.V., Das, R.K., Giri, A.S., Golder, A.K., 2016. Evaluation of bimetal doped TiO_2 in dye fragmentation and its comparison to mono-metal doped and bare catalysts. Appl. Surf. Sci. 368, 316–324.

Paulino, P.N., Salim, V.M.M., Resende, N.S., 2016a. Zn-Cu promoted TiO_2 photocatalyst for CO_2 reduction with H2O under UV light. Appl. Catal. B Environ. 185, 362–370.

Paulino, P.N., Salim, V.M.M., Resende, N.S., 2016b. Zn-Cu promoted TiO_2 photocatalyst for CO_2 reduction with H_2O under UV light. Appl. Catal. B Environ. 185, 362–370.

Quiñones, C., Ayala, J., Vallejo, W., 2010. Methylene blue photoelectrodegradation under UV irradiation on Au/Pd-modified TiO_2 films. Appl. Surf. Sci. 257, 367–371.

Ramakrishnan, R., Kalaivani, S., Amala Infant Joice, J., Sivakumar, T., 2012. Photocatalytic activity of multielement doped TiO_2 in the degradation of congo red. Appl. Surf. Sci. 258, 2515–2521.

Riaz, N., Chong, F.K., Man, Z.B., Khan, M.S., Dutta, B.K., 2013. Photodegradation of Orange II under visible light using Cu–Ni/TiO_2 : Effect of calcination temperature. Ind. Eng. Chem. Res. 52, 4491–4503.

Roy, T.K., Mondal, N.K., 2017. Biosorption of Congo red from aqueous solution onto burned root of Eichhornia crassipes biomass. Appl. Water Sci. 7, 1841–1854.

Scrocco, M., 1979. X-ray photoelectron spectra of Ti^{4+} in TiO_2. Evidence of band structure. Chem. Phys. Lett. 61, 453–456.

Tobaldi, D.M., Piccirillo, C., Rozman, N., Pullar, R.C., Seabra, M.P., Kapin, A.S., Castro, P.M.L., Labrincha, J.A., 2016. Effects of Cu, Zn and Cu-Zn addition on the

microstructure and antibacterial and photocatalytic functional properties of Cu-Zn modified TiO_2 nano-heterostructures. J. Photochem. Photobiol. A Chem. 330, 44–54.

Yang, X., Wang, S., Sun, H., Wang, X., Lian, J., 2015. Preparation and photocatalytic performance of Cu-doped TiO_2 nanoparticles. Trans. Nonferrous Met. Soc. China 25, 504–509.

Chapter 7

Conclusions, Limitations and Future Work Directions

In this chapter the remarkable accomplishments, limitations of the present work, and major conclusions of the entire doctoral work are summarized. The directions for the further extension of the present work are also provided.

7.1 Overall Conclusions

The synergistic effect of bimetal nanoparticles and bimetal doped TiO_2 exhibited excellent antimicrobial and photocatalytic activities over mono-metal and mono-metal doped nanostructures. The conclusions based on the present study are:

- **Metal nanoparticles synthesis:** Natural capping agents protected particle aggregation with 98% AgNPs formation within 24 h of synthesis time. The bio-mediated synthesis of AgNPs using the *S. edule* extract is strongly pH dependent which in turn determines the size, shape, self-stabilization, and purity of particles and, its mechanism of formation. pH

also controls the concentration of AA in the bio-extract. The synthesized AgNPs possessed excellent crystallinity with FCC crystals, and a gradual blue shift in the SPR peak at around 425 nm was observed with the decrease in particle sizes with the increase in pH of AgNPs formation. AgNPs were formed through the reduction of both Ag^+ and Ag_2O; but, the smaller particles of nearly spherical shape were found at a higher pH with a faster kinetics where Ag_2O is abundant. The average hydrodynamic diameters were 68, 60, 45, 31, 15, and 9 nm at pH 3, 5, 7, 9, 11, and 12.5, respectively. The sharp rise in negative zeta potential and formation of the silver-ascorbate layer on AgNPs from a highly acidic medium with the increase in pH was indicative of its affinity for destabilization over a wide range of pH. AgNPs exhibited the character of ascorbate free radicals (g-value 2.0052) which might cause the synergistic effects in *B. subtilis* and *E. coli* inactivation mechanisms. AgNPs also was effective for the inhibition of growth of pathogenic fungus, *A. thermomutans.* The extraction of plant based analytes in the aqueous media and the synthesis of metal NPs by using these analytes is rather simple and environmental-friendly compared to conventional techniques. The metal nanoparticles synthesized in this route could be further utilized for electrochemical sensing of H_2O_2, wound healing, and electrocatalytic CO_2 reduction to value added chemicals.

- **Tailor-made bimetallic nanoparticles:** The analytes such as AA present in *S. edule* fruit extract also could successfully synthesize prismoidal, spherical, and core-shell structures of Co, Pt, and CoPt nanoparticles. The formation of Co^0 was thermodynamically more favorable than Pt^0. So, a dense core of Co or PtCo alloy was formed followed by a porous shell consisting of mostly Pt with an average core-shell diameter of 13.2 nm–28.6 nm. CoPt core-shell structures exhibited a better colloidal stability (zeta potential –46.2 mV at pH 12) and antimicrobial activity compared to the prismoidal and spherical Co and Pt counterparts, having mean diameter of 47.3 and 25.4 nm, respectively. The activity of core-shell particles and ciprofloxacin control was comparable for the inhibition of the growth of *E. coli*, but it outperformed cefprozil control for both *E. coli* and *B. subtilis*. In a broader point of view, tailor-made composite nanoparticles would offer new ways to engineer attractive optical, chemical, or electronic properties that combine the merit of each component which in turn could be harnessed to build a series of new devices with better functionalities.

- **Bio-mediated metal doped semiconductor photocatalysts:** The analytes present in the bio-extract are excellent reducing agents and acted for both Ag-doping, and AgNPs stabilization on TiO_2 and ZnO supports during the doping test but, the commercial AA led to AgNPs ridge formation (improper doping) on the catalyst surface. The immobilized Ag^+ (70 to 85 % of the initial amount) was suitably doped on TiO_2 and ZnO because of the amount of unreduced Ag^+ ion, as well as Ag_2O clusters, was insignificant. The proposed doping method increased the crystallite size of TiO_2 and ZnO with Ag-doping because of induction of Ag^+ ions into TiO_2 or ZnO crystal lattice. The diffuse reflection spectra of Ag/TiO_2 and Ag/ZnO gave a distinct absorption band in the visible region, and the band gap of bare TiO_2 and ZnO reduced dramatically with Ag-doping to 2.5 and 2.8 eV. So, the bandgap of TiO_2 and ZnO didn't reduce as effectively as for the commercial AA in comparison with the bio-inspired Ag-doped TiO_2 and ZnO. It is also evidenced by photocurrent studies with Ag/ZnO modified Indium tin oxide (ITO) coated glass substrate electrode and electron-spin resonance spectra. The doped catalyst exhibited a significant reduction in zeta potential both at above and below the pH_{zpc} due to the induced oxygen vacancies and, it provided Ag/TiO_2 and Ag/ZnO more stability in its aqueous colloidal solution. $O_2^{\bullet-}$ radical (g-value varies from 2.01 to 2.04 as identified from ESR spectra) formed on the surface of TiO_2 and ZnO was the most reactive species for degradation of Congo red dye and dipyrone drug with 98 and 80% efficiencies. The quantum yield (7.1-35.7 %) of Ag-doped catalyst for the degradation of dipyrone showed a clear superiority over many existing studies using conventional doping methods. The bio-mediated doping technique is extremely efficient, simple, and could be cost effective as compared to the conventional doping techniques in terms of suppression of e^-/h^+ recombination, bandgap energy reduction, and quantum yield for the pollutant degradation. Various functionalized catalysts can be developed for the applications in industrial water treatment, high-efficiency solar cells, water-splitting, CO_2 reduction to value added chemicals, and electrochemical sensors.

- **Bimetal doped TiO_2 photocatalyst:** The proposed bio-mediated technique was also successful for the doping of immobilized Cu^{2+} and Zn^{2+} (74 to 81 % of the initial amount) on TiO_2 support. The crystallite size of TiO_2 at higher dopants loading was increased significantly (16.3 to 38.4 nm) because of Cu^{2+} and Zn^{2+} induction into the Ti^{4+} lattice and, there was as high as 12% transformation of the anatase phase to the rutile phase of

TiO_2. The band gap of bare TiO_2 reduced significantly with Cu-doping to 2.3 eV and achieved maximum 98 % degradation of Congo red dye with bimetal doped TiO_2. The increase in the absolute value of zeta-potentials of $Cu/Zn/TiO_2$ was notably higher (5 mV per unit pH increase) at $pH>pH_{zpc}$ which was resulted from the rise in oxygen vacancies and, $Cu/Zn/TiO_2$ were mostly present as a separated non-aggregated unit in water with a polydispersity index of 0.201. The pseudo-first order model well fitted the dye decolorization kinetics and, there was about the sixteen-fold increase in the rate constant with $Cu/Zn/TiO_2$ compared to bare TiO_2. The $Cu/Zn/TiO_2$ exhibited higher quantum yield (41.5 %) than mono metal doping (23.4 – 30.8 %) due to the synergetic effect between Cu and Zn acting for a better charge separation than the mono-metal doped counterparts. The synergetic effects of bimetals used for the doping of photocatalysts in the proposed route have a vast scope of researches in environmental pollution abatement, hydrogen generation, and CO_2 photocatalytic conversion to methane and low hydrocarbons.

7.2 Limitations of the Work

? The synthesis of metal nanoparticles and doping of semiconductor supports were carried out in a small desktop reactor (200 – 1000 mL volume) and, the reaction time was extended up to 24 h due to a slower kinetics.

? The stability (size retention without significant aggregation) of nanoparticles was tested for a short period of time (up to 30 days). Therefore, the stability of these particles for longer duration may be an issue.

? The amount of capping agents adsorbed on the nanoparticles varied from 14- 20 %. So, the purity of the particles may limit their applications in many specific fields such as in tumor-killing effects of anticancer drugs, orthopedics, medical device coatings, optical sensors and drug delivery where high purity particles are must.

? The quality of biomass (hence, bio-analytes) depends on geographical location and cultivation condition. So, the repeatability and consistency of the experimental results both in nanoparticles synthesis and bio-mediated doping may be affected.

7.3 Recommendations for the Future Work

- An attempt was made for the elucidation of the mechanism of the synthesis of AgNPs using *S. edule* extract. But, the detail studies are imperative for a clear understanding of the mechanism of nanoparticle formation and stabilization in a bio-mediated process.
- Nanoparticles synthesized in a bio-mediated route could have numerous applications such as in biosensor development, electrochemical CO_2 reduction to value-added chemicals, wound healing, etc. So, these are the prudent areas of further researches in this domain.
- The bio-mediated technique for the doping of photocatalysts is proposed with this doctoral work and, it is at the nascent stage of development. Therefore, a lot of further investigations need to be done to bring this technique to the maturity level.
- In the case of the photocatalysis, the visible light assisted activities were tested by degrading model contaminants (Congo red dye and dipyrone drug). The investigation for treating industrial wastewater needs immediate research attention.
- The photocatalytic activities of doped catalysts were tested up to four cycles for the degradation of Congo red dye. So, there are vacuums for detail studies for the prolonged use of doped catalysts functionalized using the proposed technique.
- The biodegradable nature and toxicity assay of treated wastewater using these types of doped catalysts are also the potential areas of future research.
- The doped catalysts were tested only for the decomposition of Congo red dye and dipyrone drug. These catalysts have various potential applications such as photocatalytic water splitting to generate H_2 during wastewater treatment under solar/visible light illumination.

Research Output from the Thesis

Journal Publications

Ch. V. Rao and A.K. Golder, Ag-doping on ZnO support mediated by bio-analytes rich in ascorbic acid for photocatalytic degradation of dipyrone drug, *Chemosphere*, vol 208, pp. 149-158, May 2018.

C.V. Rao, and A.K. Golder, "Development of a bio-mediated technique of silver-doping on titania," *Colloids and Surfaces A: Physicochem. Eng. Aspects*, vol. 506, pp. 557–565, Jul 2016.

C.V. Rao and A.K. Golder, "pH dependent size control, formation mechanism and antimicrobial functionality of bio-inspired AgNPs," *RSC Adv.*, vol. 6, no. 98, pp. 95483–95493, Sep 2016.

C.V. Rao, S.S. Bag, and A.K. Golder, "A biosynthesis route to nearly spherical AgNPs using chayote fruit extract," *Environ. Prog. Sustain. Energy*, vol. 36, no. 1, pp. 192–199, Jan 2017.

C.V. Rao, K. Bakal, and A.K. Golder, "Biomediated synthesis of ZnO nanoparticles (ZnONPs) for photocatalytic application," *Internat. J. Cur. Eng. Sci. Res.*, vol. 1, no. 4, pp. 26–30, Dec 2014.

C.V. Rao, and A.K. Golder, "Bimetal doping on TiO_2 for photocatalytic water treatment: A green route," *European Water*, May 2017. (Accepted)

C.V. Rao, and A.K. Golder, "One Pot green synthesis of Pt–Co bimetallic core-shell nanoparticles using plant extract," *Canadian J. Chem. Eng.*, (Revised manuscript submitted)

C.V. Rao, S. Chakraborty, and A.K. Golder, "Ag-doing on TiO_2 using plant-based glycosidic compounds for high photonic efficiency degradative oxidation under visible light," (Communicated)

Conference Publications

Ch.V. Rao, and A.K. Golder, "Bimetal doping on TiO_2 for photocatalytic water treatment: A green route," European Water Resources Association, National Technical University of Athens, Athens, Greece, Jul 2017.

Ch.V. Rao, and A.K. Golder, "Visible light activation of ZnO photocatalysts for wastewater treatment," Reflux 2017, Indian Institute of Technology Guwahati, Assam, India, Mar 2017.

Ch.V. Rao, A.K. Singh, and A.K. Golder, "Studies on bio-mediated fabrication of AgNPs," Reflux 2017, Indian Institute of Technology Guwahati, Assam, India, Mar 2017.

Ch.V. Rao, R.K. Das, S.R. Dash, P. Ghosh, S. Saha, and A.K. Golder, "A bio-mediated route of AgNPs synthesis and photocatalyst activation," IITG-KIT Joint Symposium on Soft and Biobased Materials, Kyoto Institute of Technology, Kyoto, Japan, Aug 2016.

Ch.V. Rao, R.K. Das, S.R. Dash, P. Ghosh, S. Saha, and A.K. Golder, "A biological route of AgNPs synthesis: Size control and functionality," Biotechnology, Biomaterials and Renewable Energy, GIFU University, GIFU, Japan, Aug 2016.

Ch.V. Rao, and A.K. Golder, "Nerium Oleander leaf extract mediated synthesis of nickel nanoparticles and its potential application," International Conference on Bioscience and Biotechnology, University of Sri Jayawardenepura, Colombo, Srilanka, Jan 2016.

Ch.V. Rao, A.K. Singh, and A.K. Golder, "One pot green synthesis of Pt-Co bimetallic nanoprisms using plant extract," CHEMCON 2016, A.C.Tech, Anna University, Chennai, India, Dec 2016.

Ch.V. Rao, S. Chakraborty, and A.K. Golder, "Biomediated synthesis of spherical silver nanoparticles using *S. edule* extract and its activity," CHEMCON 2015, Indian Institute of Technology Guwahati, Guwahati, Assam, India, Dec 2015.

Ch.V. Rao, and A.K. Golder, "Synthesis, characterization and photocatalytic behavior of silver-doped ZnO using chayote extract," International Conference on Water, UCentre for Environment Education and Technology, Kottayam, India, Jan 2015.

Ch.V. Rao, K. Bakal, and A.K. Golder, "Biomediated synthesis of ZnO nanoparticles (ZnONPs) for photocatalytic application," International Conference on Civil and Chemical Engineering, Warangal, India, Nov 2014.

Ch.V. Rao, S.S. Bag, and A.K. Golder, "Photolytic degradation of Brilliant Green dye: Process performance and kinetic studies," CHEMCON 2013, Institute of Chemical Technology, Matunga, Mumbai, India, Dec 2013.

Ch.V. Rao, Shivraj, and A.K. Golder, "Spectral sensitization of TiO_2 by copper doping: A biological approach," National Conference on Challenges in Environmental Research, Indian Institute of Technology Guwahati, Assam, India, Jun 2015.

Exhibition

Ch. V. Rao, S. Chakraborty and A. K. Golder, Bio-mediated synthesis of nanophotocatalyst: A greener initiative, REFLUX-2015, March 28-29, Indian Institute of Technology Guwahati, India.

Workshop

National workshop on technical writing conducted under the technical education quality improvement programme sponsored by the Ministry of Human Resource Development, Government of India, held on December 6-7, 2014.

Awards

Best presentation award for the paper entitled "One pot green synthesis of Pt-Co bimetallic nanoprisms using plant extract", in CHEMCON 2016, 27-30 December, 2013, A.C.Tech, Anna University, Chennai, India.

Best presentation award for the paper entitled "Visible light activation of ZnO photocatalysts for wastewater treatment", in Reflux-2017-Annual Chemical Engineering Symposium, Department of Chemical Engineering, 24-26 March, 2017, IIT Guwahati, Assam, India.

Other Publications

C.V. Rao, A.S. Giri, V.V. Goud, and A.K. Golder, Studies on pH-dependent color variation and decomposition mechanism of Brilliant Green dye in Fenton reaction, *Internat. J. Ind. Chem.*, 2016, 7(1), 71–80.

A.K. Behera, **C.V. Rao**, R.K. Bag, A.S. Giri, and A.K. Golder, Fabrication and characterization of Ag-doped titania: impact of dye-sensitization, phenol decomposition kinetics and biodegradability index, *Desalin. Water Treat.*, 2016, 57(20), 9488–9497.

M. Malika, **C.V. Rao**, R.K. Das, A.S. Giri, and A.K. Golder, Evaluation of bimetal doped TiO_2 in dye fragmentation and its comparison to mono-metal doped and bare catalysts, *App. Surf. Sci.*, 2016, 368, 316–324.

S. Chakraborty, **C.V. Rao**, R.K. Bag, A.S. Giri, and A.K. Golder, Bio-mediated silver nanoparticle synthesis: mechanism and microbial inactivation, *Toxicol. Environ. Chem*., 2017, 99(3) 434–447.

R.K. Das, S. Saha, **C.V. Rao**, and A.K. Golder, Bio-inspired AgNPs, multilayers reduced graphene oxide and graphite nanocomposite for electrochemical H_2O_2 sensing, *Bull. Mater. Sci.* 2018, 41(3), 86.

P. Ghosh, **C.V. Rao**, A.S. Giri, and A.K. Golder, Steroid glycosides as potential analytes for Cu-doping on TiO_2 for photocatalytic water treatment, *Environ. Prog. Sustain. Energy*, 2018. DOI 10.1002/ep.12879.